Development of a portable laser-cooled ytterbium ion microwave atomic clock



Sean Mulholland

Department of Physics

University of Oxford

Experimental work undertaken at the
National Physical Laboratory



Submitted for the degree of Doctor of Philosophy

St Peter's College

April 2019

Abstract

Portable microwave clocks that incorporate laser cooling promise to bring significantly improved performance compared to commercially available microwave clocks that are based on thermal atoms. This thesis reports on the development of a portable, laser-cooled ytterbium-171 trapped-ion microwave frequency standard from design to testing. The entire system fits into a 6U 19-inch rack unit ($51 \times 49 \times 28\,\mathrm{cm}$) and comprises laser, electronics and physics package subsystems. The performance of the system was evaluated; the fractional frequency instability was measured to be $3.6 \pm 0.2 \times 10^{-12}/\sqrt{\tau}$ for averaging times between 30 s and 1500 s.

Acknowledgements

I would like to gratefully acknowledge U.K. Defence Science and Technology Laboratory (Dstl) for funding the developments here reported and for sponsoring my DPhil.

This thesis would not have been possible without the support of my colleagues, friends and family.

Thanks to the colleagues who have worked with me on this project: Hugh Klein — for teaching me the tricks of the trade of an atomic physics lab, and for all the personal and professional support that he has given me; Sean Donnellan — for introducing me to digital electronics; Greg Walsh — for his help with analogue electronics; Geoffrey Barwood — for his knowledge of lasers and for lively discussions; Guilong Huang — for his meticulous lab work; David Gentle — for his microwaves expertise and for fixing my bike; Peter Nisbet-Jones — for his advice on designs; Steven King – for his wide knowledge and enthusiasm; and my supervisors, the Patricks Baird and Gill — for their guidance.

Thanks to the scientists who welcomed me to Oxford and the National Physical Laboratory (NPL) and have been supportive during my DPhil. Special thanks to Rachel Godun, Richard Hobson, and Guido Wilpers for always having time for my questions.

I was very fortunate to start my DPhil at the same time as two other students: Charles Baynham and William Bowden, the camaraderie has been a constant source of support and you both helped me out when I was stuck. Thanks Charles, for putting up with my numerous distractions, and thanks William, for sharing many bike rides.

On behalf of those who read this thesis I'd like to thank my Mum and Liz for reading over drafts and reigning in my tendency to write in long and confusing sentences with multiple clauses and without enough commas.

Thank you to my friends for providing welcome distractions in the dark days spent troubleshooting an experiment that would not work.

Thank you to Mum, Dad, and Roisin for all the support and guidance over the years. You have made me who I am, and from your example, I've learned the value of honest hard work.

And thank you Liz, your companionship through my DPhil has been amazing. Thanks for helping me through the difficulties, and for widening my horizons.

Contents

Contents vii

List of Figures xi

List of Tables xv

1 Introduction 1
- 1.1 Clocks . . . 2
- 1.2 Figures of merit . . . 2
  - 1.2.1 Allan variance . . . 3
  - 1.2.2 'SNRQ' — Locking to noisy resonances . . . 4
  - 1.2.3 Measuring frequency stability . . . 7
- 1.3 Microwave atomic frequency standards . . . 7
  - 1.3.1 Atomic beam-tube . . . 7
  - 1.3.2 Atomic fountain . . . 9
  - 1.3.3 Maser . . . 9
  - 1.3.4 Vapour cells . . . 10
  - 1.3.5 Ion traps . . . 11
- 1.4 Project Goals . . . 14
- 1.5 System architecture . . . 15
- 1.6 System requirements . . . 17
- 1.7 System layout . . . 18
- 1.8 Thesis outline . . . 19

2 Background Theory 21
- 2.1 Ion trapping . . . 21
  - 2.1.1 Electric potentials . . . 24
  - 2.1.2 Equations of motion . . . 26
  - 2.1.3 Trap depth . . . 28
  - 2.1.4 Trap capacity and the effect of adding extra ions . . . 29
  - 2.1.5 Coulomb crystals and ion clouds . . . 30
- 2.2 Atomic physics of ytterbium ions . . . 32
  - 2.2.1 Transitions between hyperfine states . . . 36
- 2.3 Spectroscopy . . . 39

2.3.1 Rabi Spectroscopy . . . 39
2.3.2 Ramsey Spectroscopy . . . 41
2.3.3 Double-resonance . . . 42
2.4 Systematic frequency shifts . . . 44
2.4.1 Motional shifts . . . 45
2.4.1.1 First-order Doppler effect . . . 45
2.4.1.2 Second-order Doppler effect . . . 46
2.4.2 Electric field shifts . . . 47
2.4.2.1 Light shift (AC Stark shift) . . . 48
2.4.3 Magnetic shifts . . . 49
2.4.3.1 First-order Zeeman effect . . . 49
2.4.3.2 Second-order Zeeman effect . . . 50

3 Laser System **53**
3.1 $^{171}Yb^{+}$ term scheme and overview of the required lasers . . . 53
3.2 Laser specifications . . . 54
3.3 Laser package layout . . . 56
3.4 Frequency stabilisation . . . 62
3.4.1 Wavemeter method . . . 62
3.4.2 Air absorption . . . 63
3.5 Laser system conclusions . . . 65

4 Physics Package **67**
4.1 Ion trap designs . . . 67
4.1.1 Mark 1 ion trap design . . . 67
4.1.2 Mark 2 and Mark 3 ion trap design . . . 72
4.2 Vacuum chamber and pumps . . . 79
4.3 Laser delivery . . . 80
4.4 Magnetic shielding . . . 84
4.5 Magnetic field coils . . . 84
4.6 Imaging system . . . 87

5 Electronics and Control **89**
5.1 Component overview . . . 89
5.1.1 Local oscillator and Frequency chain . . . 89
5.1.1.1 Stability measurement of the local oscillator . . . 91
5.1.1.2 Microwave switches . . . 93
5.1.2 Microwave antenna . . . 95
5.1.3 Trap drive . . . 98
5.1.4 Oven control . . . 100
5.1.5 Stable voltage sources . . . 102
5.1.6 Current supply for lasers and magnetic field coils . . . 102
5.1.7 Power supply . . . 103
5.1.8 FPGA and microcontroller . . . 103

5.2 Experiment control sequences . . . 105
5.2.1 Ion loading . . . 105
5.2.2 Spectroscopy . . . 106
5.2.3 Clock locking . . . 106

6 Dark Ions 109
6.1 Formation of dark ions . . . 111
6.2 Identification of dark ions . . . 112
6.2.1 Laser spectroscopy . . . 113
6.2.2 Ion trap measurements . . . 115
6.2.3 Dark ion conclusions . . . 119

7 Frequency Standard Operation 121
7.1 Stability . . . 122
7.1.1 Shot-noise limit to stability . . . 123
7.1.1.1 SNR limitations . . . 124
7.1.2 Stability measurement of the locked frequency standard . . . 125
7.2 Reliability . . . 128
7.3 State control . . . 129
7.3.1 Cooling . . . 130
7.3.1.1 Transition profiles . . . 131
7.3.2 State preparation . . . 134
7.3.3 Clock pulse . . . 136
7.4 Operating magnetic field . . . 137
7.5 Trap-related effects . . . 141
7.5.1 Ion heating . . . 141
7.5.2 Ion loss . . . 142
7.6 Evaluation of sources of noise, frequency shifts and instability . . . 142
7.6.1 Shot-noise and dead-time . . . 143
7.6.2 Second-order Zeeman . . . 143
7.6.2.1 Second-order Zeeman — background magnetic field . . . 143
7.6.2.2 Second-order-Zeeman — coils . . . 146
7.6.3 Second-order Doppler . . . 146
7.6.4 Quadratic Stark shift . . . 148
7.6.5 Light shift (AC Stark shift) . . . 149
7.6.6 BBR shift (AC Stark shift) . . . 149
7.6.7 Dick effect . . . 150
7.6.8 Gravitational redshift . . . 150
7.7 Frequency standard operation conclusions . . . 150

8 Outlook and Conclusions 153

References 157

A Engineering Drawings **169**

B Electronic Schematics **179**

List of Figures

1.1 Identifying noise process from Allan deviation against averaging-time . . 5
1.2 Annotated Rabi lineshape — highlighting parameters important for stability. 6
1.3 Caesium beam tube schematic. 8
1.4 Hydrogen maser schematic. 10
1.5 CPT frequency standard schematic 11
1.6 $^{171}Yb^{+}$ microwave clock schematic 12
1.7 Qualitative overview of the attributes of classes of microwave atomic clocks. 14
1.8 Schematic overview of the clock system. 15
1.9 System architecture 16
1.10 System layout 18
1.11 Microwave clock assembled in case 19

2.1 A variety of ion trap designs 23
2.2 Basic linear ion trap geometry 24
2.3 Stability diagram for linear ion trap 27
2.4 Ion position against time in one dimension. 29
2.5 ^{171}Yb partial term schemes 33
2.6 Ground state term scheme 37
2.7 Ground state energy levels in a small magnetic field. 37
2.8 Rabi lineshape and its frequency sensitivity. 40
2.9 Central Ramsey fringe and FWHM. 42
2.10 Simplified term scheme of transitions 44

3.1 ^{171}Yb partial term schemes 54
3.2 Laser bank 58
3.3 Schematic of the 369, 399 and 935 nm laser board 59
3.4 Labeled photographs of the 935-nm and 369- and 399- nm laser systems. 60
3.5 760 and 798 nm laser board beam paths andschematic 61
3.6 Coincidence between oxygen absorption and Yb transitions at 760 nm . . 64
3.7 Water vapour absorption lines in air and Yb^{+} transitions near 935 nm . . 65

4.1 Modelled radial trapping fields in Mark 1 ion trap 69
4.2 Mark 1 ion trap 70
4.3 Double resonance scan in Mark 1 trap 71

4.4 Coulomb crystal of ∼ 300 ions from Mark 1 trap . . . 72
4.5 Ion trap assembly . . . 73
4.6 Mark 2 and mark 3 ion traps . . . 75
4.7 Calculated trap parameters for the Mark 2 trap at 2 MHz drive frequency as a function of V_{pk-pk}. . . . 76
4.8 Ion cloud from Mark 2 trap . . . 77
4.9 Labelled oven photographs . . . 78
4.10 Photograph of the vacuum chamber . . . 80
4.11 Schematic of the overlap of the laser beams and ion cloud. . . . 82
4.12 Laser delivery to ion trap . . . 83
4.13 Schematic of the coil arrangement. . . . 86
4.14 Imaging system . . . 88

5.1 Detailed frequency chain . . . 92
5.2 Unlocked LO Allan deviation . . . 93
5.3 Frequency chain noise and stability measurement noise floor . . . 94
5.4 Microwave switching . . . 96
5.5 'Ramsey fringes' with poor isolation . . . 96
5.6 Improved microwave switching . . . 97
5.7 Microwave antenna . . . 99
5.8 Ion trap oscillator . . . 99
5.9 Ion trap oscillator schematic . . . 100
5.10 Oven control logic . . . 101
5.11 Experiment control overview . . . 104
5.12 Flow diagram for the clock control GUI . . . 105
5.13 Timing sequences for Rabi and Ramsey spectroscopy . . . 107
5.14 Calculating the gain . . . 108
5.15 Probe sequence . . . 108

6.1 Ion crystals and dark ions . . . 110
6.2 Signal decay due to dark ions . . . 112
6.3 Test to determine if dark ions were YbH^+ . . . 114
6.4 Test to determine if dark ions were in the F-state . . . 116
6.5 Spatial ordering by charge to mass ratio of two component ion crystal . . . 117
6.6 Separation of ions by mass . . . 118

7.1 Stability measurement . . . 122
7.2 Rabi lineshape . . . 123
7.3 Incomplete state preparation impact . . . 124
7.4 Microwave clock stability . . . 127
7.5 Ion fluorescence signal loss during the clock measurement . . . 128
7.6 Simplified term scheme of transitions . . . 130
7.7 Cooling time measurement . . . 131

7.8 Laser cooling profiles that illustrate the hysteresis effect of forming a Coulomb crystal. . . . 133
7.9 Laser transition profiles . . . 135
7.10 Spatial temperature variation in a Coulomb crystal . . . 136
7.11 Minimising residual magnetic field . . . 139
7.12 Schematic of sideband generation from a magnetic field gradient . . . 140
7.13 Magnetic shields with an imaging hole. . . . 144
7.14 Magnetic field fluctuations . . . 145
7.15 Measurement of coil current, and second-order Zeeman instability . . . 147
7.16 Temperature measurement of the ion cloud after a 4 s clock pulse . . . 149

A.1 'Hex chamber' drawings . . . 170
A.2 'Splitter chamber' drawings . . . 171
A.3 Mu-metal shields . . . 172
A.4 Soft-iron ion pump shields . . . 173
A.5 Vertical compensation plate electrode . . . 174
A.6 Rod electrodes . . . 175
A.7 Endplate electrodes . . . 176
A.8 Horizontal compensation plate electrode and oven holder . . . 177
A.9 Ground plate electrode . . . 178

B.1 Stable current source 1/7 . . . 180
B.2 Stable current source 2/7 . . . 181
B.3 Stable current source 3/7 . . . 182
B.4 Stable current source 4/7 . . . 183
B.5 Stable current source 5/7 . . . 184
B.6 Stable current source 6/7 . . . 185
B.7 Stable current source 7/7 . . . 186
B.8 Current noise density of stable current source. . . . 187
B.9 Oven control and PSU . . . 188
B.10 Microwave switch driver . . . 189
B.11 Stable voltage sources . . . 190
B.12 Power supply block diagram . . . 191
B.13 Switching and linear regulators . . . 192
B.14 Power supply schematic . . . 193

List of Tables

1.1 Noise processes — power spectral density and ADEV. 4
1.2 Comparison of microwave frequency standards. 13
1.3 Required lasers 17

2.1 Isotopic composition of terrestrial ytterbium. 32

3.1 Laser feedback methods 63

4.1 Mark 1 ion trap parameters 70
4.2 Mark 2 and Mark 3 ion trap parameters 74
4.3 Coil properties 85

5.1 Microwave switch isolation. 98

7.1 Magnetic field shielding factors. 144
7.2 Sources of noise, frequency uncertainty and frequency offsets 152

Chapter 1

Introduction

In 1714 the British government offered the 'Longitude prize' [1] for the development of a clock that was accurate, portable and robust enough to determine longitude on a rocking ship from astronomical measurements. The winning chronometer, John Harrison's H4 clock, pioneered several breakthrough technologies, such as the bimetallic strip and the caged roller bearing. However, the most significant legacy for frequency metrology was that small, high-frequency oscillators, in his case spring balance wheels at 5 Hz, were much more stable than the then conventional slowly oscillating pendulums.

In 1955, a new era of timekeeping began as Louis Essen demonstrated the first accurate atomic clock at the UK National Physical Laboratory (NPL) [2]. Essen's oscillator, the caesium atom's hyperfine splitting, 'ticked' at 9192631770 Hz. Astronomical time, referenced to the relatively unstable motion of the earth, was made obsolete.

Navigation systems based on accurate atomic clocks in space are now ubiquitous. Accurate time broadcast from these satellites plays a crucial role in many industries, ranging from defence to financial trading.

High accuracy atomic clocks now exist in national measurement institutes such as NPL. However, many field applications require highly precise timing where signals from satellites are too unreliable, imprecise or are not available. These applications' needs can be met by making compact and portable atomic clocks available for use outside of a laboratory.

This thesis presents the development of a laser-cooled, portable microwave atomic clock. The target of this clock is to achieve performance ten times better than the current state of the art, in both stability and accuracy, for a portable system.

1.1 Clocks

A clock in its simplest sense consists of an oscillator and a counter. An oscillator consists of two components, a generator and a discriminator. The generator makes a 'tick', and the discriminator defines the duration of one tick. The elapsed time is measured by counting the ticks.

In a pendulum clock, the peak of the resonance of the pendulum's motion acts as the discriminator and the electronics (or clockwork) driving the motion as the generator. In an atomic frequency standard, the discriminator is the energy separation of a 'clock transition', and the generator is a source of electromagnetic waves. Unlike in a pendulum clock, where the discriminator is actively oscillating, in many atomic clocks the discriminator is passive. A passive discriminator has its frequency-selective property interrogated by a variable-frequency oscillator. Drifts in the oscillator frequency are corrected by periodically measuring the discriminator response and applying the appropriate adjustment to the oscillator.

Since atoms of the same isotope are indistinguishable, an atomic reference does not require an artefact, for example, a pendulum or the rotation of the earth, and so can be easily reproduced. Atomic clocks use the energy difference between atomic states to define a time interval.

1.2 Figures of merit

A clock is generally assessed on its stability and accuracy. Stability is the quality of each of the 'ticks' of the clock lasting an equal time interval. This is often quoted through the measure of the Allan variance, outlined in the next section.

Accuracy, which is sometimes referred to as reproducibility, is the quality of the averaged frequency measurement and reflects the level of uncertainty in the measurement due to systematic errors (discussed in chapter 2). Inaccuracy limits the precision to which the SI (International System of Units) second [3] can be realised.

A clock with good stability but poor accuracy will display a constant time drift, which can be easily removed by calibrating against an accurate clock. A clock with good accuracy but poor stability will spend an equal amount of time running fast and slow relative to the correct time.

1.2.1 Allan variance

The Allan variance, also known as the two-sample variance, is used to characterise frequency fluctuations in the time domain. It measures the error in the ability to predict a future frequency offset, with respect to a reference oscillator, using past data; this can be thought of as the variance of frequency-extrapolation errors [4–6]. The Allan variance is given by equation (1.1). It is defined as one-half of the time average of the square of the differences between successive readings of the frequency deviation at a sampling frequency:

$$\sigma^2(\tau) = \frac{1}{2}\left\langle (\bar{y}_{n+1} - \bar{y}_n)^2 \right\rangle, \tag{1.1}$$

with $\bar{y}_n$ and $\bar{y}_{n+1}$ as successive frequency deviation measurements (over a period τ) and $\langle\,\rangle$ as the time average over all measurements.

Taking the square root of the Allan variance yields the Allan deviation (ADEV). An extension of the ADEV statistic that overlaps the samples to make more efficient use of the collected data is called the Overlapping Allan Deviation (OADEV). The OADEV provides an improved estimate of the instability, $\sigma(\tau)$. The standard way (IEEE standard 1139-1999) to express instability measurements is to quote the fractional OADEV $\sigma(\tau)/\nu = \sqrt{\sigma^2(\tau)}/\nu$. This is quoted as a series of values at specified averaging times.

Noise process	Power Spectral Density Frequency Dependence	Allan deviation
White phase	f^2	τ^{-1}
Flicker phase	f^1	τ^{-1}
White frequency	f^0	$\tau^{-1/2}$
Flicker frequency	f^{-1}	τ^0
Random frequency walk	f^{-2}	$\tau^{1/2}$
Drift	N/A	τ^1

Table 1.1: Noise processes, defined by their power spectral density frequency dependence, appear in the time domain as different averaging behaviours of the ADEV.

The gradient of the ADEV as a function of averaging-time on a log-log plot yields information about the dominant noise source at a given averaging-time. This is shown in figure 1.1 and table 1.1. At intermediate to long timescales, the noise in an atomic clock is typically limited by shot-noise in measuring the quantum state, either due to detection noise or quantum projection noise (QPN). These noise processes have the character of white frequency noise, so long-term instability is often quoted as $\sigma(\tau) = 10^{-x}/\sqrt{\tau}$.

1.2.2 'SNRQ' — Locking to noisy resonances

If the frequency of a resonance is not changing with time, the stability of a passive frequency standard locked to the resonance will depend on how well this frequency can be determined. Figures of merit for a frequency standard reference are the 'narrowness' of the resonance and the strength of the signal. The narrowness is quantified by the quality factor, Q. The quality factor is defined as the resonant frequency divided by the full-width-at-half-maximum (FWHM) of the resonance. A large Q shows that the resonance is highly frequency-selective. The signal strength is quantified by the signal to noise ratio, SNR. An illustrative trace of a noisy Rabi resonance is shown in figure 1.2.

The fractional frequency instability limit from locking to a noisy resonance is given by equation (1.2): [7–9]:

$$\sigma(\tau) = \frac{1}{K \cdot \mathrm{SNR} \cdot Q}\sqrt{\frac{t_p + t_d}{\tau}}, \tag{1.2}$$

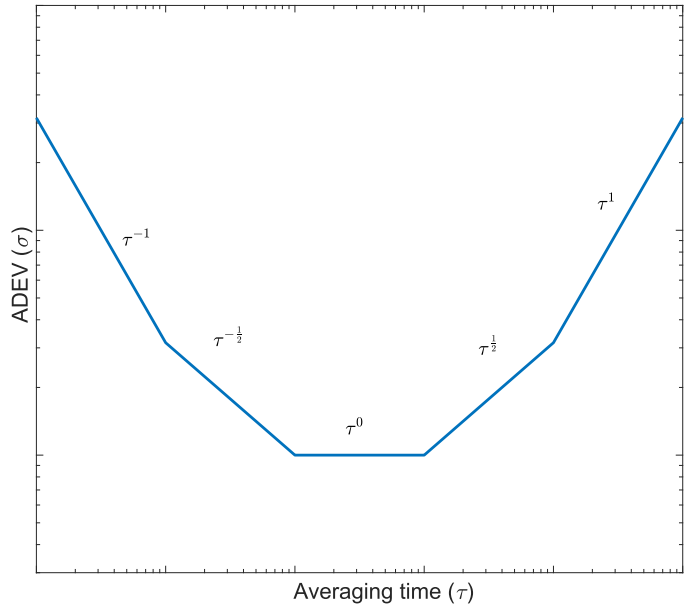


Figure 1.1: log-log plot of the Allan deviation σ against averaging time τ. The gradient of the plot provides information on the primary noise contribution over the timescale considered.

where SNR is the signal to noise ratio; Q is the quality factor[1]; t_p and t_d are the probe-time and dead-time respectively; τ is the averaging time; and K is a constant of order one that is related to the gradient of the resonance at the lock points. $K = \pi$ is normally assumed, and is exact in the case of Ramsey spectroscopy with short pulses[2].

It can be seen from equation (1.2) that the short-term instability is minimised by maximising the product $SNR \cdot Q$. As a result, the one-second 'SNRQ' is an often quoted figure of merit when comparing frequency standards. As a generalisation, neutral-atom atomic frequency standards tend to have superior SNR, but inferior Q, to trapped-ion atomic frequency standards.

The SNR is fundamentally limited by the number of atomic references. For conventional spectroscopy techniques, it increases with the square root of the number of atoms due to quantum projection noise. It may also be limited technically, for example

[1]The Q factor is proportional to the probe time for Fourier-limited spectra.
[2]For Rabi spectroscopy, $K = 0.97 \times \pi$.

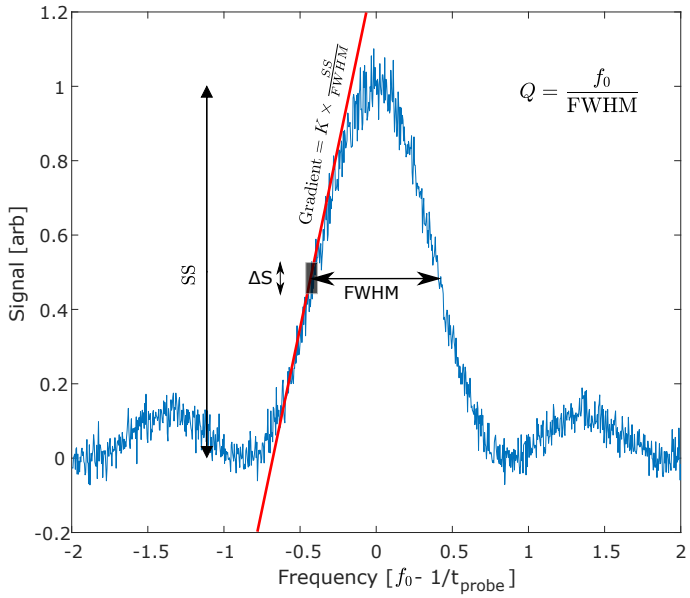


Figure 1.2: An illustrative trace of a noisy Rabi resonance, annotated with parameters that determine the achievable fractional frequency instability. Noise at the lock points, ΔS, is converted into noise in the locked frequency by the frequency discriminant, which is given by the gradient of the lineshape at the lock points. The discriminant is enhanced by having large signal height, SS, relative to the noise level and a small FWHM.

by incomplete state preparation or by inefficient detection, where a single atom's state cannot be fully determined above the noise level.

The quality factor is limited by both the resonant frequency of the chosen atomic reference and the FWHM of that resonance. The resolved FWHM reduces with the inverse of the probe-time, which is limited by technical factors, typically due to the stability of the local oscillator (LO)[3]. Other limits include decoherence, atom lifetime and trap-heating. A portable system will have reduced LO performance compared to a laboratory-based clock, and so the primary method of improving the stability is through increasing the number of atomic references.

[3]The LO is a frequency reference, ideally with good short-term stability, which acts as a flywheel between clock measurements.

1.2.3 Measuring frequency stability

The most straightforward way to measure frequency stability is to compare the device under test to a reference clock with higher stability. Fortunately, at NPL there is a maser-stabilised 10 MHz distributed to the laboratories that satisfies this requirement. The same maser-referenced 10 MHz is used to generate the UK's timescale, UTC(NPL), and it is steered three times a week by a caesium fountain (section 1.3.2). During a stability measurement, the nominal 10 MHz from the microwave clock is compared with the stable 10 MHz from the maser on a phase comparator. The phase offset is logged as a function of time, and the OADEV is calculated. To obtain a stability estimate at a given averaging period, data will typically need to be taken for at least four times this period. This is so that a statistically significant number of averages over this time period within the data can be compared.

1.3 Microwave atomic frequency standards

The following subsections contain a brief discussion of notable microwave atomic frequency standards, both laboratory-based and commercial-transportable, and their limitations. These are summarised in table 1.2. In the final subsection, I discuss trapped-ion frequency standards. This thesis details the development of a laser-cooled, trapped-ion, frequency standard, which promises to overcome limitations of the current technology, through the high levels of environmental isolation possible with this approach.

1.3.1 Atomic beam-tube

Louis Essen's 1955 atomic clock was of a beam-tube design; beam tubes then quickly left the laboratory and became commercially available one year later in 1956. The '5071A' clock is the current state of the art of commercial portable atomic clocks — despite the design being from 1988.

A beam tube consists of two state-selection magnets separated by an interaction region. A beam of thermal atoms is fired through the system and the proportion of

atoms that change state is measured. The frequency of the microwave radiation in the interaction region is then tuned so that half of the atoms change state. A schematic of the operation is shown in figure 1.3.

Caesium (Cs) beam tubes have many favourable characteristics, including reliability, robustness and insensitivity to temperature and humidity environmental noise. Their major shortcoming is their short-term stability, which is limited by the shot noise of atoms arriving in the detector. Their long-term stability and accuracy is limited by both the second-order Zeeman shift and second-order Doppler shift. The second-order Zeeman shift is due to magnetic field inhomogeneity in the interaction region, and the second-order Doppler shift is due to relativistic effects caused by rapidly moving atoms.

The interaction time of a Cs beam tube is limited by the beam length, which cannot be practically increased. The Ramsey linewidth in a 5071A is approximately 1 kHz, resulting in a Q factor of 1×10^7. The clock obtains its high performance level with its relatively large 1-second-SNR of 3000 [10, 11]. Caesium beam tube clocks consume ~60W and cost ~$50k.

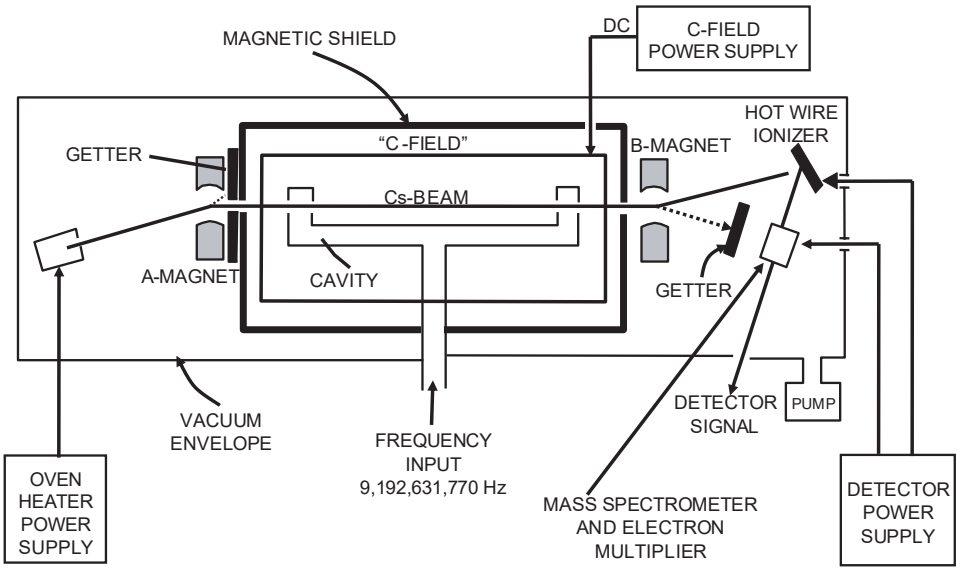


Figure 1.3: A schematic showing the operation and key components of a caesium beam tube with a Ramsey measurement scheme, from reference [12]

1.3.2 Atomic fountain

The state of the art of laboratory-based, microwave atomic clocks is the caesium fountain. Measurements of the hyperfine splitting of caesium undertaken in fountains underpin the SI second, defined as exactly the period of 9192631770 oscillations of the unperturbed transition frequency. In a fountain clock, a laser-cooled sample of atoms is launched vertically upwards and interacts with a microwave cavity once on the way up, and a second time on the way down. The current best performance is fractional inaccuracy approaching 1×10^{-16}, and instability of $1 \times 10^{-14}/\sqrt{\tau}$ [13, 14].

NPL has produced caesium fountains for other national measurement institutes (NMIs) [15], but these are not widely commercially available. However, fountains are not suitable for portable clocks, as they are extremely sensitive to tilt and acceleration.

1.3.3 Maser

A maser is the microwave analogue of a laser. It works by state-selecting atoms in a meta-stable upper hyperfine ground state, and then measuring the frequency of the decay back to the ground state. A schematic of a hydrogen maser is shown in figure 1.4. Masers are somewhat unusual within atomic frequency standards in that they can be operated in a mode where the discriminator is active. Masers are used for their excellent short-term instability typically 10^{-13} at 1 s and 10^{-15} at 1000 s, but have poor accuracy and exhibit a long-term frequency drift, which has to be periodically calibrated. They tend to be large floor standing units and are housed in environmental chambers to minimise perturbations, making them unsuitable for portable use. They typically consume 150 W and cost approximately $200k [16].

Hydrogen masers, operating in a passive-discriminator mode, form part of the Galileo ensemble of satellite-based clocks. They have a stability of $7 \times 10^{-13}/\sqrt{\tau}$ between 10 and 10,000 seconds [17].

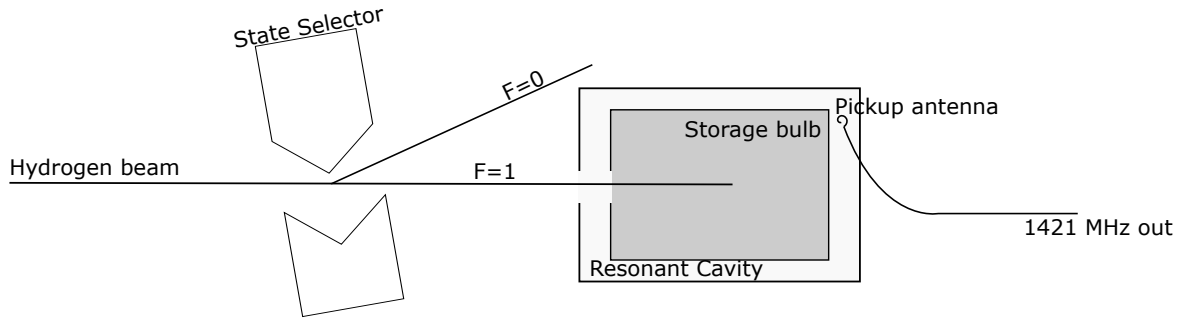


Figure 1.4: A schematic showing the key components and operation of a hydrogen maser.

1.3.4 Vapour cells

Vapour cells are commonly used for laser frequency stabilisation. A glass cell is evacuated, and a small sample of metal is introduced along with a buffer gas. The cell is sealed, and the vapour from the metal produces an absorption signal from laser beams travelling through the cell. The apparatus for a coherent population trapping (CPT) frequency standard is shown in figure 1.5. Typically, the atomic reference is either caesium or rubidium.

The chip-scale-atomic-clock (CSAC) is a new, extremely miniaturised form factor for atomic clocks (typical volumes are tens of cubic centimetres). Due to their small size and power constraints, CSAC devices tend to have lower performance than other commercially available clocks. Their accuracy and long-term stability are limited by an ageing process and by uncontrolled interactions between the atoms, background gases and the glass cell. Typical performance is $1 \times 10^{-10}/\sqrt{\tau}$ stability up to one-hour averaging time [18].

Recently an atomic clock based on laser-cooled rubidium atoms in a vapour cell has become available [19]. However, at 135 kg and 1.5 m tall, it is a laboratory device aimed to be a maser-complement, and is not suitable as a portable device.

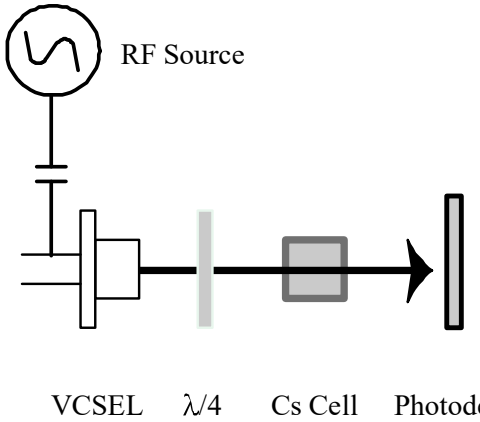


Figure 1.5: Apparatus for a CPT frequency standard. From reference [20]

1.3.5 Ion traps

A radiofrequency electric potential, typically a few hundred volts at several MHz, is applied to an array of electrodes to create an ion trap (see section 2.1). Small numbers of ions can be laser-cooled to mK temperatures and experience very low environmental noise, allowing them to be probed while virtually 'at rest'. Using ion traps, extremely small uncertainties in the clock-frequency down to the 10^{-18} level have been reported for single-ion optical frequency standards [21, 22][4]. In the microwave regime, many ions are trapped to improve the SNR in equation (1.2); this results in ions in different parts of the ion trap experiencing different environments, and so the frequency shifts are larger. A cryogenic mercury ion clock at NIST [23] with seven ions achieved a clock-frequency uncertainty of 3×10^{-15}. A millimetre long cloud of approximately 500 laser-cooled ytterbium ions achieved a clock-frequency uncertainty of 1.1×10^{-14} [24].

The robustness, deep trapping potential, and relatively low complexity of ion traps make them ideal for this project. A miniature, buffer gas cooled ytterbium ion (Yb^+) system, designed to offer high stability, has reached stability of $3.5 \times 10^{-11}/\sqrt{\tau}$, and accuracy of 2×10^{-12} [25]. By introducing laser cooling, we hope to improve on the performance of this clock, at the expense of added complexity, size and power consumption.

[4]The Chou et al. reference here is actually a quantum logic clock, with two ions of different species on the axis of a linear trap.

An overview of the trapped ion $^{171}Yb^{+}$ system is shown in figure 1.6.

$^{171}Yb^{+}$ also has two optical clock-transitions [22]. Additionally, the systems developed for a laser-cooled microwave system may provide a good starting point for a transportable optical clock.

Previous work on laser-cooled ytterbium ion microwave clocks has been undertaken by CSIRO in Austrailia [26–29] and NICT in Japan [24]. However, both these clocks are laboratory-based standards. The performance of these clocks, along with the other systems mentioned in this chapter, are tabulated in table 1.2. Figure 1.7 gives a broad qualitative overview of the attributes of various approaches to microwave atomic clocks.

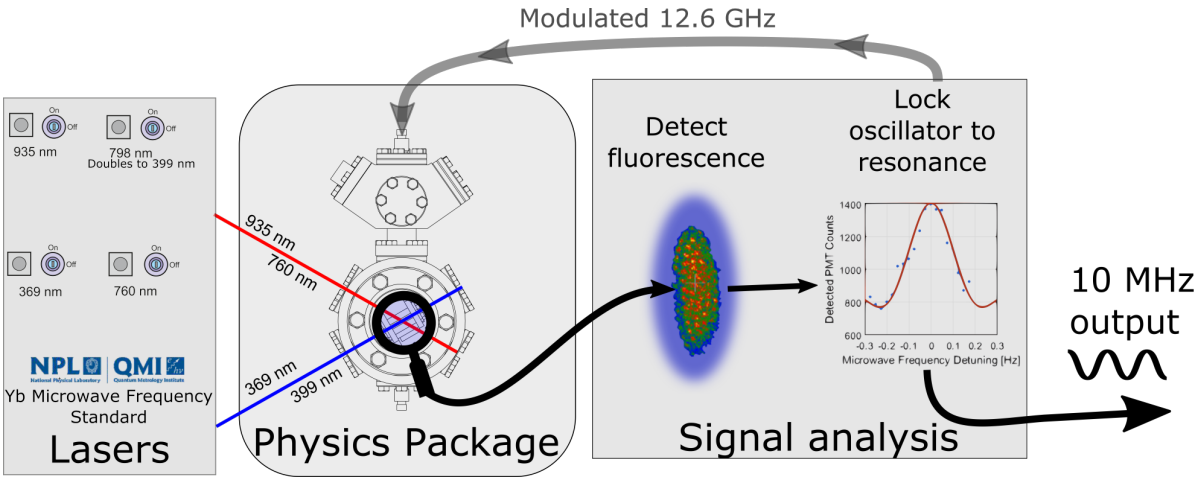


Figure 1.6: Block diagram of a $^{171}Yb^{+}$ microwave clock. The lasers and microwaves interact with the ions in the physics package, creating a fluorescence signal which is used to determine the clock frequency. Short-term stability is provided by a 10 MHz oscillator and longer-term stability from the ions.

System	**Stability**	**Accuracy**	**Limiting systematic**	**Type/ Size**	**Ref / Institute**
Cs 5071A	$10^{-11}/\sqrt{\tau}$ 10^{-15} floor	5×10^{-13}	2^{nd} order Zeeman and 2^{nd} order Doppler	Beam; 3U 19-inch rack	Microsemi [10]
H maser MHM 2010	$10^{-13}/\sqrt{\tau}$ 10^{-16} floor	N/A	Wall shift	Maser; 460×760 ×1090 mm	Microsemi [16]
Galileo passive H maser	$10^{-12}/\sqrt{\tau}$ 10^{-15} floor (lab based)	N/A	Not published	Tens of litres physics package 18 kg	Spectratime [17]
MuClock	$3 \times 10^{-13}/\sqrt{\tau}$ 2×10^{-15} floor	3×10^{-15}	Not published	Laser-cooled Rb 550 × 800 × 1550 mm, 135 kg	μQUANS [19]
CSAC	$10^{-10}/\sqrt{\tau}$ 10^{-12} floor	N/A	Cell temperature, Cs density and light-shifts	Cell; 41×36 ×12 mm	Microsemi [18]
Yb^+buffer gas cooled	$10^{-11}/\sqrt{\tau}$ 10^{-13} floor	Not specified	2^{nd} order Zeeman	Ion; tens of cc physics package	Sandia [30]
Yb^+laser cooled	$5 \times 10^{-14}/\sqrt{\tau}$ **estimated**	3×10^{-14}	2^{nd} order Zeeman	Ion; Laboratory sized	CSIRO [27]
Yb^+laser cooled	$2.1 \times 10^{-12}/\sqrt{\tau}$	1.1×10^{-14}	2^{nd} order Zeeman	Ion; Laboratory sized	NICT [24]
Hg^+	$3 \times 10^{-13}/\sqrt{\tau}$ 3×10^{-15} floor	3×10^{-15}	2^{nd} order Zeeman	Ion; Laboratory sized (cryogenic)	NIST [23]
Hg^+	$1.5 \times 10^{-13}/\sqrt{\tau}$ 1×10^{-16} floor	Not specified	Pressure Shifts	Ion; 17 litres	JPL [31]
Yb^+ laser cooled	$1 \times 10^{-12}/\sqrt{\tau}$ **target**	3×10^{-14} **target**	2^{nd} order Zeeman	Ion; 3U 19-inch rack	Long-term target for this work
	$3.6 \times 10^{-12}/\sqrt{\tau}$ (between 30-1500 s)	Not optimised	Ion loss	Ion; 6U 19-inch rack	This work, as of October 2018

Table 1.2: Comparison of microwave frequency standards.

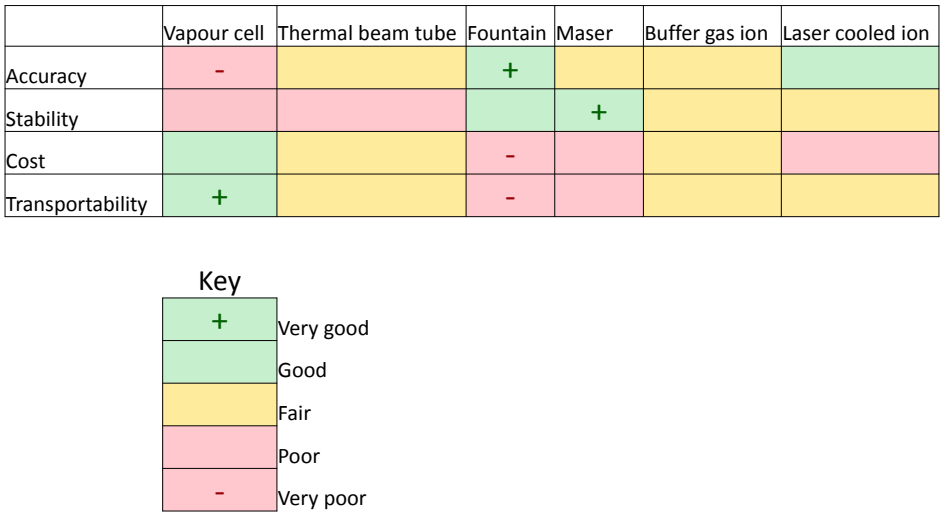


Figure 1.7: Qualitative overview of the attributes of classes of microwave atomic clocks.

1.4 Project Goals

The target of the project was to investigate the feasibility of a portable, microwave atomic clock that incorporates some of the technologies, such as laser-cooling, that are used in state of the art laboratory atomic clocks. To do this, we made a TRL4 demonstrator[5] of a laser-cooled ytterbium ion microwave clock with target performance of instability better than $1 \times 10^{-11}/\sqrt{\tau}$ — the performance level of the highly-developed industry standard 5071A caesium beam clock. The demonstrator would fit in a 6U, 19-inch rack enclosure and be powered from 240 V, 50 Hz mains. In addition to demonstrating performance at this level, an investigation into the limitations would be conducted to provide an

[5]The NASA definition of technology readiness level (TRL) 4:

> Following successful "proof-of-concept" work, basic technological elements must be integrated to establish that the "pieces" will work together to achieve concept-enabling levels of performance for a component and/or breadboard. This validation must be devised to support the concept that was formulated earlier, and should also be consistent with the requirements of potential system applications. The validation is "low-fidelity" compared to the eventual system: it could be composed of ad hoc discrete components in a laboratory [32, 33].

estimate of the ultimate performance obtainable with this technology. Working back from the objective, this required us to design a system architecture, and the components and subsystems. These are detailed in the following sections. Engineering drawings for the components described in this chapter can be found in appendix A.

1.5 System architecture

The atomic clock can be thought of as three systems: the physics package, the laser system, and the electronics and control systems. The physics package stores and interfaces with the ion references; the laser system provides light at the required frequency, power and polarisation to interact with the ions; and the electronics and control system provides the clock output and the supporting functions for the other two systems. The system architecture is summarised in figures 1.8 and 1.9. The systems are further described in the following chapters.

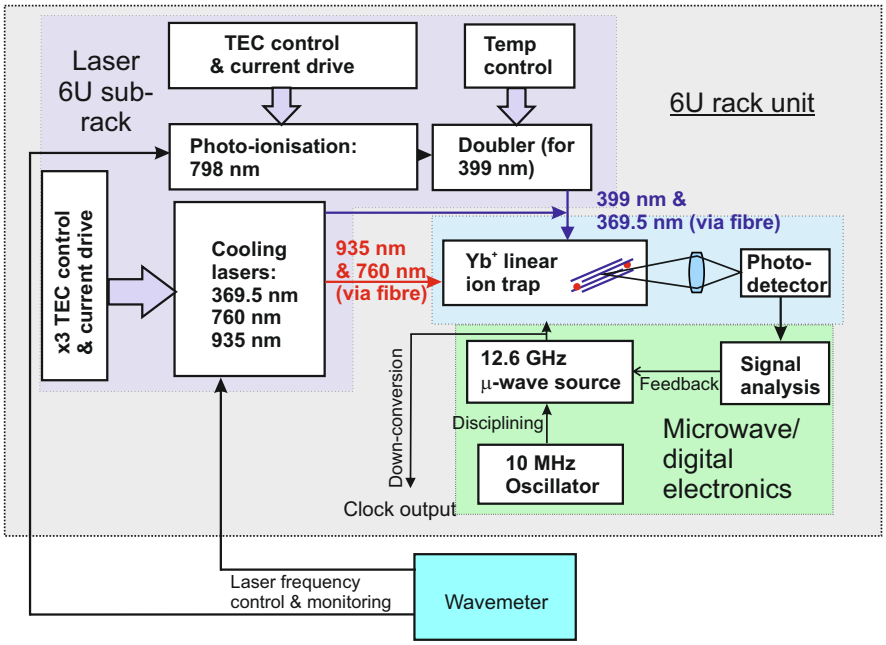


Figure 1.8: Schematic overview of the clock system. All the components are packaged into a 6U rack unit, with the exception of the wavemeter reference for the lasers.

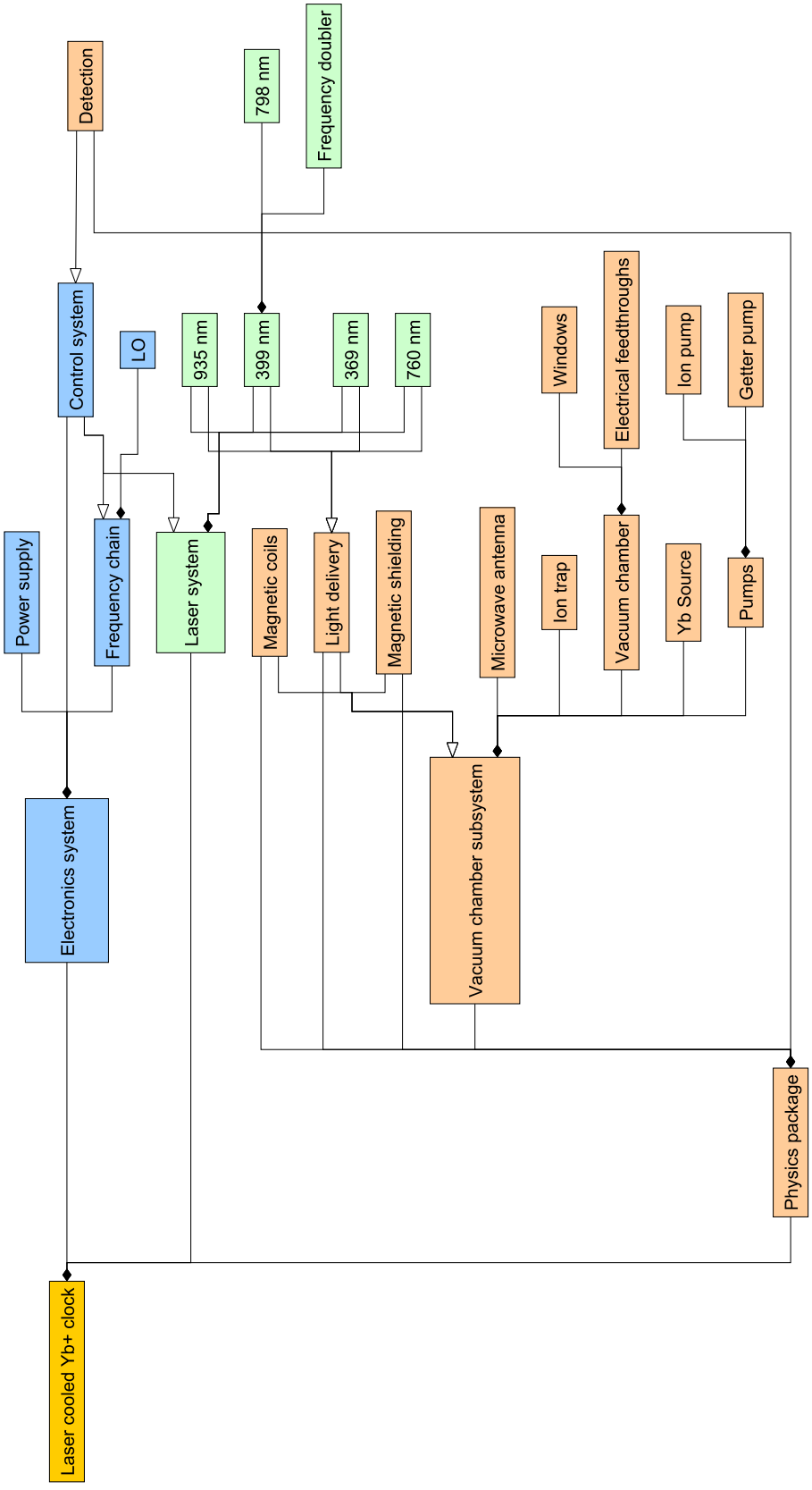


Figure 1.9: System architecture. The filled diamonds show composition (e.g. the vacuum chamber subsystem contains the ion trap), and the arrows show dependency. The dependencies of the power supply are not shown for clarity.

1.6 System requirements

At the heart of the system is the physics package. This is where the ions are trapped, probed and detected. The physics package comprises: the ion trap; the vacuum chamber and pumps; PMT and imaging optics; fibre launchers for the laser beams; magnetic bias coils; and magnetic shields. These components are described in chapter 4. The objective to build a small clock and the low TRL limited our approach to using predominantly standard components as compactly as possible. It is important to isolate the ions as much as possible from their environment, so a high level of vacuum, and shielding from unwanted electromagnetic fields are required.

Sources of laser light at 369, 399, 760 and 935 nm were required, as set out in table 1.3.

Laser wavelength [nm]	**Function**	**Power**	**Max Linewidth**
369	Cooling	1 mW	2 MHz
399	Photoionisation	50μW	10 MHz
935	D-state repump	1 mW	30 MHz
760	F-state repump	1 mW	30 MHz

Table 1.3: Required lasers, tabulated with the minimum required power and maximum linewidth.

In addition to the laser diodes, a large amount of electronic infrastructure was required in order to provide extremely low noise current and temperature control. The wavelengths are locked to a Zeeman-stabilised, helium-neon laser referenced wavemeter to ensure repeatability. The laser system is described in chapter 3

The system must run autonomously; control the experimental sequences; generate the feedback signal; and lock an oscillator. This requires a large number of subsystems, and a system architecture was chosen to allow flexibility to add functionality. The electronic system is documented in chapter 5.

1.7 System layout

A flexible and maintainance-friendly layout was chosen to aid ease of development. Figure 1.10 shows a diagram of the layout, and figure 1.11 is a photograph of the final assembly. There is a large amount of empty space in this layout, as it is a TRL4 design-for-test. Significant shrinkage would be possible in further iterations. The lasers and electronics were made to slide into a 6U rack, and electrical connections were made through a backplane; this allowed quick and easy replacements and testing. An area in the back corner was reserved for the physics package in the magnetic shields, which were mounted directly on to the case.

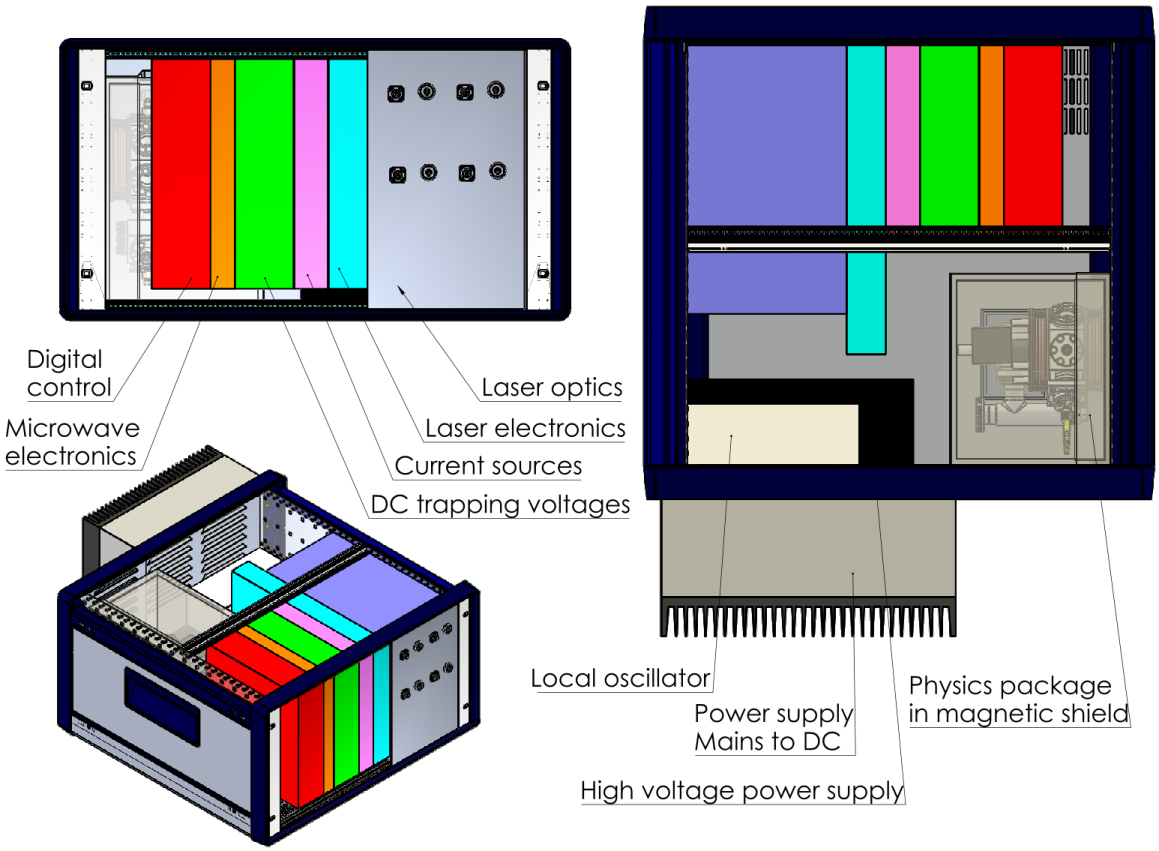


Figure 1.10: System layout in the 6U 19-inch rack case.



Figure 1.11: Microwave clock assembled in case ($51 \times 49 \times 28$ cm).

1.8 Thesis outline

This thesis details the design, build and evaluation of a portable, laser-cooled $^{171}Yb^{+}$ microwave atomic clock.

In Chapter 2, background theory is outlined, focusing on: ion trapping fundamentals; properties of ytterbium ions; transitions between hyperfine states; spectroscopy; and phenomena that affect the natural transition frequencies between hyperfine states.

Chapter 3 describes the compact laser system and the frequency stabilisation of the lasers.

Chapter 4 describes the physics package and sets out detailed designs of the ion traps, the vacuum system, magnetic bias coils, magnetic shielding, laser delivery, and imaging system used in this experiment.

Chapter 5 describes the electronic hardware required for the experiment and the experiment control sequences.

Chapter 6 details the investigations into the non-fluorescing 'dark ions' that accumulated in the ion trap, which limited the length of time for which the frequency standard could operate.

Chapter 7 details the performance evaluation of the clock, looking at the frequency offsets, stability, and reliability of the clock output, and the performance of the subsystems

of the clock. The systematic frequency shifts that affect the accuracy of the clock are measured and the uncertainties determined.

Finally, Chapter 8, draws conclusions about the work presented in this thesis, along with suggestions of future work to improve the system.

Chapter 2

Background Theory

In this chapter I give a brief overview of the relevant theory that is important to the operation and limitations of this frequency standard. In the first section, there is an overview of the theory behind ion trapping. In the second section, the properties of $^{171}Yb^{+}$ ions are introduced and the transitions that are important for the frequency standard are described. The third section discusses spectroscopy, and the fourth section explores frequency shifts that may degrade the performance of the clock. All of these aspects, along with other technical and experimental concerns, must be considered when designing the apparatus to realise the frequency standard. For example, the motion of the ions in the ion trap and the trapping fields result in frequency shifts, and the design of the ion trap must attempt to minimise these.

A good introduction to atomic physics can be found in [34]. Some recommended general references on atomic frequency standards are in the following references: [9, 12, 35, 36].

2.1 Ion trapping

Before we begin to discuss the properties of the ytterbium ions that form the basis of the clock, it is important to have an understanding of the devices that allow precision spectroscopy of ions to be performed.

In 1989, Wolfgang Paul and Hans Dehmelt were each awarded one quarter of the Nobel Prize[1] for their work on electromagnetic trapping. Paul invented RF ion traps, which is the technique used in this work. Dehmelt developed an alternative trapping technique, the Penning trap, which uses a combination of strong magnetic fields and electric fields to confine charged particles. Static electric fields are not suitable for trapping ions in three dimensions; this is because a collection of charges can only produce saddle points, trapping in certain directions but anti-trapping in others.[2] The ion trap overcomes this limitation by using radio frequency (RF) oscillating fields. The resulting time-averaged pseudo-potential can stably trap ions. The oscillating field causes the saddle potential to rotate, and the ion's inertia keeps it trapped at the saddle point.

Ion traps were originally constructed with hyperbolic electrodes, which created a spherically symmetric trapping potential. This potential has a single node in the centre but with limited laser and detector access. Contemporary designs of ion traps tend to stray far from the idealised electrode geometry and still achieve a deep, stable trapping region, as illustrated in figure 2.1. Taking liberties with the geometry affects the trap's depth, harmonicity and shape to varying degrees and so may adversely impact trap performance.

Of particular interest for this work is the linear ion trap, shown in figure 2.1-f. This form of trap was developed to store a large number of ions close to the RF null on the symmetry axis between the electrodes [37], and results in a greater number of trapped ions and less disturbance from the trapping fields relative to other designs.

I will give a brief overview of the dynamics of ions in an asymmetrically driven linear RF trap, the traps used in this project. Further detail and solutions for different geometries can be found in [34, 37–42].

[1] The other half of the Nobel Prize went to Norman Ramsey for inventing the method of separated oscillatory fields, vital to the operation of atomic clocks.

[2] The divergence of the electrostatic force, $\vec{F}$, must be negative for trapping, However, Gauss' law in free space requires it to be zero: $\nabla \cdot \vec{F} = \nabla \cdot (-\nabla\phi) = -\nabla^2\phi = 0$. This is known as Earnshaw's theorem.

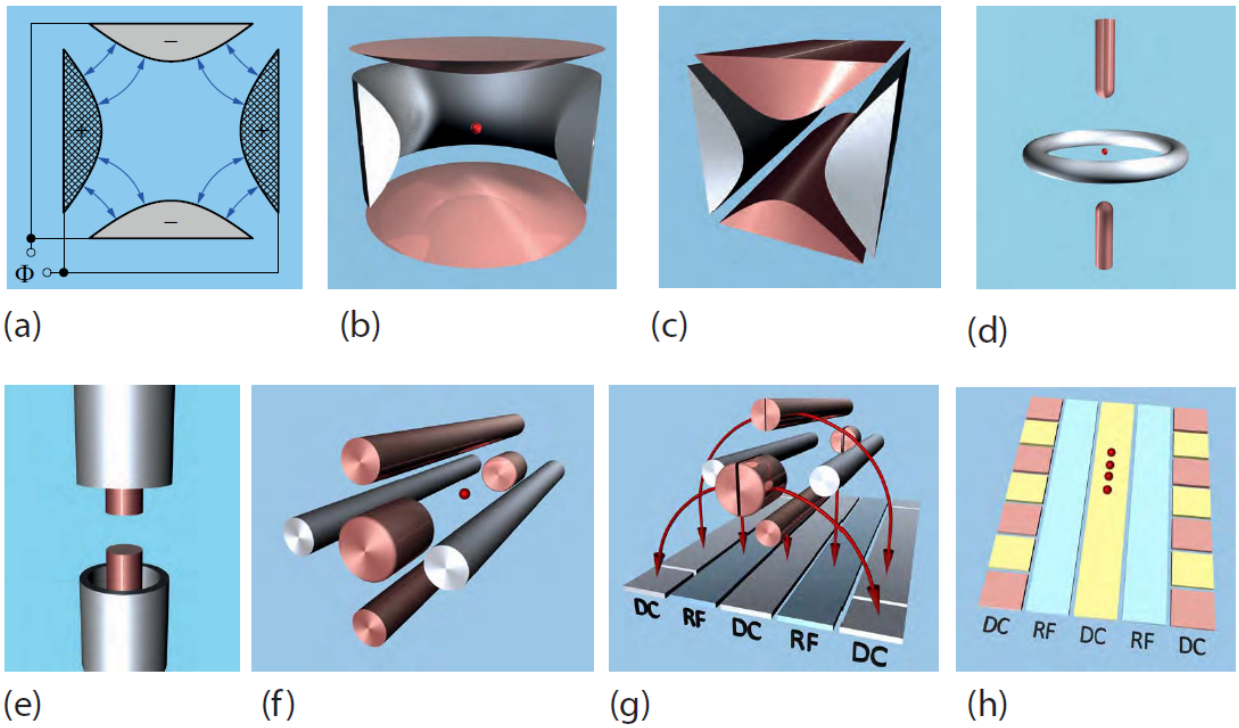


Figure 2.1: From [38], demonstrating an array of trap designs.
The foundation of all geometries is the hyperbolic electrode layout that creates a perfectly quadrupolar field: (a). Rotating the hyperbola about an axis yields the ring trap, (b), with a spherically symmetric pseudopotential. If the hyperbolae are instead extruded, a linear trap, (c) is formed, the ends of which may be plugged by the addition of two positive DC electrodes. The linear trap has a null line along the central axis.
Deforming from these idealised geometries leads to designs (d-e) from a ring trap and (f-g) from a linear trap. The surface trap (h) is segmented so that multiple trapping regions are separated on a single device.

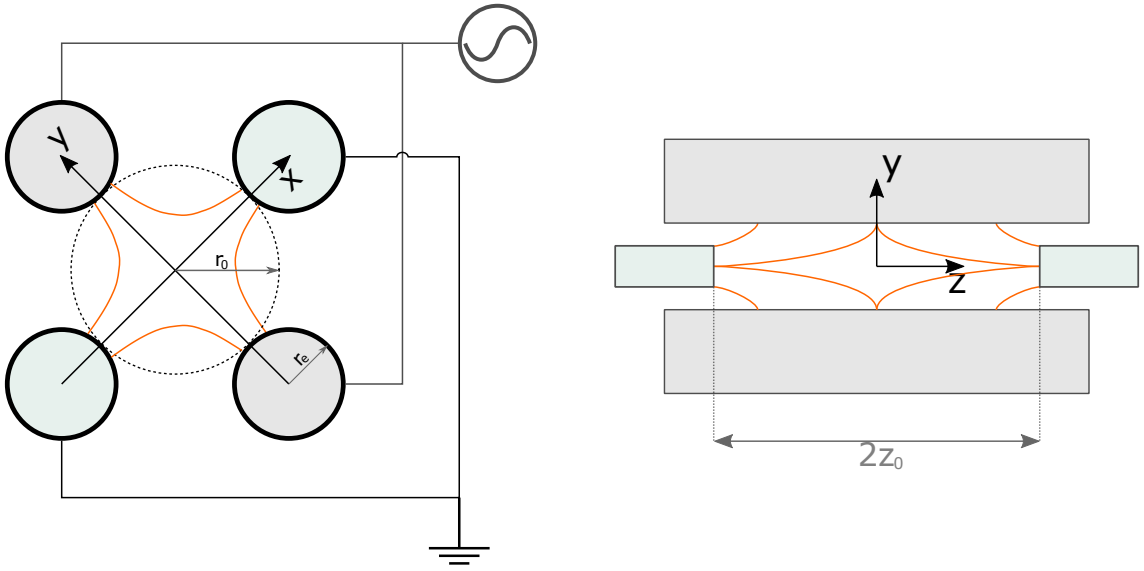


Figure 2.2: This shows the model geometry used in this section. The left-hand diagram shows the array of rod electrodes in cross-section that provide radial confinement. The right hand diagram shows the endcap electrodes, where a DC voltage is applied to the endcaps provides axial confinement. The axis-electrode distance is labelled r_0, the electrode radius r_e, and the endcap separation $2z_0$. Indicative field lines for the quadrupolar electric field that is produced between the RF electrodes and the DC electrodes [40] are shown as orange lines.

2.1.1 Electric potentials

The geometry of a linear ion trap is shown in figure 2.2. The x and y axes join the two sets of rod electrodes through the centre, and the z-axis is the axis of rotational symmetry. The trapping structure is terminated axially by two endcaps, and the rods are much longer than their separation. An AC potential, $V_0 \cos(\Omega t)$, is applied only to the rods joined by the y-axis with other electrodes at DC potentials.

First considering the x-y plane, the electrostatic potential ϕ near the z-axis is found by solving Laplace's equation, $\nabla^2\phi = 0$. Due to the symmetry, this has approximately a quadrupole form:

$$\phi = a_0 + a_2(x^2 - y^2). \tag{2.1}$$

The terms linear in x and y vanish due to the reflection symmetry of the electrodes about $x = 0$ and $y = 0$. These may be present to a small degree in real traps due

to machining errors. Higher order terms may also exist due to the geometry of the electrodes differing from the ideal case of extruded hyperbola. For electrodes of circular cross-section, the best approximation to the ideal field has been modelled numerically, and is when the ratio of the electrode radius to the axis-electrode distance, r_e/r_0, is approximately 1.145.[43, 44].

The coefficient a_0 is an arbitrary offset and will be omitted from the rest of the analysis. a_2 is determined from the boundary conditions, yielding:

$$a_2 = \frac{\kappa_{xy} V_0}{r_0^2}, \tag{2.2}$$

and

$$\phi_{xy} = \frac{\kappa_{xy} V_0}{r_0^2} \cos(\Omega t)(x^2 - y^2), \tag{2.3}$$

where κ_{xy} is a geometric constant, and r_0 is the axis-electrode distance.

Applying the same analysis the $y - z$ plane (although the quadrupolar approximation does not hold as well as in the $x - y$ plane), and remembering that only the rods joined by the y-axis in figure 2.2 have an AC potential, this finds an AC quadrupolar field on the z-axis:

$$\phi_z = \frac{\kappa_z V_0}{z_0^2} \cos(\Omega t) z^2, \tag{2.4}$$

where κ_z is a geometric constant, and z is half the inter-endcap distance. A DC voltage on the endcaps, U, provides further axial confinement. This field is anti-trapping in the $x - y$ plane:

$$\varphi_z = \frac{\alpha_z U}{z_0^2} z^2 \tag{2.5}$$

$$\varphi_{xy} = -\frac{\alpha_{xy} U}{z_0^2} (x^2 + y^2), \tag{2.6}$$

where the α terms are geometric constants. The full potential is found by summing these

potentials:

$$\Phi = U\left[\frac{\alpha_z}{z_0^2}z^2 - \frac{\alpha_{xy}}{z_0^2}(x^2+y^2)\right] + V_0\cos(\Omega t)\left[\frac{\kappa_{xy}}{r_0^2}(x^2-y^2) + \frac{\kappa_z}{z_0^2}z^2\right] \tag{2.7}$$

2.1.2 Equations of motion

As we will be trapping singly-positively charged ions, the acceleration on a particle of charge $+e$ and mass m is given by $\boldsymbol{a} = \frac{-e\nabla\Phi}{m}$. The equations of motion are separable:

$$\ddot{\boldsymbol{x}} = \frac{2e}{m}\left[\frac{\alpha_{xy}}{z_0^2}U - \frac{\kappa_{xy}}{r_0^2}V_0\cos(\Omega t)\right]\boldsymbol{x}, \tag{2.8}$$

$$\ddot{\boldsymbol{y}} = \frac{2e}{m}\left[\frac{\alpha_{xy}}{z_0^2}U + \frac{\kappa_{xy}}{r_0^2}V_0\cos(\Omega t)\right]\boldsymbol{y}, \tag{2.9}$$

and

$$\ddot{\boldsymbol{z}} = \frac{2e}{m}\left[-\frac{\alpha_z}{z_0^2}U + \frac{\kappa_z}{r_0^2}V_0\cos(\Omega t)\right]\boldsymbol{z}. \tag{2.10}$$

We see that $\boldsymbol{z}$ has a restorative force due to the DC potential and that all directions have an oscillatory force. If an AC voltage was applied to the electrodes joined by the x-axis with a phase shift of π to the other pair, the oscillating term in the z-direction would be cancelled.

Considering only the motion in the x-direction and allowing a DC voltage, U_{DC}, to be applied to the rods, a change of variable of $\tau = \Omega t/2$ allows these equations to be put in the form of the Mathieu equation:

$$\ddot{\boldsymbol{x}} + (a_x - 2q_x\cos(2\tau))\boldsymbol{x} = 0 \tag{2.11}$$

with

$$q_x = \frac{2e\kappa_{xy}V_0}{\Omega^2 m r_0^2} \tag{2.12}$$

and

$$a_x = \frac{4e\alpha_{xy}U_{dc}}{\Omega^2 m r_0^2}. \tag{2.13}$$

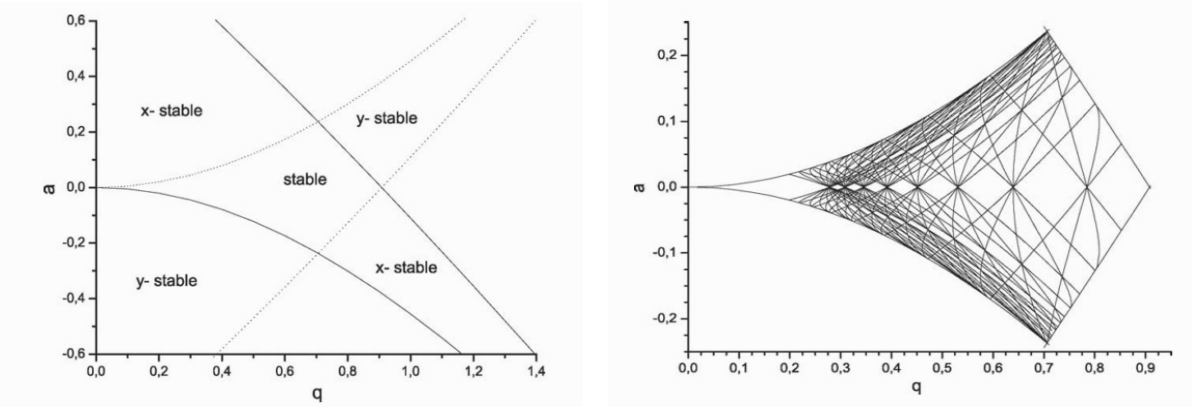


Figure 2.3: Stability diagram for linear ion trap, from [41]. There is a range of a and q parameters where stable trapping can occur. Within this stability region, there are 'lines of instability' where higher-order components of the trapping field cause unstable orbits. The trap is operated at low a and q ($a \approx 0$, $q < 0.1$) for maximum stability.

The Mathieu equation, equation (2.11), can be solved for the x, y and z-directions. It is found that if the a and q parameters are within the stable region in figure 2.3, the ion can be trapped.

The full derivation of the solution to the Mathieu equation can be found in reference [45]. The motion of the ion is described by:

$$x_i(t) = \bar{x}_i + X_i \cos(\omega_i t) - \frac{X_i q_i}{4}[\cos((\Omega + \omega_i)t) + \cos((\Omega - \omega_i)t)] - \frac{\bar{x}_i q_i}{2}\cos(\Omega t), \quad (2.14)$$

where i is a vector index, $\bar{x}_i$ is the ion's mean position relative to trap centre, and X_i is the amplitude of the slow 'secular' oscillation of the trap at ω_i. The secular frequencies are given by:

$$\omega_i = \frac{\Omega}{2}\sqrt{\frac{q_i}{2} + a_i}. \quad (2.15)$$

Typically, linear ion traps operate in the regime where the axial motion is dominated by the DC voltages on the endcaps. Under these conditions, the axial secular frequency is given by:

$$\omega_z^{DC} = \sqrt{\frac{e}{m} \cdot \alpha_z U}, \quad (2.16)$$

with e/m being the ion's charge to mass ratio. The corresponding formula for the radial

motion is:

$$\omega_r = \frac{e}{m} \cdot \frac{\kappa_{xy} v_0}{\sqrt{2} r_0^2 \Omega}. \tag{2.17}$$

It is common to describe the slow motion of the ions in terms of the pseudopotential, Φ:

$$\Phi_r = \frac{m}{2}(\omega_r^2 - \frac{1}{2}\omega_{z-DC}^2) r^2, \tag{2.18}$$

and

$$\Phi_z = \frac{m}{2}\omega_z^2 z^2, \tag{2.19}$$

where ω_z is given by equation (2.15), which need not be equal to equation (2.16). We see that the force from the RF confinement is mass dependent. For two similarly charged ions of different mass, the lighter mass will be tighter bound, pushing the heavier mass ion away from the trap centre. This separation was used to identify the presence of trapped molecular ions, as set out in chapter 6.

The third term in equation (2.14) is the 'intrinsic micromotion' and is always present. The fourth term, which is non-zero when the ion is separated from the centre of the trap, is known as 'excess micromotion' and is usually unfavourable. It is common to use additional electrodes to nudge the ion back into the trap centre to avoid motional frequency shifts, and there is a large body of work on the mitigation of micromotion [46]. The motion of an ion in an ion trap, displaying micromotion, is visualised in figure 2.4.

2.1.3 Trap depth

The depth of the confining time-averaged potential, D_r, in the radial direction for hyperbolic electrodes is given by:

$$D_r = \frac{eV_0^2}{4mr_0^2\Omega^2}. \tag{2.20}$$

This formula ignores the anti-trapping effect of the DC potential that is applied to add confinement to the z-axis.

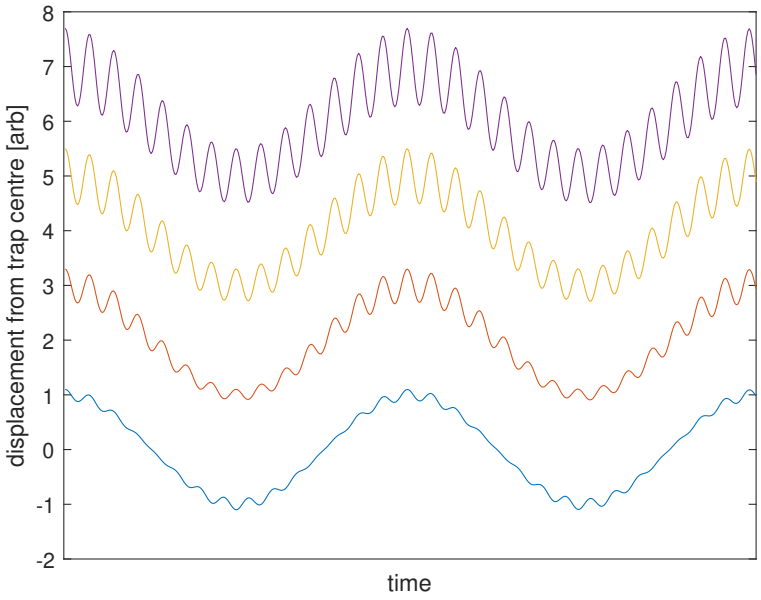


Figure 2.4: A plot of ion position against time in one dimension. Both axes are arbitrary. The low frequency oscillations are the ion's secular motion and the frequency is unchanged by small deviations from the trap centre. The higher frequency oscillations at the trapping frequency Ω, is called micromotion. Micromotion grows linearly in amplitude with separation from trap centre.

The z-axis will have some confining potential due to the asymmetric trap drive and the finite size of the electrodes. Typically the majority of the trapping comes from the voltage applied to the endcaps and the depth is then trivially:

$$D_z = eU_{dc}. \tag{2.21}$$

2.1.4 Trap capacity and the effect of adding extra ions

Many factors set the capacity of an ion trap. Most fundamentally, the trap depth must be greater than the space-charge potential caused by compressing positively charged particles into a small volume in space.

The equations in section 2.1.2 describe the motion of a single ion in a linear ion trap. The introduction of additional ions will cause additional — coupled and non-linear — terms in the equations of motion due to the ions' pairwise Coulomb interaction. The ions'

mutual repulsion will push ions away from the trap centre, where they experience higher micromotion; this micromotion is then converted to incoherent thermal motion amongst the ions by the Coulomb force. This process and others that result in ion heating from the trapping field are known as RF heating effects [47].

The limit for the number of ions that can be stored is therefore determined by a combination of having a deep enough trapping potential to contain the space charge, and having a cooling mechanism that exceeds the ion-heating rate. The effect of ions being separated from the centre of the trap can be mitigated by increasing the dimensions of the trap. The number of ions that can be trapped scales linearly with the volume [37].

2.1.5 Coulomb crystals and ion clouds

When the energy from the inter-particle Coulomb interaction becomes large compared to the kinetic energy, ions in an ion trap form a regular lattice known as a Coulomb crystal. This condition can be quantified in terms of the plasma coupling parameter Γ:

$$\Gamma \equiv \frac{Q^2}{4\pi\epsilon_0 a} \cdot \frac{1}{k_B T} \tag{2.22}$$

$$\sim \frac{E_{\text{Coulomb}}}{E_{\text{Kinetic}}}. \tag{2.23}$$

Here Q is the charge of the ions (in our case $+e$), a is the Wigner-Seitz radius, and T is the temperature of the ions. The Wigner-Seitz radius is a measure of the average distance between particles and it is related to the number density n by $n = 3/(4\pi a^3)$. Coulomb crystals have been shown to form for $\Gamma \geq 175$ [48, 49]. This inequality leads to a temperature limit for a typical value of the ion separation, $a = 10\,\mu$m, of

$$T_{\text{crystal}} < 10\,\text{mK}, \tag{2.24}$$

which is twenty times higher than the Doppler cooling limit for ytterbium ions. Examples of Coulomb crystals can be seen in figures 4.4 and 6.1 in following chapters. In these images, the ions occupy the lowest-field volume of the ion trap, which gives the spheroidal shape, and have a uniform density. Ions in a Coulomb crystal may be thought of as a set of coupled oscillators, and it follows that the number of normal modes for the crystal

increases with the number of ions that it contains. If electric field noise coincides with a normal mode of the system, the energy will be resonantly absorbed, leading to rapid heating.

Increasing the temperature of the crystal causes what might loosely be called a phase transition to a cloud state [47, 48, 50]. The cloud state is characterised by lower density and a Gaussian density distribution. An example may be seen in figure 4.8 in chapter 4. A consequence of the ion cloud's greater spatial extent is that the ions experience greater micromotion. This micromotion alters the laser cooling dynamics [51] and specifically causes ions to be heated for small red detunings that would effectively cool single ions and crystals. This change in laser cooling dynamics is responsible for a hysteresis effect in the formation of Coulomb crystals [47, 52]. It was found to be difficult to maintain a Coulomb crystal reliably for a few hours (particularly due to the formation of dark ions, detailed in chapter 6), as required for a clock measurement. This was because the ions would occasionally heat into the cloud phase when the cooling laser was extinguished for the clock pulses. Because of the hysteresis effect, the laser cooling parameters that were optimal for the formed crystal heat the ion cloud; the crystal can not be reformed without tuning the cooling laser to a large red detuning. This point is expanded upon and illustrated with experimental data in figure 7.8 in chapter 7. By using a larger trapping voltage, the RF heating can be increased and the denominator of equation (2.23) can be increased to a point where the cloud phase is the only stable phase. This results in a large technical simplification, however, the Coloumb crystal has the advantages of lower micromotion and more rapid cooling, so for this simplification we trade off some performance.

The theory that has been outlined so far in this chapter has concerned how ions may be trapped in RF electric fields. The following section outlines the properties of the ytterbium ions that are trapped in this frequency standard.

Mass Number	Relative abundance [mole fraction]	Nuclear spin
168	0.0013(1)	0
170	0.0304(15)	0
171	0.1428(57)	1/2
172	0.2183(67)	0
173	0.1613(27)	5/2
174	0.3183(92)	0
176	0.1276(41)	0

Table 2.1: Isotopic composition of terrestrial ytterbium. Data from [54]. The 171 isotope is used for its nuclear spin of $^1/_2$.

2.2 Atomic physics of ytterbium ions

Ytterbium is a lanthanide, of atomic number 70 with electronic structure [Xe] $4f^{14}$ $6s^2$. Natural ytterbium is a mixture of seven stable isotopes ranging in mass from 168 to 176 amu, and it is present in the earth's crust with an abundance of 3 mg/kg [53]. Isotopic selection is possible by selective photoionisation (see section 2.2), but enriched isotopes are also available commercially. The isotopic content of terrestrial ytterbium is tabulated in table 2.1.

Singly-ionised ytterbium has a relatively simple energy-level structure, resulting from the single valence electron. The term scheme is shown in figure 2.5 [55]. The simple structure enables efficient manipulation of the ions' state. The ^{171}Yb isotope is used for its relatively magnetically-insensitive hyperfine transition between the two ground states, $^2S_{1/2}(F = 0 \rightarrow F' = 1, \Delta m_F = 0)$, which is at 12.6 GHz.

Another attractive property of $^{171}Yb^+$ is that the lasers required for laser-cooling are all commercially available diode-lasers. An interesting property of $^{171}Yb^+$ is that it also contains two optical-frequency clock transitions, $6s^1 : {}^2S_{1/2} \rightarrow 5d^1 : {}^2D_{3/2}$ and $6s^1 : {}^2S_{1/2} \rightarrow 6f^{13}6s^2 : {}^2F_{7/2}$ [22, 56]. The upper states of the 935-nm and 760-nm transitions are labelled with some uncommon notation. This is a result of the intermediate-coupling that is best approximated as $LSJLKJ$ coupling in these states [57]. This coupling occurs because in these states there is a hole in the core and the

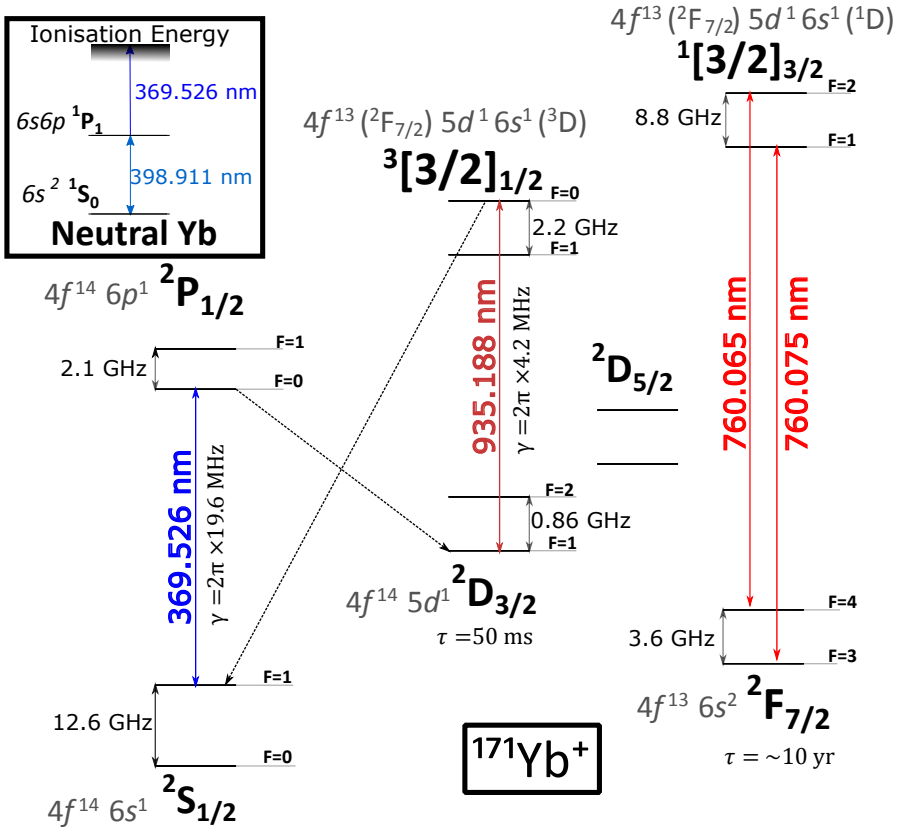


Figure 2.5: Partial term schemes for neutral (inset), and singly-ionised ^{171}Yb. The driven atomic transitions and the required laser wavelengths and microwave frequencies are shown.

outer-electrons are 'far away' from the core electrons. The core is described by LS coupling which then couples with the resultant orbital angular momentum of the outer electrons to form a new quantum number, $\boldsymbol{K} = \boldsymbol{J_{core}} + \boldsymbol{L_{outer}}$. $\boldsymbol{K}$ then couples to the coupled spins $\boldsymbol{S}$ of the outer electrons to give $\boldsymbol{J_{total}} = \boldsymbol{K} + \boldsymbol{S}$. The full terms are given in figure 2.5. The notation used for the full terms is to write the electronic configurations, with the LS coupling terms of the inner- and outer-electrons in parentheses, and then write the other quantum numbers in the following format: $^{2\boldsymbol{S}+1}[\boldsymbol{K}]_{\boldsymbol{J_{total}}}$. The shortened form, which I have used in the text thought this thesis, only states the $^{2\boldsymbol{S}+1}[\boldsymbol{K}]_{\boldsymbol{J_{total}}}$ part of the term.

The principal cooling transition in $^{171}Yb^{+}$ is at 369.5 nm; fluorescence at this wavelength is also used for state detection. This wavelength, together with a source at 399 nm

tuned to a transition in neutral ^{171}Yb, is also used for photoionisation of an atomic beam to create the ions. Finally, two lasers at 935 nm and 760 nm are used to drive ions out of long-lived $^2D_{3/2}$ and $^2F_{7/2}$ states respectively. The low-lying F-state in ytterbium has a natural lifetime of the order of 10 years [58, 59]. The long lifetime can be exploited to provide a narrow linewidth for an optical clock, but for microwave clocks it is problematic, as ions can populate the state by collisions with background gas [25, 60]. Once in the F-state, ions will not interact with the cooling laser or provide a clock signal, but they will still cause the other ions to heat up and take up space in the ion trap. As the F-state is populated extremely infrequently, it does not play a significant role in the dynamics of the measurement sequence.

The clock operation requires a sequence of manipulations to the ions' state. This state control is achieved by driving transitions between some states, and exploiting decays between others. The measurement sequence consists of laser cooling, state-preparation, spectroscopy and state-detection. Infrequently, the ions will also need to be loaded into the trap.

To load ions into the ion trap, a flux of neutral ytterbium is effused from the oven. At the trap axis, the neutral ytterbium crosses a laser beam at 90° that contains both 399 nm and 369 nm. The 399 nm beam drives the $^1S_0 \rightarrow {}^1P_1$ transition in neutral ytterbium [61–63]. From the $^1P_1$ state, the cooling wavelength of 369 nm has sufficient energy to remove an electron and produce $^{171}Yb^+$ in the trapping region. If the atomic beam crosses the 399-nm laser beam at close to 90 degrees, it is possible to selectively drive the transition for ^{171}Yb without driving Doppler-broadened transitions from other isotopes.

To laser cool the ions, microwaves at 12.6 GHz are applied and a 369 nm laser is tuned to the $F = 1 \rightarrow F' = 0$ component of the $^2S_{1/2} \rightarrow {}^2P_{1/2}$ transition. The cooling transition is a strong, dipole-allowed transition with a natural linewidth, γ_{369}, of $2\pi \times 19.6$ MHz [64]. The cooling cycle is not entirely 'closed'. From the upper state, the ion can decay with a probability of about $1/200$ into the $^2D_{3/2}$ state [65], which requires quadrupole radiation to decay back to the ground state. This results in a significant lifetime of 50 ms [65], which would hinder cooling. To prevent 'shelving' the ions in this state, a laser of 935 nm is

tuned to the $^2D_{3/2}(F=1) \rightarrow {}^3[3/2]_{1/2}(F'=0)$, with sufficient intensity to also off-resonantly drive the $F = 2 \rightarrow F' = 1$ components. The $^3[3/2]_{1/2}$ state decays to the $^2S_{1/2}$ ground state with a lifetime of 38 ns [66].

The laser-cooling of $^{171}Yb^+$ has a further complication. In the absence of an external magnetic field, the ions will become optically-pumped into a dark state comprised of a superposition of the $^2S_{1/2}$, F=1, $m_F = \pm 1$ ground states. Applying a magnetic field of at least a few hundred microtesla (we typically use 700 μT) induces a precession of the ions' dipole moments that destabilises the dark states [67]. This large magnetic field must be at an oblique angle to the polarisation of the 369-nm laser. In addition this field must be turned off during the probe phase of the clock cycle in order to reduce the uncertainty in the second-order-Zeeman shift, as described in section 2.4.3.2. An alternative method to destabilise the dark states works by modulating the polarisation of the laser field so that the three polarisation components π, σ_+, σ_- are non-zero and have linearly independent time dependencies [67]. This method does not require the few-hundred-microtesla magnetic field. However, in addition to the optical components required to produce and modulate the three polarisations, this would require two non-collinear 369-nm laser beams [23]. The size, complexity and cost of such a system makes it unattractive for this project.

The Doppler limit for laser-cooling is given by equation (2.25) and is around 470 μK, or alternatively, the minimum rms velocity is $\sim 0.2\,\mathrm{ms}^{-1}$. This limit, however, was not achieved under the operating conditions used, due to micromotion and other heating mechanisms that are typically large for big clouds and crystals.

$$T_{Doppler} = \frac{\hbar\gamma_{369}}{2k_B} \tag{2.25}$$

$$\approx 470\,\mu\mathrm{K} \tag{2.26}$$

2.2.1 Transitions between hyperfine states

Due to the spin ½ nucleus in $^{171}Yb^{+}$, the ground state is a simple hydrogen-like $^{2}S_{1/2}$ manifold shown in figure 2.6. The microwave clock transition in $^{171}Yb^{+}$ is the so-called 'field-insensitive'[3] $F = 0 \rightarrow F = 1$, $\Delta m_F = 0$ at $\Delta\nu_{clock} = 12.642812118.4682(4)$ GHz [24]. The $F = 0 \rightarrow F = 1$, $\Delta m_F = \pm 1$ transitions can be used to measure the residual magnetic field by measuring the Larmor frequency, $\Delta\nu_{Larmor} = 1.401\,\mathrm{MHz/T}$. The energies of these states vary with the applied DC magnetic field, B, as given by the Breit-Rabi formula:

$$E(F = \begin{matrix} I+S \\ I-S \end{matrix}, m_F) = -\frac{h\Delta\nu_{clock}}{4} - g_I\mu_B B m_F \pm \frac{h\Delta\nu_{clock}}{2}\sqrt{1 + 2m_F\frac{(g_J+g_I)\mu_B B}{h\Delta\nu_{clock}} + \left(\frac{(g_J+g_I)\mu_B B}{h\Delta\nu_{clock}}\right)^2}, \quad (2.27)$$

where $g_I = 0.53577$ and $g_J = 2.0023$ [35] are the gyromagnetic ratio of the nucleus and electron, μ_B is the Bohr magneton and h is Planck's constant. The energies are plotted for small magnetic fields (where F and m_F are qood quantum numbers) in figure 2.7.

Transitions between hyperfine states do not obey the electric dipole selection rules and occur instead by a magnetic dipole interaction. In the case of an electromagnetic (EM) wave incident on an atom, a Taylor expansion of the magnetic vector potential about the position of the nucleus, $\boldsymbol{R_0}$, gives the multipole expansion of the interaction Hamiltonian:

$$\mathcal{H}_{\text{int}} = e\boldsymbol{r}\cdot\boldsymbol{E}(\boldsymbol{R_0},t) - \boldsymbol{\mu}\cdot\boldsymbol{B}(\boldsymbol{R_0},t) + \text{smaller, higher-order terms}, \quad (2.28)$$

where $\boldsymbol{r}$ is the vector between the nucleus and the outer-electron, $\boldsymbol{E}$ is the electric field, $\boldsymbol{B}$ is the magnetic field and $\boldsymbol{\mu}$ is the totalmagnetic moment. The second term in this expansion is the magnetic dipole interaction. This is typically smaller than the electric dipole interaction by a factor of $\sim (Z\alpha)^2$, where Z is the nuclear charge and α is the fine structure constant [34]. This weak coupling means that spontaneous emission between hyperfine states is negligible, and very long coherences are possible. The total magnetic

[3] More accurately, field insensitive to first order at low magnetic fields, as shown in figure 2.7.

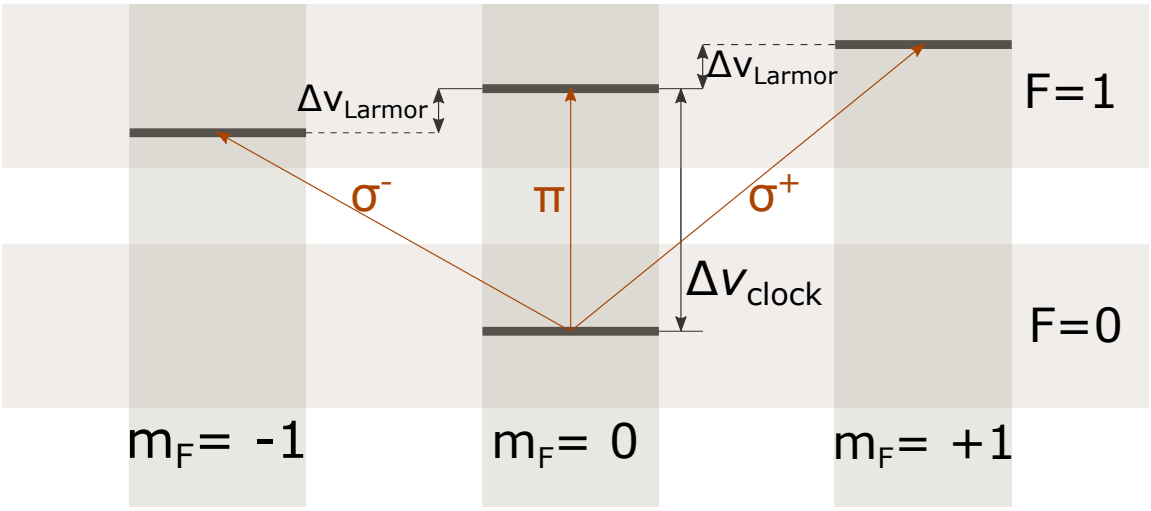


Figure 2.6: Term scheme showing the ground state hyperfine levels and microwave polarisations of the transitions. The unperturbed clock frequency is $\Delta\nu_{clock} = 12.642812118.4682(4)\,\mathrm{GHz}$ [24], the Larmor frequency is $\Delta\nu_{Larmor} = 1.401\,\mathrm{MHz/T}$ [35].

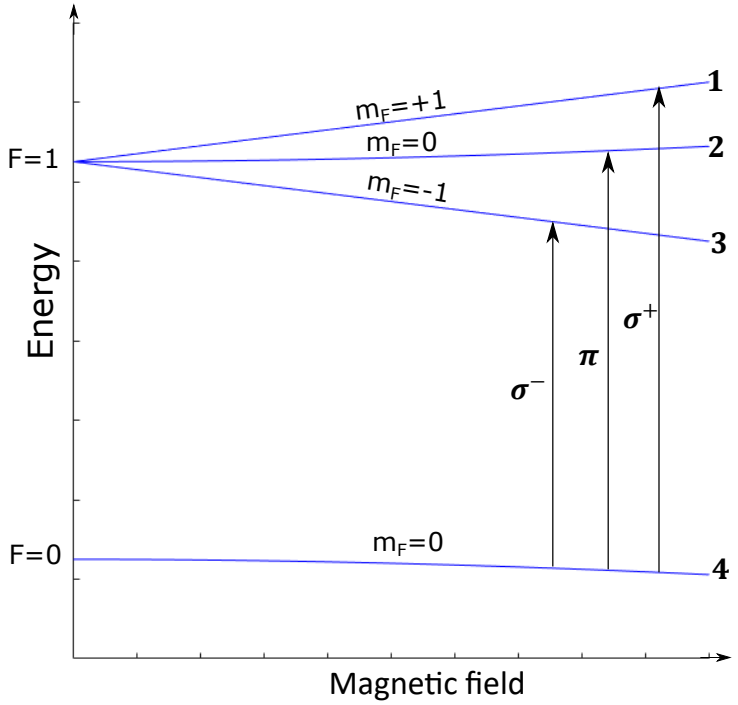


Figure 2.7: Ground state energy levels in a small magnetic field. The numbering of the states 1-4 follows the conventions of the equations (2.34)-(2.38).

moment, $\boldsymbol{\mu}$,arises from the addition of theorbital angular momentum $\boldsymbol{L}$, and the spins of theelectron, $\boldsymbol{S}$, and nucleus, $\boldsymbol{I}$:

$$\boldsymbol{\mu} = \boldsymbol{\mu_L} + \boldsymbol{\mu_J} + \boldsymbol{\mu_I}, \tag{2.29}$$

with

$$\boldsymbol{\mu_L} = -\frac{e\hbar}{2m_e}\boldsymbol{L}, \tag{2.30}$$

$$\boldsymbol{\mu_J} = -g_j\mu_B\boldsymbol{S}, \tag{2.31}$$

and

$$\boldsymbol{\mu_I} = g_I\mu_B\boldsymbol{I}. \tag{2.32}$$

Combining equations (2.29), (2.31), (2.32) and (2.30) with (2.28) gives equation (2.33):

$$\mathcal{H}_{\text{int}} = e\boldsymbol{r}\cdot\boldsymbol{E}(\boldsymbol{R_0},t) + \frac{e\hbar}{2m_e}\boldsymbol{L}\cdot\boldsymbol{B} + \underbrace{g_j\mu_B\boldsymbol{S}\cdot\boldsymbol{B}(\boldsymbol{R_0},t) - g_I\mu_B\boldsymbol{I}\cdot\boldsymbol{B}(\boldsymbol{R_0},t)}. \tag{2.33}$$

In the case of hydrogen like systems, with an $S_{1/2}$ ground state, such as $^{171}\text{Yb}^+$, $\boldsymbol{L} = 0$, and magnetic dipole radiation will cause a precession in the relative spins of the electron and nucleus. We are left with the two terms in equation (2.33) above the brace. Numbering the states in figure 2.7 1-4 from high to low energy, we can write the interaction Hamiltonian matrix elements:

$$\mathcal{H}_{12} = \frac{\sqrt{2}}{4}\mu_B(g_J - g_I)B_{EM}\cos\omega t\sin\theta, \tag{2.34}$$

$$\mathcal{H}_{23} = \frac{\sqrt{2}}{4}\mu_B(g_J - g_I)B_{EM}\cos\omega t\sin\theta, \tag{2.35}$$

$$\mathcal{H}_{14} = -\frac{\sqrt{2}}{4}\mu_B(g_J + g_I)B_{EM}\cos\omega t\sin\theta, \tag{2.36}$$

$$\mathcal{H}_{34} = -\frac{\sqrt{2}}{4}\mu_B(g_J + g_I)B_{EM}\cos\omega t\sin\theta, \tag{2.37}$$

and

$$\mathcal{H}_{24} = -\frac{1}{2}\mu_B(g_J + g_I)B_{EM}\cos\omega t\cos\theta, \tag{2.38}$$

where $B_{EM}\cos\omega t$ is the time dependence of the magnetic field component of the EM wave, which is at an angle θ to the background field that defines the quantisation axis.

It can be seen that to drive the 'field-insensitive' transition, $2 \to 4$, the oscillating magnetic field should be parallel with the background field; to drive the 'field-sensitive' transitions, the oscillating magnetic field should be perpendicular. During cooling the ${}^2\mathrm{S}_{1/2}(F = 0 \to F' = 1)$ transition is driven in saturation to maximise cooling fluorescence. When measuring the frequency of the clock transition, the spectroscopy techniques outlined in the following section are used.

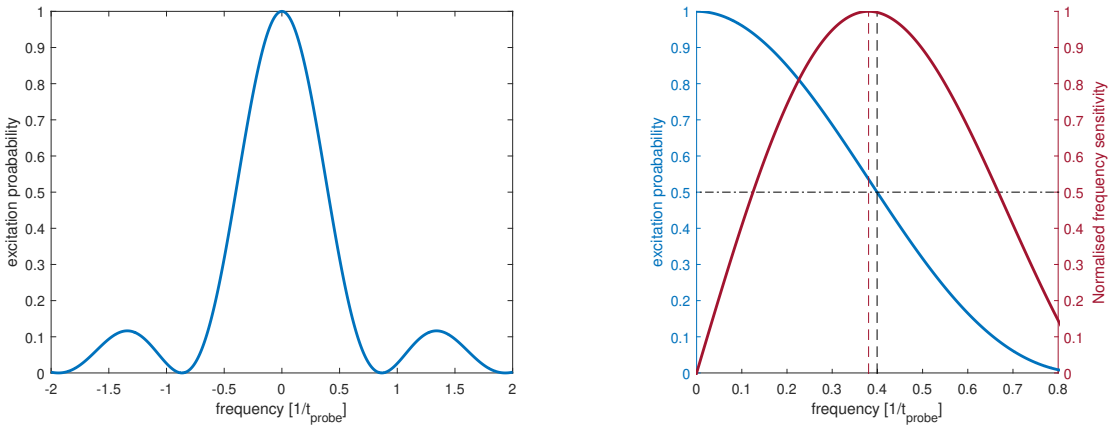
2.3 Spectroscopy

To make a clock from the energy levels discussed in the previous section, it is necessary to measure the energy difference between them accurately. To do this, we measure the frequency of EM waves that are used to transfer the system's state from one energy level to another. As we are making a microwave atomic clock, we are fortunate that the frequency of the microwaves can be simply generated, tuned and counted by electronics. The spectroscopy methods used to measure the clock frequency are described in the following sections.

2.3.1 Rabi Spectroscopy

Starting in the ground state, in the presence of some near-resonant EM radiation of the correct polarisation, solving the time-dependent Schrodinger equation gives the probability of finding the system in the excited state, P_e, as [68]:

$$P_e = \frac{\Omega^2}{\widetilde{\Omega}^2}\sin^2\left(\frac{\widetilde{\Omega}t}{2}\right), \tag{2.39}$$



(a) (b)

Figure 2.8: Rabi lineshape—2.8a and its frequency sensitivity— 2.8b. The Rabi lineshape is subtly different from the sinc-squared function that is often used to approximate it, being narrower and with more excitation probability in the wings. The lock points are slightly displaced from the half-maximum frequencies.

where the Rabi frequency, Ω, is given by:

$$\Omega = \frac{\langle g| \left(\boldsymbol{\mu_J} + \boldsymbol{\mu_I}\right) \cdot \boldsymbol{B} \, |e\rangle}{\hbar}, \tag{2.40}$$

and the effective Rabi frequency, $\widetilde{\Omega}$, is a function of the detuning of the probing radiation from resonance $\Delta = \omega - \omega_{res}$:

$$\widetilde{\Omega} = \sqrt{\Omega^2 + \Delta^2}. \tag{2.41}$$

On resonance a pulse of microwaves with $\Omega t = \pi$ (known as a π pulse) causes a complete transfer to the excited state. By scanning the frequency and applying π pulses, we obtain the Rabi lineshape shown in figure 2.8a. The full-width-at-half-maximum is $0.7987/t$, where t is the π pulse time. The points of maximum frequency sensitivity, which are used for locking, are at $\pm 0.3805/t$ from the resonance peak, as seen in figure 2.8b.

2.3.2 Ramsey Spectroscopy

In Ramsey spectroscopy, two $\pi/2$ pulses of duration $\tau_{\pi/2}$ are separated by a free evolution time, t_{dark}, when no radiation is incident on the atom. The result is an excitation spectrum given by [68]:

$$P_e = 4\frac{\Omega^2}{\widetilde{\Omega}^2}\sin^2\left(\frac{\widetilde{\Omega}\tau_{\pi/2}}{2}\right)\left[\cos\left(\frac{\Delta t_{dark}}{2}\right)\cos\left(\frac{\widetilde{\Omega}\tau_{\pi/2}}{2}\right) - \frac{\Delta}{\widetilde{\Omega}}\sin\left(\frac{\Delta t_{dark}}{2}\right)\sin\left(\frac{\widetilde{\Omega}\tau_{\pi/2}}{2}\right)\right]^2. \tag{2.42}$$

This is plotted in the left panel of figure 2.9 for different microwave pulse and free evolution times. In the limit of very short free evolution time, equation (2.42) is equivalent to equation (2.39). In the limit of very short $\pi/2$ pulses, the dark time is equal to the measurement time; the Ramsey fringes are separated by $1/t_{dark}$ and the width of the fringes are $1/2t_{dark}$. Under these conditions, Ramsey spectroscopy gives a factor of 1.60 reduction in the linewidth and a factor of 1.65 increase in the frequency sensitivity, S, compared to Rabi spectroscopy:

$$\frac{\mathrm{FWHM_{Rabi}}}{\mathrm{FWHM_{Ramsey}}} = \frac{0.7987}{0.5} \tag{2.43}$$

$$\approx 1.6 \tag{2.44}$$

$$\frac{\mathrm{S_{Ramsey}}}{\mathrm{S_{Rabi}}} = \frac{1}{0.6055} \tag{2.45}$$

$$\approx 1.65. \tag{2.46}$$

The linewidth ratio and the frequency sensitivity ratio are plotted as a function of relative duration of $\tau_{\pi/2}$ and t_{dark} in the right panel of figure 2.9, for intermediate values between the Rabi and short-pulse-Ramsey limits. Ramsey spectroscopy has the advantage over Rabi spectroscopy in that it is easy to tune the dark time, and therefore to tune the linewidth. In Rabi spectroscopy, this would also require adjusting the power of the microwaves. However, as will be discussed in section 5.1.1.2, it is difficult to achieve the high levels of microwave isolation that are required during the dark time for Ramsey spectroscopy.

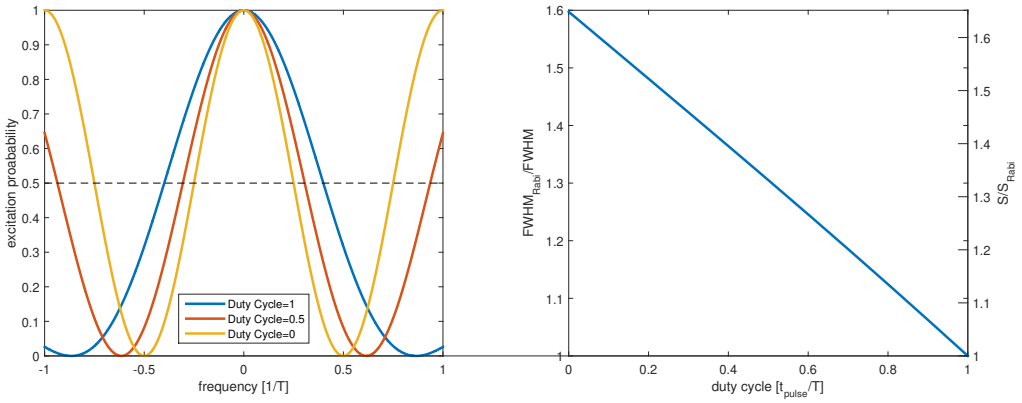


Figure 2.9: Central Ramsey fringe (left) plotted for two $\pi/2$ pulses separated by a dark time. The fraction of the cycle with the microwave power on is called the duty cycle. Three different duty cycles are plotted. The frequencies on the x-axis are in units of the inverse of the measurement time, T. In the limit of the duty cycle equalling 1, the two $\pi/2$ pulses run together giving a Rabi lineshape such as in figure 2.8a. The limit of the duty cycle equalling 0 is called the short-pulse-Ramsey limit, and this corresponds to infinitely short $\pi/2$ pulses. The plot on the right shows that the FWHM decreases as a larger fraction of the measurement time is spent between $\pi/2$ pulses. This causes an increase in the frequency sensitivity of the lock points.

2.3.3 Double-resonance

In microwave-optical double-resonance, two transitions are simultaneously and continuously excited. For ytterbium ions, these transitions are the ground state hyperfine splitting ('1' on figure 2.10) and the cooling/detection transition ('2' or '4' on figure 2.10). The $^2S_{1/2}(F = 1)$ state is common to both these transitions, and so we may anticipate some state-mixing and frequency-shifts. In addition to these main transitions, the repump transitions are also driven. The dynamics are therefore the same as has been outlined for laser cooling in section 2.2.

Keeping the microwaves on resonance and detuning the cooling laser is called laser-sweep double-resonance. The lineshape of a laser-sweep double-resonance scan is a convolution of the Lorentzian lineshape from the damped resonance driven by the laser field, where the damping is provided by the spontaneous emission from the upper state, with the distribution of first-order Doppler shifts of the ions. From this convolution it is possible to extract information about the velocity distribution of the ions. The first-order

Doppler shift is discussed in more detail in section 2.4.1. A notable result is that, as the trapped ions are confined within dimensions much smaller than the wavelength of the microwave-frequency clock transition, there is no broadening of the clock transition due to the first-order Doppler effect. This is known as the Lamb-Dike regime.

Keeping the cooling frequency fixed, and tuning the microwaves, probes the ground state hyperfine structure. The lineshape is a Lorentzian, but in this case the damping is due to optical pumping from the upper hyperfine state to the ground state via the 369-nm transition.

The linewidth of the hyperfine transition in double resonance spectroscopy is given by the power broadening [69]:

$$\mathrm{FWHM} = \frac{1}{\pi}\sqrt{\frac{1}{2}\Omega^2 + \left(\frac{\Gamma_{369}}{2}\right)^2}, \tag{2.47}$$

where Ω is the clock transition Rabi frequency and Γ_{369} is the optical pumping rate at which the $^2S_{1/2}$,F = 1 is pumped to the $^2S_{1/2}$,F = 0 state via the 369-nm transition.

The motional frequencies (described in section 2.1) of the ions in the trap appear as sidebands on the microwave transition, as may be seen in the microwave-sweep double resonance scan in figure 4.3 in chapter 4.

The first-order-Zeeman shift of the 'field-sensitive' $\Delta m_F = \pm 1$ transitions may be used to measure the magnetic field. Driving the 'field-insensitive' clock-transition continuously, in order to derive an error signal for a frequency standard, has been investigated by Schwindt et al. [70] in a buffer-gas cooled ytterbium-ion system, and previously by Jardino et al. [71] in a buffer-gas cooled mercury-ion system. The advantage of this form of spectroscopy is that, as it is continuous, no optical or microwave switch is required. However, there are downsides to using this form of spectroscopy to lock to the clock transition, particularly for a laser-cooled system. These downsides include AC Stark shifts, also known as light shifts, that are present when the two nearly-resonant fields excite transitions between the three states. To reduce these shifts, exacting requirements are placed on the power, polarisation and frequency stability of the cooling-laser. Furthermore, the need to scatter sufficient photons for laser cooling conflicts with the low powers of the

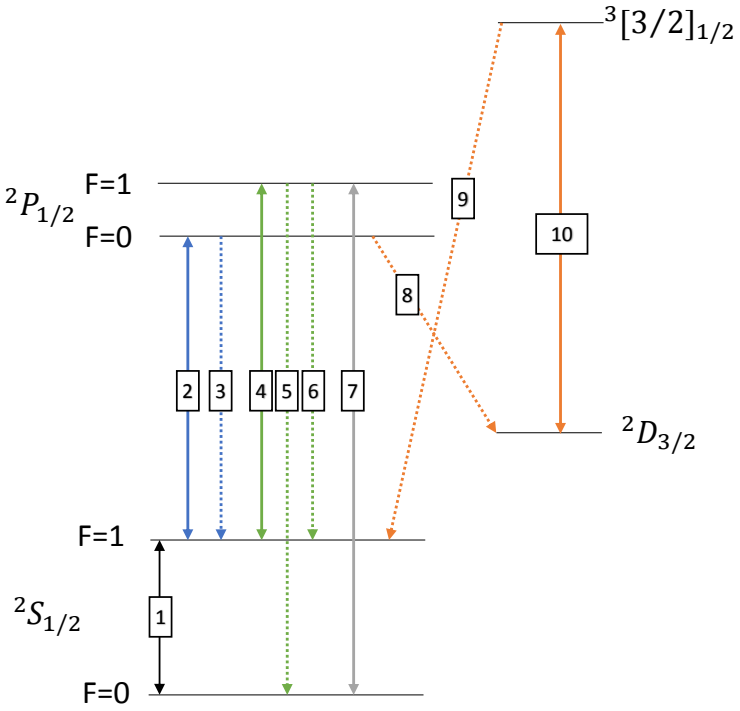


Figure 2.10: Term scheme where the transitions between the states are represented by numbered arrows. Solid arrows represent a driven transition, and dotted arrows represent a decay. The relative magnitude of these transitions determines the steady-state populations of the energy levels.

microwaves and cooling laser required for effective spectroscopy with a narrow linewidth (equation (2.47)). This means that it is not viable to lock to the clock transition using this form of spectroscopy in our system.

2.4 Systematic frequency shifts

The frequency that is measured in an atomic clock will depend on the environmental conditions that the atoms experience. The shifts in the resonance frequency due to these perturbations are known as systematic frequency shifts, as they are a source of systematic error. Additionally, if these frequency shifts are left uncontrolled they can lead to instability of the clock frequency.

The most important shifts for an ytterbium-ion microwave clock are the magnetic second-order Zeeman shift and the motional second-order Doppler shift [24, 72, 73]. Many ytterbium-ion clocks rely on buffer gas cooling to control the second-order Doppler shift, and this results in a third large frequency shift, the pressure shift, due to the

ion-gas collisions [72, 73]. However, this effect will be negligible in our ultra-high-vacuum ($< 10^{-10}$ mbar operating pressure) laser-cooled system [22, 24, 74]. Another frequency shift that is large in some comparable systems is the AC Stark shift from the lasers, known as the light-shift [70, 75]. However, this can be made negligible in our system by ensuring that the cooling and detection beams are extinguished when probing the clock transition.

There are some smaller frequency shifts that are also worth considering when designing an atomic clock. There will be an AC Stark shift from the RF trapping field, and also a small light-shift from thermal black-body radiation. If the clock under development was planned to be deployed at extreme heights, the gravitational redshift would have to be taken into account. This shift is around 1.1×10^{-16} per metre of height near the Earth's surface [76], and therefore for our clock, with the target accuracy of 1×10^{-13}, the height of the clock must be known to 1 km. The gravitational redshift will not be a limitation for the clock we are developing, but it is significant for space clocks [17, 31, 77] and high-accuracy laboratory optical clocks [21].

2.4.1 Motional shifts

The ions' motion causes the frequency of incoming radiation to be Doppler shifted. There are two effects: the first-order shift, which is due to the classical Doppler effect, and the second-order Doppler shift, which is due to time-dilation from the motion of the ions. These effects are mitigated by trapping and laser-cooling the ions.

2.4.1.1 First-order Doppler effect

For atoms moving at a velocity u and at an angle θ to incident radiation at frequency ν, the first-order-Doppler shift is given by:

$$\Delta\nu_{FOD} = \nu\frac{u}{c}\cos\theta. \tag{2.48}$$

Assuming a thermal distribution of velocities, this gives rise to a Doppler-broadened line with FWHM:

$$\mathrm{FWHM}_{\mathrm{Doppler}} = 2\nu \cdot \sqrt{\frac{2k_B T}{mc^2} \ln(2)}. \tag{2.49}$$

Fortunately, there is no first-order Doppler shift for ions confined to linear dimensions much smaller than the wavelength of radiation [78]. It is said that systems that meet this criterion are in the Lamb-Dicke regime. The wavelength of the microwaves used to probe the clock transition is 23.7 mm and so we are comfortably within the Lamb-Dicke regime. First-order Doppler shifts are still seen on the optical transitions and can be used to characterise the temperature of the ions.

2.4.1.2 Second-order Doppler effect

The second-order Doppler effect arises from the relativistic time-dilation experienced by the ions. It is given by the formula [35]:

$$\Delta\nu_{SOD} = -\frac{\nu}{2} \cdot \frac{u^2}{c^2}. \tag{2.50}$$

In an ion trap, the motion can be separated into two components, the secular motion and the micromotion (see section 2.1.2). Meis et al. [79] show that, under the assumptions of a spherical ion cloud[4] that has thermalised to a well-defined characteristic temperature, T, both the secular motion and micromotion contributions to the second-order Doppler shift may be calculated from three observables. The first of these observables is the characteristic temperature of the ions, and the other two are the secular frequencies for a single ion in the ion trap, and for trapped cloud of ions.

Space charge effects from the ions' mutual repulsion push the ions away from the trap centre. This has the effect of lowering the secular frequency of the cloud of ions relative to the single-ion case, and the difference is a function of the (temperature invariant) ion density at the centre point of the trap. The characteristic ion temperature, along with

[4] The formula assumes a Gaussian radial profile of atoms, typical of a cloud. However, in a Coulomb crystal the density is constant.

the observed cloud secular frequency, gives information about the radius of the ion cloud and the mean squared velocity of the micromotion.

Fisk et al. adapt this analysis to a cylindrical ion cloud to make the result applicable to linear ion traps, and this yields the formula for the fractional frequency shift [72]:

$$\frac{\nu_{SOD}}{\nu_{clock}} = -\frac{3k_BT}{2mc^2}\left(1+\frac{2}{3}\left(\frac{\omega_{single}}{\omega_{cloud}}\right)^2\right). \tag{2.51}$$

The first term accounts for the secular motion contribution and the second for the micromotion contribution. $\frac{\omega_{single}}{\omega_{cloud}}$ is the ratio of the single-ion secular frequency to the secular frequency measured for the cloud.

The assumption of a thermalised ion cloud is not valid for the laser-cooled system that is developed in this work. However, the result is useful for comparison with buffer-gas cooled systems that have well defined characteristic temperatures of the ions, typically ranging between 370 K [80] and 1000 K [70, 81]. The method used to evaluate the second-order Doppler shift in this work is to use a laser-sweep double-resonance spectrum to determine the mean squared velocity from the distribution of first-order Doppler shifted frequencies. Equation (2.50) is then used directly to determine the frequency shift. This method is detailed further in section 7.6.3.

2.4.2 Electric field shifts

Due to its spherical symmetry, the S-state of ytterbium has no permanent dipole moment, $\boldsymbol{d}$, and therefore interactions of the type $H_{Stark} = \boldsymbol{d}\cdot\boldsymbol{E}$, where $\boldsymbol{E}$ is the electric field, will be zero to first order [82]. Additionally, for a trapped ion, the net force is zero (otherwise it would not be trapped), and as the trapping force is directly proportional to the ions' charge and the electric field, so too is the time-average of the electric field. The electric field however does induce an instantaneous dipole moment on the ions, $\boldsymbol{d} = \alpha\boldsymbol{E}$, where α is the atom's polarisability. This dipole may interact with the instantaneous electric field in a second order effect proportional to $\boldsymbol{E}^2$. This shift may be calculated for an atom without a permanent dipole moment as a second-order perturbation. The frequency ν_m

of the unperturbed state $|m\rangle$ is shifted by an amount given by [9]:

$$\Delta\nu_m = \sum_{n\neq m} \frac{|\langle m|\,\boldsymbol{d}\,|n\rangle|}{\nu_m - \nu_n}\boldsymbol{E}^2, \tag{2.52}$$

where the sum is over all states $|n\rangle$ that are coupled with the state $|m\rangle$ by the dipole operator.

The RF trapping field gives a shift that is proportional to the mean squared electric field experienced by the ions $\left\langle \boldsymbol{E}^2 \right\rangle$. The electric field is zero at the centre of the ion trap, but for ions displaced from the centre where $\boldsymbol{E} \neq 0$ there will be a shift (see section 2.1). The analysis of Meis et al. [79], modified by Fisk et al. [72] that was used to obtain equation (2.51) is used to estimate the spatial extent of the ion cloud as a function of the measured secular frequencies and a characteristic temperature for the ions. Although, as was noted previously, that the ion cloud in this work is not well thermalised, it is still possible to estimate a characteristic temperature to provide an upper bound for this shift. We can tolerate the error for this approximation as the quadratic Stark shift is smaller than other significant shifts (see section 7.6). The resulting formula for the quadratic Stark shift is [72]:

$$\frac{\Delta\nu_{Quad\,Stark}}{\nu_{clock}} = -k_s \left\langle \boldsymbol{E}^2 \right\rangle \tag{2.53}$$

$$= -4k_s \left(\frac{\omega_{single}}{\omega_{cloud}}\right)^2 \frac{m\Omega_{trap}^2}{e^2} k_B T, \tag{2.54}$$

where e is the elementary charge and Ω_{trap}, is the RF trap frequency. The value of the coefficient k_s, that incorporates the polarisability of the ytterbium ion and the strength of the interaction between the polarised ytterbium ion and the electric field, has been measured experimentally [83] as $k_s = 2 \pm 1 \times 10^{-21}\, m^2 V^{-2}$. A lower temperature results in a higher density of ions in low-field volume of the ion trap close to the centre.

2.4.2.1 Light shift (AC Stark shift)

For radiation on-, or near- resonance: $h\nu_{rad} \approx \nu_m - \nu_n$, and there is significant mixing of the two coupled states. Therefore, if the 369 nm laser is not extinguished, such as in

double resonance spectroscopy (see section 2.3.3), or due to poor shuttering, it will affect the frequency of the transition between the clock states. The frequency shift depends on both the laser power and detuning, and has been evaluated as $1.09 \times 10^{-11}/(\mathrm{GHz} \cdot \mathrm{nW})$ [70]. To eliminate this shift, we take great care when shuttering the laser before probing the transition.

There is an AC stark shift due to the thermal radiation produced by the ions' surroundings, T, given by [84]:

$$\frac{\Delta\nu_{BB}}{\Delta\nu_{clock}} = \beta \left(\frac{T}{T_0}\right)^4 \left[1 + \epsilon \left(\frac{T}{T_0}\right)\right]^2, \tag{2.55}$$

where T_0 is room temperature (300 K). The coefficients for ytterbium ions are $\beta = -9.83 \times 10^{-16}$ [84], and $\epsilon = 2 \times 10^{-3}$ [85]. The small coefficients for ytterbium, and the fact that our system is operated near room temperature, make this shift insignificant.

2.4.3 Magnetic shifts

It is not possible to measure the ground state hyperfine splitting in the absence of a magnetic field. A background magnetic field is required to drive transitions between hyperfine states, as set out in section 2.2.1, and there will also be unavoidable technical noise due to the clock's environment. The behaviour of the hyperfine states in the presence of a magnetic field is given by equation (2.27) and shown in figure 2.7. These shifts are discussed further in the following sub-sections. The emphasis is on how to extract the unperturbed clock frequency from the frequency that is measured in a magnetic field.

2.4.3.1 First-order Zeeman effect

From equation (2.27), and shown in figure 2.7, the $\mathrm{m_F} = \pm 1$ states have a linear dependence on the applied B field given by equation (2.56) [35]. By choosing a transition between two $\mathrm{m_F} = 0$ states, the first-order Zeeman shift is eliminated. The sensitivity to magnetic field of the $\mathrm{m_F} = \pm 1$ states can be exploited to measure the residual magnetic

field and estimate the magnitude of the second-order Zeeman effect:

$$\frac{\Delta\nu_{Larmor}}{B} = \frac{\Delta\nu_{FOZ}}{B} = 1.401 \times 10^{10}\,\mathrm{Hz\,T^{-1}} = 14.01\,\mathrm{kHz}\,\mu\mathrm{T}^{-1}. \tag{2.56}$$

2.4.3.2 Second-order Zeeman effect

In microwave frequency standards, the operating magnetic field is chosen to be very low, typically on the order of $10\,\mu$T. For a transition between states with $\Delta\mathrm{F} = 1$, $\Delta\mathrm{m_F} = 0$, and in the approximation that $(\frac{g_J\mu_B\boldsymbol{B}}{h})^2 \ll \nu_{clock}^2$, equation (2.27) gives the energy difference:

$$\frac{\Delta E_{\Delta F=1,\Delta m_F=0}}{h} = \nu_{clock} + \frac{\boldsymbol{B}^2}{\nu_{clock}} \cdot \left(\frac{(g_J + g_I)\,\mu_B}{h}\right)^2, \tag{2.57}$$

for $^{171}\mathrm{Yb}^+$ [35]:

$$\frac{1}{\nu_{clock}} \cdot \left(\frac{(g_J + g_I)\,\mu_B}{h}\right)^2 = \frac{\Delta\nu_{SOZ}}{\boldsymbol{B}^2} = 3.108 \times 10^{10}\,\mathrm{Hz\,T^{-2}} \tag{2.58}$$

$$\frac{\Delta\nu_{SOZ}}{\boldsymbol{B}^2} = 31.08\,\mathrm{mHz}/(\mu\mathrm{T})^2. \tag{2.59}$$

Small fluctuations, $\delta\boldsymbol{B}$, on a background magnetic field, $\boldsymbol{B}$, will give by a simple expansion:

$$\Delta\nu_{SOZ} = 6.216 \times 10^{10}\,[\mathrm{Hz\,T^{-2}}]\,\boldsymbol{B}\cdot\delta\boldsymbol{B} \tag{2.60}$$

$$\frac{\Delta\nu_{SOZ}}{\nu_{clock}} = 4.92\,[T^{-2}]\,\boldsymbol{B}\cdot\delta\boldsymbol{B} = 4.92 \times 10^{-12}\,[\mu T^{-2}]\,\boldsymbol{B}\cdot\delta\boldsymbol{B}. \tag{2.61}$$

It is clear that to reduce the influence of the second-order Zeeman effect, it is important to operate at a small and stable background magnetic field. This requires the use of bias coils and passive magnetic shields to address both terms in equation (2.61).

The size of the second-order Zeeman shift can be measured through the first-order Zeeman splitting of the $\mathrm{m_F} = \pm 1$ states. Rearranging equation (2.56) in terms of $\mathbf{B}$ and

then substituting this into equation (2.59) gives:

$$\Delta\nu_{SOZ} = 310.8 \left(\frac{\Delta\nu_{Larmor}}{1.401 \times 10^6} \right)^2 . \tag{2.62}$$

Many microwave frequency standards implement a secondary lock to a magnetically-sensitive transition to reduce the uncertainty in the second-order Zeeman shift of the 'magnetically-insensitive' clock transition [23, 80].

Chapter 3

Laser System

In this section, I outline the lasers required to laser-cool and control the state of the ytterbium ions, and discuss the implementation chosen for this work. In section 3.1, I introduce the term scheme for $^{171}Yb^{+}$ and discuss the role of the required lasers. In section 3.2, there is an account of the lasers used, their specifications, and the supporting hardware. Sections 3.3 details how the optical components were laid out and packaged. In section 3.4, the requirements and methods for frequency stabilisation are explored, including a new method for stabilising the IR lasers to air absorption lines. The light delivery to the ion trap is discussed in section 4.3 in the following chapter.

I would like to acknowledge the contributions of Geoffrey Barwood and Guilong Huang to the work described in this chapter: Geoffrey Barwood led the design of the laser system and sourced the lasers; and Guilong Huang led on the assembly and packaging of the compact laser system.

3.1 $^{171}Yb^{+}$ term scheme and overview of the required lasers

The term schemes showing the relevant atomic transitions for both neutral and singly-ionised ^{171}Yb are shown in figure 3.1. The notation has been described in section 2.2. In the following subsections, the methods of photoionisation and laser-cooling are discussed.

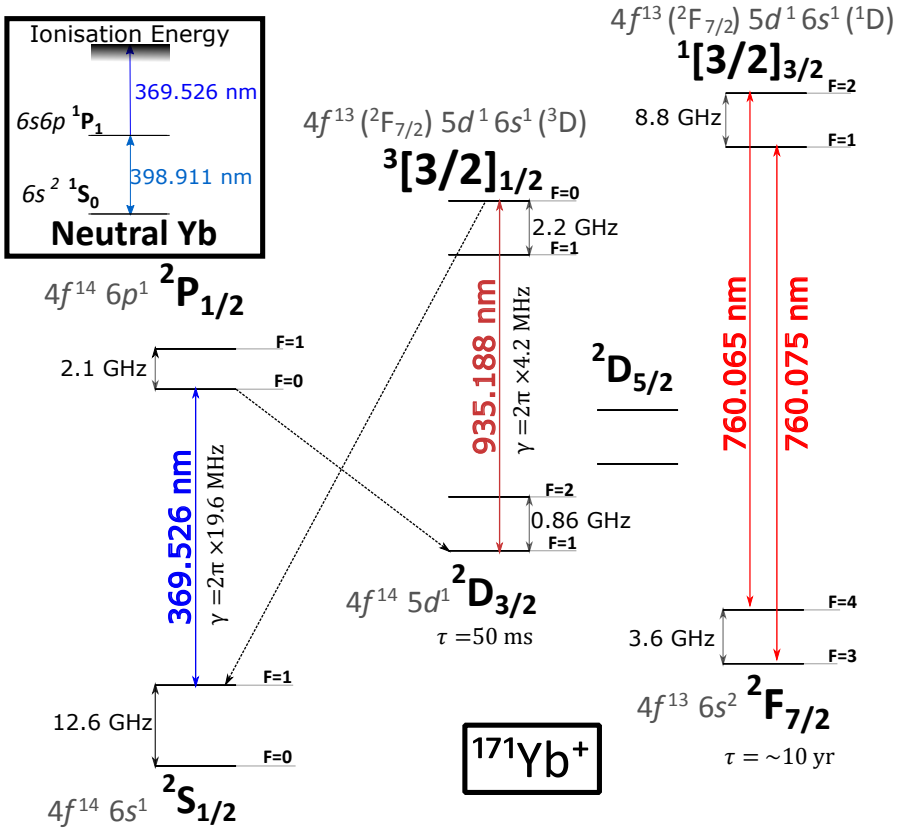


Figure 3.1: Partial term schemes for neutral (inset), and singly-ionised ^{171}Yb. The driven atomic transitions and the required laser wavelengths and microwave frequencies are shown.

3.2 Laser specifications

A portable laser-cooled atomic clock requires lasers that are compact, robust against external perturbations, and have low power consumption. The lasers must also have suitable linewidths, frequency stabilities and control, and optical power. The laser current is provided by electronics that are described in section 5.1.6. Temperature control of the thermometric coolers (TECs) on the laser diodes and doubling crystal are all performed by an NPL-designed temperature controller [86].

369 nm light is provided by a Toptica DL100-PRO ECDL with a laser diode from Nichia Corporation. The laser head includes beam-shaping optics (anamorphic prism

pairs), a half-wave plate (to adjust the polarisation of the light into an optical isolator) and the optical isolator itself. The linewidth of this laser is below 100 kHz [87]. Also of note is the large amplified stimulated emission (ASE) plateau 15 dB down from the laser line that is tens of GHz wide. This may reduce the efficiency of state preparation by off-resonantly driving out of the ground state, as is observed in calcium [88]. Typical output power at the ions is 300 μW, focused to 200 μm. The bulky size ($240 \times 90 \times 90$ mm) and moving parts mean that it is the least suitable laser for a portable system.

The long-term aim is therefore to replace the 369-nm laser with a smaller and more robust unit and, for this reason, we evaluated frequency doubling of a (Sacher Micron) 739-nm diode laser that provides up to 60 mW output in free space. Using an AdvR waveguide frequency doubler with a pig-tailed fibre input and free-space output, $\sim 24\,\mu$W was produced at 369 nm from 15 mW input to the doubler. With further optimisation of the fibre input coupling and minimisation of the transmission losses between the laser and doubler, we expect that up to 100 μW could be produced for 30 mW in fibre at 739 nm. However, for the current trap, we require a minimum 100 μW of 369 nm light for photoionisation and efficient cooing, and so our doubler efficiency is currently marginal. Fortunately, rapid progress is being made in commercially available doublers and lasers at 739 nm, and it seems that this route to generating 369 nm light will be viable in the near future.

The 399 nm light is generated by frequency doubling of a laser source at 798 nm. The 798 nm is from a Sacher Micron laser [89], packaged in a TO-39 can, that uses volume holographic grating technology to provide wavelength selectivity. It has a linewidth below 100 kHz and a tuning range of 30 GHz. During the course of the project, two of these lasers failed under normal operating conditions. The mechanism of the failures is not known, but the symptom was that, after months of stable operation, the output power would suddenly decrease to about 20% of the normal level.

The frequency doubling is via a waveguide doubler from ADVR. The doubler is coupled to single mode, polarisation maintaining (SMPM) fibre on both the input and output. Current control for the 798 nm laser is by a ThorLabs OEM board. Typical

399 nm output power at the ion trap is 50 μW, in a $1/e^2$ beam waist of 200 μm, which is sufficient for photoionisation. After the ion trap is loaded, the 798 nm laser is blocked to prevent scattered light adding noise to the fluorescence signal.

With its small size ($37 \times 30 \times 8$ mm) and fibre output, the 760 nm laser has by far the most attractive packaging for this project, as may be seen from figure 3.5, a photograph of the laser system that is discussed in the following section. This laser is well-developed due to its commercial use in oxygen detection. Unfortunately, there was a high failure rate with this component due to the difficulty of integrating the optical isolator before the fibre output, which is essential to provide reliable frequency tuning. A ThorLabs OEM current driver was used to supply this diode. Power of 2 mW in a waist of 300 μm is delivered to the ions. The wavelength is stepped between 760.065 nm and 760.075 nm to drive both hyperfine sublevels out of the F-state.

F-state trapping was not found to be an issue or the cause of the observed dark ions[1]. Therefore, this laser could be omitted without an impact on performance.

The 935 nm laser is a distributed feedback laser (DFB) from Eagleyard Photonics marketed for water vapour detection. To tune this laser to the ytterbium frequency, it has to be cooled to 2°C. The diode can output up to 80 mW, but we use 3 mW focused to a 1 mm waist at 60° the ions.

3.3 Laser package layout

To fit in our compact system, the lasers and their support hardware were packaged compactly in a 6U high sub-rack, as seen in figure 3.2. The laser bank consists of two boards, visible in figure 3.2a. One board, vertical in figure 3.2a, contains the 369 nm and 935 nm lasers. The second board contains the 798 nm and 760 nm lasers. The layout of the laser boards are shown in figure 3.3, and figure 3.5.

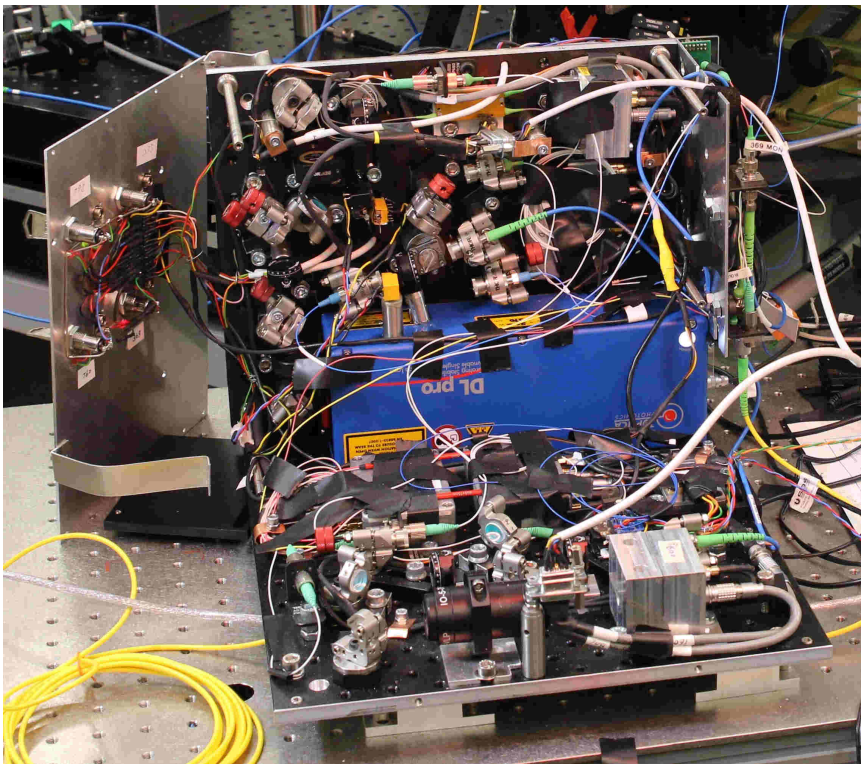
On first laser board, the 369-nm beam comes out of the Toptica DL Pro box, which contains the isolator and beam-shaping optics; some of the power is picked off by a

[1] Dark ions are non-fluorescing ions, they are discussed in chapter 6.

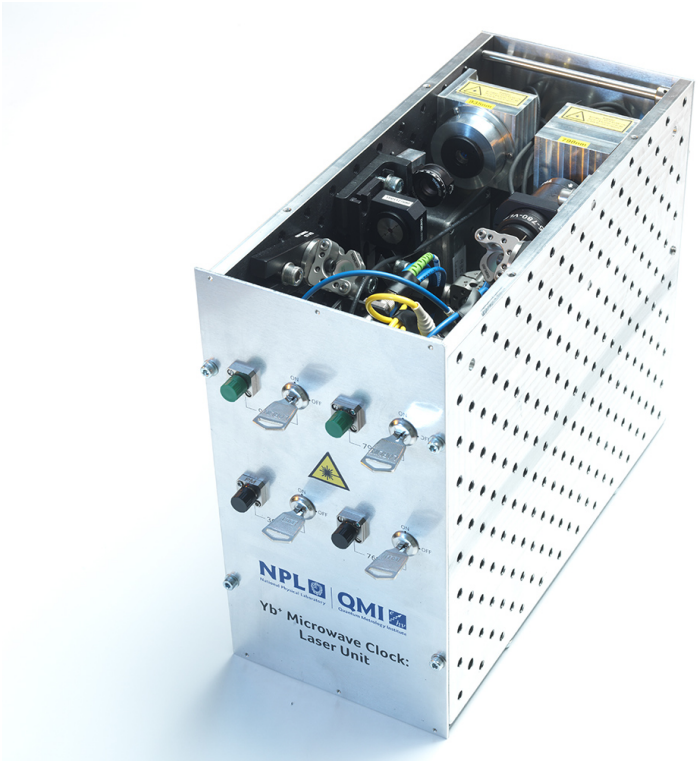
beamsplitter and sent to the wavemeter. The majority of the power passes through two shutters to completely extinguish the beam. Also in the beam-path are a 90% neutral density filter, which reduces the power during state-readout, and a $\lambda/2$ retardation plate to align the polarisation in the SMPM fibre. The 399 nm output from the frequency doubler is combined with the 369 nm on a dichroic mirror. The 935-nm beam passes through an isolator and a retardation plate before being coupled into the fibre. A fibre splitter sends a fraction of the power to the wavemeter, and the remainder is sent over to the second board of the laser bank.

On the second board, the 798-nm laser passes through an isolator on its way to being coupled into two fibres via a retardation plate. Most of the power goes to the frequency doubler, which produces 399 nm light for photoionisation. A shutter on the input side controls the output of the doubler. A small fraction of the power goes to the wavemeter. The 760-nm laser is a pigtailed fibre coupled device with an integrated isolator. The power from the output fibre is split, with a small fraction going to the wavemeter. The remainder of the power is passed to a fibre multiplexer to mix with the other infrared wavelength, 935 nm, and sent to the ion trap via a fibre shutter.

The rear of the laser bank contains the frequency doubler to 399 nm and a plug for the electrical connections that connects to the backplane socket in the main case. The front of the laser bank contains switches to control the power to the lasers, and LED indicators that show the status of the lasers' temperature control. While the front panel contains fibre outputs, the fibres are typically routed within the case.



(a)



(b)

Figure 3.2: Laser bank: open in 3.2a, and closed in 3.2b.

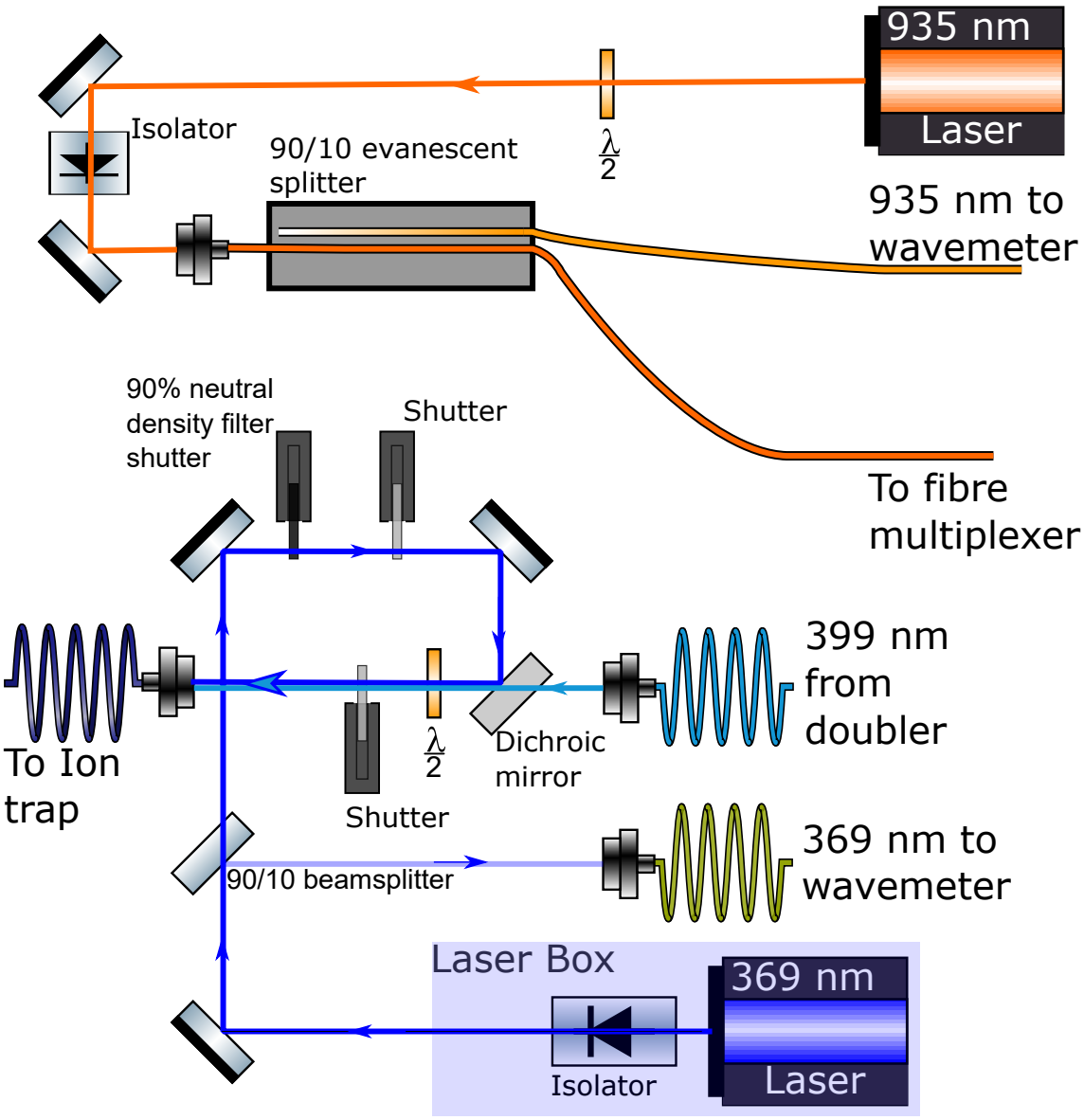
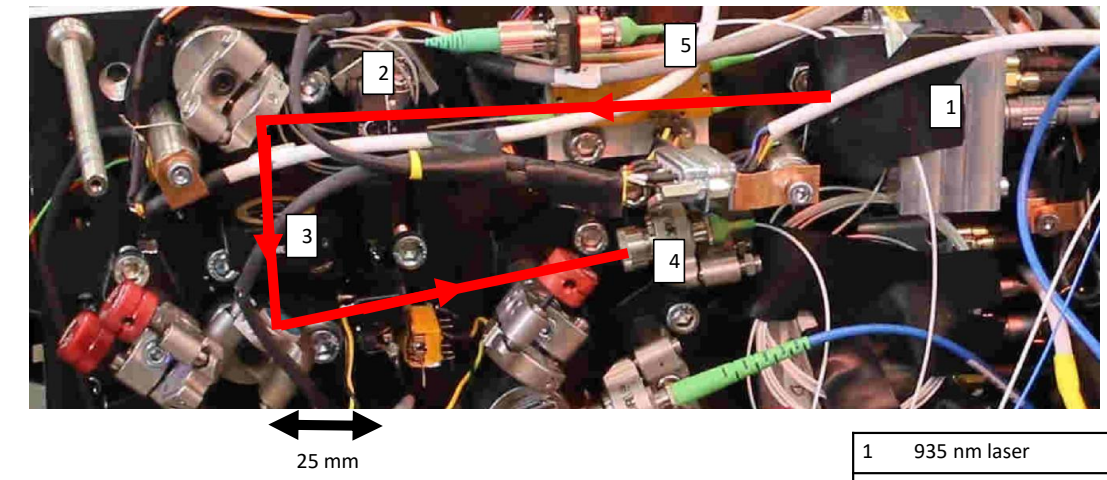
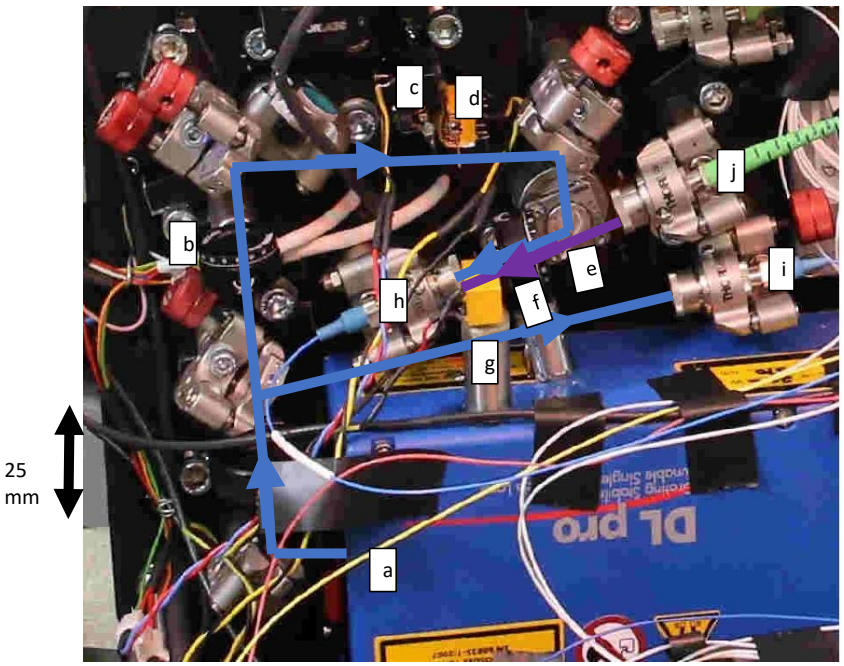


Figure 3.3: Schematic of the 369, 399 and 935 nm laser board. This is the vertical board in figure 3.2a. A labelled photograph of the implementation is shown in figure 3.4.



1	935 nm laser
2	$\lambda/2$
3	isolator
4	fibre input
5	90/10 fibre splitter



a	369 nm laser
b	$\lambda/2$
c	filter shutter
d	shutter 1
e	dichroic mirror
f	$\lambda/2$
g	shutter 2
h	369 nm and 399 nm to ions
i	369 nm to wavemeter
j	399 nm from doubler

Figure 3.4: Labeled photographs of the 935-nm (top) and 369- and 399-nm (bottom) laser systems. The schematics are shown in figure 3.3.

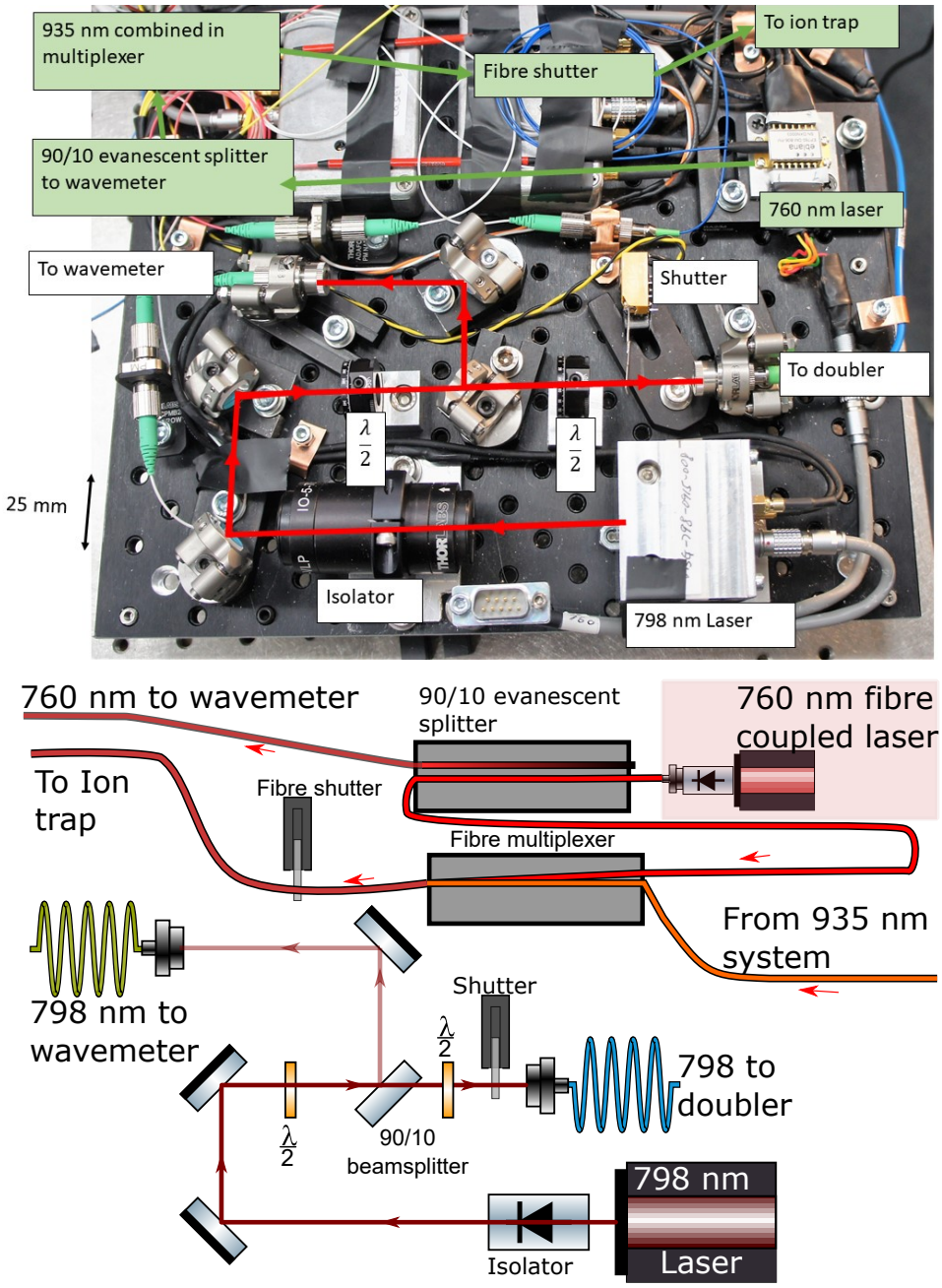


Figure 3.5: Labelled photograph, and schematic of the of the 760- and 798-nm laser board. Note how the size of the 760-nm laser is significantly more compact than the 369-nm laser that is visible in figures 3.2a and figure 3.4.

3.4 Frequency stabilisation

The frequencies of the lasers are not passively stable at the level required for long-term operation of this device, and so require active feedback to keep them on resonance. To apply the feedback, we monitor the laser frequencies on a wavemeter. This method [90], while effective, requires the use of an expensive and relatively bulky component. The use of a high-end wavemeter was necessitated due to the wavelength range of the required lasers spanning the IR to the UV. Frequency-doubling to the UV for the 399 nm and 369 nm allows the wavelength range to be entirely in the IR, allowing the use of a compact and relatively inexpensive wavemeter. Once the ions are trapped and fluorescing, it is possible to stabilise the lasers to the ions using the transition profiles, shown in section 7.3.1.1. The problem with this method of wavelength stabilisation is that when the system is initially turned on, the wavelength of the lasers is not reliably known, even when returning to their previous parameters. The uncertainty in frequency from a cold-start also makes using a cavity for the wavelength reference problematic, as the lasers may move across free-spectral-ranges. An additional laser may also be required to stabilise the cavity to a reference, for example, the absorption from a Rb cell. Lasers for this purpose are reliable and commercially available. Lasers can also be stabilised to an ytterbium discharge lamp [91], but the short operational lifetime ($\sim$ 100 days) of the lamps is impractical.

3.4.1 Wavemeter method

The laser frequencies were stabilised to a High Finesse WSU (1 MHz absolute accuracy 500 kHz resolution) wavemeter. To remove long-term frequency drift from the wavemeter, it was periodically calibrated to a Zeeman-stabilised HeNe optical reference [92]. The experiment control program sets the target frequency for each of the lasers, and an error signal is generated from the difference. A digital integrator feedback loop is used to control the wavelengths. Feedback is applied by tuning the current to the laser diode to most of the lasers. The exception is the 369 nm laser, where the feedback tunes the

position of an interference grating. Feedback is typically applied once per second. The feedback methods are summarised in table 3.1.

Laser	Technology	Feedback Method
369 nm	EDCL @ 369 nm	Grating adjustment by voltage tuning piezo
760 nm	Doubled VHG ECDL @ 798 nm	Diode current tuning, switches between setpoints to clear F=3 and F=4 state every 30 s
798 nm	DFB @ 935 nm	Diode current tuning
935 nm	DMLD @ 760 nm	Diode current tuning

Table 3.1: A table summarising the laser feedback methods. All lasers are stabilised to a wavemeter.

3.4.2 Air absorption

As has been mentioned previously, it is fortunate that some of the required laser diodes for an ytterbium-ion clock have alternative industrial uses. Two of the lasers — 760 nm for the F-state repump and 935 nm for the D-state repump — have alternative uses in gas-detection. The 760-nm laser may be used for oxygen detection, and the 935-nm for water vapour detection. We decided to investigate if these gas absorption lines, both present in air, could be used as a frequency reference for the lasers. There is a particularly pleasing coincidence between an oxygen absorption and F-state frequencies, shown in figure 3.6. The nearest water absorption from the 935 nm transition is 0.1 nm away, as seen in figure 3.7.

To measure the air-absorption lines, a laser beam's frequency was scanned by temperature-tuning, and the power in the beam was sampled at two points separated by 1.6 m. The results, shown in figures 3.6 and 3.7, were found to be in good agreement

to the HITRAN molecular absorption database [93]. It can be seen that the oxygen absorption lines can provide a useful wavelength reference very close to the transition frequencies in Yb^+. There are also detectable water vapour transitions within the tuning range of the 935 nm laser that may be used as wavelength references. However, as these are approximately 0.5 nm away from the Yb^+ transitions, their practicality as a wavelength reference is limited.

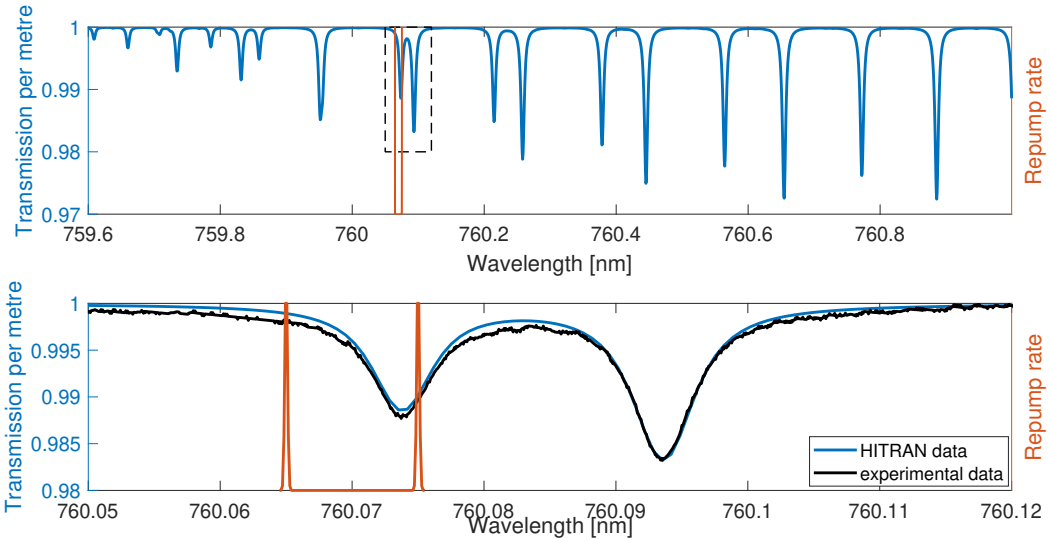


Figure 3.6: Coincidence between oxygen absorption and Yb^+transitions at 760 nm. The data were taken in 1.6 m of air. The experimental data were scaled in the vertical axis to match the peak height from HITRAN, shown here for air at room temperature and pressure with 21% oxygen, and a linearly-varying background was removed.

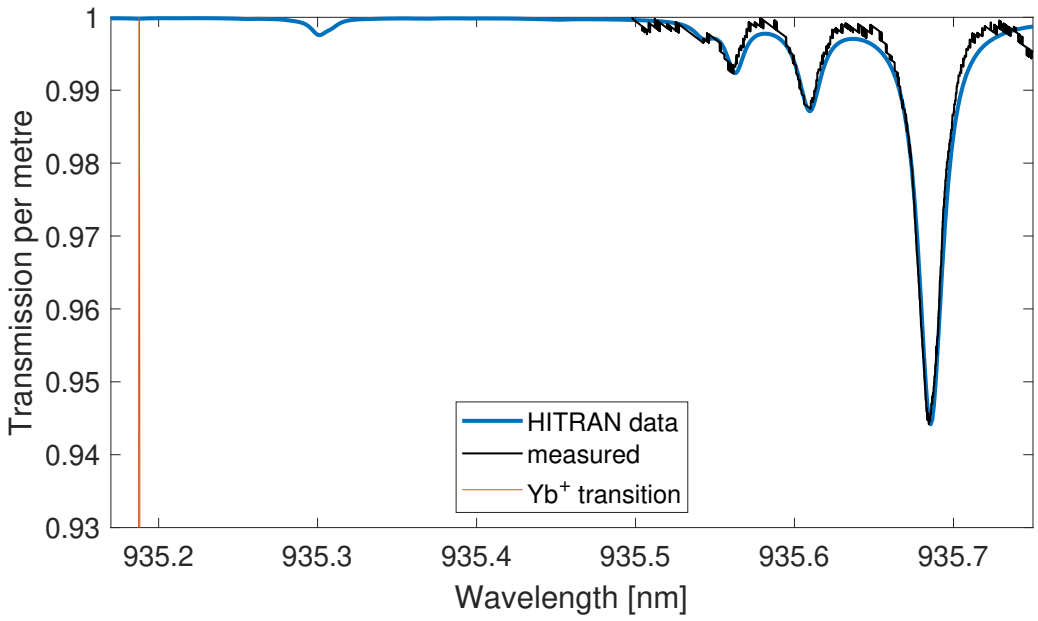


Figure 3.7: Water vapour absorption lines in 1.6 m air and Yb^+ transitions near 935 nm. The data were obtained by temperature tuning the 935 nm laser away from the Yb^+ transition to the water vapour absorption. The experimental data were scaled in the vertical axis to match the peak height from HITRAN, shown here for air at room temperature and pressure with 50% relative humidity, and a linearly-varying background was removed.

3.5 Laser system conclusions

This chapter has detailed the compact laser system that was used in this project and its performance. It was found that the 760 nm laser was not required as described in chapter 6. The complexity and cost of the laser system is an obstacle to a commercially viable system. It is envisaged that a commercial system would probably not use the photoionisation laser, and would instead ionise the ytterbium using an alternative solution such as electron-bombardment. It may also be attractive for a commercial system to deliver light to the trap using a free-space beam, as this would reduce polarisation fluctuations, and is potentially a simpler solution.

Air absorption spectroscopy was investigated to provide wavelength references for the lasers. It was found that there was an overlap between a molecular oxygen absorption

line and an F-state clearout transition in Yb^+. An additional air absorption line due to water vapour can be used to reference the 935 nm laser. This requires significant frequency tuning of the laser to observe, and so is more suited for use as an occasional calibration.

Chapter 4

Physics Package

The physics package comprises a linear ion trap within a vacuum housing and is mounted inside a mu-metal magnetic shield. A photomultiplier (PMT) with imaging optics, magnetic bias coils, and fiber optic collimators are attached outside the vacuum chamber. This chapter details the design of these components.

4.1 Ion trap designs

During this project, we have used three ion traps. The designs are detailed in the following subsections. The Mark 1 design was based on an ion trap used by Sandia [30]. The Mark 2 trap was a new design for this project that allowed axial laser access. The Mark 3 is a variant of the Mark 2 with some design improvements, and increased performance. As the Mark 3 trap has only recently come online, unless otherwise stated, the data in this thesis is from the Mark 2 trap.

4.1.1 Mark 1 ion trap design

In the first year of my DPhil, I designed and made a testbed system from mostly commercial-off-the-shelf (COTS) parts. This was used to learn about trapping and laser cooling and to test the development of the laser system. This system used a design similar to that used by Sandia during the development of their buffer gas cooled ytterbium ion

clock [30]. An array of 1 mm diameter wires formed the trapping structure. We used molybdenum for the rod electrodes and tantalum for the end caps. Molybdenum was chosen for its similar work function to ytterbium; this reduces the impact of surface charging that occurs when ytterbium metal that has been effused by the oven sticks to the electrodes. Tantalum is softer and easier to work; it was chosen for the endcaps, as it had to be deformed and wedged into the Macor (a machinable glass ceramic) support to ensure a tight fit.

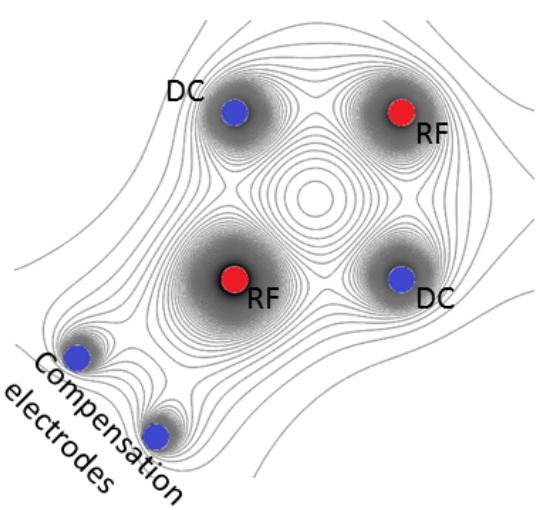
Four of the rod electrodes formed a square, with the centres of the rods separated by 3 mm. This gives an r_e/r_0 ratio of 0.45, with an endcap separation, $2z_0 = 6$ mm. RF is applied to two diagonally opposite rods, and the other two are independently biased DC. It is not practical to independently bias the RF electrodes, as these are typically run off a single line in order to reduce any phase differences caused by asymmetries. A further pair of compensation electrodes are added so that the ions can be pushed to the trap centre along the RF electrode axis to reduce micromotion. Finite element modelling was used to find an optimal design for these compensation electrodes. It was found that by splitting the compensation electrodes to allow line-of-sight to the ions, smaller compensation voltages were required and the RF trapping potential was minimally affected. The RF trapping potential from the electrode arrangement is shown in figure 4.1.

Due to the presence of endcap electrodes made from solid wire, the laser beams could not enter the trap along the trapping axis. Holes were machined in the Macor to allow two beams to pass through the trap structure at 60° to the axis. A table of the design parameters of the Mark 1 trap is shown in table 4.1, and figure 4.2 shows a labelled diagram.

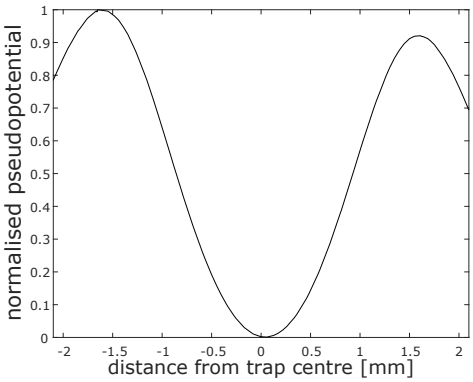
A double resonance scan taken in the Mark 1 trap is shown in figure 4.3. The radial secular frequency can be seen to be 240 kHz.

The Mark 1 trap could trap a few hundred ions. Its limitations were that it was not very easy to construct; the r_e/r_0 was optimised for optical access, not reducing RF heating [30, 43, 44]; and, due to the endcaps, there was no laser path down the axis of the trap. This limited the overlap of the ions and the laser beam and limited the number

of ions that could be stored to below 1000. The vacuum system that it was housed in was also not suited for miniaturisation or magnetic shielding. An image of a Coulomb crystal of ~300 ions from the Mark 1 trap is shown in figure 4.4. It is notable that although some dark ions[1] were observed in this trap, it was rare to see them, and the ion loss rate was much lower than the Mark 2 trap.



(a)



(b)

Figure 4.1: figure 4.1a shows the radial pseudopotential from the array of electrodes. RF electrodes are in red and DC electrodes are in blue. The two electrodes at the bottom left provide a means to push the ions radially along the axis of the RF electrodes (y-axis in figure 2.2). The other radial-axis DC compensation is achieved by biasing the two DC rods. The presence of the two compensation electrodes reduces the trap depth by 10% (figure 4.1b).

[1]Dark ions are non-fluorescing ions, they are discussed in chapter 6.

rod electrodes	1 mm ⌀ molybdenum
endcap electrodes	1 mm ⌀ tantalum
rod spacing	3 mm
laser access	2×2 mm ⌀ bore in Macor, 60° to trap axis
r_0	1.1 mm
r_e/r_0	0.45
z_0	3 mm

Table 4.1: Mark 1 ion trap parameters

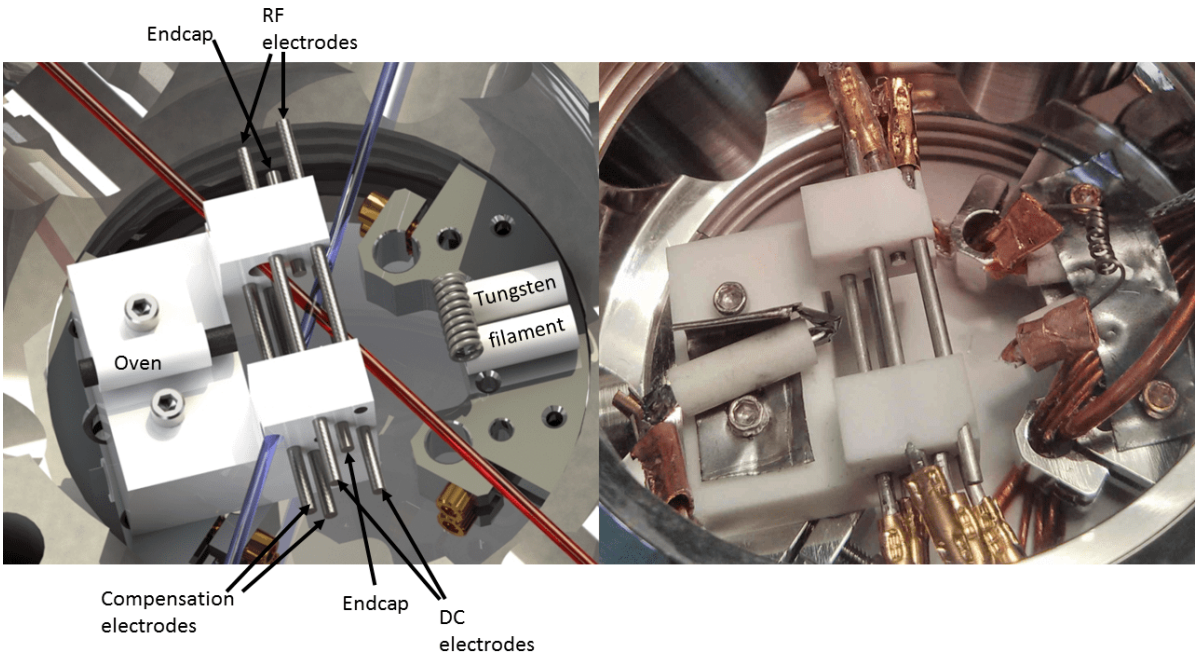


Figure 4.2: A labelled render and photograph of the Mark 1 trap assembled in the vacuum chamber. The lasers enter the trap through bores in the Macor.

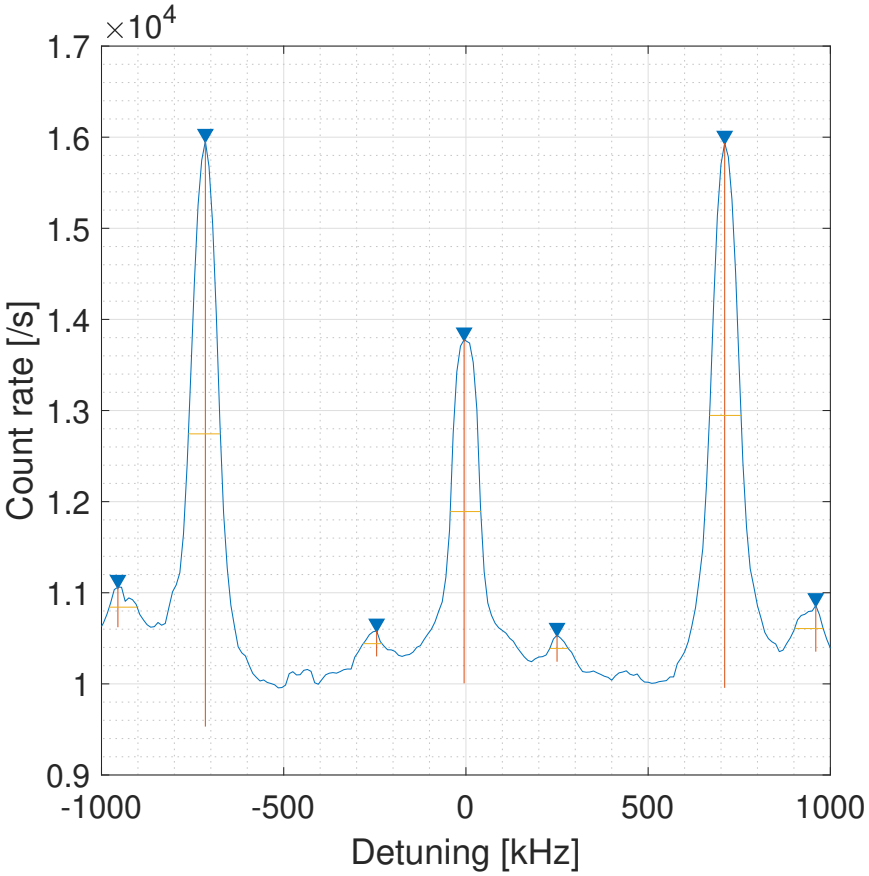


Figure 4.3: Double resonance scan in Mark 1 trap. The centre peak is the $m_F = 0 \rightarrow m_F = 0$ transition. The two large peaks at roughly ± 710 kHz are the $m_F = 0 \rightarrow m_F \pm 1$ transitions. There are smaller peaks, due to the radial motion of the ions in the trap, symmetrically spaced at the secular frequency of 240 kHz on either side of these main peaks. The sidebands due to the axial motion of the ions are at low frequencies and are not resolved from the carrier peaks. The 369-nm and 935-nm lasers are at 60° to the trap axis.

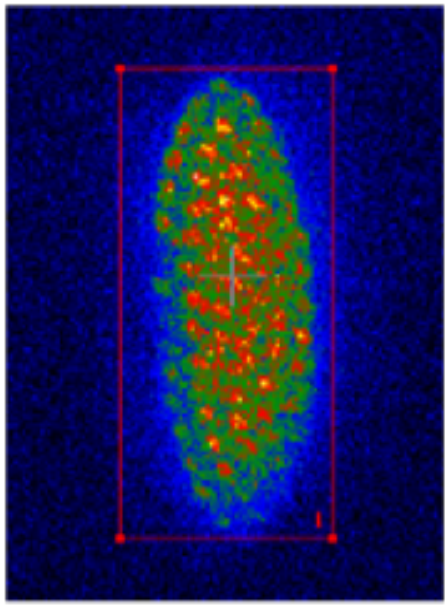


Figure 4.4: Coulomb crystal of ~300 ions from Mark1 trap. Ion spacing is of the order of 10 microns.

4.1.2 Mark 2 and Mark 3 ion trap design

The Mark 2 trap was designed to facilitate a laser beam travelling through the trap axis. This arrangement ensures the best overlap between the laser and the trapped ions. The trap size was increased to the largest that could be easily installed in a DN40 bore of a vacuum chamber. The ion trap also provides a mounting point for the oven that is embedded in the horizontal compensation electrode. The electrode radius was chosen to be as large as possible while still allowing for 45° of optical access. The ion trap was assembled as shown in figure 4.5.

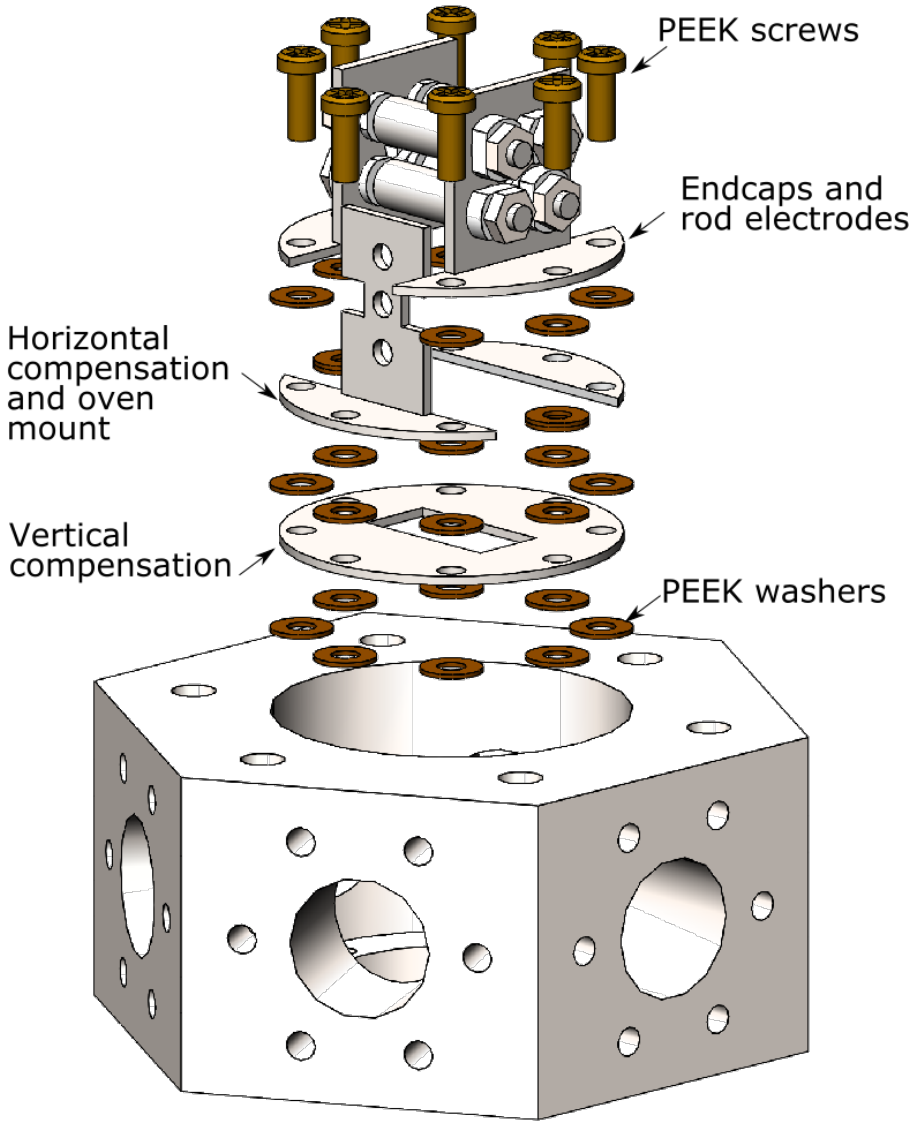


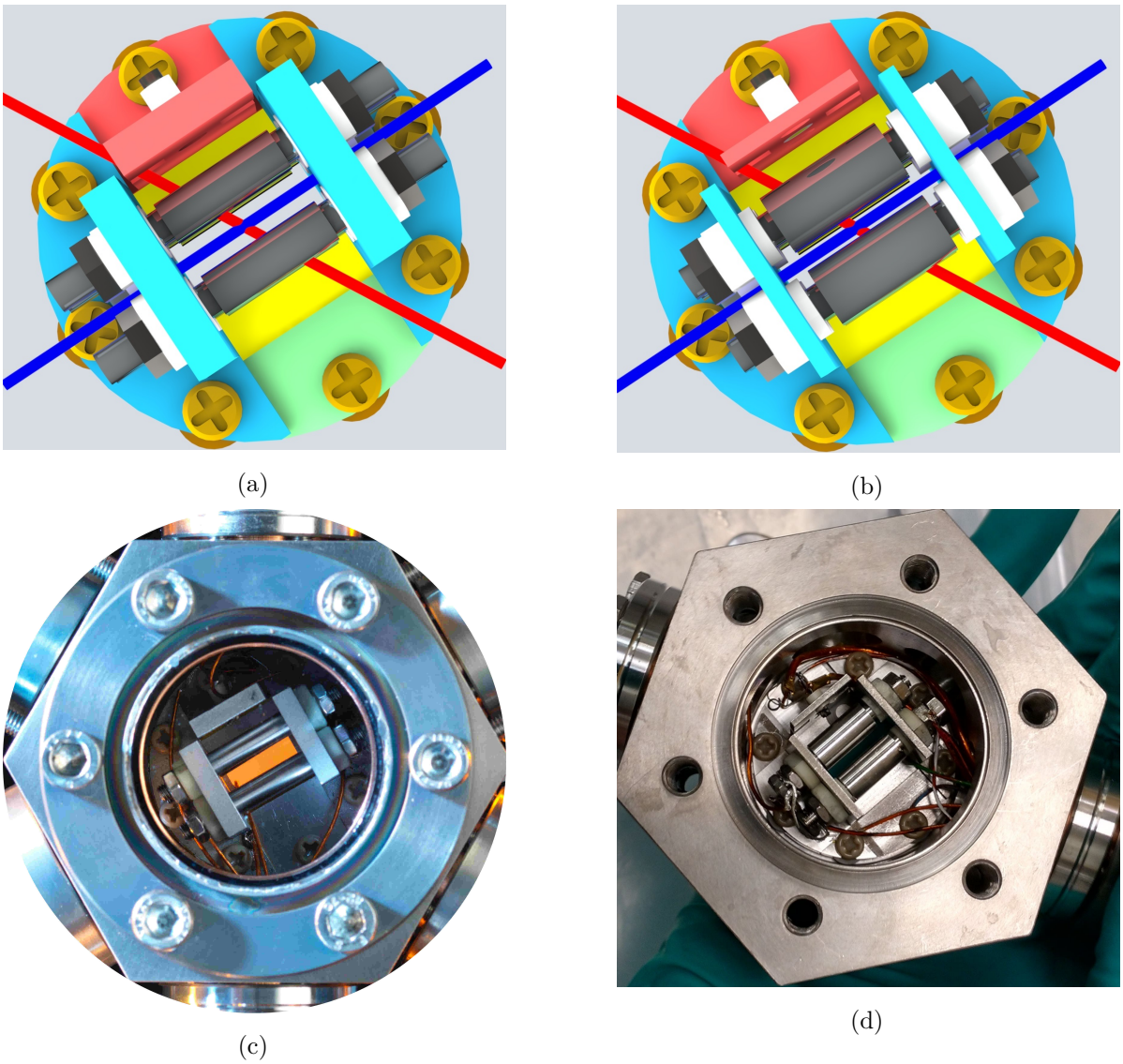
Figure 4.5: Ion trap assembly. PEEK screws hold the layers of the ion trap together; they are spaced and electrically isolated from each other and the vacuum chamber by PEEK washers.

The trap assembly screws directly into internal tapped through-holes inside the vacuum chamber (engineering drawings of the vacuum chamber and ion trap are in

appendix A), with PEEK (Polyether ether ketone — a UHV-suitable plastic) screws and PEEK washers providing electrical isolation between the plates. The rods are electrically isolated from the endcaps by ceramic bushes and kept in place by M3 nuts tightened onto the tapped ends of the rods. This also provides a means for securing the wires for the electrical connections. With no line of sight to the insulator, the ions will be less susceptible to surface charging effects. Table 4.2 summarises the trap parameters, and images of the Mark 2 ion trap are shown in figure 4.6.

	Mark 2	**Mark 3**
rod electrodes	4 mm ⌀ titanium	5.5 mm ⌀ 316 SS
endcap electrodes	aluminium plate	316 SS
rod spacing	7.3 mm	7.3 mm
laser access	on-axis 4.8 mm ⌀ bore through endplates. 3.5 × 4 mm notch in oven holder 60° to axis.	on-axis 4.8 mm ⌀ bore through endplates. 3.5 × 4 mm notch in oven holder 60° to axis.
r_0	3.16 mm	2.41 mm
r_e/r_0	0.63	1.14
z_0	7.9 mm	8 mm
Oven	Welded to horizontal compensation electrode	Thermally isolated from horizontal compensation electrode

Table 4.2: Mark 2 and Mark 3 ion trap parameters.



(a) (b) (c) (d)

Figure 4.6: Renders and photographs of the ion traps used in this project. The mark 2 design is on the left, and the mark 3 is on the right. In the renders, false colour is added to identify the electrodes: blue - endplates; red - horizontal compenstation; yellow - vertical compensation; and green - ground. Note the thinner plate electrodes, and the wider rods in the mark 3 design.

Although it is well known that the optimal parameters for trapping a large cloud of ions in a buffer-gas cooled spherical trap are $q \approx 0.5$ and $a \approx -0.03$ [94, 95], it is found that the denser clouds or crystals of ions that large laser cooling promotes are more stable near the $q = 0$ and $a = 0$ region of the stability diagram [48]. This is because unstable oscillations may be driven either by coupling between the ions' vibrational degrees of

freedom, or by non-quadrupolar electric fields that are generated by the electrodes when they deviate from the idealised hyperbolic shape [41]. The target trapping parameters for the ion traps used in this project are to have $q < 0.1$ and a=0, and for ease of generation, this must be generated by a AC voltage that is below 500 V_{pk-pk} and 3 MHz (see section 5.1.3). Additionally, a potential depth of the trap of the order of 1 eV will allow energetic particles to remain trapped (1 eV $\approx 1 \times 10^4$ K). The trapping parameters, calculated as a function of voltage for the Mark 2 trap driven at 2 MHz are shown in figure 4.7. For a trapping voltage of 200 V_{pk-pk} and 2 MHz, these conditions are met.

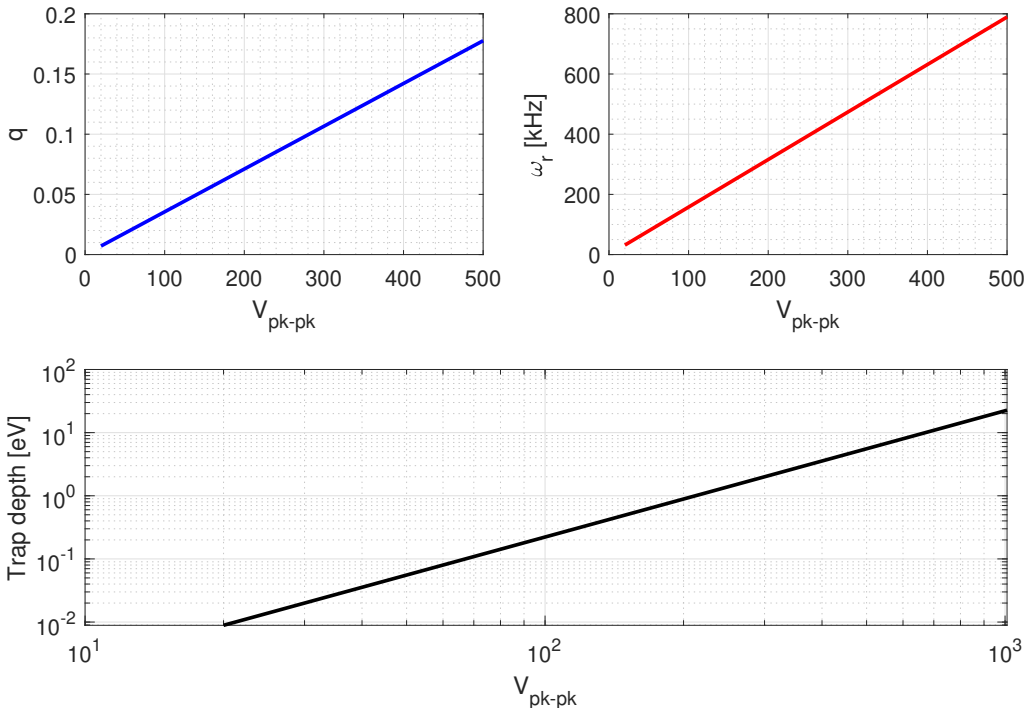


Figure 4.7: Calculated trap parameters for the Mark 2 trap at 2 MHz drive frequency as a function of V_{pk-pk}.

Having a larger volume, the Mark 2 trap allowed a larger number of ions (figure 4.8 shows an image of a cloud of a few thousand ions in the Mark 2 trap) to be trapped than the Mark 1; however, it was plagued by dark ion formation. As has been discussed in section 2.1.4, the number of ions that are trapped is proportional to the volume of the trap [37]. However, this analysis does not take into account non-quadrupolar potentials

that will arise from the finite-length of the electrodes or the micromotion that increases with the size of the ion cloud. In order to store more than a few thousand ions, the length of the ion trap would have to increase, and the RF to be applied symmetrically to all electrodes to reduce the axial micromotion effect [96].

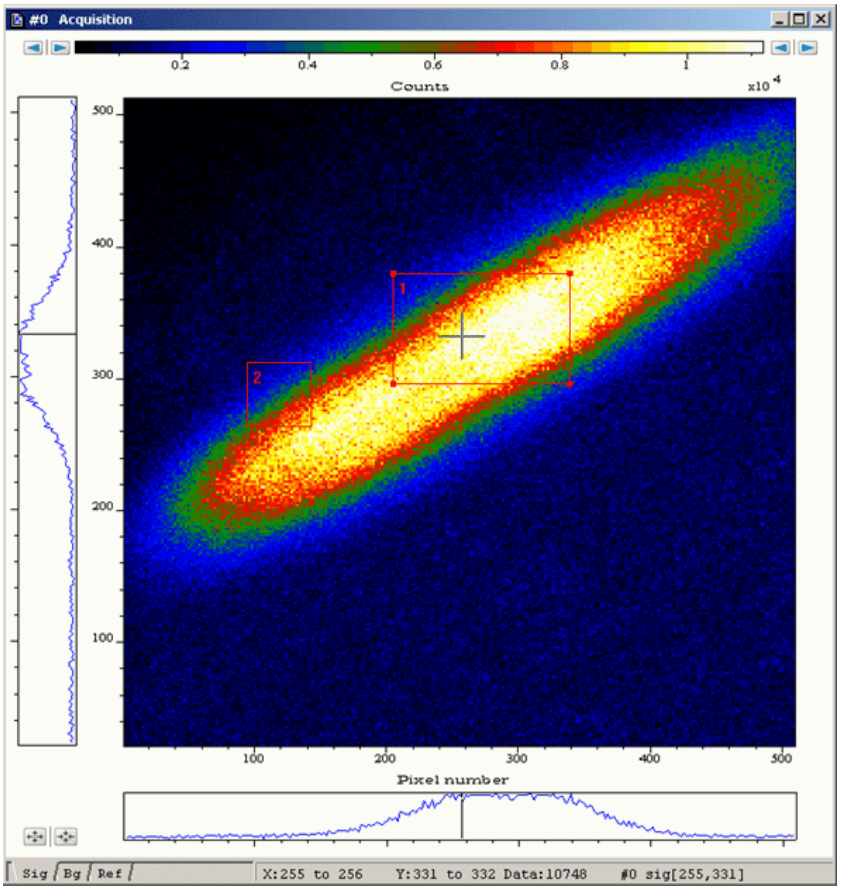


Figure 4.8: Ion cloud from Mark 2 trap. The side length of the image is 820 μm.

Dark ions, and the methods used to identify them are discussed in chapter 6. It is believed that the reason for the increased presence in the Mark 2 trap is because of the design of the oven.

The oven was embedded in the horizontal compensation electrode to align the atom source in a compact arrangement. As space was extremely limited, the front of the oven was spot-welded on the horizontal compensation electrode. This resulted in the electrode acting as a large heatsink, and to get enough flux out of the oven to load the trap by photoionisation (section 2.2) required applying 8 Amps at 8 Volts (64 W) for two minutes.

As the heat is not localised, there was increased outgassing from the large horizontal compensation electrode and the pressure during loading would rise to 1×10^{-9} mbar.

It is standard practice to fire the oven at a high temperature during vacuum processing to remove volatile gasses that are sorbed on the surface. As this was not feasible, volatile gasses continue to be released when the oven is fired. An improved design for the oven is implemented in the Mark 3 trap and provides a thermally isolated return path for the current; the designs are shown side-by-side in figure 4.9.

The Mark 3 trap varies from the Mark 2 in three other ways: it is made from 316 stainless steel; the plate electrodes are thinner; and the diameter of the rod electrodes has been increased. The wider rods allow the optimal ratio of rod electrode radius to ion-electrode distance, $r_e/r_0 = 1.14$ [43, 44], to be achieved. Early results from the Mark 3 trap are promising, showing an improvement in ion storage and an improvement in background scatter rate by a factor of 10 (see figure 7.9 in chapter 7). The Mark 3 oven also only requires a power of 3–4 W to load ions, which is a significant improvement.

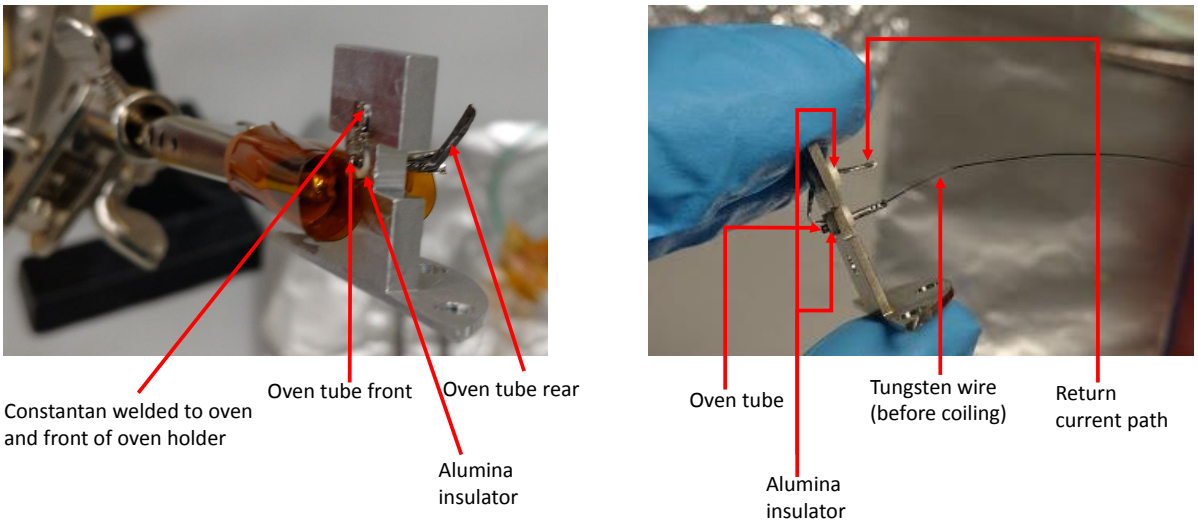


Figure 4.9: The original design of the oven, (left) has the front of the oven welded to the front of the horizontal compensation electrode via some constantan foil. This resulted in a large heat sinking effect, requiring large currents and causing poor vacuum. An improved design (right) thermally isolates the oven from the electrode. The front of the oven is connected to tantalum foil that passes through a ceramic insert in the electrode; the rear of the oven is crimped on to some tungsten wire to provide thermal isolation from the copper wires and additional resistive heating at the back of the oven.

4.2 Vacuum chamber and pumps

To trap a large number of ions without their atomic state or temperature being disturbed by gas-collisions, an ultra-high-vacuum (UHV) of lower than 10^{-10} mbar was required. The vacuum system should also provide sufficient optical and electrical access, and robust mounting points for the laser launchers, PMT and magnetic shields.

The material chosen for the vacuum chamber was titanium, as it is non-magnetic and has a low outgassing rate. The windows were a low-profile design indium-sealed to titanium flanges. Standard components and techniques were used in order to have a sufficiently low leak rate and outgassing rate. The vacuum system was sealed and raised to 130°C (limited by indium seals on the viewports) for a week, while connected to an external turbo-molecular pump to remove the outgassing material sorbed to the chamber walls. After the 'bake-out' procedure was completed, the internal getter pump[2] was activated and the external turbo-molecular pump was 'valved-off' and removed. Getter pumps do not pump noble gases so, for long-term operation, an ion pump[3] was included. Ion pumps have the unattractive quality of requiring strong permanent magnets to operate, but they provide a useful indication of the pressure in the system through the current that they draw. The monitoring, increased pumping, and redundancy significantly reduces the risk of a time-consuming vacuum problem. Engineering drawings of the vacuum chamber parts can be found in appendix A. Figure 4.10 is a photograph of the vacuum chamber, ion trap, pumps and light delivery.

In addition to having internal tapped holes for mounting the ion trap, the vacuum chamber also had external tapped holes for attaching the magnetic shield and for mounting fibre launchers and coils. This made the system much more suitable for a compact clock than the vacuum system used for the Mark 1 trap.

[2]SAES CAPACITORR CF16 getter pump - 2 l/s H_2 pumping speed.
[3]Gamma Vacuum TiTan 3s - 2 l/s.

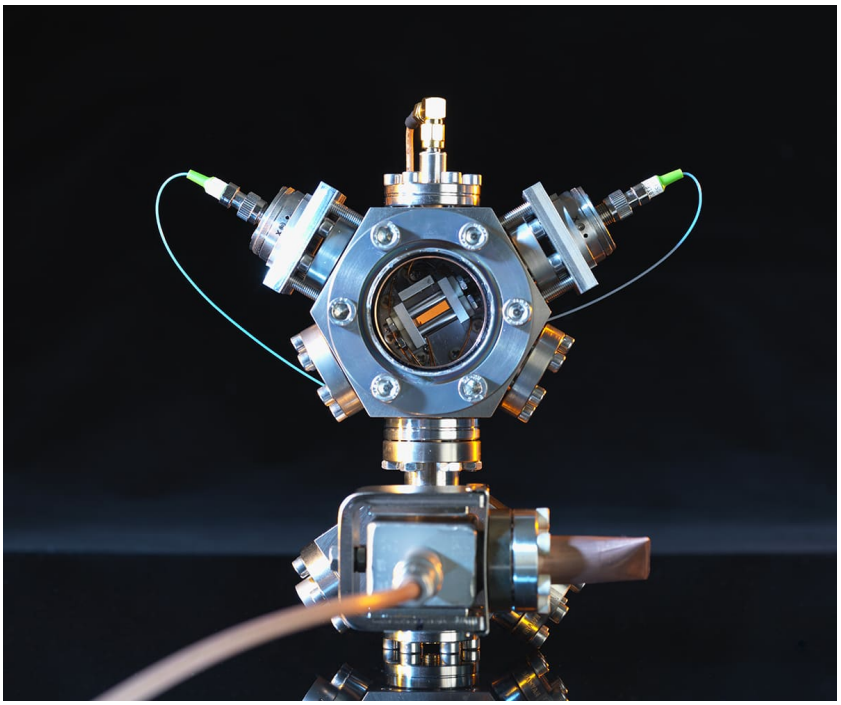


Figure 4.10: The vacuum chamber of the 'physics package'. The Mark 2 ion trap, viewports, ion pump, electrical feedthroughs, and an early version of the fibre launchers are visible. For scale, the glass viewport has a diameter of 35.6 mm.

4.3 Laser delivery

The lasers are sent from the laser bank by SMPM fibres into fibre launchers (ThorLabs PAF-X-2) with aspheric lenses. The fibre launchers send the UV beam down the trap axis, and the IR beam at 60° to the axis, and the beams illuminate the ions as seen in figure 4.11. Both beams are focused to a point after the ions. It is advantageous for both beams to travel down the trap axis as it ensures the best overlap with the ions. However, as the two beams contain very different wavelengths, to send them through the same fibre would require an expensive photonic crystal fibre. The other method to send the light through two opposing windows was unattractive because it would add additional length to the physics package and require larger magnetic shields. It was originally planned to attach the fibre launchers directly to the exterior of the vacuum chamber, but it was found to be more space efficient — due to the PMT and ion pump protruding vertically — to also mount the fibre launchers vertically. This arrangement is shown in figure 4.12.

The tip-tilt mirror mount allows for additional control of the beam.

The laser-cooling and detection transitions are strongly dependent on the polarisation of the 369 nm laser. Population trapping occurs if the laser is polarised in the plane of or perpendicular to the applied magnetic field. Therefore, a polarisation angle of 45° to the magnetic field is used. Due to the population trapping (section 2.2), the stability of the polarisation affects the efficiency of the cooling transition. The 369 nm laser is delivered by a UV PM fibre; this fibre is strongly birefringent, and susceptible to stress and thermally induced perturbations to this birefringence. By aligning linearly polarised light along the slow axis of the fibre, the polarisation should be maintained throughout the fibre and made minimally sensitive to thermal and stress perturbations. However, absolute polarisation stability is not possible, due to both deficiencies in the PM fibre, and the difficulty in perfectly aligning the polarisation axes. Due to these problems initial spectroscopy measurements were very noisy.

The polarisation stability was optimised by measuring the susceptibility of the fibre to polarisation noise, resulting from thermal and mechanical stresses, as a function of the input polarisation to the fibre. The polarisation is measured by placing two polarisers between the fibre launcher and the calibrated photo-diode. The first polariser is aligned with the slow axis of the PM fibre. Maximum sensitivity is when the second polariser is at 45° to the first.

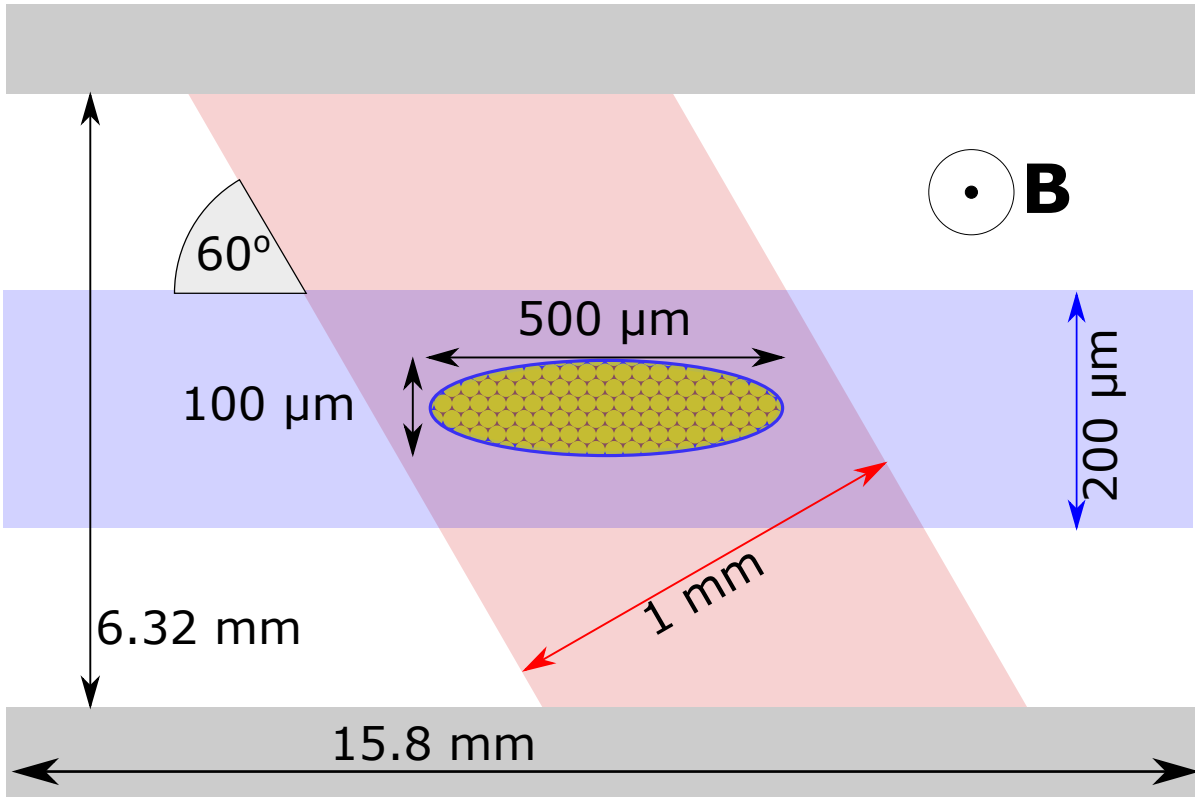


Figure 4.11: Schematic of the overlap of the laser beams and ion cloud (not to scale). The axial UV beam and the IR beam cross at 60° at the centre of the ion trap, where the ions are positioned. At this point the UV beam has a waist of 200 μm — double the minor axis width of the ion cloud — and the IR beam waist is 1 mm. This is more than sufficient to illuminate the projection of the ion cloud's major axis. Also shown are the length and separation of the ion trap rod electrodes, and the orientation of the cooling magnetic field.

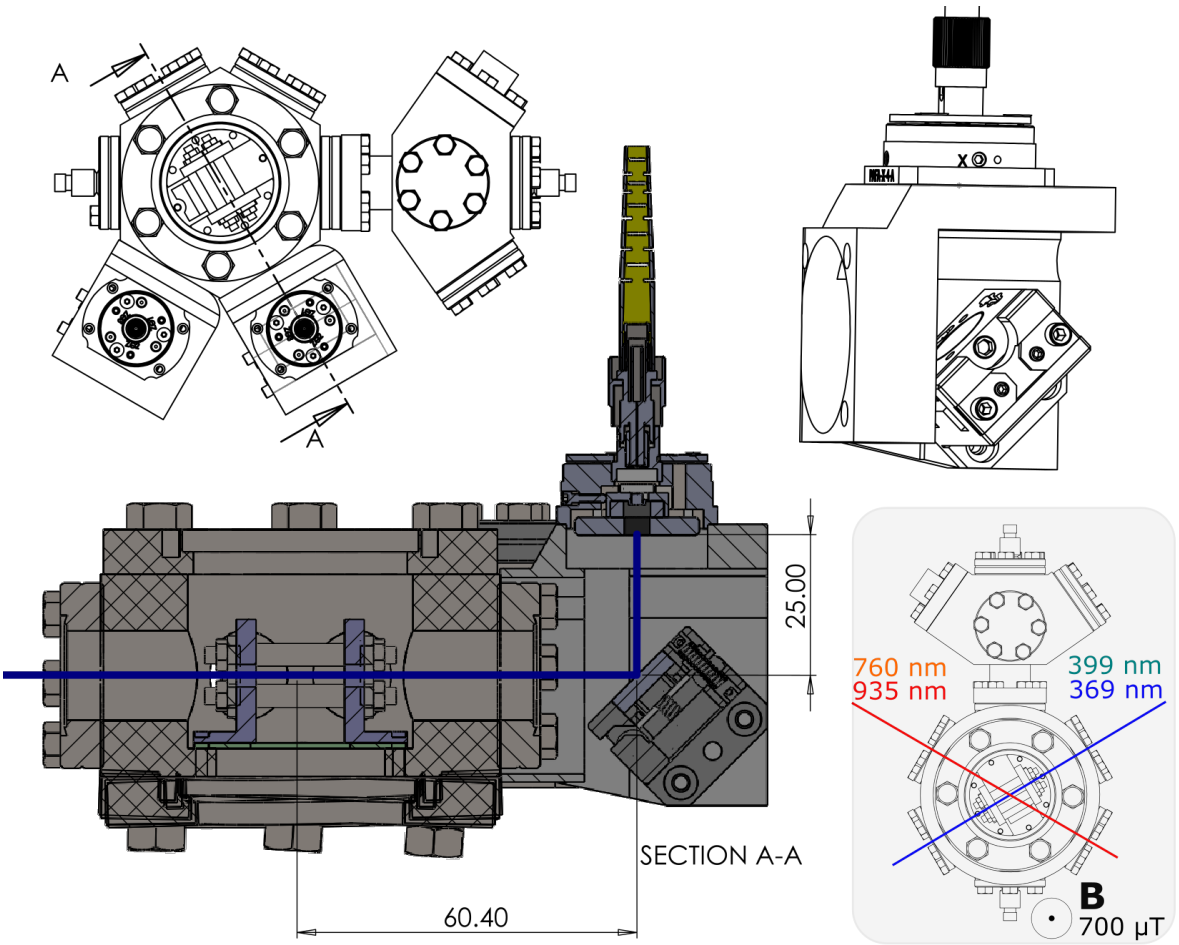


Figure 4.12: Laser delivery to ion trap. Showing the design of the fibre launcher optomechanics; how the mounts attach to the chamber; and the laser paths through the ion trap.

4.4 Magnetic shielding

As already stated, the most significant cause of systematic uncertainty in the operation of a well-designed, laser-cooled microwave clock is likely to be the second-order Zeeman shift (section 2.4.3.2). To minimise this shift, it is important to operate in a small magnetic field, and for fluctuations in the magnetic field to be minimised at the ions.

The residual magnetic field can be minimised at the ions through compensation coils. Reducing the magnitude of magnetic field fluctuations requires passive shielding. There are two magnetic shields in this system. The first is used to reduce the leakage field from the ion pump magnets. This was made of soft iron to prevent the shield from saturating in the large magnetic field local to the permanent magnet. A second, two-layer shield made of mu-metal surrounds the entire physics package. Mu-metal has an extremely high magnetic susceptibility, and this results in a high shielding factor for DC fields. The vacuum chamber is mounted on supports that are glued to the inside of the magnetic shield, which in turn has mounting supports for fixing the shield assembly to the case. Designs for the magnetic shields can be found in appendix A. The performance of the magnetic shields is investigated and discussed in section 7.6.2 when evaluating the second-order Zeeman shift.

4.5 Magnetic field coils

The coil arrangement that is used to apply a controlled magnetic field to the ions is shown in figure 4.13. The coils comprise of three orthogonal pairs — x, y and z — that are arranged compactly around the vacuum chamber. The properties of these coil pairs are summarised in table 4.3.

The $x-$ pair are wound around formers that sit over the 70 mm outer diameter windows. The cooling coil is coaxial with the $x-$ pair and wound on top of the $x-$ coil on the upper window. This provides a magnetic field of 700 μT that destabilises the dark states during cooling (section 2.2). The $y-$ pair of coils are rectangular and wound around supports that are screwed into the vacuum chamber around the smaller windows.

Coil	**diameter / mm**	**turns**	**pair-separation / mm**	**colour in figure 4.13**
x	90	33	70	red
y	rectangular — 41×82	40	64	orange
z	36	40	84	blue
cooling	95	400	—	green

Table 4.3: Coil properties

The $z-$ pair of coils are wound around the small DN16 flanges perpendicular to the other coils.

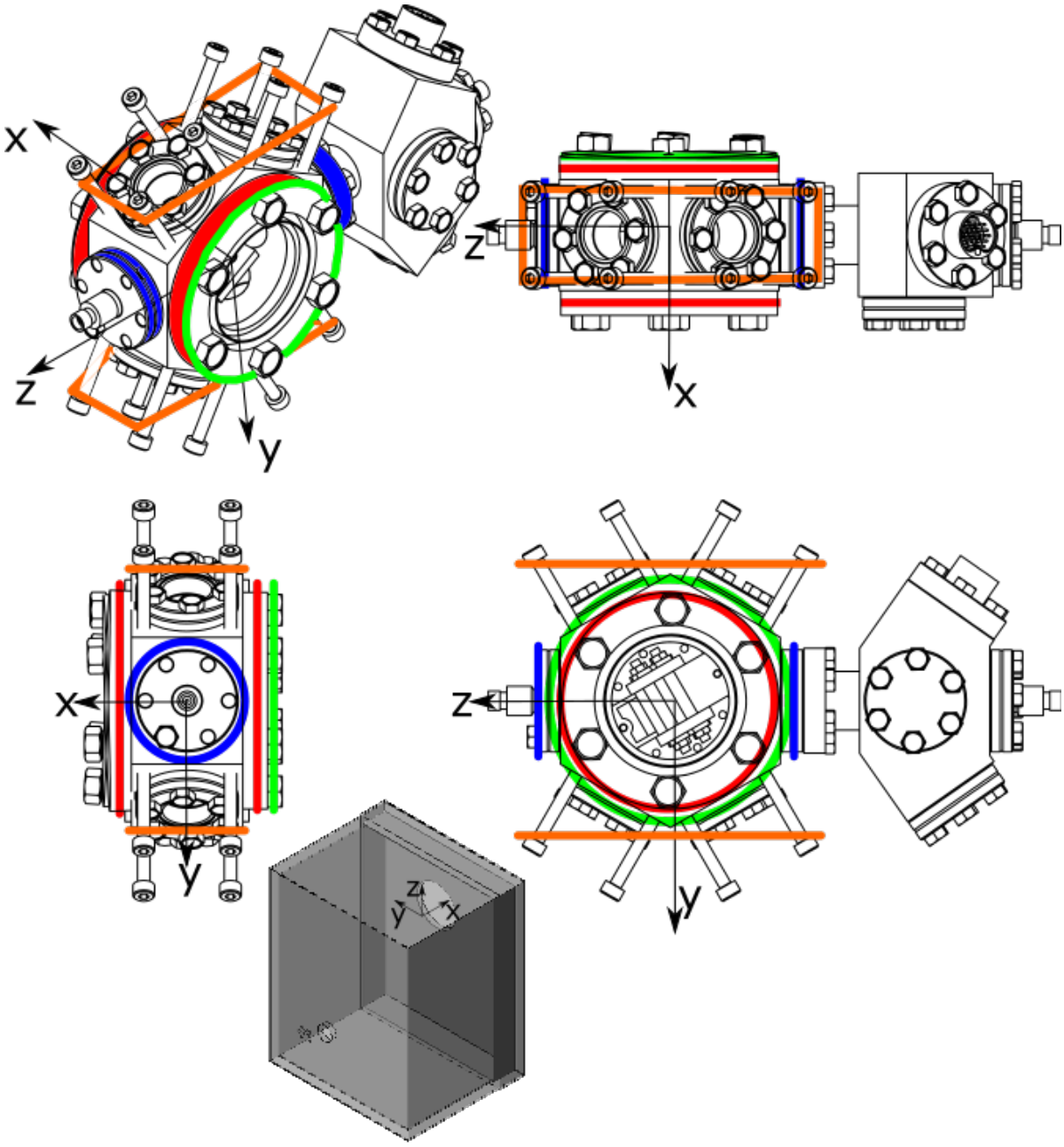


Figure 4.13: Schematic of the coil arrangement. The coils are detailed in table 4.3. Also shown is the magnetic shield and the coordinate system that is used to label the coils. The position and orientation of the vacuum chamber within the magnetic shield is represented by the position of the axes within the shield (the $x-$axis is coaxial with the larger hole in the shield).

4.6 Imaging system

A compact PMT H12386-210 from Hamamatsu (Quantum efficiency $\sim 40\%$ at 369 nm) is used to count photons from the ions in the trap. To provide spatial filtering, the centre of the rod trap is imaged onto a 150 micron slit using a pair of (Edmund Optics #49-696) 25 mm diameter UV coated, fused silica, aspheric lenses (NA 0.42). These are mounted in a tube connected to a custom adapter. The magnification factor is approximately one. The slit and PMT are mounted on an adjustable cage system for alignment. This consists of a rotation mount and a slip plate positioner so that the slit can be adjusted and overlapped with the image of the ions. In order to monitor the ion fluorescence during the setup phase of the project, a live image was observed through the opposite large vacuum system window using an Andor iXon Ultra 897 camera. Figure 4.14 shows a schematic of the imaging system. As the camera and PMT look at the ion trap from opposite sides, it is possible to image the PMT slit on the camera and align it with the ions. The calculated collection efficiency of the imaging system, including optical losses, is 2.7%.

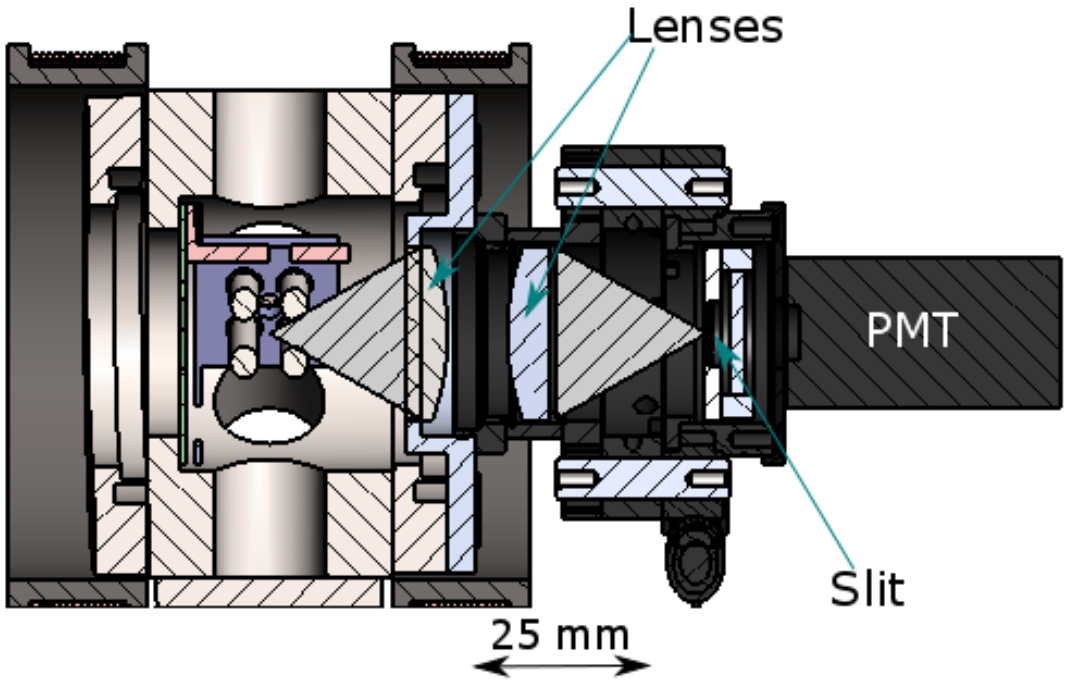


Figure 4.14: Schematic showing a cross-section of physics package. Components of the imaging system are labelled.

Chapter 5

Electronics and Control

In this chapter, I describe the electronic components that comprise the clock and the control sequences that are used to lock the local oscillator to the atomic resonance. I would like to acknowledge the contributions of Sean Donnellan and Greg Walsh in the work described in this chapter: Sean Donnellan led on designing the digital electronics and frequency chain; and Greg Walsh designed the power supply, oven current supply and ion trap oscillator.

5.1 Component overview

The components of the clock and their functions are described in this section. These are the local oscillator, frequency chain, microwave antenna, RF trap drive, oven current control, stable voltage and current controllers, microcontrollers and FPGA.

5.1.1 Local oscillator and Frequency chain

The Local Oscillator (LO) is a continuous active oscillator that is counted to provide the clock output. The LO acts as a flywheel between clock measurements. It is periodically compared with the atomic reference and, if it has drifted, these drifts are corrected. The important requirements for a local oscillator are the stability during timescales shorter than the planned clock interrogation time, and, for a portable system, that it is insensitive

to environmental influences. As this work is a development project, we decided to use a high-quality LO to ensure it would not be a limitation. For a commercial product, there is obviously an incentive to use cheaper, lower quality LOs. A lower quality LO can limit the maximum interrogation time by drifting significantly within the loop time.

The LO chosen was an oven-controlled crystal oscillator (Rakon HSO 13). This was chosen for its high performance in a compact package. The measured stability is shown in figure 5.2 and discussed in the following subsection. Both are measured after the frequency chain.

The LO has to provide both the clock output at 10 MHz and the ground-state hyperfine splitting frequency of $^{171}Yb^{+}$ at 12.6 GHz. To do this, we use the LO to clock a frequency chain and a Direct Digital Synthesiser (DDS). By using this method, we avoid having to alter the frequency of the LO directly and can leave it free running. Frequency tuning in crystal oscillators is typically done by applying a tuning voltage across an element that produces a strain on the crystal. For the HSO 13 the voltage-tuning coefficient is (2 ppb/V to 20 ppb max). Our approach has two significant advantages to the LO-tuning method. The first is that to voltage-tune the LO, an extremely low-noise tuneable voltage source must be made, as any voltage noise will be transcribed into frequency noise. A secondary advantage of our system is that the LO used does not need to contain the strain-tuning element. The strain-tuning element causes damping to the vibrating crystal and thus lowers the Q factor and stability. Without the strain-tuning element, oscillators can be made cheaper and more stable.

The frequency chain firstly converts the 10 MHz LO to the 12.6 GHz clock frequency and secondly, through feedback from the ions, stabilises the output frequencies. The schematic for the frequency chain is shown in figure 5.1. The frequency chain begins by multiplying a 10 MHz input up to 12.8 GHz. The multiplication consists of two phase-locked loops and was made for us by Plextek Consulting as part of the Dstl quantum navigator project. This 12.8 GHz signal is split into two paths, the first path is divided by 16 to clock two DDSs (Analog Devices AD9912) and the second path is sent into a mixer. The second input of the mixer is a signal of around 158 MHz that is used to

generate the clock frequency as the low-frequency sideband of the mixer output. The 12.8 GHz and the high-frequency sideband are then removed by a band-pass filter, and the clock frequency is then applied to the ions via an antenna. The power of the applied microwaves can be controlled in the switching network (section 5.1.1.2). An error signal is derived though modulating the probe frequency to measure the high- and low- frequency sides of the resonance (described further in section 5.2.3) and the frequency offset between the free-running frequency chain and the ions is determined. This frequency offset is used for both locking 12.6 GHz to the ions and for providing the stabilised RF outputs.

The stabilised RF outputs are generated by updating the second DDS. As this second DDS outputs at 300 MHz, the frequency corrections that are calculated by the feedback loop at 12.6 GHz are divided by 42.14 (12.642 GHz / 300 MHz) to ensure the appropriate fractional change. This removes the drift from the free-running frequency chain and transfers the stability from the ions' frequency discriminant to the clock output. The AD9912 DDSs have a resolution of 4 μHz, this means that the RF outputs can be tuned with a fractional-frequency resolution of 1.4×10^{-14}. The fractional frequency resolution of the probe frequency at 12.6 GHz is 4×10^{-16}.

5.1.1.1 Stability measurement of the local oscillator

The fractional frequency stability of the clock when it was unlocked from the ion resonance is shown in figure 5.2. In this measurement, the LO clocked the frequency chain, and the nominal 10 MHz from the frequency chain was measured against the maser on a Microsemi 3021A phase comparator. The most stable averaging time for the LO was around 30 s, where the Allan deviation reached a few parts in 10^{13}. At longer timescales, the frequency began to drift, and the stability was decreased to close to 1 part in 10^{12} at 10000 s.

It was a concern that the frequency chain may have added noise to the output frequency. To measure the noise contributed from the frequency chain, the maser-clocked-frequency-chain stability was measured relative to the maser. This measurement is shown

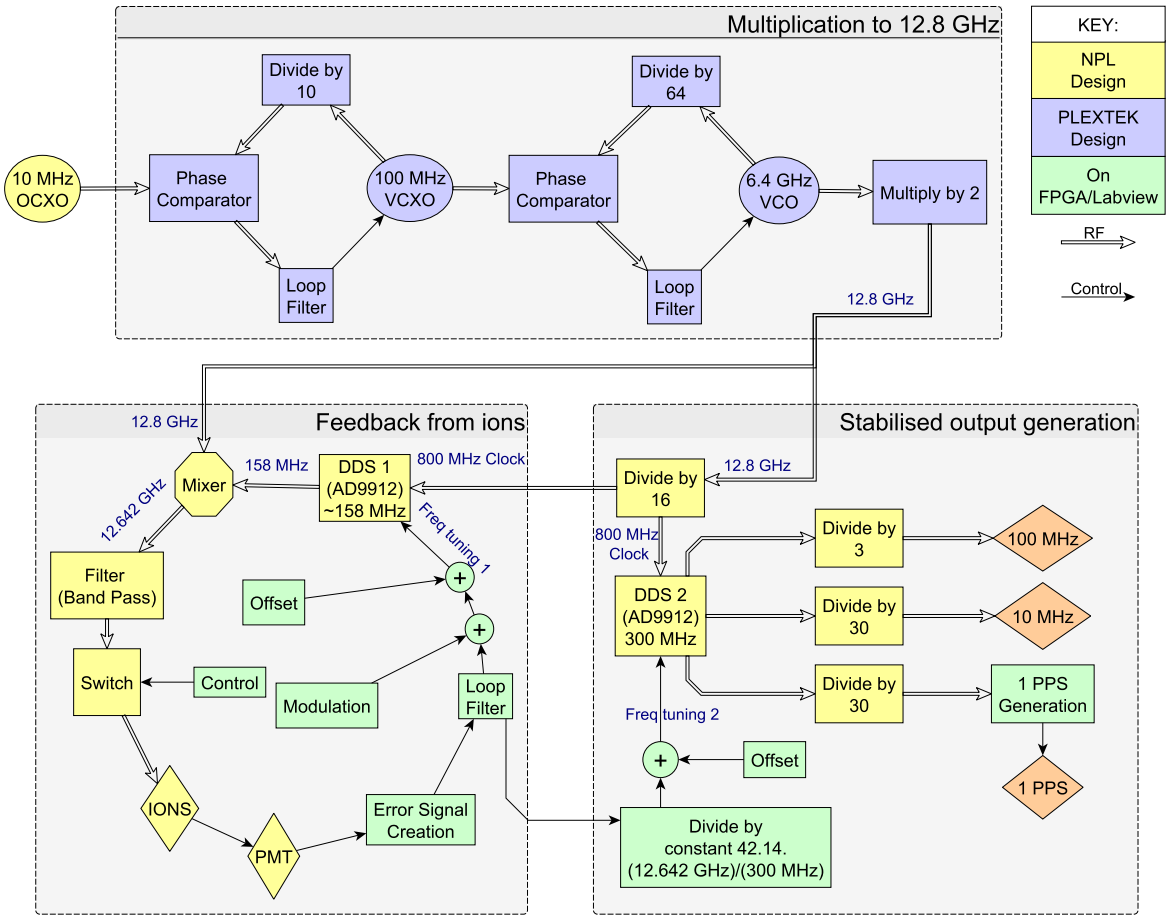


Figure 5.1: Oscillator and locking scheme designed by Sean Donnellan.

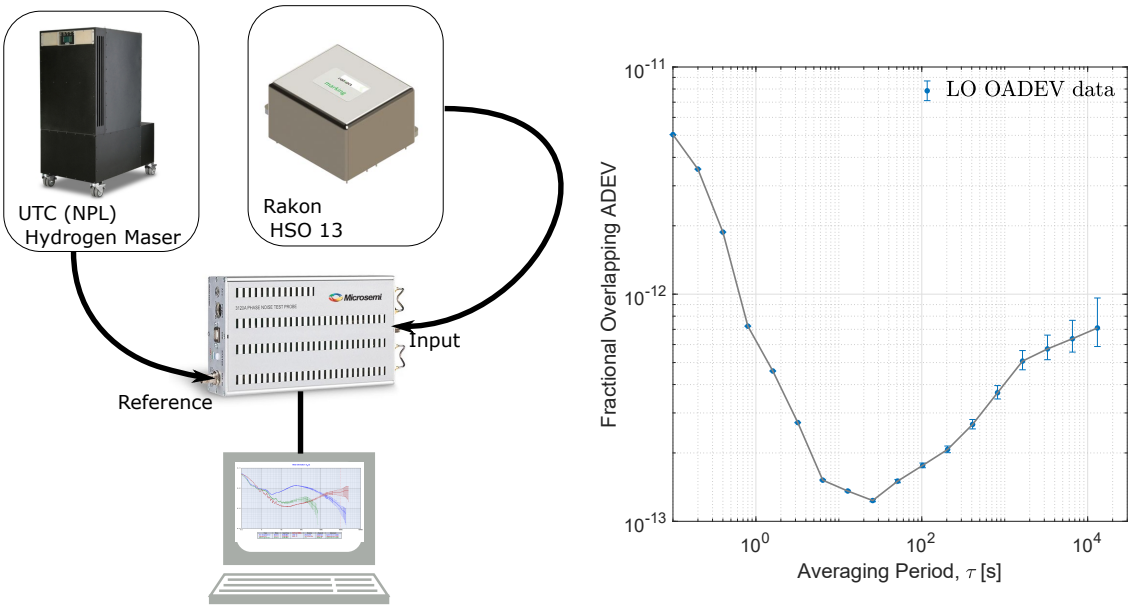


Figure 5.2: Stability of unlocked LO 10 MHz measured against hydrogen maser 10 MHz. The LO reaches peak stability in the low parts in 10^{13} at 30 s. At longer timescales, the frequency drifts and the stability is reduced.

in figure 5.3, which also shows the noise floor of the stability measurement equipment. It can be seen from the figure that between 0.1 and 10,000 s, a line of best fit of $4\times10^{-13}\tau^{-0.8}$ is a good estimate of the instability added by the frequency chain. This noise is not a significant contribution to the overall instability of the system.

5.1.1.2 Microwave switches

Microwaves are required for mixing the ground state hyperfine levels during cooling (section 2.2) and for applying the clock pulses (section 2.3). The power and noise levels required for these two uses are very different: laser-cooling requires high power and is tolerant to noise, while spectroscopy requires low power and low noise microwaves. For effective laser-cooling, the Rabi frequency for the microwaves should be greater than the decay rate into the F=0 ground state. In our system, this rate was found to be quite high (>100 kHz), and so an amplifier was driven at the point of saturation, providing +30 dBm at the input of the antenna (section 5.1.2) and effectively mixing the two ground states.

For spectroscopy, particularly Rabi spectroscopy, a low Rabi frequency (for this work

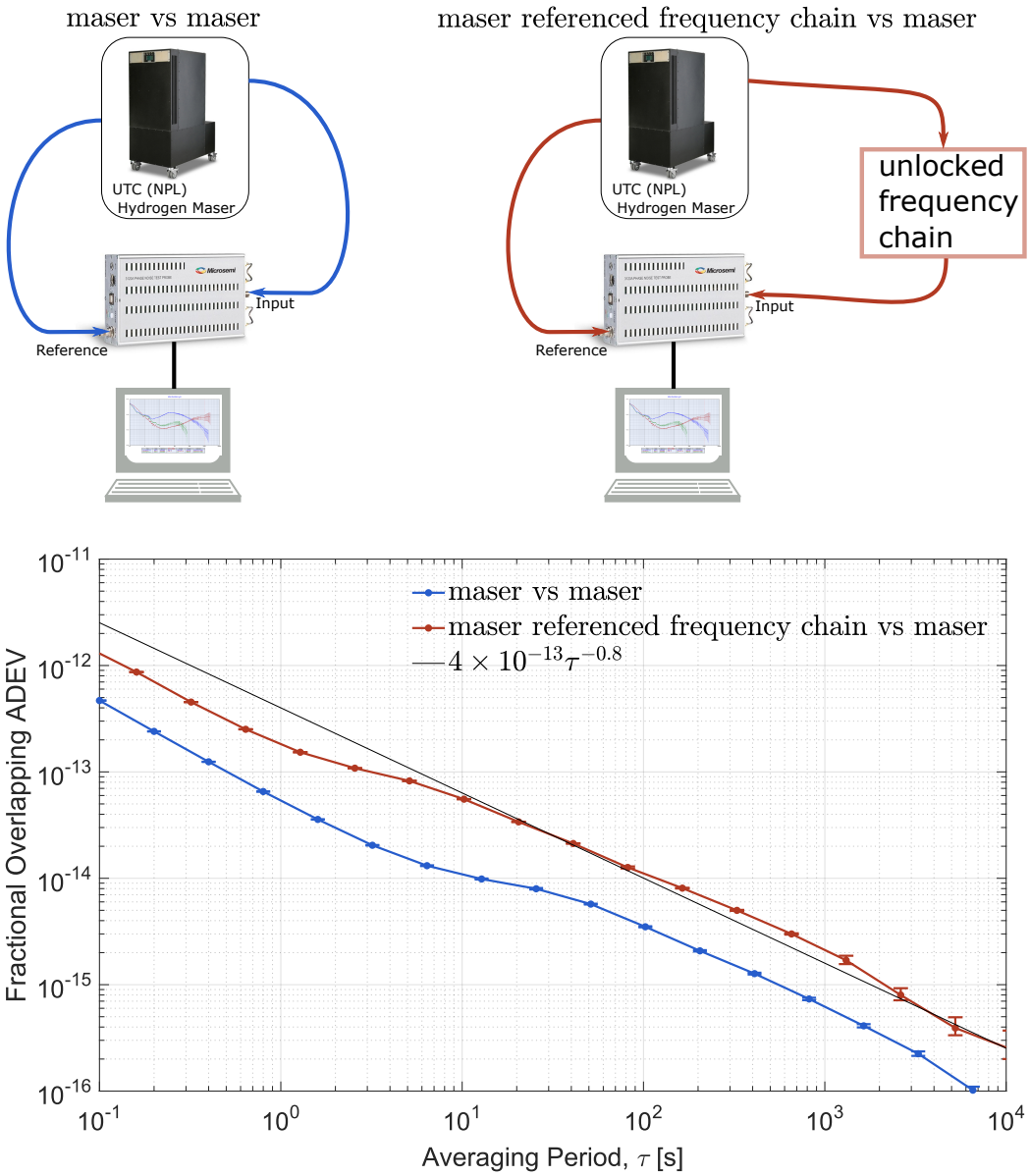


Figure 5.3: Stability measurement of the frequency chain and phase comparator. The stability of the phase comparator is obtained by measuring the maser in both input and reference ports. The stability of the frequency chain was measured in a similar fashion. A maser signal was split in a power divider, and one channel of the maser was used to reference the phase comparator. The second was used to reference the frequency chain. The output of the frequency chain was connected to the input port of the phase comparator.

typically ($2\pi\times$) 1 Hz to 0.1 Hz) enables narrow Fourier-limited features to be observed. Ramsey spectroscopy does not in principle require a low Rabi frequency, but this helps identify the central fringe of the interference pattern. However, during the free evolution period, microwave leakage must be minimised, as this will cause the ions to accumulate polar angle on the Bloch sphere. These demands require three switching states: 'Cooling', 'Clock', and 'Off', spanning 130 dB of dynamic range between Cooling and Clock and as much isolation as possible for the 'Off' state.

To achieve this, two networks of single-pole-double-throw (SPDT) switches (General Microwave M870) were designed. The first and simpler design is shown in figure 5.4. Between the SPDT switches are two paths with different attenuation levels. This switching network was sufficient for Rabi spectroscopy. However, it could not provide sufficient attenuation in the 'Off' state for Ramsey spectroscopy, as is seen in figure 5.5.

To improve the dynamic range, a second network of SPDT switches was designed, this is shown in figure 5.6 and described in the caption. The performance of the two networks is tabulated in table 5.1. A driving circuit was designed to convert a TTL input to the required switching current of ±30 mA for the M870 switches. A schematic is shown in figure B.10 in appendix B.

5.1.2 Microwave antenna

For the microwave antenna, a simple solution was used that involved exposing a quarter wavelength (5.93 mm) of the centre conductor from a piece of semi-rigid coaxial cable. This can be seen in figure 5.7. In the far-field of the radiation pattern from a quarter-wave antenna, the magnetic field is perpendicular to the exposed conductor. To drive primarily the 'field-insensitive' transition, but still allow the 'field-sensitive' transitions to be monitored (angular dependence in section 2.2.1), the antenna is positioned so that the radiated magnetic field is offset by a small angle (<10° from both axes) from the bias magnetic field. Due to the ions being strongly localised in space, it is not necessary to make a microwave cavity, unlike many neutral atom clocks [35]. A return loss of -7.3 dB was measured in the Mark 2 trap using a network analyser, and, while this coupling to

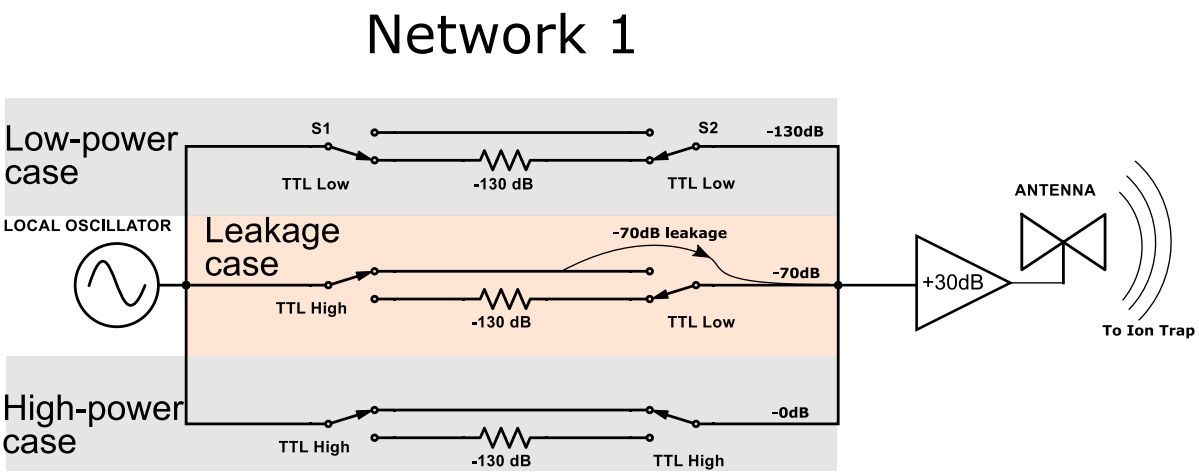


Figure 5.4: Showing the three possible configurations of the two-SPDT switching system. The high power state is shown on the bottom path. The microwaves pass through the two switches with no attenuation and through the amplifier. The top path is the low power state. Here the microwaves must travel through 130 dB of attenuation before passing through the amplifier. The maximum attenuation is limited by the 70 dB of leakage through the switches, as shown on the middle path. This switching arrangement allows the power levels for cooling (high), and Rabi spectroscopy (low), but does not provide an effective 'off' state for Ramsey spectroscopy. There are potential microwave-power stability issues as the leakage-imposed low power limit is reached and the amplifier is not helpful for achieving high isolation.

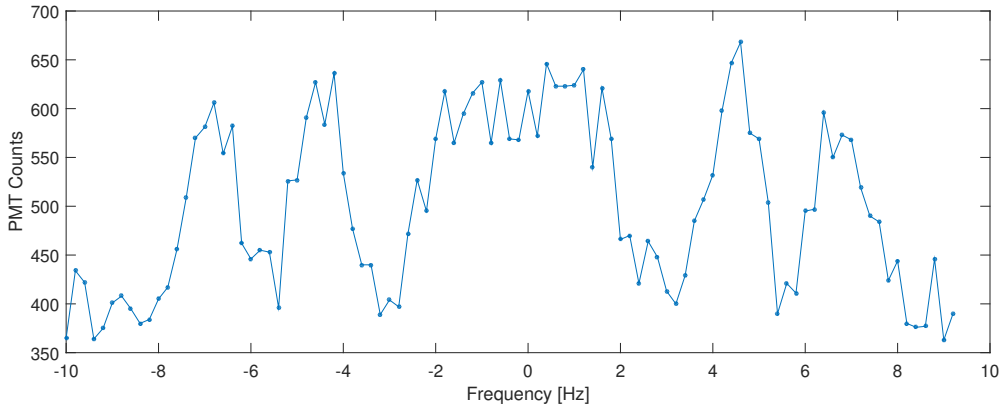


Figure 5.5: An unexpected lineshape from an attempted Ramsey experiment. The broad peak in the centre is due to the microwave power during the 'free evolution period' being higher than during the π-pulses. This alerted us to the microwave isolation issue.

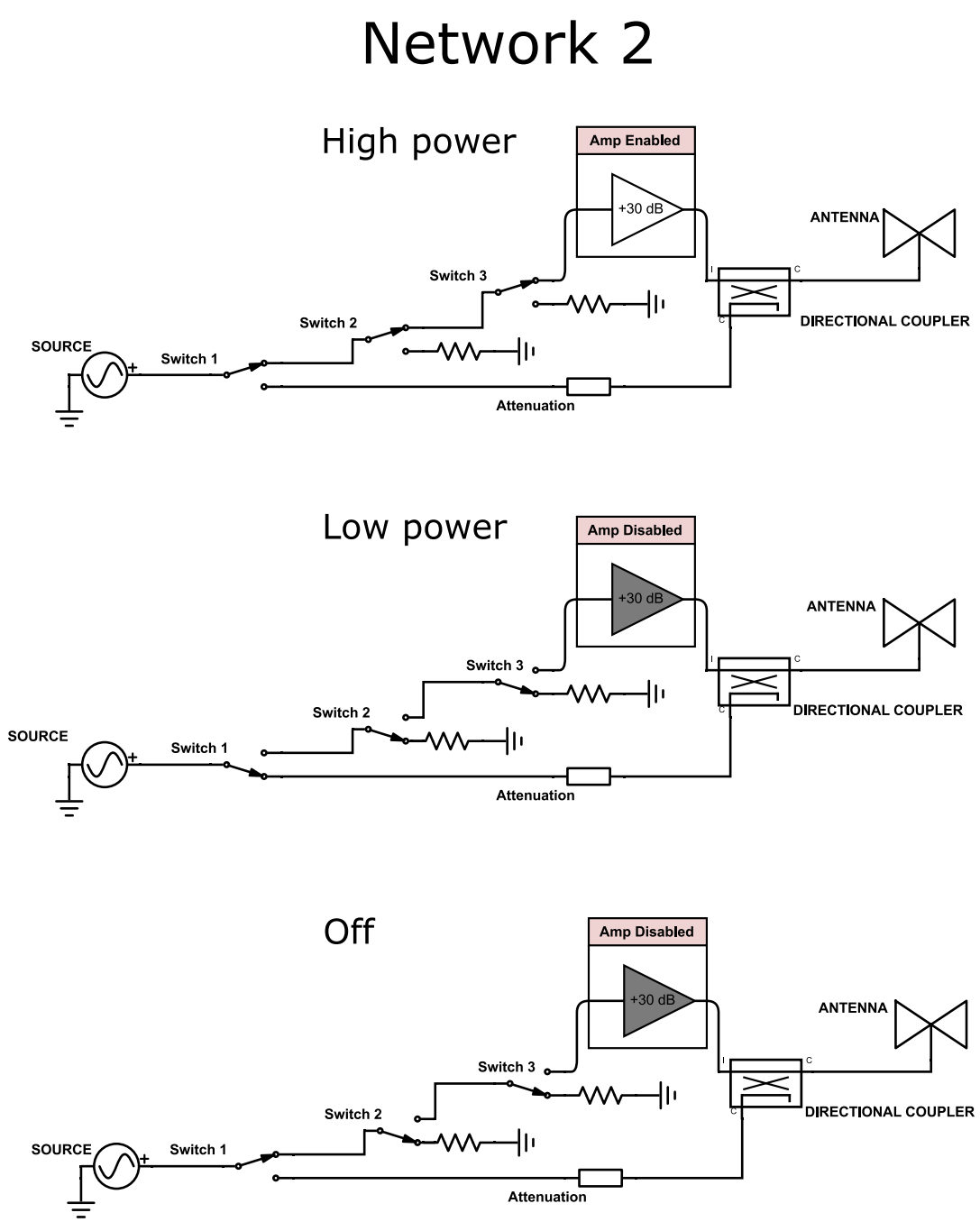


Figure 5.6: An alternative switching arrangement. Three SPDT switches are used because they were available, allowing for higher isolation. This scheme could also be simplified to two or one switches by omitting switch 2 and/or 3. In the high power state, the microwaves pass through an unattenuated path through an amplifier and enter the antenna through a directional coupler. In the low power state, the microwaves pass through the attenuation and through the coupled port of the directional coupler. Any leakage through the upper path on switch 1 is terminated, and the amplifier is switched off to avoid adding noise. In the 'off' state, the microwaves pass through the upper path on switch 1 and are terminated in subsequent switches. Again the amplifier is disabled to provide further isolation and to reduce noise. Leakage through the first switch must pass through the attenuation.

Network 1		
TTL1	TTL2	Isolation/dB
0	0	-130 max
0	1	-70
1	0	-70
1	1	-3

Network 2		
TTL1	TTL2	Isolation/dB
0	0	-14 + attenuation
0	1	-14 + attenuation + amplified noise
1	0	<-140 (noise floor)
1	1	+26

Table 5.1: Measured switch isolation using the two switching networks detailed. Two Transitor-Transitor Logic (TTL) inputs determine the state of the switches. The unstable cases, where the majority of the power is due to leakage, are shaded grey. Network 2 has at least 46 dB more dynamic range. In network 2, TTL1 controls switch 1 and TTL2 controls switches 2 and 3 and the amplifier enable control (see figure 5.6).

the radiated field is far from optimal, this was sufficient for us to couple the required microwave power to the ions.

5.1.3 Trap drive

The ion trap oscillator design is a variant of a design from Sandia [97]. The requirement is to generate a sine wave at approximately 2 MHz, with a peak-to-peak amplitude of up to 200 volts, driving the capacitive load of the trap (around 30 pF). A photograph of the unit, with the box lid removed, is shown in figure 5.8 and a schematic of the circuit is shown in figure 5.9. The active elements of the oscillator are inverting logic gates, three of which (U1-3) are arranged in a feedback loop to provide the necessary gain and phase shift for oscillation. An additional inverter outside the loop (U4) compensates for the phase inversion of the output MOSFET (Q2). Eight further inverters (U5-12) are connected in parallel to provide a low-impedance gate drive. The oscillator output voltage is directly proportional to the DC input and reaches a maximum of 350 V_{pk-pk} at 2 MHz with an input voltage of 15 V.

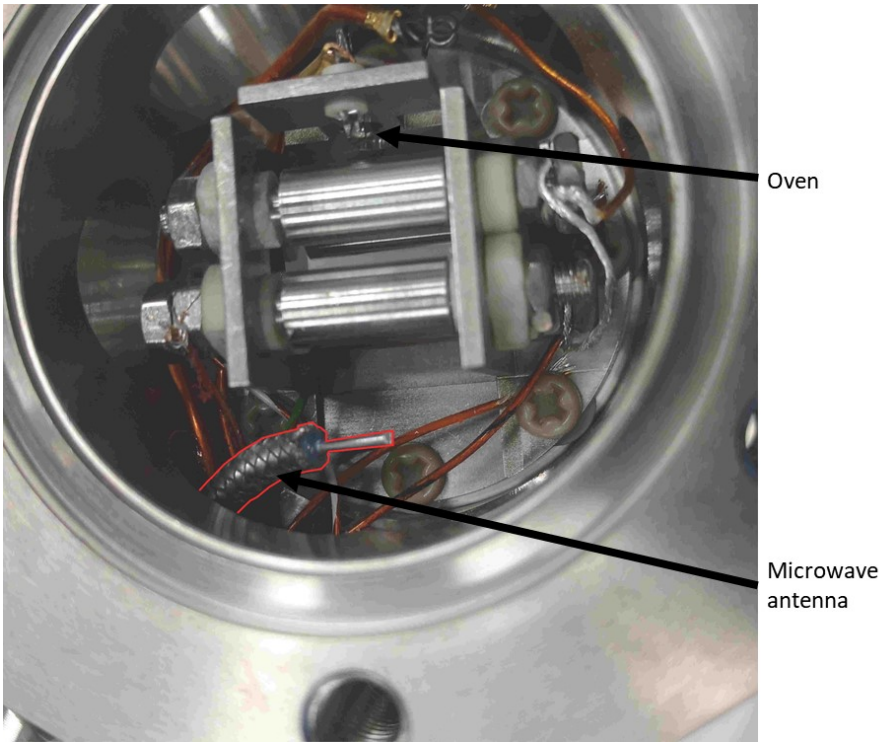


Figure 5.7: A stripped piece of coax, which forms a microwave antenna, can be seen outlined in red. For scale, the diameter of the bore is 40 mm.

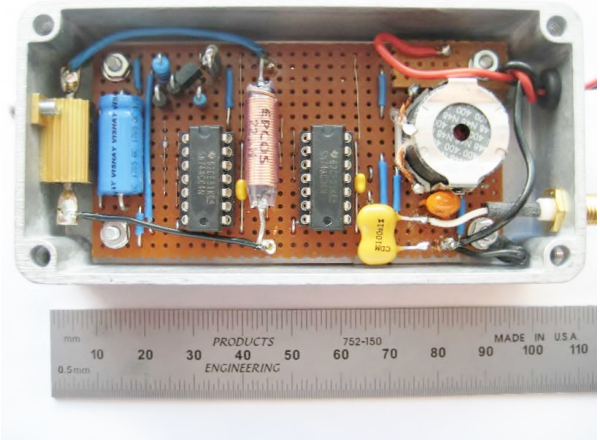


Figure 5.8: Ion trap oscillator. Designed and constructed by Greg Walsh.

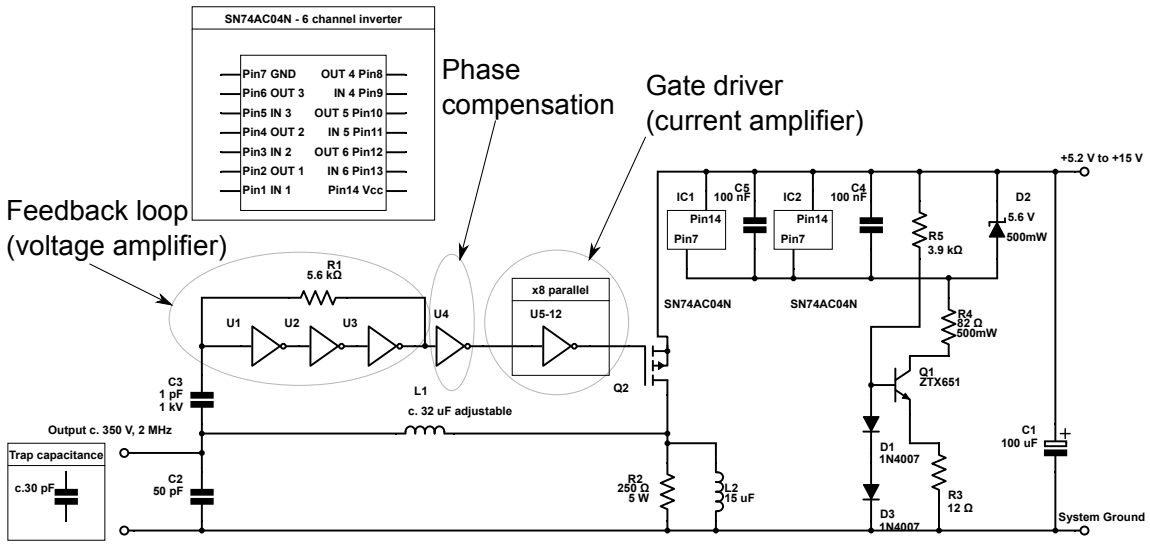


Figure 5.9: Schematic for the ion trap oscillator. The RF driving circuit is made of 12 CMOS inverters (two SN74AC04N ICs) with an LC loop.

5.1.4 Oven control

Due to the lengthy repair that would be required if the oven was left on and the supply of ytterbium was exhausted, a conservative approach was taken when designing the oven controller. A flow chart of the control logic is shown in figure 5.10. To switch on the oven, a hardware switch and a software control must both be in the enable state. When in the enabled state, the software may then attempt to load the ion trap by firing the oven subject to two hardware-enforced restraints. Both the number of automated reload attempts and the frequency of these attempts are limited. The implementation of this logic may be seen in figure B.9 in appendix B. As a final security measure, a buzzer sounds when the controller is supplying current to the oven.

In the Mark 2 system, the required current (8A at 8V) was much higher than expected due to excessive heat sinking of the oven (see section 4.1.2), and firing the oven caused a large perturbation to the system. Due to this flaw, it was not prudent to fire the oven automatically during a frequency measurement, as the large power dissipation in the system caused a frequency shift.

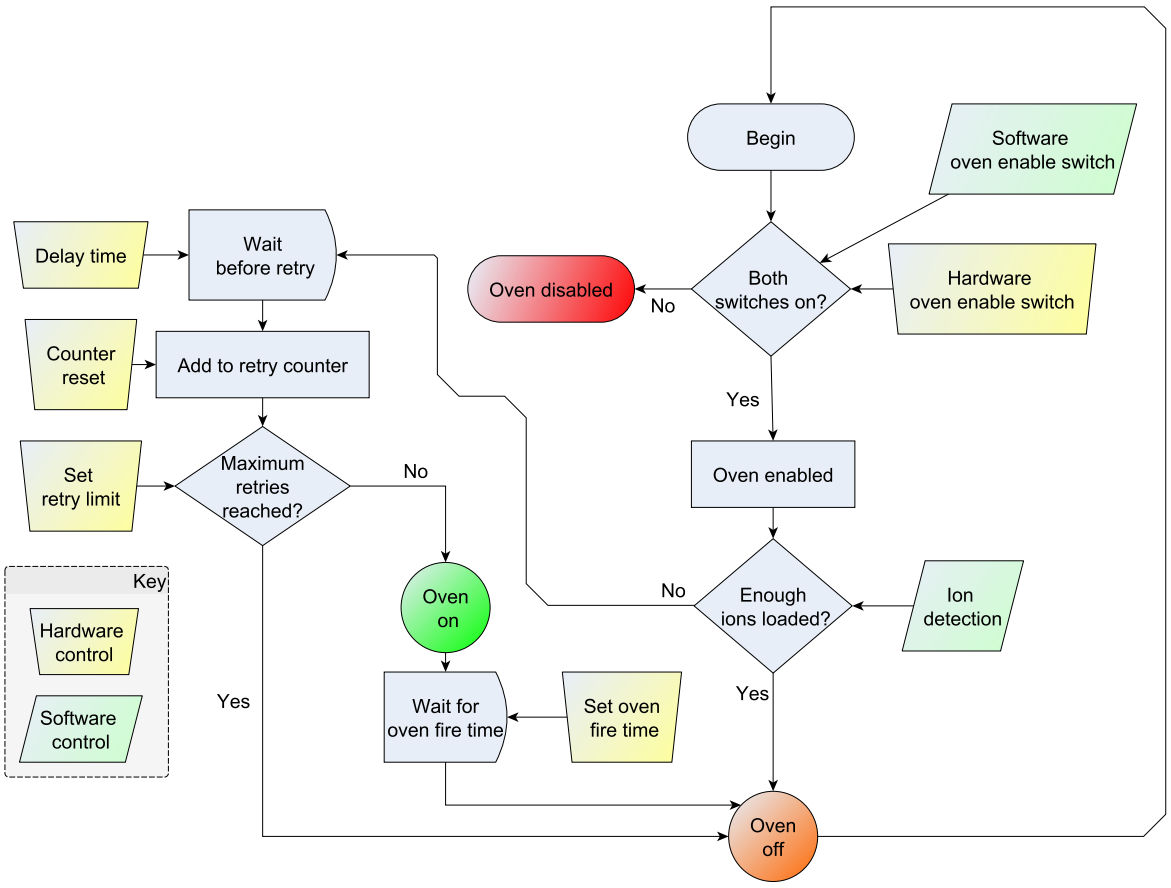


Figure 5.10: Oven control logic flow diagram.

5.1.5 Stable voltage sources

Configurable voltage sources are required to set voltages on the trap electrodes as well as other components such as the oven. A 4-channel, 16-bit DAC board from Linear Technology (DC2376A) was chosen for its low noise and high precision within a small footprint. A high voltage supply is required to tune the frequency of the 369 nm ECDL using a piezoelectric transducer to adjust the grating. The tuning sensitivity of the 369 nm laser to the piezoelectric transducer voltage is 460 MHz/V. One of the channels of the DC2376A is amplified to provide the supply for the piezoelectric transducer. A schematic of the PCB that contains the DC2376A and the amplifier is shown in figure B.11 in appendix B.

5.1.6 Current supply for lasers and magnetic field coils

The current sources used to drive three magnetic field coils (see section 7.6.2.2 for noise measurement) and the 369 nm laser current were previously developed, in-house designs used at NPL for laser current supplies. These were developed by Jochen Kronjaeger and are based on the circuit in [98]. The schematics are shown in figures B.2-B.7 in appendix B. The current source is optimised for low noise density and low drift, as shown by the measurements in figure B.8 and figure 7.15 respectively. A slave microcontroller board is used to communicate with the 16-bit DAC on each of the current sources. The board has an analogue monitor output of the set current, and this is detected by one of the ADC channels on the microcontroller board. For the magnetic field coils, one channel was set to operate up to 250 mA while the other two channels operate up to 125 mA. This is enough to null the earth's field and provides an 8 μT bias field.

A relatively large magnetic field has to be present for laser-cooling [67]. This current does not need to be especially stable, so it is simply provided by connecting a coil across a 5 V rail on the main power supply, which provides 700 μT. The current is switched off within 2 ms during clock measurements by a transistor.

A ThorLabs OEM board (1255R) provides the stable current sources for the other

lasers.

5.1.7 Power supply

A power supply was made to provide low noise DC to the electronics from 240 V-50 Hz mains. The DC voltages output are at +24 V, +15 V, +12 V, +8 V, +5 V, -5 V, -8 V, and -15 V. A combination of linear and switching regulators was chosen to provide a compromise between low noise and high efficiency. The power supply was designed to have lots of headroom in terms of power output relative to what would be required for a portable clock. This allowed additional laboratory equipment to be powered from the same supply. Schematics of the power supply and regulation are shown in figures B.12, B.13, and B.14 in appendix B.

5.1.8 FPGA and microcontroller

The architecture for the experimental control is shown in figure 5.11. The FPGA acts as the main controller of the digital outputs and controls the experimental sequence in addition to counting the output of the PMT. It is slaved to a master microcontroller that sends commands to the FPGA about what sequence to run and processes the data. The master microcontroller also controls a communication bus that is used to slave further microcontrollers on current and voltage supplies. The processed data is sent to a laptop that displays the data graphically. The experiment was controlled via a GUI on the laptop for ease of use; a state machine that shows the functions of the GUI is shown in figure 5.12. A separate program running on the laptop was used to stabilise the lasers to a wavemeter.

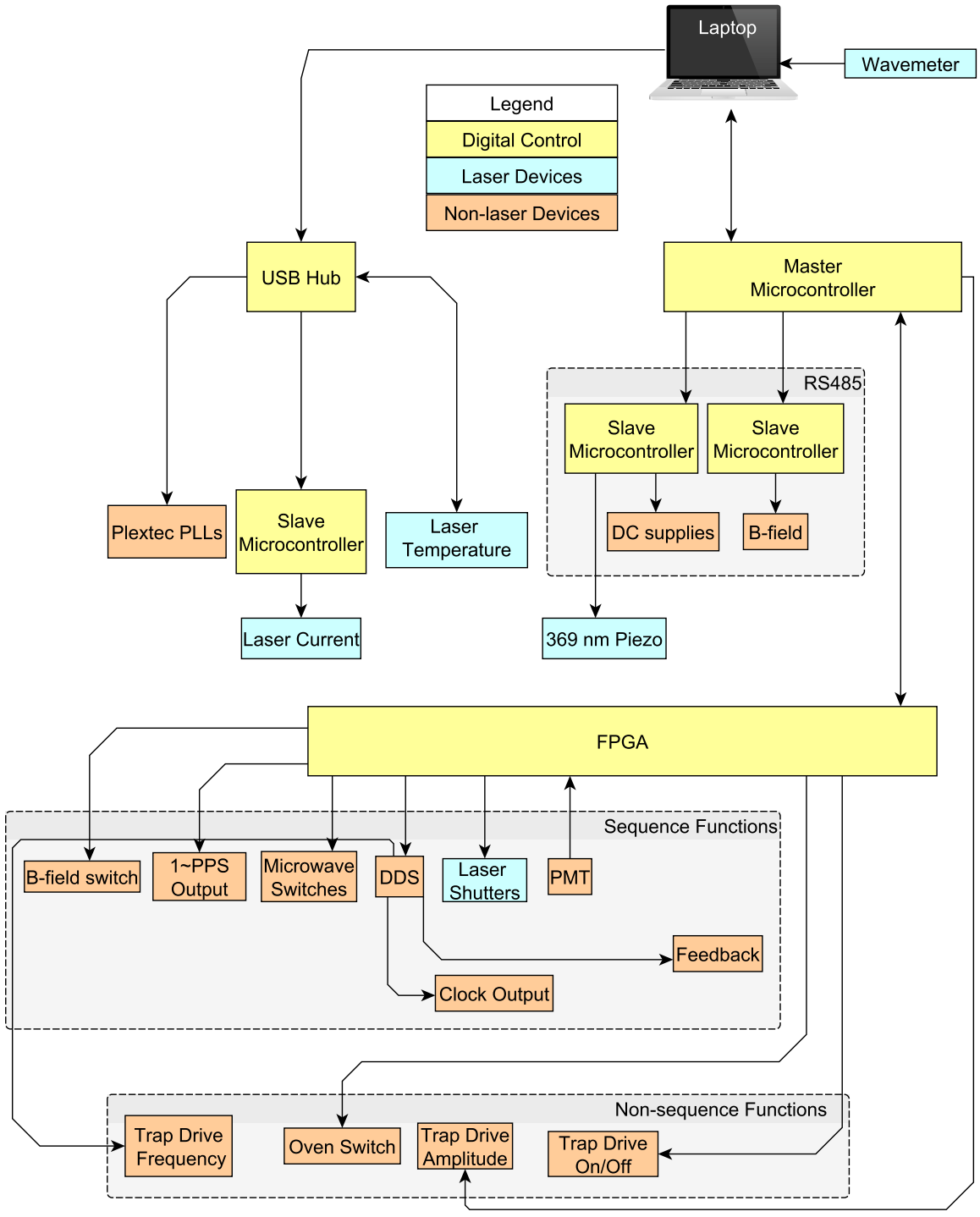


Figure 5.11: Experiment control overview. The arrows show the direction of data flow. A laptop contains the user interface and is used to trigger experimental sequences and view graphical output. The laptop also stabilises the laser frequencies by reading the wavemeter and sending the appropriate corrections to the digital laser drivers. A microcontroller sends commands to and interprets the output from the FPGA. The FPGA directly interfaces with most of the experimental functions and provides repeatable timing for the experimental sequence. The microcontroller also controls a communication bus that is used to communicate with stable current and voltage supplies.

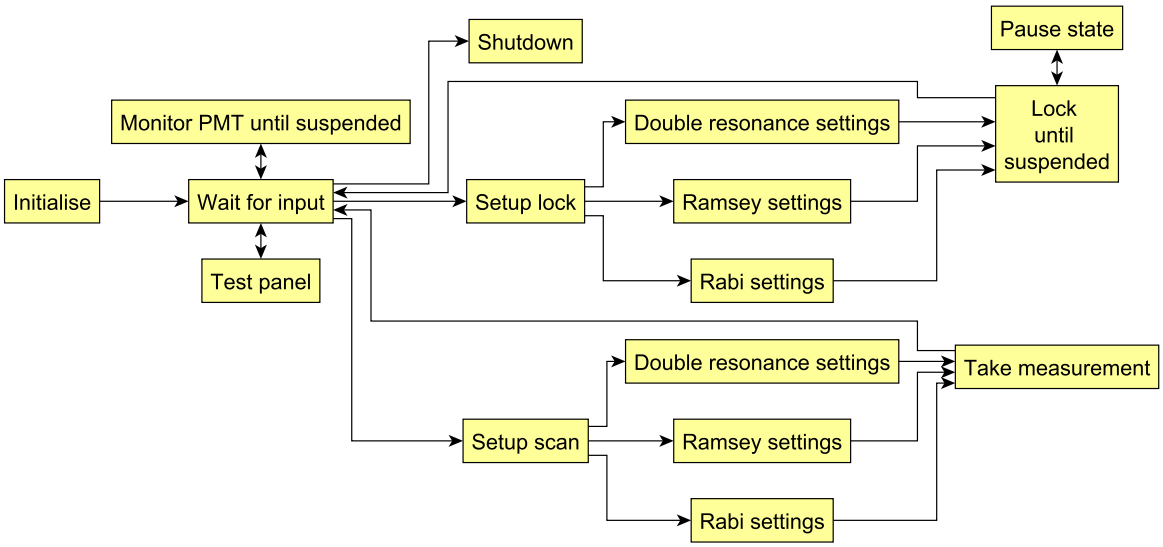


Figure 5.12: Flow diagram for the GUI that runs on the laptop.

5.2 Experiment control sequences

In this section, the functions of the hardware during the various stages of clock operation and their digital control are outlined. The state of the components are toggled via digital signals. These sequences are shown in figure 5.13.

5.2.1 Ion loading

During ion loading, the oven power supply passes current through the oven. The Mark 2 trap required 8 A at 8 V for 120 s to fill the ion trap. The Mark 3 trap's oven has improved thermal isolation and only requires 2 A at 2 V for 120 s to fill the trap. While the oven is hot, vapour from the ytterbium metal being heated is released in a collimated beam towards the centre of the trap.

To ionise the vapour, both 399 nm and 369 nm lasers illuminate the neutral ytterbium. The two-photon ionisation process is described in more detail in section 2.2.

After the ions have been created, they are laser-cooled. This requires the microwaves and other laser wavelengths to also be on at this stage. Once the loading process is finished the 399 nm light is shuttered, and the oven is turned off.

5.2.2 Spectroscopy

Measurements of the frequencies of energy levels are used as the basis of the clock, and also for diagnostic functions such as measuring the ion temperature and the magnetic field.

A Rabi sequence begins with laser-cooling the ions. All the lasers are on, the cooling coil is on, and the microwaves are at high power. To state prepare, the microwaves are turned off and the ions are optically pumped into the ground state. The lasers are shuttered and the cooling coil is switched off. A π-pulse of low power microwaves transfers ions to the excited hyperfine state. When the lasers and coil are turned back on, the population in the excited hyperfine state is read out from the fluorescence signal on the PMT. During the readout, a filter is inserted into the 369 nm beam to reduce the power to below saturation intensity, improving SNR. A timing diagram is shown in figure 5.13a.

The Ramsey sequence is mostly similar to the Rabi sequence, except the π-pulse is split into two $\pi/2$-pulses with a time interval between them where the ion is in the dark. The timing diagram is shown in figure 5.13b.

In double resonance, the lasers are on continuously and the fluorescence on the cooling transition is measured as a function of microwave detuning. In order to get narrow linewidths, low power microwaves and a low power 369-nm beam are used.

5.2.3 Clock locking

A linear-drift insensitive digital integrator feedback scheme is used to find the new frequency of the offset, f_i, from the previous frequency, f_{i-1}, and the fluorescence imbalance between two probe-frequencies $(S_L - S_H)$. The two probe frequencies are offset from f_{i-1} by the same amount. The gain, g, is calculated by numerically modelling the error signal from a fit to the Rabi lineshape before the lock is started. This is done by subtracting two points of the lineshape separated by the modulation frequency, as seen in figure 5.14. During the lock, the gain is scaled proportionally to the signal level. The loop

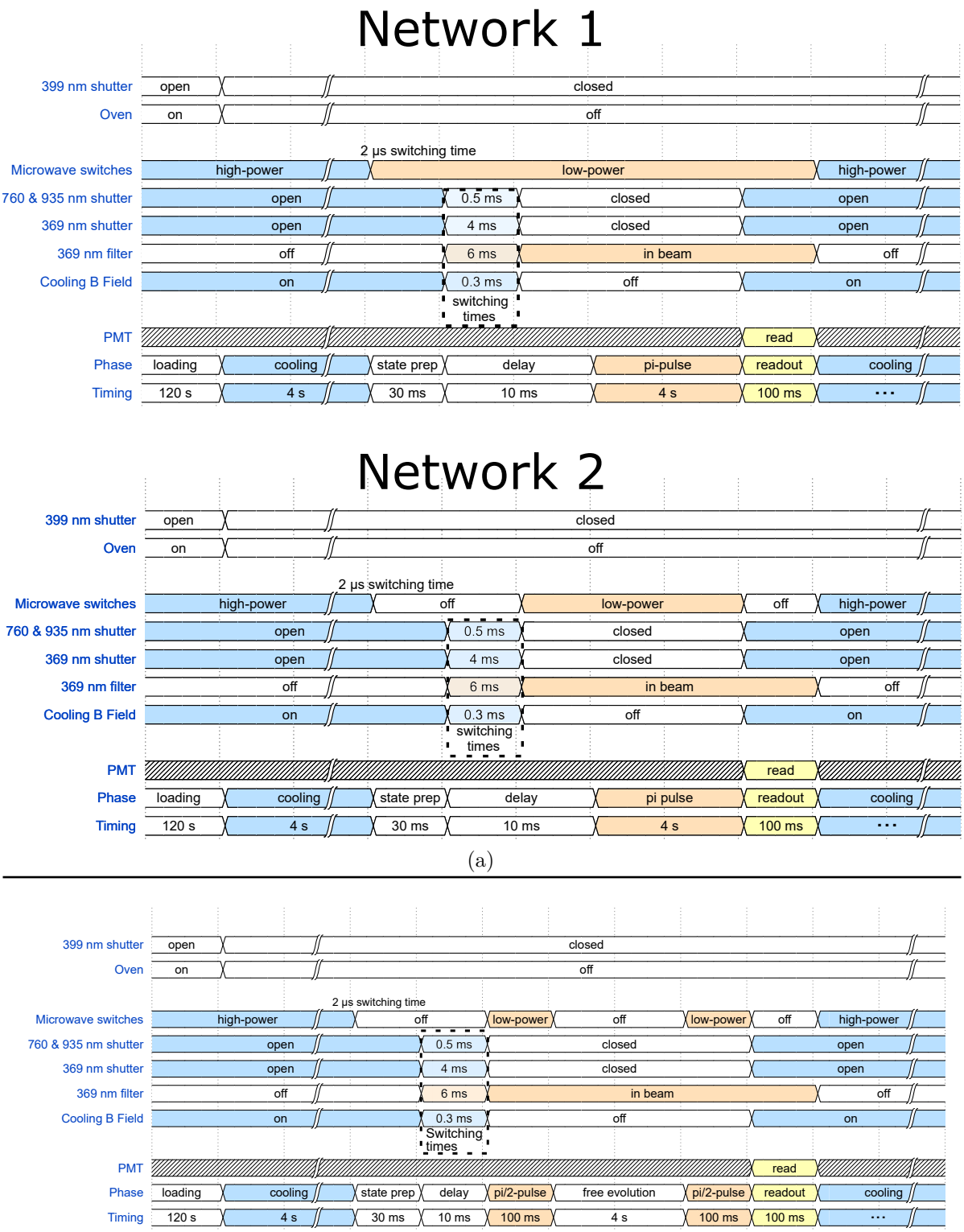


Figure 5.13: Experimental timing sequences for Rabi, 5.13a, and Ramsey, 5.13b, spectroscopy. The diagrams show the states of the hardware during each of the phases of the measurement cycle. For Ramsey spectroscopy,'network 2' must be used for switching due to the superior isolation (table 5.1).

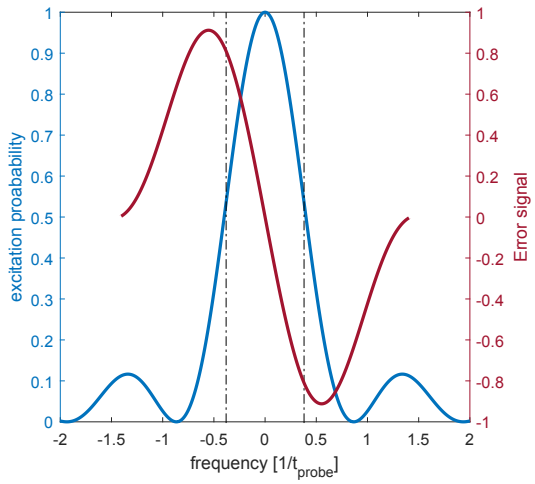


Figure 5.14: The gain is calculated from the gradient of the modelled error signal. The error signal is modelled by subtracting points on a fit to the lineshape that are separated by the modulation frequency.

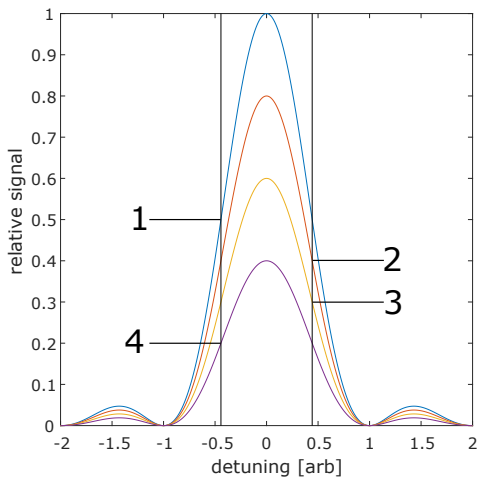


Figure 5.15: The error signal is made insensitive to a linear drift in the signal strength (represented by the sequence of coloured resonances) by probing the high- and low- frequency sides of the resonance twice before applying a correction, in the pattern: low, high, high, low.

is made insensitive to a linear signal-level drift by probing the high- and low- frequency sides of the resonance twice before applying a correction, in the following pattern: low, high, high, low. This is shown in figure 5.15. The corrected frequency is calculated by:

$$f_i = f_{i-1} + \frac{g}{2}(S_{L1} + S_{L4} - S_{H2} - S_{H3}). \tag{5.1}$$

The gain, g, is divided by two in equation (5.1) because both sides of the line are sampled twice before a correction is made. Frequency corrections are applied digitally in a DDS that is clocked to the LO.

Chapter 6

Dark Ions

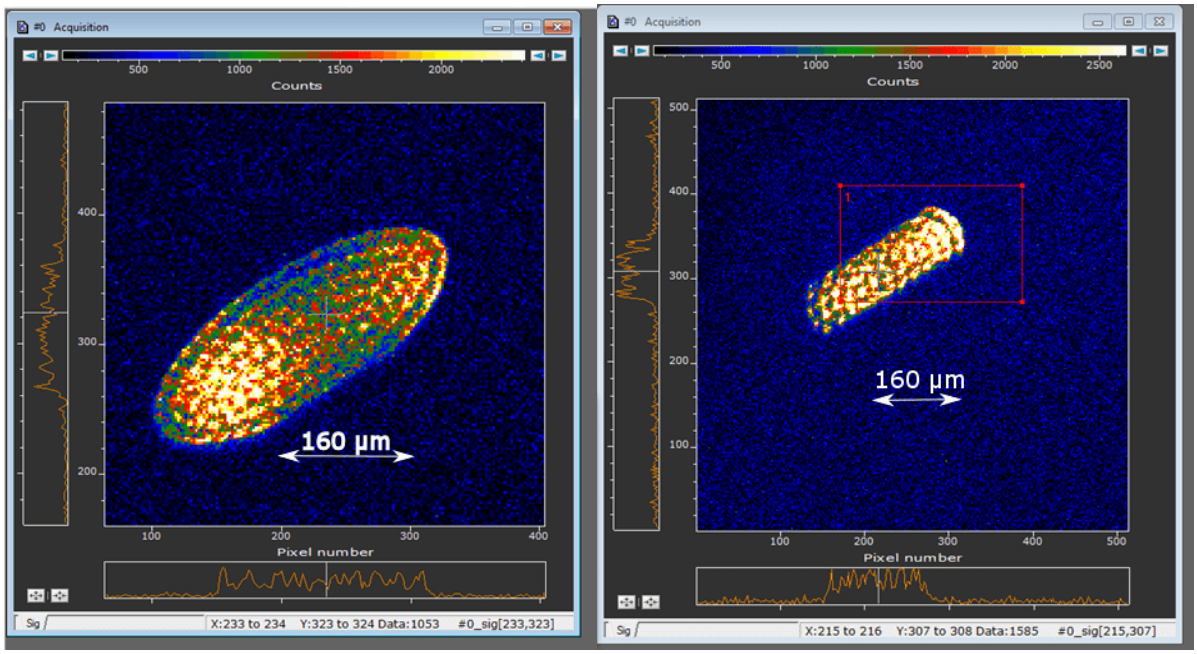
While operating the ion trap, it was observed that fluorescing ions were converting into non-fluorescing (but still trapped) 'dark ions' over a timescale of a few hours.

As seen from figure 2.3, and equations (2.13) and (2.12) from chapter 2, an ion trap can trap stably over a range of a and q parameters. A consequence of this is that it is possible to trap ions other than $^{171}Yb^{+}$ that are not useful for this experiment.

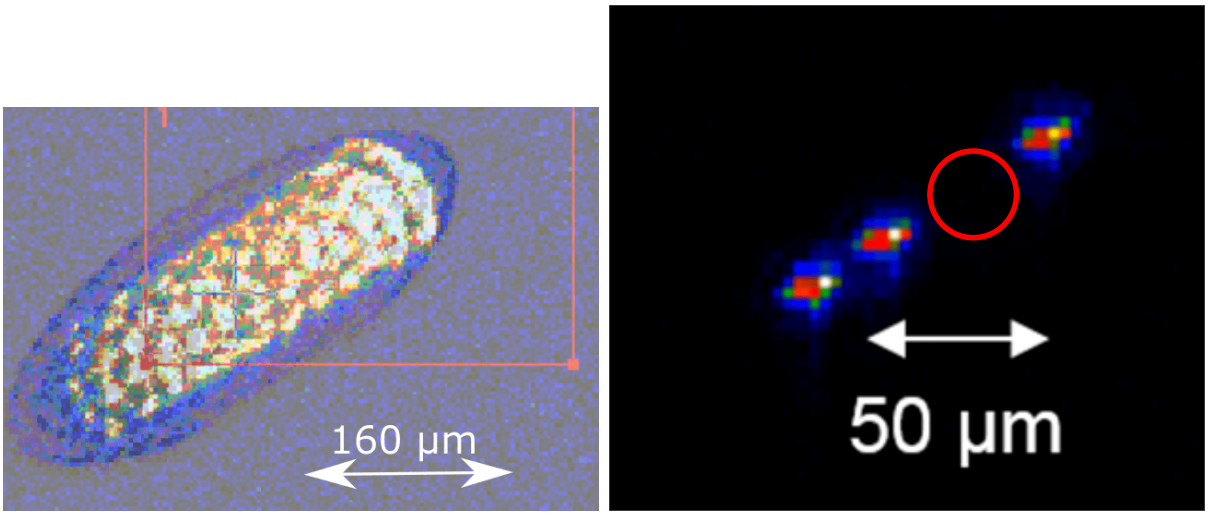
During ion loading, we take the dual precautions of using an isotopically enriched[1] sample of ytterbium metal in our oven and ionising it by isotopically-sensitive resonant photoionisation (see section 2.2). This results in an initially pure sample of $^{171}Yb^{+}$ such as that seen in figure 6.1a. Despite this, some ions enter a state where they no longer interact with the cooling laser, for example, because they have undergone a chemical reaction [99] or entered a long-lived atomic state such as the F-state in ytterbium [58, 59].

Dark ions contribute to all of the performance-limiting processes in an ion trap such as RF heating, while not producing any useful signal. A string of four ions, of which one is dark, is shown in figure 6.1d.

[1] Isotopic composition: 171: 87.98%, 172: 7.87%, 173: 1.43%, 174: 1.67%. It is useful to have some of the 172 isotope when initially commissioning the ion trap as its simpler energy level structure reduces the number of parameters to search.



(a) (b)



(c) (d)

Figure 6.1: Images of ion crystals in the Mark 2 trap. 6.1a, 6.1b and 6.1c show an initially pure crystal of $^{171}Yb^{+}$; the same ions 14 hours later; and the two images overlaid with different colour schemes to show the positions of dark ions. It is clear that both the number of fluorescing ions and the aspect ratio of the crystal has changed. The apparent change in aspect ratio is due to heavier molecular ions moving to the radial and axial edges of the trap. 6.1d shows a string of four ions. A dark ion occupies the vacant lattice site in the centre, and typically changes position in the string once every 15 seconds. For figures a, b and c, the scale is marked on the figure.

6.1 Formation of dark ions

A measurement of the lifetime of the ions during clock-operation found a half-life of 1.2 hours, as shown in figure 6.2. This lifetime was found to vary with the vacuum conditions. These were primarily affected by the electrical power applied to the oven, and the time for which this power was applied. The Mark 2 trap had a design flaw, which meant that excessive power had to be applied to the oven for it to emit atoms. This was discussed in section 4.1.2. This decay rate was much higher than we were expecting and limited the performance of the clock.

The main candidates for the dark ions were either molecular ions of YbH^+ [100] or the F-state [101]. The term scheme is shown in figure 3.1. Buffer gas cooled ytterbium ion experiments have reported both to be a loss mechanism. The mechanism proposed for these two types of dark ion formation is collisions with a background gas molecules from the $D_{3/2}$-state, which may itself be collisionally populated. These mechanisms ought to be suppressed in a laser-cooled system at UHV, with a 935 nm laser depopulating the D-state [83]. To test if population trapping in the $D_{3/2}(F = 2)$-state (which is only off-resonantly cleared in routine clock operation) may be a precursor to dark ion formation, the trap was loaded with $^{172}Yb^+$. $^{172}Yb^+$ has a simpler term scheme due to its lack of hyperfine structure, which means that there is only one D-state for the 935 nm to clear-out and there is no potential for population trapping. The dark ions were found to occur at the same rate in $^{172}Yb^+$. In addition, the rate of dark ion formation was not significantly different if the 935 nm laser was extinguished. These investigations suggest that mechanism for dark ion formation in the Mark 2 trap does not require the ion to be in the $D_{3/2}$-state.

It has been reported [102] that dark ions form faster in the presence of O_2 and H_2O than H_2. This suggests that these molecules or their fragments can bond with Yb^+.

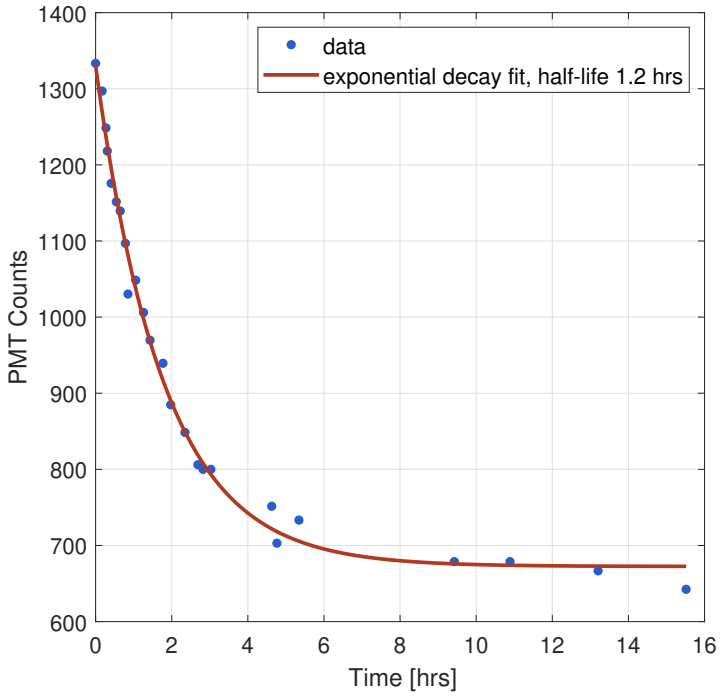


Figure 6.2: Signal decay due to dark ions. A fit to a decaying exponential gives a half-life of 1.2 hours.

6.2 Identification of dark ions

The properties that can be used to discriminate between ions of different species are their electronic structure and their charge to mass ratio. It is possible to run a linear ion trap as a mass filter, as this is the operating principle of a mass spectrometer. However, these devices operate close to the $q \approx 0.7, a \approx 0.2$ instability [103], whereas large Coulomb crystals and ion clouds are most stable with small a and q parameters, typically on the order of 0.01 [96]. The large voltages required to get to the mass-sensitive instability region in a large trap, far from the designed operating condition, makes this method impractical. The mass filter method would also have trouble differentiating between $^{171}Yb^+$ F-state and YbH^+, as the mass ratio $\Delta m/m = m_H/m_{Yb} = 0.00585$. In the following sections, some methods to identify the dark ions are presented. Laser spectroscopy was used to test if the dark ions were due to either $^{171}Yb^+$ F-state or YbH^+.

Other ion trap measurements can also be used to gain information about the masses of the trapped ions, some of these methods are outlined in a following section.

6.2.1 Laser spectroscopy

Using laser spectroscopy, it is possible to change and detect the ion's electronic state. In the case of F-state trapping, a laser at 760 nm could be used to drive the ion to the ground state via a short-lifetime state. For molecular ions, it is possible to drive an electron from a molecular orbital with bonding symmetry to one with anti-bonding symmetry, causing the ion to dissociate.

369 nm test for YbH^+: The dissociation wavelength for YbH^+ is reported in the literature as 369.482 nm [104]. Fortunately, being very close to the cooling wavelength (369.526 nm) it is within the tuning range of the cooling laser. A 369-nm laser (600 μW in a spot size of 300 μm) was tuned to the dissociation wavelength, and its overlap was ensured by observing fluorescence when it was tuned to the cooling transition. The ion crystal was also illuminated by a second 369 nm laser tuned to the cooling transition, and the D-state repump laser, as shown in figure 6.3. The number of dark ions was inferred from counting the empty lattice sites and monitoring the total fluorescence from the ions. No regeneration of the dark ions was observed.

Ion stabilised 760 nm test for F-state trapping: A 760 nm laser, stabilised to the fluorescence signal from an $^{171}Yb^+$ optical clock that actively populates the F-state, was measured on a wavemeter that was stabilised and referenced to a Sr lattice clock-laser. A Titanium-sapphire (Ti:S) laser was tuned to (and scanned in the vicinity of) the two wavelengths, which were measured to be 760.065(1) and 760.075(1) nm, and to literature values of an alternative depopulating transition at 638 nm. This light was overlapped with the 935-nm laser and shone on to the ions with a spot size of 500 μm. The power in the 760 nm beam was 30 mW, as shown in figure 6.4. The dark ions in the trap did not start fluorescing, nor did the rate of ion loss into the dark state reduce. This is evidence

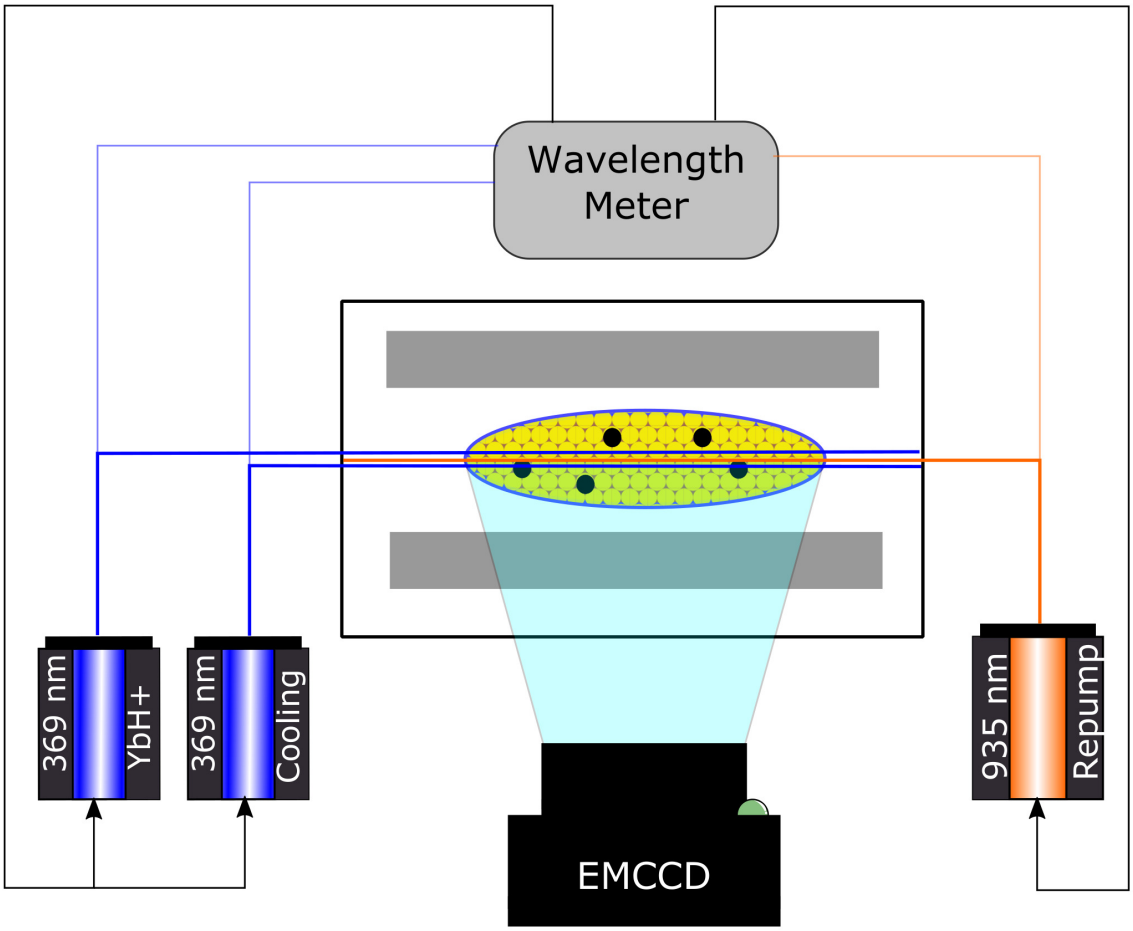


Figure 6.3: Test to determine if dark ions were YbH^+. Two 369 nm lasers were locked to a wavemeter, one was tuned to the cooling transition, and the other was tuned to reported YbH^+ dissociation wavelengths. A 935 nm laser repumped from the D state. The number of dark ions was monitored by watching the dark lattice sites on an image from an electron-multiplying camera (EMCCD).

that the dark ions are not due to trapping in the F-state.

6.2.2 Ion trap measurements

In these sections methods to determine the mass of trapped ions from measurements of mass-sensitive motion of the ions in the ion trap are outlined. Crystal-ordering points to the dark ions being due to molecular ions; the other methods are being considered for future work.

Crystal-ordering: As seen from equations (2.18) and (2.19), the mass dependence of the RF trapping potential means that lighter ions are attracted to the trap centre more strongly than the heavier ions. This causes heavier ions to accumulate at the edges of the crystal in the low-temperature limit. Examples of this phenomenon can be seen in figures 6.1 and 6.5. Most linear ion traps operate in the regime where equation (2.16) is a good approximation to ω_z. This generally results in lower axial micromotion and higher axial secular frequencies. These benefits are often important in quantum information experiments but are not so important for a many-ion microwave frequency standard. If equation (2.16) does not hold, due to a significant contribution to the axial trapping from the RF, and if the ions are centred in the trap, the heavy ions will accumulate at the radial and axial edges. This effect is seen in figures 6.1a, 6.1b and 6.1c. Axial separation is not seen in figure 6.1d, suggesting that a phase change occurs between axially separated and axially integrated crystals for different trapping parameters.

As it is possible to move the ions along the trap axis by biasing one endcap voltage relative to another, it should be possible to separate heavy and light ions into two pure phases. This is shown schematically in figure 6.6. It would therefore be possible to selectively remove the dark ions by briefly dropping an endcap voltage so that the ions closest to that electrode are removed from the trap. A similar technique was used to isotopically enrich trapped strontium ions at Universite Paris–Diderot [105]. However, the axial separation in their ion trap was obtained by radiation pressure of the cooling laser that only interacted with one isotope. Axial separation due to radiation pressure

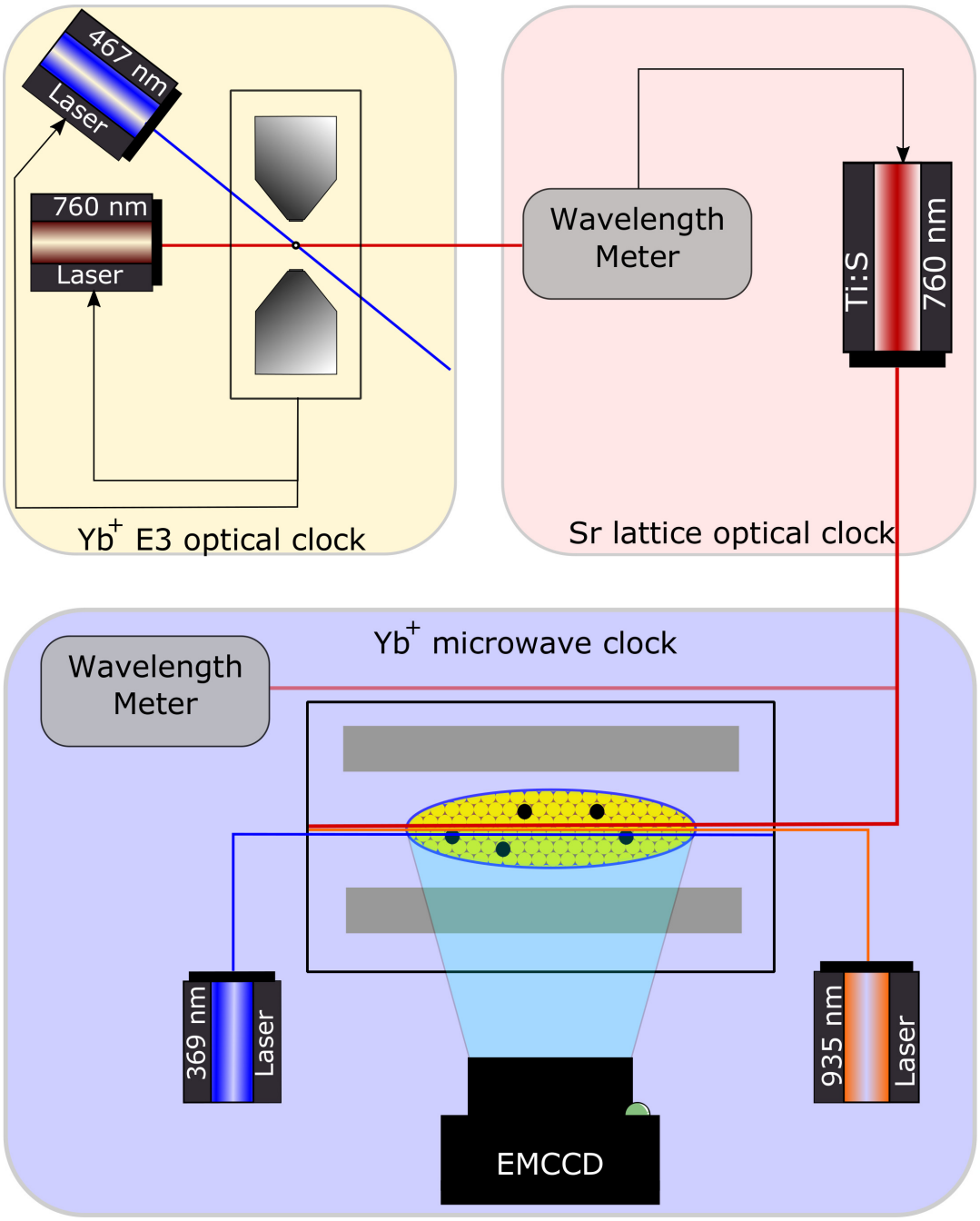


Figure 6.4: Test to determine if dark ions were in the F-state. An ytterbium optical clock, driving the clock transition at 467 nm, populates the F-state; a 760 nm laser is locked to the ${}^2F_{7/2}\begin{cases}F=3\\F=4\end{cases} \rightarrow {}^1[3/2]_{3/2}\begin{cases}F=1\\F=2\end{cases}$ transitions. The frequency of this laser is measured on a wavelength meter in an adjacent lab from where a Ti:S laser is disciplined to match the optimal 760 nm wavelength. The light from the Ti:S is overlapped with a 935 nm laser using a fibre combiner and sent through the linear ion trap containing dark ions. 30 mW of 760 nm was focused to a beam waist of 300 μm at the ions. The fluorescence from the 369 nm cooling transition was measured on an electron-multiplying camera (EMCCD).

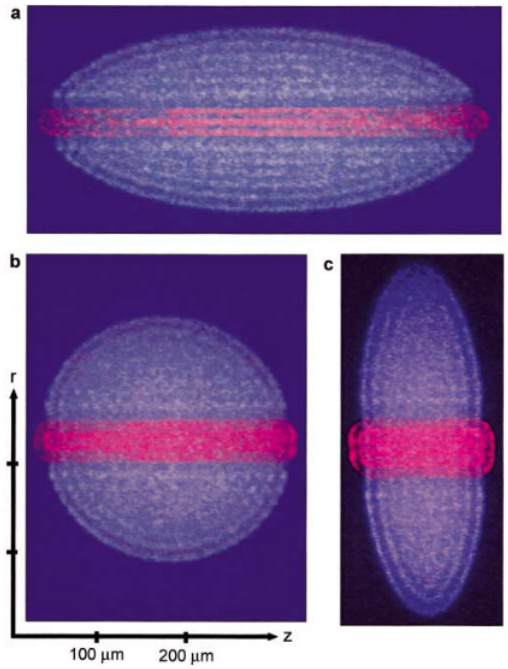


Figure 6.5: A $^{40}Ca^{+}$(blue) $^{24}Mg^{+}$ (red) bicrystal in a symmetrically driven linear ion trap at three different endcap voltages. The heavier Ca ions are pushed radially to the edge. Reproduced from [106].

was not observed in our ion trap. This is likely due to our stronger axial confinement and the large atomic mass of ytterbium.

Normal mode resonance: A method that measures the normal modes of a two-ion crystal is reported to be sensitive to $\Delta m/m = 1 \times 10^{-4}$ [107], which, if reproducible in our system, would be sensitive enough to resolve the difference between Yb^{+} and YbH^{+}. The disadvantages are that this would require a departure from normal operating conditions. A method to measure larger ion-crystal centre of mass frequencies is used by Sheridan and Keller [108], although mass determination was only demonstrated in small crystals of up to 14 ions. If measuring the mass of a whole crystal, assuming 50% dark ions, this would require an accuracy of $\Delta m/m \geq 2.9 \times 10^{-3}$.

RF absorption signals: Initial evidence of molecular ion formation was discovered by Sugiyama [102], who noted that the RF absorption signal evolved in a way that suggested

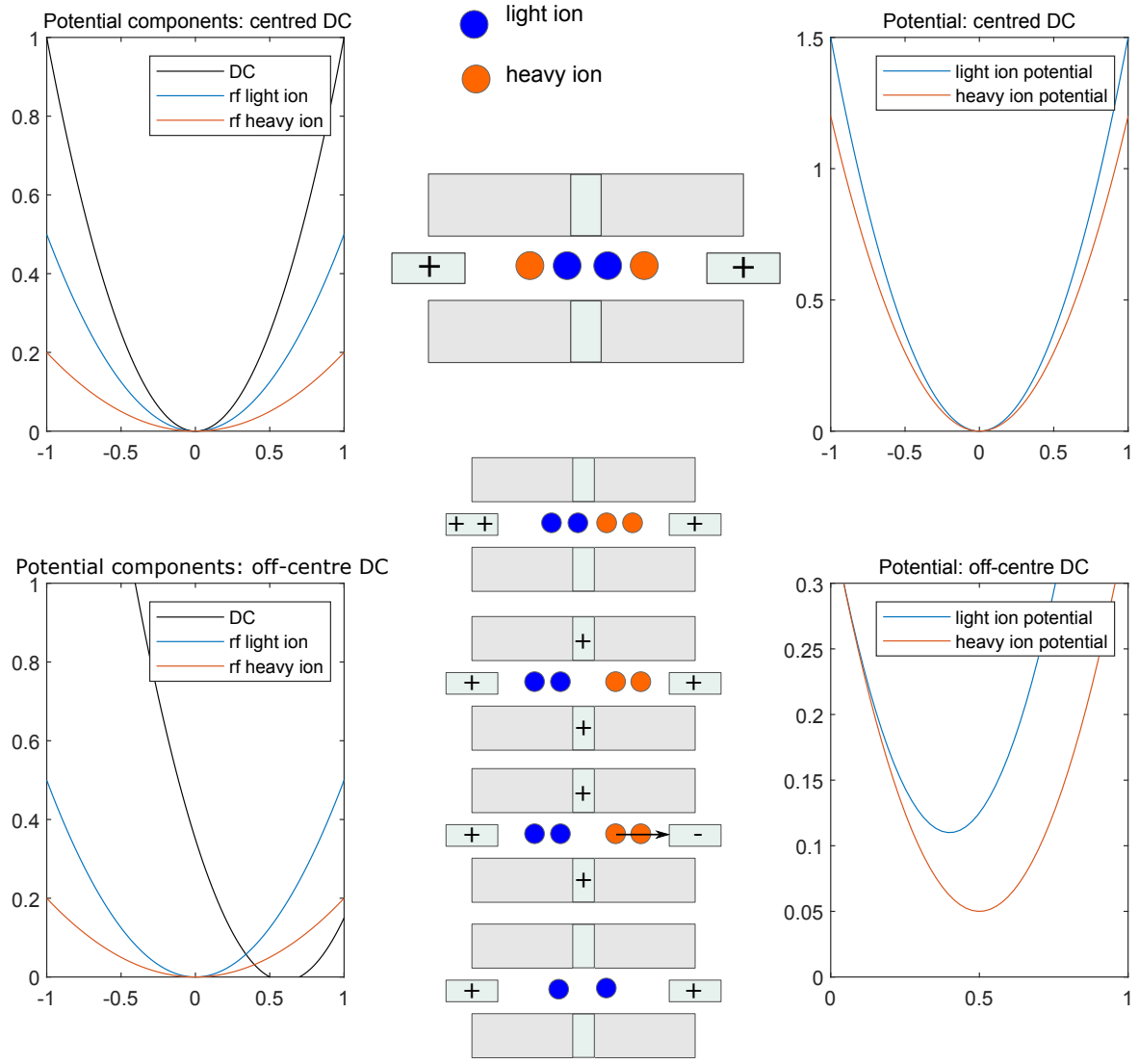


Figure 6.6: By displacing ions along the axis with unbalanced endcap electrodes, it is possible to separate an ion crystal by charge to mass ratio. For two ion species with the same charge but different masses, the lighter ions, being more tightly bound by the RF trapping force, stay closer to the trap centre; heavier ions feel a weaker centring RF confinement force and are pushed further by the DC. By using a segmented linear trap, it would be possible to obtain pure samples of a given ion or isotope by splitting the ion crystal axially with DC potentials.

that the trapped ion cloud was getting heavier. The production of ytterbium molecular ions was confirmed later in the same laboratory by a mass spectrometry study, where the ion trap fed a quadrupole mass analyser with samples of ions [104]. This led to the attribution of the $^{174}YbH^+$ dissociation wavelengths of 339.482 nm, 369.202 nm, and 368.947 nm, each with a linewidth of approximately 5×10^{-3} nm.

6.2.3 Dark ion conclusions

Dark ions were found to be a limitation of the Mark 2 ion trap. The resulting signal loss is the major source of instability when the clock is locked.

To identify the dark ions, laser-spectroscopy was used to identify either F-state-trapping or formation of YbH^+ ions. The negative results suggest that neither of these candidates are responsible. Observations of the ordering of Coulomb crystals containing dark ions imply that the dark ions are molecules. It seems likely that the molecular ions are due to reactions with water molecules. Further work is planned to identify the dark ions, including measurements of the dynamics of the ion trap.

Chapter 7

Frequency Standard Operation

In this chapter the operation of the frequency standard is detailed and the performance is evaluated. I have used the term 'frequency standard' here rather than 'clock'. This is because in the presented measurements the atomic-clock-under-development did not run continuously, autonomously and indefinitely in the locked state — as one might expect of a clock. The ions were loaded manually, and the atomic-clock-under-development stayed locked until the signal from the ions was lost, and reloading was required. Throughout the rest of the thesis I have used the terms 'frequency standard' and 'clock' interchangeably.

The two figures of merit for a frequency standard are the level of uncertainty in the frequency output and the stability of the frequency. The focus of this project was stability; as a result, for the data presented, the uncertainty on the absolute frequency of the unperturbed clock transition is relatively high, at 8 parts in 10^{12}.

In the first section, I discuss the metric of stability; how it is measured; factors that influence stability; and the measurement of the stability of the frequency standard. The next section discusses the reliability of the system. The operation of the clock at stages in the measurement cycle, the manipulation of the ions' internal state, and the choice of operating parameters for the clock, such as the background magnetic field, are all discussed in following sections. A further section evaluates sources of noise and frequency shifts present in the frequency standard. The uncertainty of the output frequency is calculated.

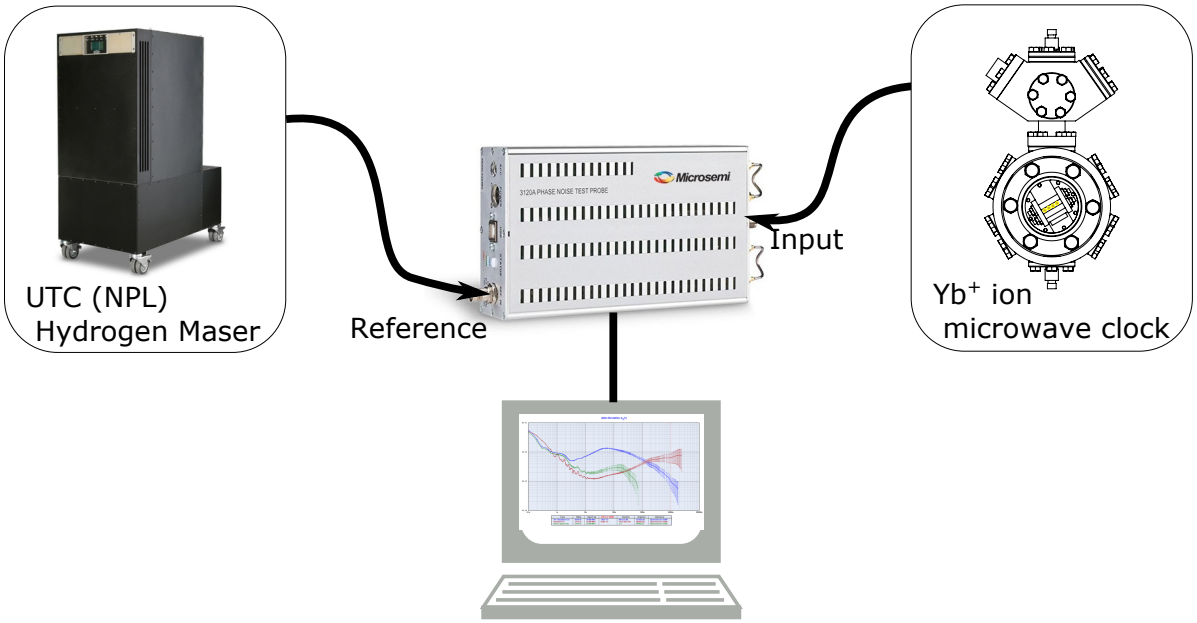


Figure 7.1: The 10 MHz output of the Yb^+ ion microwave clock was compared to the 10 MHz from a caesium-steered hydrogen maser on a phase comparator (Microsemi 3120A). This provides a direct measurement of the system's stability and absolute frequency.

7.1 Stability

An outline of stability and the Allan variance is given in section 1.2. An in-depth account can be found in the NIST Handbook of Frequency Stability Analysis [5]. During a stability measurement, the nominal 10 MHz from the microwave clock is compared with the stable 10 MHz from the maser on a Microsemi 3021A phase comparator. The phase offset is logged as a function of time, and the Allan variance is calculated in real time and displayed on a PC. The scheme is shown in figure 7.1. To obtain a stability estimate at a given averaging period, data will typically need to be taken for at least four times this period. This is so that a statistically significant number of averages over this time period can be compared.

Stability can be limited by the shot-noise of the arriving photons on the PMT, or by changing environmental conditions causing unstable frequency shifts to the ions. The stability of the frequency standard is currently limited by shot-noise. These effects are discussed in section 7.6.

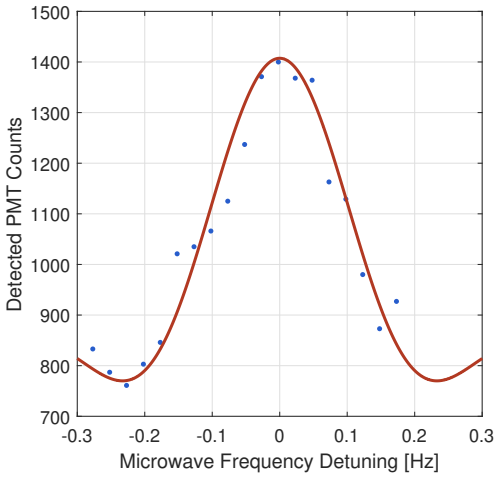


Figure 7.2: The Rabi lineshape of the clock transition at 12.6 GHz taken shortly after loading and prior to the stability measurements presented later in this chapter. The data are obtained from a single scan with a microwave pulse length of 4 s and 4 s of cooling between points. The frequency scale is relative to the peak of the resonance, offset from the unperturbed frequency by about 2 Hz. The SNR at the peak was 16. Assuming no signal loss, the shot-noise limitation to the instability would be $9 \times 10^{-13}/\sqrt{\tau}$.

7.1.1 Shot-noise limit to stability

The shot-noise limit to stability is given by equation (1.2), reproduced here as equation (7.1):

$$\sigma(\tau) = \frac{1}{\pi \mathrm{SNR} \cdot Q} \sqrt{\frac{t_p + t_D}{\tau}}, \tag{7.1}$$

where the SNR is calculated at the maximum. The noise is caused by the random arrival of photons, and so has a Poisson nature. The signal-to-noise ratio is therefore given by equation (7.2):

$$\mathrm{SNR} = \frac{\text{Peak height}}{\sqrt{\text{Background} + \text{Peak height}}}, \tag{7.2}$$

where the peak height is defined relative to the background off-resonance level. Calculating SNR for the lineshape shown in figure 7.2 gives a shot-noise limit to the instability of $9 \times 10^{-13}/\sqrt{\tau}$.

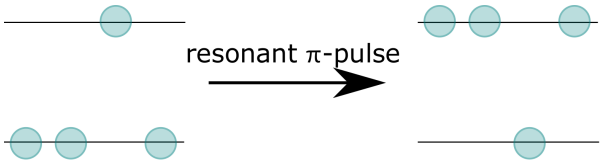


Figure 7.3: If incomplete state preparation leaves one quarter of the ions in the excited state, as in the left-hand side of the diagram, a resonant π-pulse will only result in $^3/_4$ of the fully-state-prepared signal. However, an off-resonant π-pulse will leave the state unchanged and give $^1/_4$ of the on-resonance-fully-state-prepared signal. This means that the contrast between resonant and off-resonant cases is reduced to $^1/_2$ of the fully state prepared case.

7.1.1.1 SNR limitations

Processes that affect the SNR of each measurement are listed as follows:

1. Quantum projection noise (QPN) from the number of ions; this limits the maximum single-measurement SNR to $\sqrt{N_{\text{ions}}}$;
2. State preparation efficiency;
3. Number of photons scattered per ion in F=1 state before information loss;
4. 369 nm laser scatter off windows and trap components;
5. Detection efficiency;
6. Short timescale laser intensity and polarisation noise; and
7. Coherence of the ions.

The QPN is improved by trapping more ions; this requires a large trap with a low heating rate (section 2.1.4).

Inefficient state preparation causes both a reduction in the clock signal and an increase in the background signal. The signal height, h, is related to the fraction, G, of ions prepared in the ground state before a clock pulse by $h \propto 2G - 1$. The reasoning is shown in figure 7.3. State preparation is further discussed in section 7.3.2.

Readout is related to state preparation as they operate on the same atomic transition. This is discussed in section 7.3.3.

The imaging system is discussed in section 4.6; the collection efficiency is 2.7%. Collection of 369 nm light that is not scattered by the ions results in a fluctuating background, as seen in equation (7.2). To combat this, the 369 nm laser intensity is reduced during readout to below saturation intensity for the ions. An imaging system focuses on the ions and provides spatial filtering to remove line-of-sight from reflective surfaces. The interaction of the ions with the detection laser is ion-temperature sensitive due to the first-order-Doppler effect. The ions scatter the laser photons at different rates depending on where in the Doppler temperature distribution they are. This causes the 'cooler' ions to leave the cycling detection transition and contribute noise before the information from the 'hotter' ions has been detected. It is found that the SNR decreases for longer probe times due to this effect.

Laser polarisation fluctuations and drift were initially found to be issues; however, careful alignment of the cooling beam into a polarisation maintaining fibre improved the polarisation noise to an acceptable level.

7.1.2 Stability measurement of the locked frequency standard

The stability of the clock when it was locked to the ions was measured as shown in figure 7.1. The experimental sequence has been explained in section 5.2. For these measurements, Rabi spectroscopy was used. The microwave pulse time was 4 s and the cooling time was also 4 s. The output frequency was updated every four measurements, yielding a loop time of 32 s. Data is presented in figure 7.4 for the locked clock with a fitted line showing an averaging rate of $3.6 \times 10^{-12}/\sqrt{\tau}$. The error in the fit is estimated to be $\pm 0.2 \times 10^{-12}/\sqrt{\tau}$. Figure 7.5 (also shown as figure 6.2) shows the signal loss over this period due to the generation of dark ions. The data presented are from the first $2^1/_4$ hrs of clock operation. At longer times, the reducing SNR decreased the stability.

The period between successive corrections applied to the local oscillator's frequency is known as the loop time. An Allan deviation plot from a frequency standard shows instability from the unlocked local oscillator at averaging times smaller than the loop time. This is because the local oscillator acts as a flywheel between successive clock

measurements. At averaging times larger than the loop time, instability is due to the ion references. At averaging times comparable to the loop time, it is common to see noise added by the servo as it applies the frequency corrections. These effects are seen by comparing the local oscillator stability, plotted in figure 5.2, with the stability of the frequency standard locked to the ions in figure 7.4. The loop time in figure 7.4 was 32 s.

The optimal loop time is a function of the relative performance of the local oscillator and the lock to the atomic reference. The loop time should be chosen to be the intercept between the local oscillator ADEV and the stability of the ions. In practice, feedback was applied more frequently than optimal to track the ions' stability at shorter timescales. This provided a useful diagnostic of the quality of the feedback coming from the ion-signal. Also, by extending the region of the ADEV plot proportional to $1/\sqrt{\tau}$, this allowed improved confidence in estimating the shot-noise instability.

A relatively small load of ~200 ions was used to limit the effects of the large power dissipation required to release the atoms from the oven. This improves ion lifetime and reduces transient effects, which result from the increased temperature, pressure and magnetic field after firing the oven. Another positive effect of using fewer ions is that, being closer to the centre of the trap, their heating rate is lower than that of a large cloud.

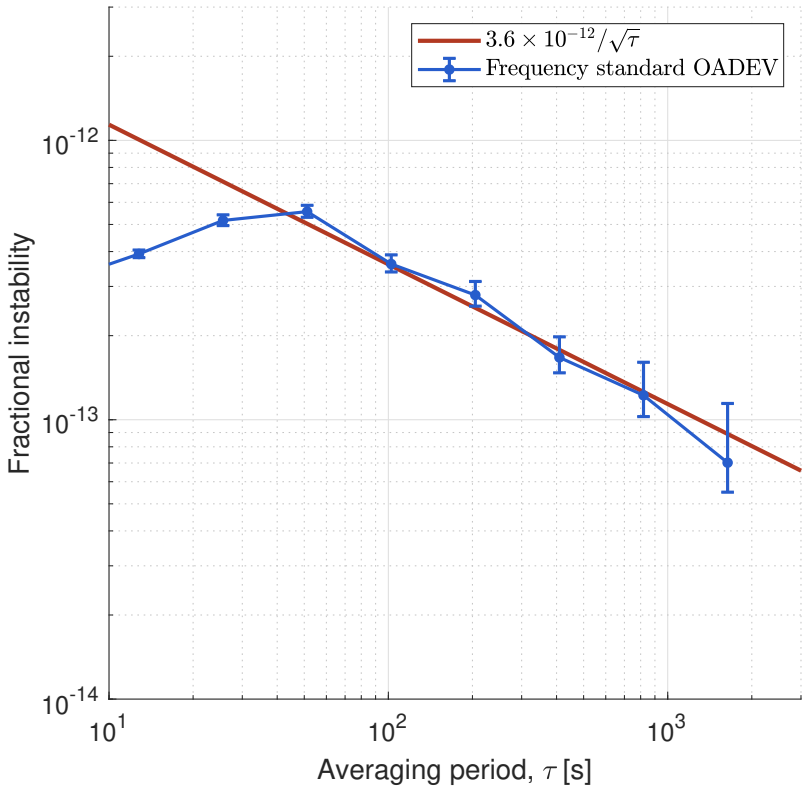


Figure 7.4: Stability of the clock output measured against a hydrogen maser. A stability of $3.6 \pm 0.2 \times 10^{-12}/\sqrt{\tau}$ is measured for averaging times longer than 30 s, when feedback is applied, until the data ends at averaging times of 1500 s. Signal loss, shown in figure 7.5 and discussed in the text, limited the measurement to $2^{1}/_{4}$ hrs of continuous data.

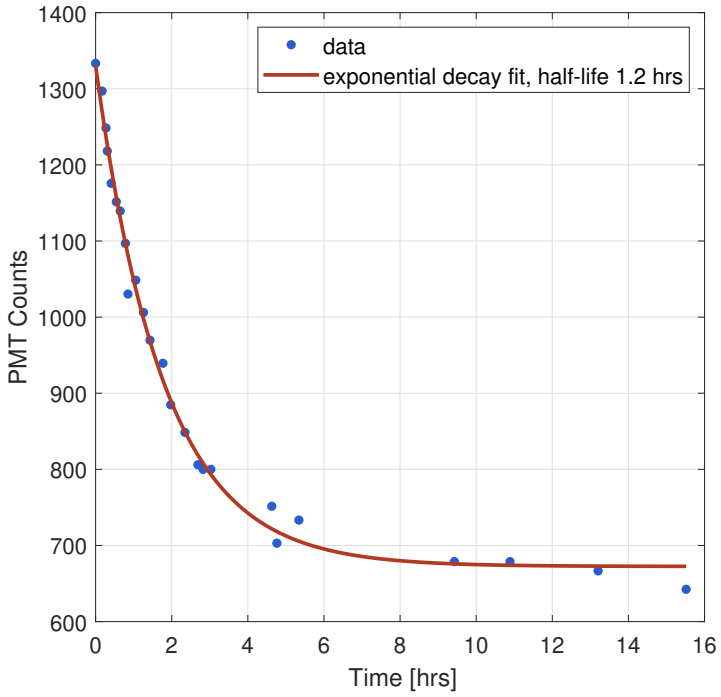


Figure 7.5: Signal loss during clock operation for the data shown in figure 7.4. The signal-to-noise ratio decreases over time, affecting the stability.

7.2 Reliability

The primary cause of the clock becoming unlocked was ion loss. The longest continuous lock for was 72 hrs over a weekend. This lock was manually aborted after all of the signal from the ions was lost. Occasionally the clock would become unlocked for other reasons, such as failures were due to the laser systems; as these components were often the least developed and were very sensitive.

The laser alignment was found to be robust over the timescales of a typical clock measurement. However, we would tweak the alignment of the lasers into the fibres approximately once every two weeks to keep the laser powers optimised. This adjustment frequency increased when the laboratory lost temperature control. The mechanical shutters that are used to extinguish the 369 nm laser undergo cycling every few seconds, and once every few months they need to be realigned. A commercial version of the clock

would require a more integrated and robust laser system. Ensuring that the mechanical shutters operate reliably over the service life of a system is likely to be an engineering challenge.

7.3 State control

During clock operation, the state of the ions has to be constantly manipulated through the stages of the measurement cycle. The sequence diagrams for both Rabi and Ramsey spectroscopy are shown in figure 5.13 in chapter 5.

To discuss state preparation, spectroscopy, and detection, it is helpful to introduce a term scheme that focuses on transitions between the states. This is shown in figure 7.6, where the transitions have been labelled with numbers to aid the discussion.

During laser cooling, '1' mixes the hyperfine states and '2' is driven resonantly by the 369-nm laser. The 369-nm laser also off-resonantly drives '4' and '7' and the 935-nm laser drives '10' to clear the D-state.

To state-prepare the atoms, we aim to move as many of the ions as possible into the F=0 ground state. To do this, '1' is turned off and the off-resonant transitions '4' (followed by decay '5') and '7' compete to establish the steady-state. Ideally, '4' would be much stronger than '7', and to achieve this many groups add an EOM-sideband to their 369-nm laser to drive '4' resonantly. However, EOMs add cost, size and complexity to the system, and so we decided against using them for this project.

After the ions are state-prepared, a spectroscopy technique is used to transfer the ions into the F=1 state. The spectroscopy techniques are detailed in section 2.3 in chapter 2. The population in the F=1 state is then detected by driving '2' (with '1' turned off) and detecting fluorescence photons. To reduce the amount of stray light detected, and also to inhibit the off resonant transitions '4' and '7', a filter attenuates the 369-nm laser at this point in the measurement cycle.

The following subsections detail the performance of each of the operations on the ions.

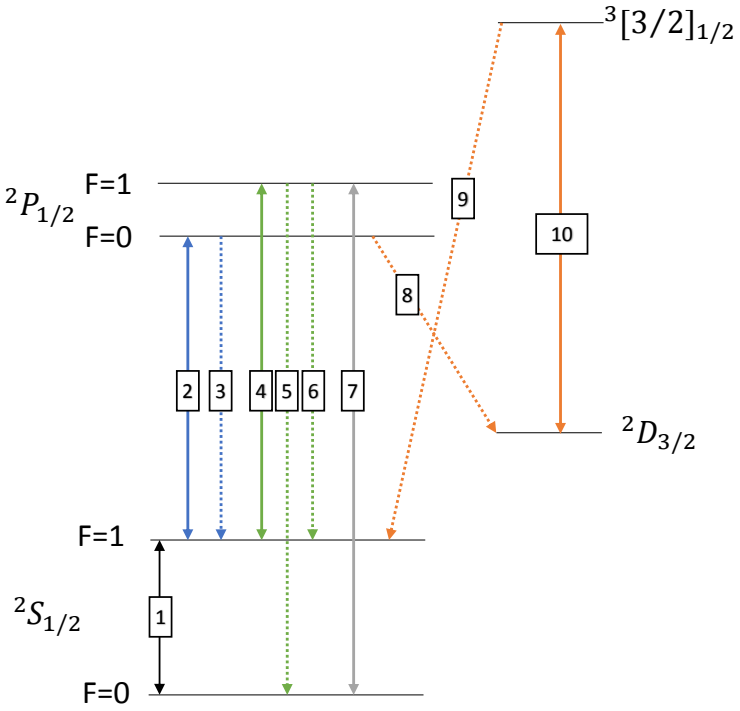


Figure 7.6: Term scheme where the transitions between the states are represented by numbered arrows. Solid arrows represent a driven transition, and dotted arrows represent a decay. The relative magnitude of these transitions determines the steady-state populations of the energy levels. (also appears as figure 2.10)

7.3.1 Cooling

To laser cool the ions, all the lasers are turned on, and high power microwaves (Rabi frequency ~1 MHz) mix the ground state hyperfine levels. A magnetic field of around 700 μT causes the Zeeman sub-levels to become non-degenerate (see section 2.2). During the preceding clock pulse the ions will have heated; by monitoring the fluorescence rate, we can see the time it takes the ions to cool back to a temperature where they are resonant with the cooling laser. The cooling laser is typically detuned about 60 MHz away from the resonance. This is to speed up the interaction with the 'hotter' ions. The fluorescence signal during the cooling cycle is shown in figure 7.7. As can be seen from the figure, cooling took a significant fraction of the cycle time, and in practice the cooling time was set to be at least a factor of two larger than necessary to ensure consistent cooling. Cooling for a large fraction of the measurement not only impacts the stability through reducing the measurement rate, as in equation (7.1), but can also lead to high-frequency local oscillator noise becoming aliased. This is known as the Dick

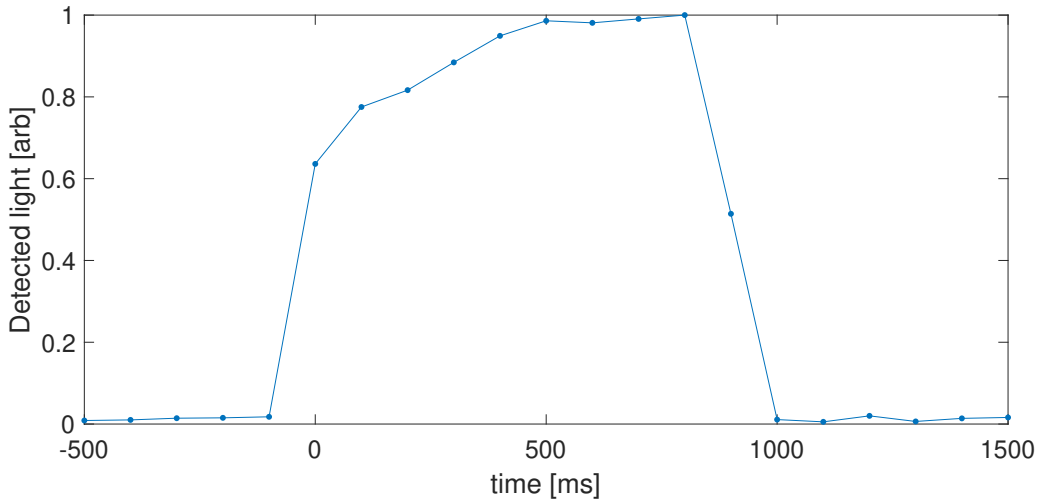


Figure 7.7: Measurement of cooling time. The cooling laser is blocked for 1 s and the detected light as a function of time is measured by the camera. The shutter is opened at 0 ms on the horizontal scale, and the detected light immediately rises to 60% of the maximum value. This is due to both scattered light and fluorescence. The fluorescence increases for 500 ms and then plateaus. The detuning was -100 MHz and the data were taken one hour after loading the trap.

effect, and is described in section 7.6.7 [109–112].

7.3.1.1 Transition profiles

Transition profiles of the lasers, where one laser frequency is scanned while the others are held constant, are discussed in the following subsections. The shape and features of the transition profiles may reveal how strongly the transitions of the cooling cycle are being driven, the temperature of the ions, and whether the ions are in a cloud or crystal. These transition profiles are shown in figure 7.9. The position of the cooling beams, their polarisations and the direction of the magnetic field are indicated on the diagram. In the 369-nm beam, 300 μW is focused to a $(1/e)$ waist at the ions of 200 μm, the 935-nm beam has 3 mW focused to $300 - 500\,\mu$m.

369 nm — cooling: The cooling transition profiles are shown in scans a, b and d of figure 7.9. In these scans the 935-nm laser was held at it's peak value. In the top row, the RF trapping voltage is lowered to a value where Coulomb crystals form (150 V_{pk-pk}

at 2 MHz). A fluorescence dip is seen at the onset of the phase transition as the laser is scanned towards the optimal frequency from the low-frequency side [48]. At frequencies higher than the optimal value, the crystal melts as the ions are heated by the laser [113]. It was observed that in the crystal phase, the ion velocities were spatially dependent, with the edges of the crystal having larger velocities. This is shown in figure 7.10.

In scan b of figure 7.9, the RF trapping voltage is higher (300 V_{pk-pk} at 2 MHz). Under these conditions in the Mark 2 trap, Coulomb crystals do not form. The shape of this profile matches the form described by DeVoe et al. [51], and results from micromotion-induced second-order Doppler shifts. In the rest frame of the ion, the laser appears to be frequency modulated at the trap frequency, Ω ($\Omega = 2$ MHz for these data). A monochromatic laser at frequency ω_L will be broadened into a comb of sidebands at $\omega_L \pm n\Omega$, which may span a few hundred megahertz. Near to resonance, the most effective sidebands of this laser-spectrum may lie on the blue side of the resonance and heat the ions, resulting in the peak of fluorescence occurring before resonance.

The clock is typically operated in the cloud phase but containing a few hundred ions, rather than the trap capacity of a few thousand. This results in a lower spread in the velocity profile, and more efficient laser cooling than when the trap is filled to capacity. The trapping voltage of 300 V_{pk-pk} at 2 MHz is used to prevent crystals forming (section 2.1.5). Figure 7.8 shows the difference in the fluorescence curves between the cloud and crystal phases. Under conditions that are optimal for cooling and detection in the cloud phase, crystallisation will result in a decrease in fluorescence and a reduced SNR. Under conditions that are optimal for cooling and detection in the crystal phase, a phase change to the cloud (which may occur during the clock pulse, when the ions are not cooled) will also result in a decrease in fluorescence. Additionally, as discussed in the previous paragraph, the ions will be heated by the 369-nm laser. In both cases the fluorescence fluctuations from changing phases may also be misinterpreted by the servo and result in erroneous frequency corrections.

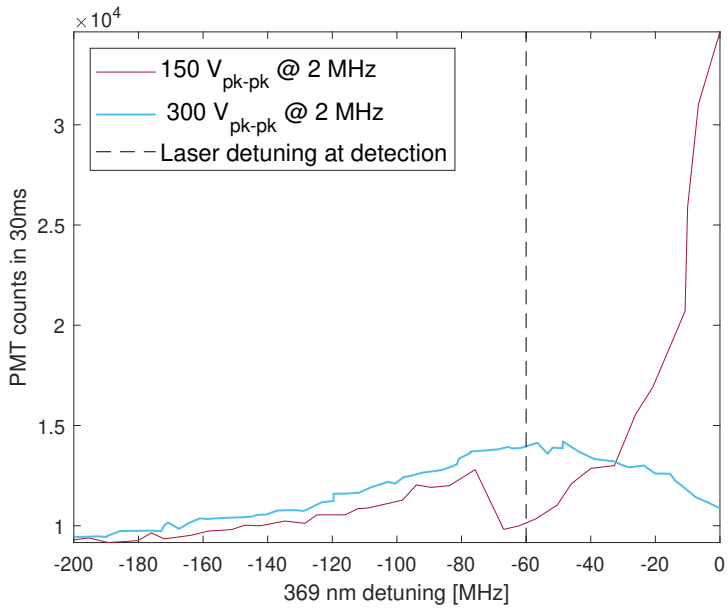


Figure 7.8: Laser cooling profiles that illustrate the hysteresis effect of forming a Coulomb crystal. The red and blue traces are traces 'a' and 'b' from figure 7.9. A larger trapping voltage prevents the blue trace from crystallising. Both traces are scanned from large to small detunings. The red trace starts by approximately following the blue; the retrace is not exact as the trapping voltages affect the laser-cooling. At -75 MHz the red trace changes phase from cloud to crystal and the profiles diverge. Heating the ion crystal so that a cloud reformed would cause the red trace to continue to approximately follow the blue. At the typical operating detuning of -60 MHz where the cloud phase fluorescence is maximised, the crystal phase fluorescence is significantly lower. At low detunings the crystal fluorescence is significantly higher than the cloud, and the ion cloud is heated rather than cooled by the 369-nm laser.

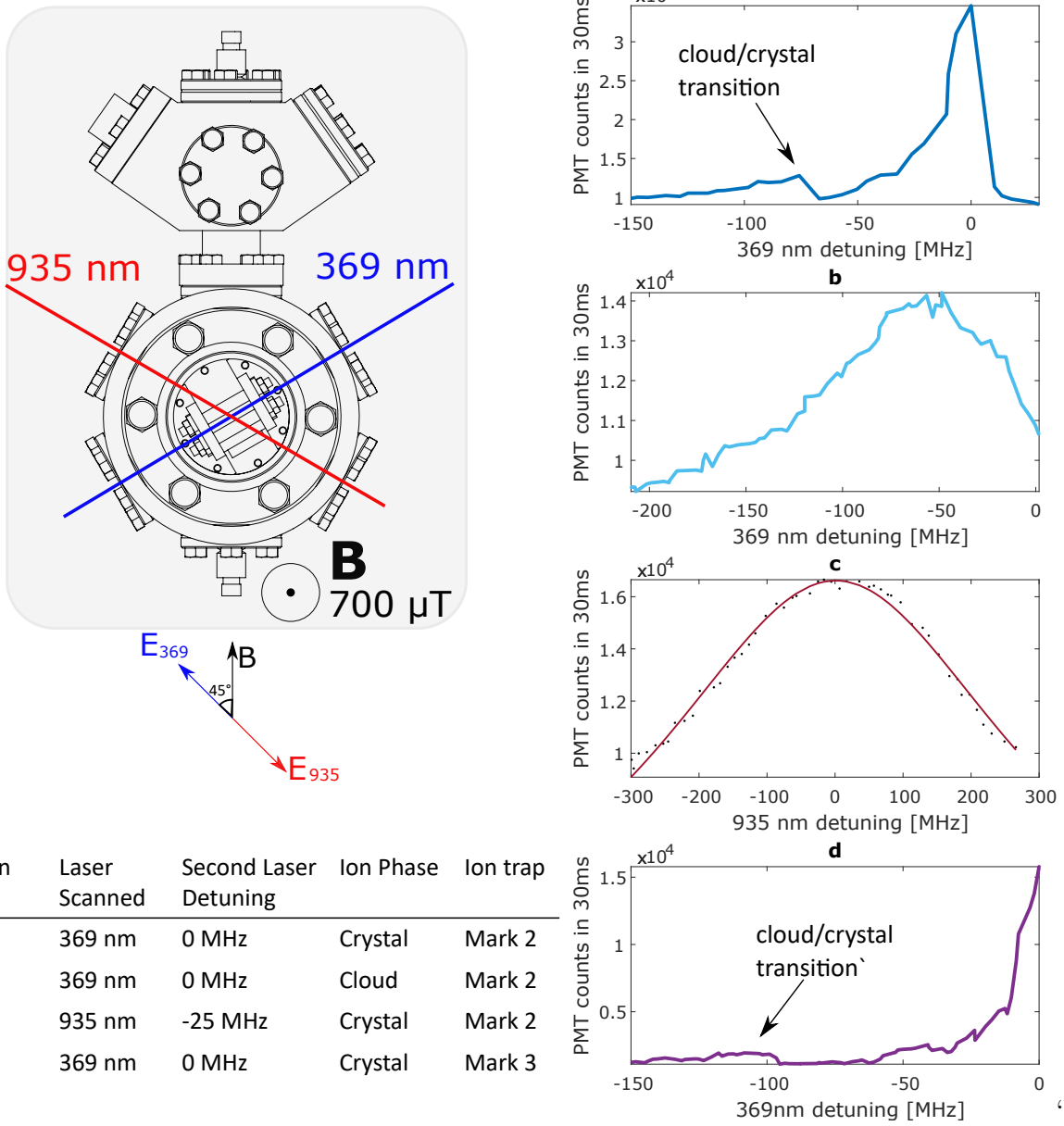
935 nm — D-state repump: The profile of the $^2D_{3/2}(F=1) \rightarrow {}^2D[3/2]_{3/2}(F'=0)$ transition is shown in scan c of figure 7.9. A fit of a Lorentzian with FWHM of 660 MHz implies that this transition is power broadened and driven at 25000 times above its saturation intensity. The ions were in the crystal state with the 369 nm detuning -25 MHz, implying only a small Doppler broadening of the order of 10 MHz.

7.3.2 State preparation

For state preparation, the high-power microwaves used to mix the ground state during cooling are turned off. The ions are then optically pumped into the F = 0 ground state, via a decay from the off-resonantly excited $^2P_{1/2}$, F = 1 state. This process was found to be quite rapid in our system, requiring only 20 photons on average to be scattered per ion. 30 ms of the cycle time was typically used for state preparation.

It was found that the fluorescence from the 369 nm laser does not entirely disappear when the microwaves are turned off for state preparation, instead falling to 10% of the value due to some off-resonant excitation. After this was observed in the portable microwave system, we checked if the same effect was seen in the NPL single-ion ytterbium optical clock. In the optical clock, under normal operation, a sideband is added to the cooling laser with an EOM. This drives the $F = 1 \rightarrow F' = 1$ component of the cooling transition to accelerate state preparation, and state preparation levels well in excess of 99% are achieved. When the EOM-sideband was removed from the single-ion ytterbium optical clock, they found that their single trapped ion also fluoresced roughly 10% of the time. This shows that the effect is not unique to our system, and also suggests a possible route to increasing state preparation. One of the few things in common between the optical and microwave ytterbium ion clocks at NPL is the 369 nm laser; both use Toptica DL100-PRO ECDLs with Nichia Corporation diodes. It seems likely that the effect that is driving the ions out of the ground state is caused by the lasers, possibly the ASE as mentioned in section 3.2.

As discussed in section 7.1.1.1, the incomplete state preparation of 90% results in the contrast in the readout signal falling to 80% of the fully state-prepared value.



Scan	Laser Scanned	Second Laser Detuning	Ion Phase	Ion trap
a	369 nm	0 MHz	Crystal	Mark 2
b	369 nm	0 MHz	Cloud	Mark 2
c	935 nm	-25 MHz	Crystal	Mark 2
d	369 nm	0 MHz	Crystal	Mark 3

Figure 7.9: Laser transition profiles for ions in crystal and cloud phases. The table summarises the conditions for each of the scans. Scans a and b are 369-nm laser scans from the mark 2 trap, and d is a 369-nm laser scan from the mark 3 trap. There is a factor of ten improvement in the background scatter rate and a narrower linewidth in the Mark 3. Scan c is a scan of the 935-nm laser.

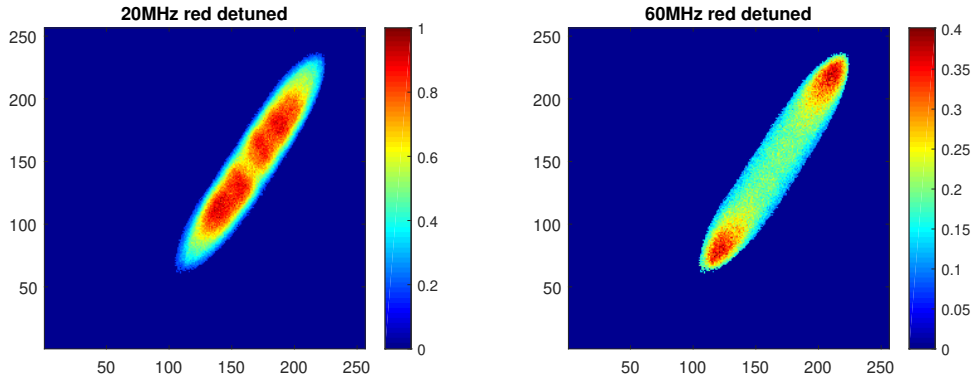


Figure 7.10: Spatial temperature variation in a Coulomb crystal. The cooling laser interacts strongest with different parts of the crystal depending on the detuning because of the distribution of velocities. The side length of the image is 820 μm and the colour scale is relative to the peak detected fluorescence rate, which was 8000 Hz per pixel.

7.3.3 Clock pulse

The clock pulse sequence is different for Rabi and Ramsey spectroscopy, and the procedures for both are outlined in this section.

Rabi: Due to the simpler hardware requirements, Rabi spectroscopy was mostly used in this work. A resonance from Rabi spectroscopy is shown in figure 7.2, and the stability of a lock to this Rabi resonance is shown in figure 7.4. Rabi spectroscopy requires a pulse of microwaves, at a stable power level, to coherently change the ions' state. The length of this pulse gives greatest frequency sensitivity at a given probe time if the product of the Rabi frequency and the probe time is equal to π. Rabi frequencies in the range of $(2\pi\times)$ $0.1 - 1$ Hz were typically used. This required a large amount of attenuation relative to the microwave power needed for cooling. The hardware implementation is discussed in section 5.1.1.2.

Ramsey: Ramsey spectroscopy requires two short microwaves pulses and a longer dark period between the pulses. The frequency sensitivity of this method scales primarily with the length of the dark time. To implement Ramsey spectroscopy in our system,

Rabi frequencies of approximately $(2\pi\times)$ 10 Hz are used for the $\pi/2$-pulses. During the dark period, microwave leakage must be kept to a minimum; this challenge is discussed in section 5.1.1.2. Two benefits of Ramsey spectroscopy are: firstly, that the stability can be up to 1.65 times better than from Rabi pulses of equal time; and secondly, that the width of the fringes can be changed just by adjusting the dark time. Implementing Ramsey spectroscopy is planned for future work.

Readout: Readout occurs on the same transition as is used for state-preparation. However, the state-preparation process that causes optical pumping to the F = 0 ground state limits the number of photons collected. To inhibit that process and also limit light scattered from the background, the intensity of the 369 nm laser is reduced during readout to below saturation intensity. Depending on the experimental conditions, we collect from a few hundred to a few thousand signal photons during a 100 ms detection on the PMT. Processes such as reflected light from the detection laser, and spurious signal from ions in the wrong state, contribute to a background level of light detected by the PMT. The background level is typically similar in size to the prominence of the signal. This is seen in figure 7.2, where the background level is 800 counts and the signal prominence is 600 counts.

7.4 Operating magnetic field

The dominant frequency shift for this clock was the second-order Zeeman shift (see section 2.4.3.2) with a magnitude of $\Delta\nu_{SOZ} = 3.108 \times 10^{10}\,\mathrm{Hz\,T^{-2}} = 31.08\,\mathrm{mHz}/(\mu\mathrm{T})^2$ [35]. This means that small fluctuations, $\delta\boldsymbol{B}$, on a background magnetic field, $\boldsymbol{B}$, result in a fractional shift of $\frac{\Delta\nu_{SOZ}}{\nu_{clock}} = 4.92 \times 10^{-12}\,[\mu T^{-2}]\,\boldsymbol{B}\cdot\boldsymbol{\delta B}$ to first order in $\boldsymbol{\delta B}$ (equation (2.61)).

A stable second-order Zeeman shift is not a problem, provided that it is measured and corrected; unstable and fluctuating magnetic fields provide a greater challenge. To mitigate this effect, the scalar product of the terms $\boldsymbol{B}$ and $\boldsymbol{\delta B}$ in equation (2.61) were minimised.

$\boldsymbol{B}$ was minimised by adjusting the currents in three orthogonal sets of Helmholtz coils to null the background magnetic field and provide a small and well-controlled bias. The magnetic field was minimised by scanning the current of the Helmholtz coils. The second order Zeeman shift is positive for the clock transition, so the magnetic field was minimised when the frequency of the clock transition was minimised. This procedure is shown in figure 7.11. It is not possible to perform Rabi spectroscopy in zero magnetic field as a quantisation direction must be defined.

In low magnetic fields, and in the presence of a magnetic field gradient, the $\Delta F = 1, \Delta m_F = \pm 1$ transitions are weakly driven when the trap secular frequencies overlap with the Larmor frequency [30]. An ion oscillating in a magnetic field gradient, in the rest frame of the ion, will experience an oscillating magnetic field. This will mix with the magnetic field of the microwaves and will result in adding power to sidebands of the microwave transition at the secular frequency. As the wavelength of the microwave radiation that drives the clock transition is large compared to the dimensions in which the ions are trapped, the magnetic field from the microwave radiation will also appear as a spatial gradient to the ions and result in sidebands to the carrier at the secular frequencies. This effect is described schematically in figure 7.12. The result of this effect is decrease in signal amplitude and a line-broadening from driving all of the transitions to the upper hyperfine state simultaneously. This is seen in the top right sub-figure of figure 7.11.

A bias field resulting in a shift of about 2 Hz, or fractionally 1.6×10^{-10}, was used to minimise the sensitivity to fluctuations to $\frac{\Delta\nu_{SOZ}}{\nu_{clock}} \simeq 4 \times 10^{-11}/\mu T$, whilst also maintaining a good resonance feature.

The $\boldsymbol{\delta B}$ term was minimised by operating the trap in a two-layer magnetic shield (see section 4.4), and by using low noise power supplies to drive the Helmholtz coils. The number of windings on the Helmholtz coils was also limited to reduce the magnetic field fluctuation from a given current fluctuation.

The scalar product of the two terms was further minimised by applying the bias field orthogonal to the direction of largest magnetic field noise. Measurements of the

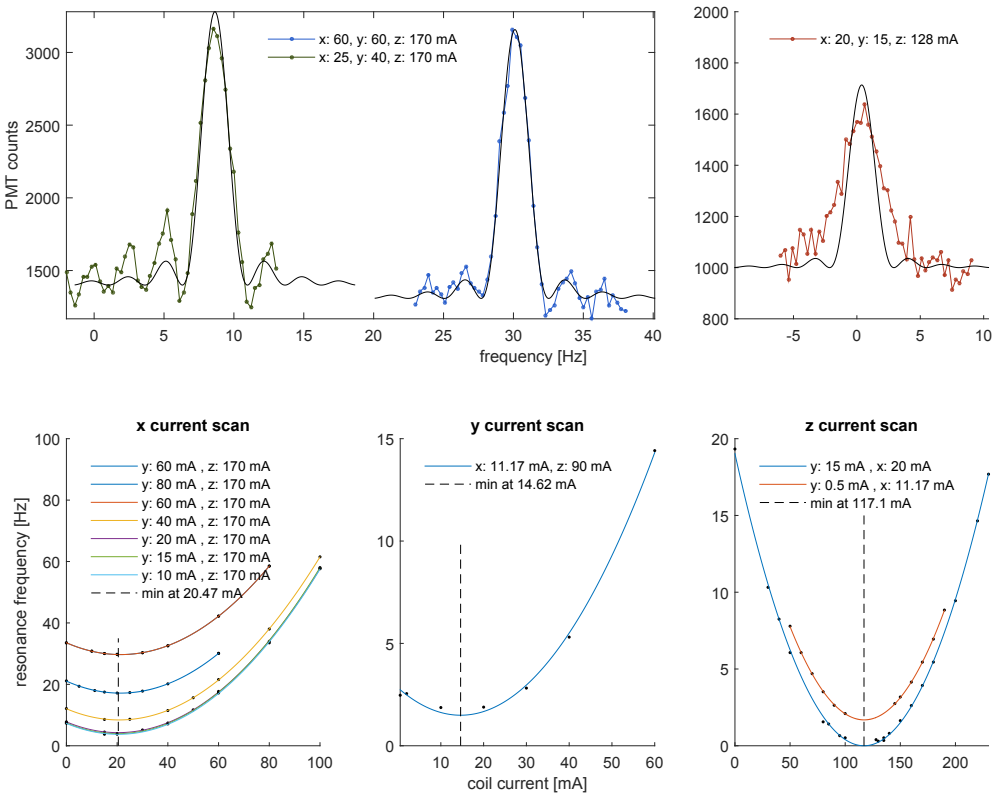


Figure 7.11: Minimising residual magnetic field. The x,y, and z coil directions are shown in figures 4.13 and 7.13. The upper row shows some resonances from the 400 ms microwave pulse and fits to the expected lineshape; the x-axis is frequency relative to the zero-field resonance, and the y-axis is PMT counts. In the upper-left figure, two Rabi resonances are shown. The resonance in a higher background magnetic field occurs at a higher frequency. The upper right figure shows a line-broadening effect seen at low magnetic fields. As a result, it was not possible to take data at the minima of the parabolas in the z current scan. The clock was typically operated with a second-order Zeeman shift of about 2 Hz. The lower row of the figure shows the procedure for minimising the magnetic field, the y-axis shows the resonance frequency relative to the zero-field resonance, and the x-axis shows the coil's current in mA. The coils were varied systematically until a minimum frequency was found, and then offset to obtain a good lineshape.

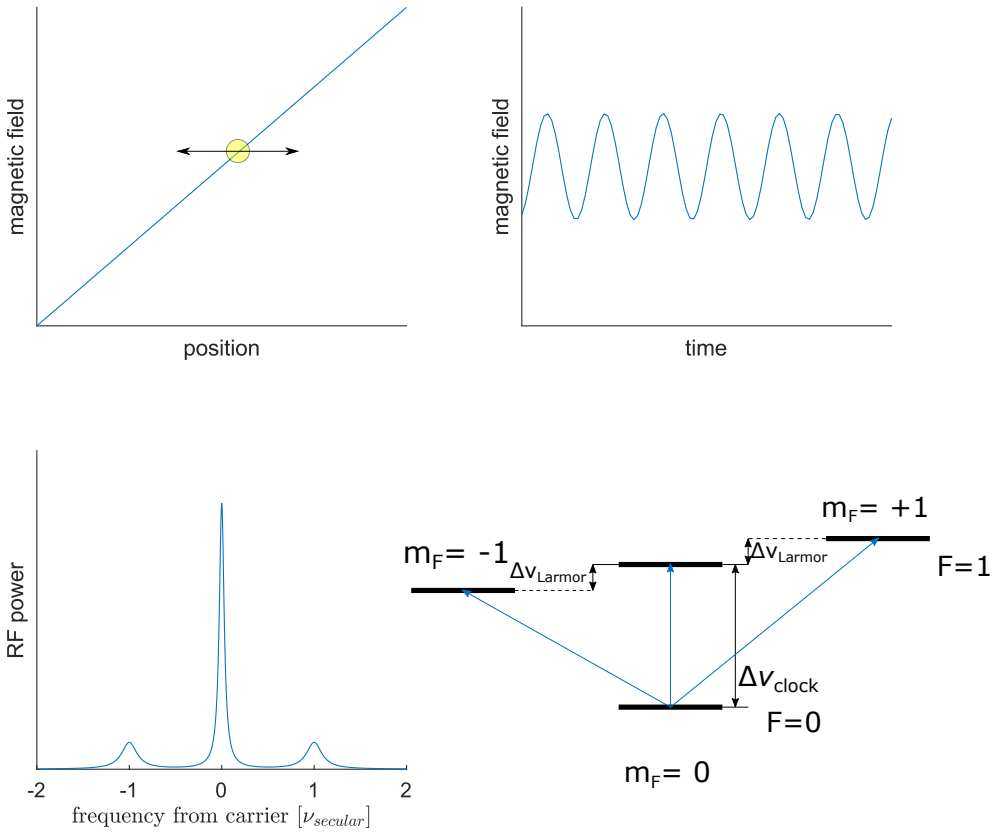


Figure 7.12: An ion oscillating in a magnetic field gradient, in its rest frame, experiences an oscillating magnetic field. This can be thought of as adding sidebands to the carrier of the clock frequency at $\pm\nu_{secular}$. This field may drive transitions to the $m_F \pm 1$ states of the F=1 hyperfine level if the Larmor frequency coincides with the secular frequency.

background magnetic field are shown in section 7.6.2.1.

A more sophisticated method of monitoring and correcting the second-order Zeeman shift is to periodically monitor the positions of the $\Delta F = 1, \Delta m_F = \pm 1$ transitions and use the formula: $\Delta\nu_{SOZ} = 310.8 \left(\frac{\Delta\nu_{Larmor}}{1.401\times10^6}\right)^2$. This is planned for future implementation.

7.5 Trap-related effects

An ideal ion trap would trap a large number of ions and still maintain a low heating rate. However, there is typically a trade-off between these two desirable qualities. Trapping more ions increases the stability by improving the SNR, but putting more ions in the trap tends to push ions away from the trap centre. When ions are displaced from the trap centre, they experience increased trap heating. Ion heating can add significant dead-time into the measurement cycle, and can also cause a second-order Doppler shift.

In our trap, there was a further undesirable effect, the formation of dark ions. The implications of ion heating and dark ion formation are discussed in the following sections.

7.5.1 Ion heating

As was discussed earlier in section 7.3.1, a large portion of the cycle time is devoted to cooling the ions. This impacts both the accuracy and the stability, and depending on the LO used may also cause Dick instability. The heating rate and the resulting time taken to cool the ions is clearly a limitation of the Mark 2 ion trap.

The formation of dark ions presents a challenge in keeping the temperature of the ions constant. As a larger fraction of the ions enters the dark state, the cooling rate decreases but the heating rate stays constant. For this reason, it is not possible to reliably operate the clock in the crystal phase, as its formation becomes unfavourable at higher dark ion fractions. Another implication of the dark ion fraction increasing over time is that the cooling time must be set longer, and the detuning set to larger than initially optimal, at the beginning of the measurement. These precautions ensure that by the end of the measurement similar temperatures are achieved to at the beginning, although there are

fewer ions participating in laser-cooling.

7.5.2 Ion loss

Ions can leave the ion trap in one of three ways. They can either gain enough kinetic energy to overcome the trapping potential (typically on the order of 1 eV). This could occur after the ion has collided with a background gas molecule, or by RF heating from the ion-trapping field. Alternatively, the ion could become deionised by a charge exchange reaction ($Yb^+ + X \rightarrow Yb + X^+$) with a background molecule, or the trap depth might also be lowered due to an electrical glitch. These loss mechanisms are countered in this work by operating in UHV, laser-cooling, and using a reliable oscillator and power supply. At the $< 10^{-10}$ mbar pressure that is reported by the ion pump during clock operation, the ion-neutral collision rate approximately is 15 /hr per ion [55, 114] and under these conditions ion lifetimes of over a month are reported [115]. As has been discussed in chapter 6, it appears that the rate of ion loss in the trap is small compared to the rate of dark ion formation.

7.6 Evaluation of sources of noise, frequency shifts and instability

In this section, the processes that affect the performance of the clock are evaluated. Table 7.2 on page 152 contains a summary of all these effects. The following subsections detail the methodology used to evaluate these effects. Section 2.4 contains more information about the systematic frequency shifts. Many of the formulae used to evaluate the shifts are also found in section 2.4.

The stability is limited by photon shot-noise, and the shot-noise is worsened by ion loss. The largest frequency shift is due to the second-order Zeeman at 2 Hz.

7.6.1 Shot-noise and dead-time

At the beginning of the measurement the shot-noise limit to the instability was estimated as $9 \times 10^{-13}/\sqrt{\tau}$. This was estimated from the lineshape shown in figure 7.2, using the formulae in section 7.1.1. The clock transition was probed for $\tau_p = 4\,\mathrm{s}$ and there was $\tau_d = 4\,\mathrm{s}$ of cooling time between measurements. The SNR was estimated as 16, and the quality factor of the resonance was 6.32×10^{10}. Signal loss, shown in figure 7.5, caused the SNR to decrease over time and so this instability was not achieved. The instability was measured over $2^1/_4\,\mathrm{hrs}$ and the instability was found to be $3.6 \pm 0.2 \times 10^{-12}/\sqrt{\tau}$ between averaging times of 30 s and 1500 s. Shot-noise was the dominant cause of this instability.

7.6.2 Second-order Zeeman

The second-order Zeeman effect causes a shift that is dependent on the ions' magnetic field environment. To evaluate the magnitude of the effect, I have separated the sources of magnetic field into those inside and those outside of the magnetic shield. This is because the ions will have differing sensitivities to these fields as a result of the magnetic shielding. The determination of the frequency shifts and instabilities from these two sources of second-order Zeeman are detailed in the following sections.

7.6.2.1 Second-order Zeeman — background magnetic field

The background magnetic field is first attenuated by the two-layer magnetic shields that enclose the vacuum system; it is then nulled by the coils. The shielding factor is dependent on the direction of the magnetic field. As a diagnostic tool, we used a CCD camera that was outside of the vacuum system. This required a hole in the magnetic shield and reduced the attenuation. The attenuation of the shields was measured by applying external fields and measuring the response of a fluxgate magnetometer at the position of the ions. The results are tabulated in table 7.1. The axes are shown in figure 7.13; the x-axis joins the two detection windows, the z-axis is vertically upwards,

	Shielding factor	
	no hole	hole
x	1190	40
y	560	20
z	2980	750
geometric mean	1260	84

Table 7.1: Magnetic field shielding factors. The definitions of the x, y, and z axes are shown in figure 7.13 and given in the text. The uncertainties of the tabulated shielding factors are estimated to be ±10%.

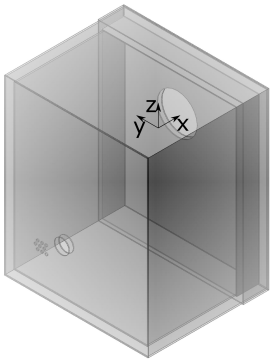


Figure 7.13: Magnetic shields with an imaging hole. This shows the coordinate system used in this section.

and the y-axis is perpendicular to both.

The magnetic field in the laboratory was also measured with a fluxgate magnetometer at a location a few centimetres away from the ion trap. The definitions of the axes are consistent with the shielding measurements. The fluctuations are shown in figure 7.14.

The second-order Zeeman shift depends on the magnitude of the magnetic field. As discussed in section 7.4, to first order, the fractional frequency sensitivity to fluctuations is $4.0 \pm 0.1 \times 10^{-11}\,/\mu\mathrm{T}$, under the applied $8\,\mu\mathrm{T}$ bias field that is along the x-axis. The bias field was orientated along the quietest axis of the laboratory's magnetic field. The sensitivity to external magnetic field fluctuations was reduced by enclosing the ion trap in mu-metal shields. The shielding along the x-axis is reduced by the imaging hole, but external magnetic fields are still attenuated by a factor of 40 ± 4. This reduces the ions' sensitivity to external fields to $1.0 \pm 0.1 \times 10^{-12}\,/\mu\mathrm{T}$.

For averaging periods below 10 s, the magnetic field noise is dominated by oscillations at 50 Hz that average as $1.4 \pm 0.1 \times 10^{-2}/\tau$. Between averaging periods of 10 and 100 seconds, the dominant magnetic field noise is white noise at $4.6 \pm 0.3 \times 10^{-3}/\sqrt{\tau}$. A

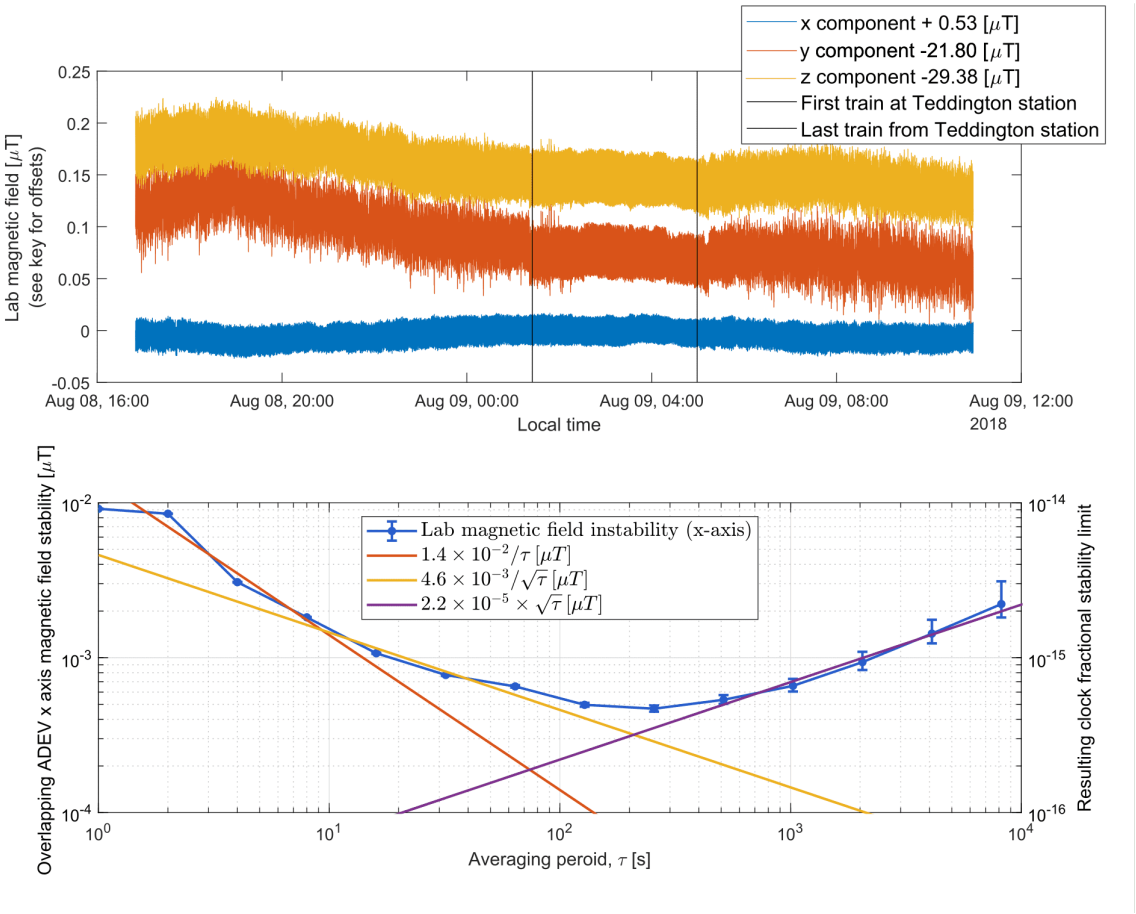


Figure 7.14: Magnetic field fluctuations in three axes as measured a few centimetres outside the magnetic shields. A DC offset has been removed from the three axes and these can be found in the key. The bias field is aligned with the quietest axis. The noisiest axis is the z-axis, which is vertical in the lab. The first and last train times from Teddington station are marked on the chart [116]. The magnetic field is significantly quieter overnight. The magnetic field caused by the electric current of the trains is mostly in the vertical direction. The instability of the field in the x-axis is shown in the lower plot. The left y-axis shows the instability in microtesla, and this is converted into a fractional frequency instability contribution that is shown on the right y-axis.

random walk in the magnetic field dominates for averaging periods beyond a few hundred seconds at $2.2 \pm 0.1 \times 10^{-5} \times \sqrt{\tau}$. This random-walk drift could be removed by actively stabilising the magnetic field using the bias coils.

7.6.2.2 Second-order-Zeeman — coils

The coils provide a stable bias field, resulting in a fractional frequency shift measured to be $1.6 \pm 0.1 \times 10^{-10}$. This corresponds to a bias field of around $8\,\mu$T. Two orthogonal pairs of coils null the residual magnetic field in their axes. The third pair of coils, orthogonal to the other pairs (orientated along the x-axis in figure 7.13), apply a field of about $14\,\mu$T to reduce the field in that axis to around $8\,\mu$T.

The current source that was used to supply the coils is discussed in section 5.1.6. Short-term fluctuations and longer-term drifts of the current in the coils may also cause the second-order Zeeman shift to be unstable. The magnitude of the effect can be evaluated by measuring the current noise passing through the coils. As the second-order Zeeman shift is proportional to the squared magnitude of the magnetic field, the fluctuations along the bias field direction will dominate its instability. A measurement of the second-order Zeeman instability arising from the coil current instability is shown in figure 7.15. The coil current was measured across a $20\,\Omega$ precision resistor on a Keithley 2000 voltmeter. The magnetic field was calculated from the current measurements. The second-order Zeeman shift was obtained from the magnetic field by multiplying the fractional frequency sensitivity of $4 \times 10^{-11}\,/\mu$T at the $8\,\mu$T bias. Instability in the current noise is measured as $4.00 \pm 0.50 \times 10^{-3}/\tau$ from 2 to 200 seconds, due to current oscillations; and $3.50 \pm 0.25 \times 10^{-4}/\sqrt{\tau}$ from 200 to 10,000 seconds due to white noise. These correspond to instability in the second-order Zeeman shift of $1.6 \pm 0.2 \times 10^{-13}/\tau$ and $1.4 \pm 0.1 \times 10^{-14}/\sqrt{\tau}$ over the stated timescales.

7.6.3 Second-order Doppler

The frequency shift due to the second-order Doppler effect is given by $\Delta\nu_{2OD} = -\frac{\nu}{2} \cdot \frac{u^2}{c^2}$, where ν is the center frequency of the resonance, u is the velocity of the ion and c is the

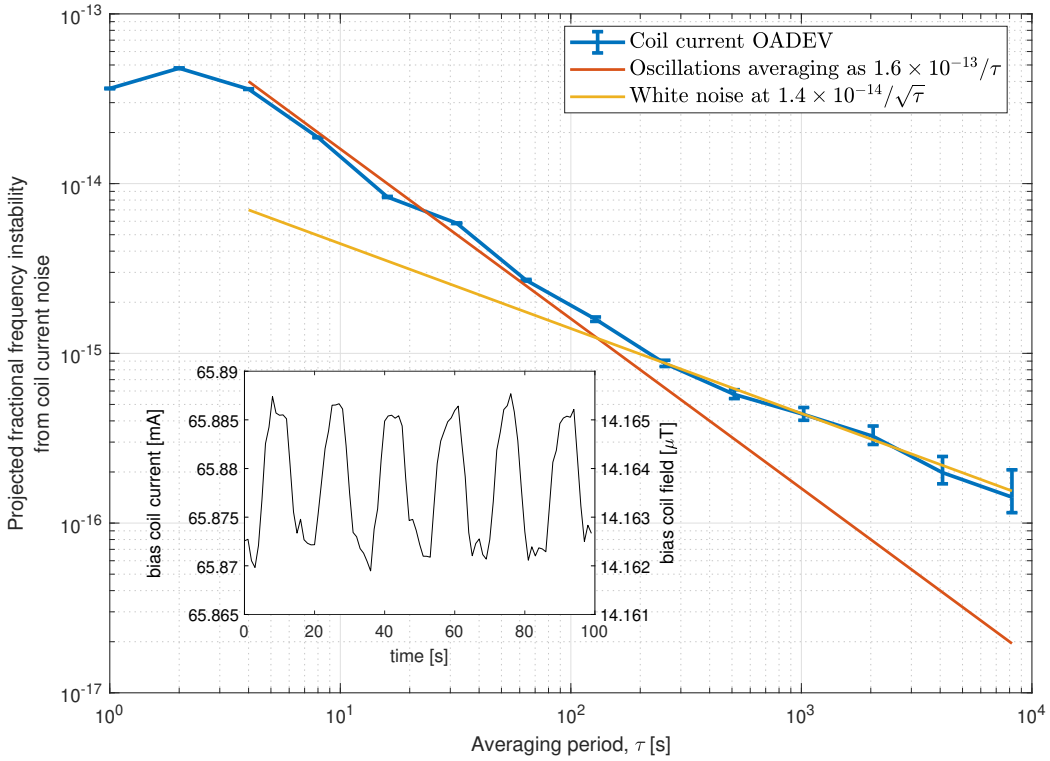


Figure 7.15: Measurement of coil current instability and the implied instability on the second-order Zeeman shift. The current instability is converted to a contribution towards the fractional frequency instability. First, the current is converted to magnetic field using the measured relationship for the coils: $0.215 \pm 0.005\,\mu\mathrm{T/mA}$. Secondly, the calculated magnetic field is multiplied by the fractional frequency sensitivity: $4 \times 10^{-11}\,/\mu\mathrm{T}$.

speed of light (see section 2.4.1.2).

A measurement of the ion velocities was made by observing the first-order Doppler shift broadening of the 369-nm laser-sweep double-resonance spectrum. The laser detuning was scanned from the red side of the resonance towards line centre both when the ions were continuously cooled and when the laser was extinguished for 4 s between measurements to simulate a clock measurement. These spectra are shown in figure 7.16.

It is evident that the spectrum taken after the 4 s dark time is similar to that of the large cloud in figure 7.9. However, the undamped micromotion has resulted in a more extreme distortion from the low-temperature limit of a power-broadened Lorentzian lineshape.

To calculate the second-order Doppler shift, the root mean square (rms) velocity was calculated by numerical integration of the velocity distributions implied from these scans over the cooling transition. The rms velocties were calculated to be 18 ± 2 m/s before the clock pulse, and 55 ± 10 m/s after. These calculated velocities are over-estimates as the method assumes that all the broadening of the transition is due to first-order Doppler shifts and because laser heating effects have suppressed the fluorescence of the ions at small detunings. Between measurements the laser is not returned to line-center and the effect of this incomplete recooling will also contribute to an over-estimate of the rms velocity. From these measurements the second-order Doppler shift was estimated to be below $-2.0 \pm 0.5 \times 10^{-14}$ and have an instability less than 5×10^{-15}.

7.6.4 Quadratic Stark shift

Although the ion cloud is not well described by a thermal velocity distribution, it is possible to extract a conservative estimate of the secular temperature of the ions from the width of the velocity distribution in figure 7.16 ($T < 200 \pm 100$ K), and to use equation (2.54), $\frac{\Delta\nu_{Quad\,Stark}}{\nu_{clock}} = -4k_s \left(\frac{\omega_{single}}{\omega_{cloud}}\right)^2 \frac{m\Omega_{trap}^2}{e^2} k_B T$, to estimate an upper limit of the size of the quadratic Stark shift (section 2.4.2). The trap drive was at 2 MHz, and the peak-to-peak voltage was 300 V. The ratio of the ion cloud secular frequency to the single-ion secular frequency was not found to be significantly different from unity, and

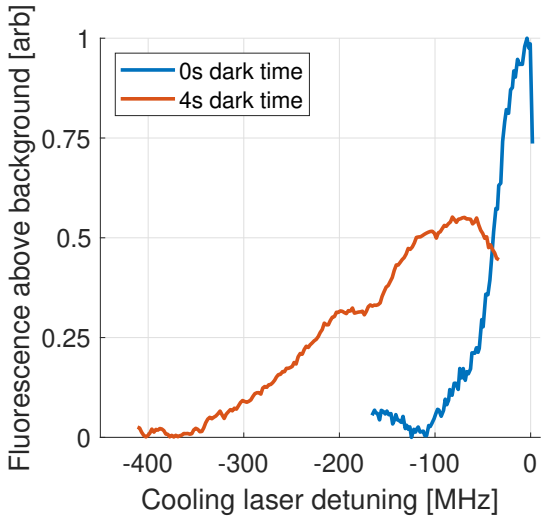


Figure 7.16: Temperature measurement of the ion cloud after a 4 s clock pulse. The trace in blue shows the fluorescence profile with no dark time . Each of the points on the orange trace is a measurement immediately after a 4 s period where the cooling laser was blocked. To avoid cooling the ions, the measurements were taken within 10 ms of the cooling laser becoming unblocked.

was measured as 1.0 ± 0.1. This resulted in an estimated fractional frequency quadratic Stark shift of $2 \pm 1 \times 10^{-15}$ with an instability below 1×10^{-15}.

7.6.5 Light shift (AC Stark shift)

The light shift is effectively eliminated by extinguishing the 369 nm beam using the two shutters (and the filter shutter) during the Rabi excitation. The sensitivity of the light shift from 369 nm light is $1.09 \times 10^{-11}/(\text{GHz} \cdot \text{nW})$ [70]. The light leakage of the 369-nm laser, which is detuned from resonance by ~ 100 MHz is measured to be below 1 pW. The resulting fractional frequency shift is therefore below 1×10^{-15} and the instability is estimated to be below 1×10^{-16}.

7.6.6 BBR shift (AC Stark shift)

There is an AC stark shift due to the thermal radiation produced by the ions' surroundings. This is detailed in section 2.4.2.1. An estimate of the fractional frequency shift due to BBR of $-1 \pm 0.1 \times 10^{-15}$ is obtained by assuming a 20 K range in temperature for the

ions' surroundings, ranging from 300 K to 320 K. A fractional frequency sensitivity to the temperature close to 310 K is calculated to be $-1 \times 10^{-17}\,/\mathrm{K}_{\mathrm{T}\approx 310\,\mathrm{K}}$. Assuming an unstable temperature at the 10 K level gives a conservative estimate of the fractional frequency instability of the BBR shift of $< 1 \times 10^{-16}$.

7.6.7 Dick effect

In the measurements reported in this chapter, the duty cycle — defined as the fraction of the measurement spent probing the clock-transition — was 1/2. Due to the ions not being continuously measured, some high-frequency noise on the oscillator will be aliased to lower frequencies and will add instability to each clock measurement. The instability added for a duty cycle of 1/2 was calculated by Dick [109] as 1.4 times below the local oscillator instability at the measurement time. As we used an LO with stability better than the shot-noise from the ions at the measurement time (figure 5.2), we are not limited by the Dick effect. Currently, our system has a large dead-time due to the laser-cooling, as set out in section 7.3.1. This may need to be improved to allow the use of an inexpensive LO for a commercial system.

7.6.8 Gravitational redshift

The gravitational redshift has a magnitude of 1.1×10^{-16}/m at sea level [76]. The laboratory where the frequency standard was evaluated is one floor above the caesium fountain that references the hydrogen maser. This results in a fractional frequency shift of $\sim 5 \times 10^{-16}$. As the clock is not moving, 1 cm of height stability is assumed. The resulting gravitational redshift fractional instability is $< 1 \times 10^{-18}$.

7.7 Frequency standard operation conclusions

In this chapter, the factors that influence the output of the frequency standard have been detailed. A careful analysis of the sources of frequency shifts and instabilities was undertaken and the results are summarised in table 7.2.

The fractional frequency uncertainty in the clock transition for the data presented is 8×10^{-12}, due to uncertainty in the magnitude of the magnetic field. However, the focus of this project was on stability, with less time spent on absolute frequency uncertainty. With further work, significant improvements in the absolute frequency uncertainty would be achieved.

The frequency standard achieved an instability of $3.6 \times 10^{-12}/\sqrt{\tau}$ for averaging times between 30 s and 1500 s, limited by ion loss. This stability exceeds the (laboratory-based) performance of many rival portable systems and is competitive with laboratory-based ytterbium ion microwave clocks (see table 1.2). As the ion-loss mechanism appears to be unique to our Mark 2 trap system and not reported by other groups, it seems very likely that the stability can be improved in a future system.

Effect	Parameter values	Fractional frequency: Sensitivity	Offset	Instability
Shot-noise and dead-time[a]	~650 initial signal and ~750 background photons, duty cycle 1/2, signal loss with half-life 1.2 hrs	—	—	$3.6\pm0.2\times10^{-12}/\sqrt{\tau}$ $30<\tau<1500$ s
Frequency chain[b]	described in sec. 5.1.1	—	—	$\approx 4\times10^{-13}\tau^{-0.8}$ $10^{-1}<\tau<10^{4}$ s
Second-order Zeeman: coils[c]	$B_{bias}=8.0\pm0.2\,\mu$T δB_{bias} from fig. 7.15	$4.0\pm0.1\times10^{-11}/\mu$T	$1.60\pm0.08\times10^{-10}$[d]	$<1\times10^{-13}$ $1<\tau<10^{2}$ s, $1.4\pm0.1\times10^{-14}/\sqrt{\tau}$ $10^{2}<\tau<10^{4}$ s
Second-order Zeeman: background[e]	$B_{lab}\approx 50\,\mu$T δB_{lab} from fig. 7.14	$1.0\pm0.1\times10^{-12}/\mu$T	nulled by coils	$<1\times10^{-14}$ $1<\tau<10^{4}$ s
Second-order Doppler	$v_{rms}\approx 18$ m/s $\rightarrow 55$ m/s from fig. 7.16	$-5.6\times10^{-18}/v_{rms}^2$	$-2.0\pm0.5\times10^{-14}$	$<5\times10^{-15}$
Quadratic Stark shift: trap drive[f]	$\Omega=2$ MHz, $V_{pk-pk}=300$ V	$<1\times10^{-16}\,V_{pp}$	$2\pm1\times10^{-15}$	$<1\times10^{-15}$
Light shift[g]	light extinguished to at most 1 pW of 369 nm, $\Delta_{369}\sim100$ MHz	$1.09\times10^{-11}/$(GHz nW)	$<1\times10^{-15}$	$<1\times10^{-16}$
Black-body shift[h]	$300\le T_{\rm trap}\le 320$ K	$-1\times10^{-17}/K_{T\approx310\,K}$	$-1\pm0.1\times10^{-15}$	$<1\times10^{-16}$
Dick effect[i]	duty cycle 1/2, LO stability: figure 5.2, Feedback at 30 s	—	—	$\sim1\times10^{-13}/\sqrt{\tau}$
Gravitational redshift[j]	Yb^+ frequency standard 5.0 ± 0.1 m above Cs fountain	$1.1\times10^{-16}/m_{\rm sea\,level}$	$\sim5\times10^{-16}$	$<1\times10^{-18}$
Total			$1.60\pm0.08\times10^{-10}$	$3.6\pm0.2\times10^{-12}/\sqrt{\tau}$ $30<\tau<1500$ s

Table 7.2: Sources of noise, frequency uncertainty and frequency offsets.

[a] Signal decaying during measurement, as seen in figure 7.5.

[b] Measurement in figure 5.3

[c] Assuming orientation in Earth's field is fixed. Not actively stabilised. Sensitivity from [35] with uncertainty from bias field.

[d] This uncertainty is due to the method used to measure the second-order Zeeman shift during this stability measurement. For a full-accuracy implementation of our clock, we would monitor this shift using the $F=1, m_F=\pm1$ magnetically sensitive Zeeman components of the clock transition and this uncertainty could be reduced to below 1×10^{-14}.

[e] External fields are attenuated by a factor of 40 in quantisation direction. The frequency offset is nulled by the coils when the orientation of the clock relative to the Earth's field is fixed. Sensitivity from [35].

[f] Trapping voltage is stable to within 10 V at all timescales. Sensitivity from [83].

[g] Two shutters extinguish 369 nm. In addition the neutral density filter, used to attenuate the laser for detection, also adds to the extinction. Sensitivity from [70].

[h] Sensitivities from: [84], and [85].

[i] Sensitivity for Rabi excitation and duty cycle 1/2 from [109].

[j] Relative to Cs-steered hydrogen maser. Stability assuming relative height stability of 1 cm. Sensitivity from [76].

Chapter 8

Outlook and Conclusions

This thesis has detailed the development of a portable microwave atomic clock based on laser-cooled ytterbium ions.

For the physics package, a small vacuum chamber, ion trap, imaging system and laser optomechanics were developed. In addition to this, a versatile platform of supporting electronics were developed for experiment control. Many of the technologies are relevant to other portable atomic clocks. This includes a novel locking scheme, which by providing frequency-correction feedback digitally, should allow higher performance from lower-cost oscillators. The laser system and its required electronics were packaged very compactly into a small section of the rack unit.

The stability of this clock was characterised and found to be $3.6 \pm 0.2 \times 10^{-12}/\sqrt{\tau}$ from 30 to 1500 s, limited by ion loss. A thorough analysis of the effects that influence the stability and accuracy of the clock was undertaken. It was found that photon-arrival shot-noise limited the stability. Formation of dark ions made the shot-noise worse. This added instability and limited the length of time for which the clock could remain locked. It seems likely that the ion loss was due to a heat-sinking effect in the atom source, which caused the vacuum to degrade when the oven was fired. A new design has been tested and found to be a significant improvement. The oven requires a factor of sixteen less power when loading the ion trap, and the vacuum level after loading is much better. Preliminary measurements of the new physics package also show that it offers lower

trap-heating and a better signal to noise ratio when detecting fluorescence.

The limitation caused by ion loss and the formation of dark ions led to some research into candidates for the dark ions. It was established, by analysing CCD images, that the dark ions were molecular ions. The molecular ions were observed to accumulate at the axial edges of the linear trap. This may provide a means for ejecting the dark ions by briefly dropping the endcap voltage.

Although dark ions limited the performance of our system, they are not intrinsic to laser-cooled ytterbium systems. Dark ions did not appear in significant numbers in our testbed trap, which was constructed in the first year of my DPhil, and are not widely reported to be a limitation of ytterbium ion optical clocks. They therefore should not be considered a major obstacle in further developing this technology.

Interest in the ytterbium F-state lead us to develop a novel method of stabilising the repump laser. This method uses an air-absorption line from molecular oxygen that is coincident with an F-state clear-out transition. Another air-absorption line, from water vapour, was found to appear close to the 935 nm D-state clear-out transition. This absorption can also be used as an optical frequency reference for tuning the lasers.

The outlook for this work is very promising. Although we were not able to demonstrate the full potential of the performance from this system, the performance that we have demonstrated is encouraging. When the clock is locked, the stability is better than the industry-standard 5071A and the system is very competitive with other portable atomic clocks being developed. Several early shortcomings in performance — including the number of ions stored, their heating rate, dark ion formation, and inability to reload the ion trap during operation — have been addressed in new designs. The first two issues relate to the ion trap geometry and the second two to the oven design.

Significant engineering challenges still stand in the way of this next-generation portable clock technology being commercialised. Although we developed the system in a 6U rack case, there is significant empty space, and the footprint of the device would fall dramatically with further development. The key enabling technology that requires the most development is a high-quality compact 369 nm laser source. The other lasers, and a

wavelength stabilisation method, also require further engineering. Solving the remaining engineering challenges would allow this system to become a very high-performance portable timekeeping device, independent from GNSS. Availability of such a device would enable large performance increases in telecommunications and navigation, and remove vulnerability to GNSS outages. My thesis is a significant contribution towards this goal.

References

[1] Rupert Thomas Gould. *The Marine Chronometer: Its History and Development*. J. D. Potter [1923].

[2] L. Essen and J. V. L. Parry. *An Atomic Standard of Frequency and Time Interval: A Cæsium Resonator*. Nature [1955]. **176(4476)**:280–282. doi:http://dx.doi.org/10.1038/176280a0.

[3] *SI, International System of Units (SI brochure)*. Technical report, BIPM [2006]. URL https://www.bipm.org/utils/common/pdf/si{_}brochure{_}8.pdf.

[4] D.W. Allan. *Statistics of atomic frequency standards*. Proceedings of the IEEE [1966]. **54(2)**. ISSN 0018-9219. doi:10.1109/PROC.1966.4634.

[5] W J Riley. *Handbook of Frequency Stability Analysis*, volume 31 [1994]. ISBN 3019753058. doi:10.1016/0148-9062(94)92706-5.

[6] J Levine. *Introduction to time and frequency metrology*. Review of Scientific Instruments [1999]. **70(6)**:2567–2596. ISSN 00346748. doi:10.1063/1.1149844.

[7] Erling Riis and Alastair G. Sinclair. *Optimum measurement strategies for trapped ion optical frequency standards*. Journal of Physics B: Atomic, Molecular and Optical Physics [2004]. **37(24)**:4719–4732. ISSN 09534075. doi:10.1088/0953-4075/37/24/001.

[8] Ekkehard Peik, Tobias Schneider, and Christian Tamm. *Laser frequency stabilization to a single ion*. Journal of Physics B: Atomic, Molecular and Optical Physics [2006]. **39(1)**:145–158. ISSN 09534075. doi:10.1088/0953-4075/39/1/012. 0511168.

[9] Fritz Riehle. *Frequency Standards: Basics and Applications*. Wiley-VCH [2005]. ISBN 9783527605996. doi:10.1002/3527605991.

[10] Microsemi Coporation. *Data Sheet: 5071A Primary Frequency Standard* [2014]. URL http://www.microsemi.com/document-portal/doc{_}view/133269-5071a.

[11] Eric Burt. *Introduction to Microwave Atomic Clocks*. In *EFTF-IFCS* [2017] .

[12] Leonard S Cutler. *Fifty years of commercial caesium clocks*. Metrologia [2005]. **42(3)**:S90–S99. ISSN 0026-1394. doi:10.1088/0026-1394/42/3/S10. URL http://stacks.iop.org/0026-1394/42/i=3/a=S10.

[13] Thomas P Heavner, Elizabeth A Donley, Filippo Levi, Giovanni Costanzo, Thomas E Parker, Jon H Shirley, Neil Ashby, Stephan Barlow, and S R Jefferts. *First accuracy evaluation of NIST-F2*. Metrologia [2014]. **51(3)**:174. ISSN 0026-1394. doi:10.1088/0026-1394/51/3/174. URL http://stacks.iop.org/0026-1394/51/i=3/a=174.

[14] Jocelyne Guena, Michel Abgrall, Daniele Rovera, Philippe Laurent, Baptiste Chupin, Michel Lours, Giorgio Santarelli, Peter Rosenbusch, Michael E. Tobar, Ruoxin Li, Kurt Gibble, Andre Clairon, and Sebastien Bize. *Progress in atomic fountains at LNE-SYRTE*. IEEE Transactions on Ultrasonics, Ferroelectrics, and Frequency Control [2012]. **59(3)**:391–410. ISSN 08853010. doi:10.1109/TUFFC.2012.2208. 1204.3621.

[15] Scott Beattie, Bin Jian, A. John Alcock, Marina Gertsvolf, Rich Hendricks, Krzysztof Szymaniec, and Kurt Gibble. *Preliminary Evaluation of NRC-FCs2 Fountain Clock at the National Research Council Canada*. In *2018 IFCS Proceedings*. IEEE [2018] pages 176–177.

[16] Microsemi Corporation. *Data Sheet: MHM 2010 Maser* [2010]. URL https://www.microsemi.com/document-portal/doc_download/133261-mhm-2010-datasheet.

[17] F. Droz, P. Mosset, Q. Wang, P. Rochat, M. Belloni, M. Gioia, A. Resti, and P. Waller. *Space passive hydrogen maser - performances and lifetime data-*. In *2009 IEEE International Frequency Control Symposium Joint with the 22nd European Frequency and Time forum*. ISSN 2327-1914 [2009] pages 393–398. doi:10.1109/FREQ.2009.5168208.

[18] Microsemi Corporation. *Quantum SA.45s CSAC datasheet* [2017]. URL https://www.microsemi.com/document-portal/doc_download/133305-sa-45s-csac-datasheet.

[19] μquans. *A high-performance frequency standard based on cold atoms* [2017]. URL http://www.muquans.com/index.php/products/mclock.

[20] R Lutwak, D Emmons, W Riley, and R M Garvey. *The Chip-Scale Atomic Clock â Coherent Population Trapping Conventional Interrogation*. 34th Annual Precise Time and Time Interval (PTTI) Meeting [2002]. pages 539–550.

[21] C. Chou, D. Hume, J. Koelemeij, D. Wineland, and T. Rosenband. *Frequency Comparison of Two High-Accuracy Al + Optical Clocks*. Physical Review Letters [2010]. **104(7)**:070802. ISSN 0031-9007. doi:10.1103/PhysRevLett.104.070802. URL http://link.aps.org/doi/10.1103/PhysRevLett.104.070802.

[22] R. M. Godun, P. B. R. Nisbet-Jones, J. M. Jones, S. A. King, L. A. M. Johnson, H. S. Margolis, K. Szymaniec, S. N. Lea, K. Bongs, and P. Gill. *Frequency Ratio of Two Optical Clock Transitions in $^{171}Yb^{+}$ and constraints on the time variation of fundamental constants*. Physical Review Letters [2014]. **113(21)**:1–5.

[23] D. J Berkeland, J. D Miller, J. C Bergquist, W. M Itano, and D. J Wineland. *Laser-Cooled Mercury Ion Frequency Standard*. Physical Review Letters [1998]. **80(1523)**:2089–2092. ISSN 0031-9007. doi:10.1103/PhysRevLett.80.2089. URL http://cat.inist.fr/?aModele=afficheN{&}cpsidt=9472651{%}5Cnhttp://cat.inist.fr/?aModele=afficheN{&}cpsidt=13689932.

[24] Piyaphat Phoonthong, Michiaki Mizuno, Kohta Kido, and Nobuyasu Shiga. *Determination of the absolute microwave frequency of laser-cooled* $^{171}Yb^{+}$. Applied Physics B [2014]. **117(2)**:673–680. ISSN 0946-2171. doi:10.1007/s00340-014-5882-2. URL http://link.springer.com/10.1007/s00340-014-5882-2.

[25] Y.-Y. Jau, H. Partner, P. D. D. Schwindt, J. D. Prestage, J. R. Kellogg, and N. Yu. *Low-power, miniature 171Yb ion clock using an ultra-small vacuum package*. Applied Physics Letters [2012]. **101(25)**:253518.

[26] P. T H Fisk, M. A. Lawn, and C. Coles. *Laser cooling of* $^{171}Yb^{+}$ *ions in a linear paul trap*. Applied Physics B Photophysics and Laser Chemistry [1993]. **57(4)**:287–291. ISSN 07217269. doi:10.1007/BF00325208.

[27] R.B Warrington, P.T.H Fisk, M.J Wouters, M.A Lawn, and C. Coles. *The CSIRO trapped* $^{171}Yb^{+}$ *ion clock: improved accuracy through laser-cooled operation*. Frequency and Time Forum, 1999 and the IEEE International Frequency Control Symposium, 1999., Proceedings of the 1999 Joint Meeting of the European [1999]. **1**:125–128. ISSN 1075-6787. doi:10.1109/FREQ.1999.840724. URL http://ieeexplore.ieee.org/xpls/abs{_}all.jsp?arnumber=840724.

[28] R.B. Warrington, P.T.H. Fisk, M.J. Wouters, and M.A. Lawn. *Temperature of laser-cooled* $^{171}Yb^{+}$ *ions and application to a microwave frequency standard*. IEEE Transactions on Ultrasonics, Ferroelectrics and Frequency Control [2002]. **49(8)**:1166–1174. ISSN 0885-3010. doi:10.1109/TUFFC.2002.1026029.

[29] S. J. Park, P. J. Manson, M. J. Wouters, R. B. Warrington, M. A. Lawn, and P. T. H. Fisk. $^{171}Yb^{+}$ *Microwave Frequency Standard*. 2007 IEEE International Frequency Control Symposium Joint with the 21st European Frequency and Time Forum [2007]. pages 613–616. ISSN 1075-6787. doi:10.1109/FREQ.2007.4319145. URL http://ieeexplore.ieee.org/lpdocs/epic03/wrapper.htm?arnumber=4319145.

[30] Heather L Partner. *Development and Characterization of a* $^{171}Yb^{+}$ *Miniature Ion Trap Frequency Standard*. Ph.D. thesis, University of New Mexico, Albuquerque [2013]. arXiv:1208.5622v1.

[31] Robert L. Tjoelker, John D. Prestage, Eric A. Burt, Pin Chen, Yong J. Chong, Sang K. Chung, William Diener, Todd Ely, Daphna G. Enzer, Hadi Mojaradi, Clay Okino, Mike Pauken, David Robison, Bradford L. Swenson, Blake Tucker, and Rabi Wang. *Mercury ion clock for a NASA technology demonstration mission*. IEEE Transactions on Ultrasonics, Ferroelectrics, and Frequency Control [2016]. **63(7)**:1034–1043. ISSN 08853010. doi:10.1109/TUFFC.2016.2543738.

[32] NASA. *Technology Readiness Level Definitions* [2012]. page 1. URL https://www.nasa.gov/pdf/458490main{_}TRL{_}Definitions.pdf{%}0Ahttps://www.nasa.gov/directorates/heo/scan/engineering/technology/txt{_}accordion1.html.

[33] John C Mankins. *Technology Readiness Levels: A White Paper*. Technical Report December, NASA, Office of Space Access and Technology, Advanced Concepts Office. [2004].

[34] C.J. Foot. *Atomic Physics*. OUP Oxford [2005]. ISBN 0191037079.

[35] Jacques. Vanier and Claude. Audoin. *The quantum physics of atomic frequency standards*. Hilger, Bristol [1989]. ISBN 9780852744321.

[36] James Camparo. *The rubidium atomic clock and basic research*. Physics Today [2007]. **60(11)**:33–39. ISSN 0031-9228. doi:10.1063/1.2812121. URL http://physicstoday.scitation.org/doi/10.1063/1.2812121.

[37] J. D. Prestage, G. J. Dick, and L. Maleki. *New ion trap for frequency standard applications*. Journal of Applied Physics [1989]. **66(3)**:1013–1017. ISSN 00218979. doi:10.1063/1.343486.

[38] M. Brownnutt, M. Kumph, P. Rabl, and R. Blatt. *Ion-trap measurements of electric-field noise near surfaces*. Rev. Mod. Phys. [2015]. **87**:1419–1482. doi:10.1103/RevModPhys.87.1419. URL https://link.aps.org/doi/10.1103/RevModPhys.87.1419.

[39] M. Drewsen and A. Brøner. *Harmonic linear paul trap: Stability diagram and effective potentials*. Phys. Rev. A [2000]. **62**:045401. doi:10.1103/PhysRevA.62.045401. URL https://link.aps.org/doi/10.1103/PhysRevA.62.045401.

[40] Sarah R Woodrow. *Linear Paul trap design for high-fidelity, scalable quantum information processing*. Master's thesis, University of Oxford [2015].

[41] A. Drakoudis, M. Söllner, and G. Werth. *Instabilities of ion motion in a linear Paul trap*. International Journal of Mass Spectrometry [2006]. **252(1)**:61–68. ISSN 13873806. doi:10.1016/j.ijms.2006.02.006. URL http://linkinghub.elsevier.com/retrieve/pii/S1387380606001047.

[42] Wolfgang Paul. *Electromagnetic Traps for Charged and Neutral Particles(Nobel Lecture)*. Angewandte Chemie International Edition in English [1990]. **29(7)**:739–748. ISSN 0570-0833. doi:10.1002/anie.199007391.

[43] J. Pedregosa, C. Champenois, M. Houssin, and M. Knoop. *Anharmonic contributions in real RF linear quadrupole traps*. International Journal of Mass Spectrometry [2010]. **290(2-3)**:100–105. ISSN 13873806. doi:10.1016/j.ijms.2009.12.009. 1001.1403.

[44] D R Denison. *Operating Parameters of a Quadrupole in a Grounded Cylindrical Housing*. Journal of Vacuum Science and Technology [1971]. **8(1)**:266–269. doi: 10.1116/1.1316304. URL https://doi.org/10.1116/1.1316304.

[45] H.G. Dehmelt. *Radiofrequency Spectroscopy of Stored Ions I: Storage*. volume 3 of *Advances in Atomic and Molecular Physics*, pages 53 – 72. Academic Press [1968]. doi:https://doi.org/10.1016/S0065-2199(08)60170-0. URL http://www.sciencedirect.com/science/article/pii/S0065219908601700.

[46] D J Berkeland, J D Miller, J C Bergquist, Wayne M Itano, and D J Wineland. *Minimization of ion micromotion in a Paul trap*. Journal of Applied Physics [1998]. **83(10)**:5025–5033. 1211.0101.

[47] R. Blümel, J. M. Chen, E. Peik, W. Quint, W. Schleich, Y. R. Shen, and H. Walther. *Phase transitions of stored laser-cooled ions*. Nature [1988]. **334(6180)**:309–313. ISSN 0028-0836. doi:10.1038/334309a0. URL http://www.nature.com/nature/journal/v334/n6180/pdf/334309a0.pdf.

[48] L. Hornekær and M. Drewsen. *Formation process of large ion Coulomb crystals in linear Paul traps*. Physical Review A - Atomic, Molecular, and Optical Physics [2002]. **66(1)**:134121–1341212. ISSN 10502947. doi:10.1103/PhysRevA.66.013412.

[49] Jean Pierre Hansen. *Statistical mechanics of dense ionized matter. i. equilibrium properties of the classical one-component plasma*. Phys. Rev. A [1973]. **8**:3096–3109. doi:10.1103/PhysRevA.8.3096. URL https://link.aps.org/doi/10.1103/PhysRevA.8.3096.

[50] Daniel H E Dubin. *Theory of structural phase transitions in a trapped Coulomb crystal*. Physical Review Letters [1993]. **71(17)**:2753–2756. ISSN 00319007. doi: 10.1103/PhysRevLett.71.2753.

[51] R. G. DeVoe, J. Hoffnagle, and R. G. Brewer. *Role of laser damping in trapped ion crystals*. Phys. Rev. A [1989]. **39**:4362–4365. doi:10.1103/PhysRevA.39.4362. URL https://link.aps.org/doi/10.1103/PhysRevA.39.4362.

[52] F. Diedrich, E. Peik, J. M. Chen, W. Quint, and H. Walther. *Observation of a phase transition of stored laser-cooled ions*. Phys. Rev. Lett. [1987]. **59**:2931–2934. doi:10.1103/PhysRevLett.59.2931. URL https://link.aps.org/doi/10.1103/PhysRevLett.59.2931.

[53] John Emsley. *Nature's building blocks : an A-Z guide to the elements*. Oxford University Press, Oxford [2001]. ISBN 9780198503415.

[54] John R. de Laeter, John Karl Böhlke, P. De Bièvre, H. Hidaka, H. S. Peiser, K. J. R. Rosman, and P. D. P. Taylor. *Atomic weights of the elements. Review 2000 (IUPAC Technical Report)*. Pure and Applied Chemistry [2003]. **75(6)**:683–800. ISSN 1365-3075. doi:10.1351/pac200375060683. URL https://www.degruyter.com/view/j/pac.2003.75.issue-6/pac200375060683/pac200375060683.xml.

[55] Charles Baynham. *Frequency metrology at the* 10^{-18} *level with an ytterbium ion optical clock*. Ph.D. thesis, University of Oxford [2018].

[56] N. Huntemann, M. Okhapkin, B. Lipphardt, S. Weyers, Chr. Tamm, and E. Peik. *High-Accuracy Optical Clock Based on the Octupole Transition in* $^{171}Yb^{+}$. Physical Review Letters [2012]. **108(9)**:090801. ISSN 0031-9007. doi:10.1103/PhysRevLett.108.090801. URL http://link.aps.org/doi/10.1103/PhysRevLett.108.090801.

[57] B C Fawcett and M Wilson. *Computed oscillator strengths Lande g values and lifetimes in YbII*. At. Data Nucl. Data Tables [1991]. **47(2)**:241–317.

[58] M. Roberts, P. Taylor, G. P. Barwood, P. Gill, H. A. Klein, and W. R. C. Rowley. *Observation of an electric octupole transition in a single ion*. Physical Review Letters [1997]. **78(10)**:1876–1879. ISSN 10797114. doi:10.1103/PhysRevLett.78.1876.

[59] E. Biémont and P. Quinet. *Theoretical study of the* $4f^{14}6s\ ^2s_{1/2} - 4f^{13}6s^2\ ^2f^0_{7/2}$ *E3 transition in Yb II*. Phys. Rev. Lett. [1998]. **81**:3345–3346. doi:10.1103/PhysRevLett.81.3345. URL https://link.aps.org/doi/10.1103/PhysRevLett.81.3345.

[60] Y. Y. Jau, J. D. Hunker, and P. D D Schwindt. *F -state quenching with* CH_4 *for buffer-gas cooled* $^{171}Yb^{+}$ *frequency standard*. AIP Advances [2015]. **5(11)**:117209. ISSN 21583226. doi:10.1063/1.4935562. URL http://dx.doi.org/10.1063/1.4935562.

[61] Dipankar Das, Sachin Barthwal, Ayan Banerjee, and Vasant Natarajan. *Absolute frequency measurements in yb with* 0.08 ppb *uncertainty: Isotope shifts and hyperfine structure in the* 399−nm $^1S_0 \rightarrow^1 P_1$ *line*. Phys. Rev. A [2005]. **72**:032506. doi:10.1103/PhysRevA.72.032506. URL https://link.aps.org/doi/10.1103/PhysRevA.72.032506.

[62] M Johanning, A Braun, D Eiteneuer, C Paape, C Balzer, W Neuhauser, and C Wunderlich. *Resonance-enhanced isotope-selective photoionization of YbI for ion trap loading*. Applied Physics B [2011]. **103(2)**:327–338. ISSN 1432-0649. doi:10.1007/s00340-011-4502-7. URL https://doi.org/10.1007/s00340-011-4502-7.

[63] Y. Onoda, K. Sugiyama, M. Ikeda, and M. Kitano. *Loading rate of* Yb^{+} *loaded through photoionization in radiofrequency ion trap*. Applied Physics B [2011]. **105(4)**:729–740. ISSN 1432-0649. doi:10.1007/s00340-011-4576-2. URL https://doi.org/10.1007/s00340-011-4576-2.

[64] S. Olmschenk, D. Hayes, D. N. Matsukevich, P. Maunz, D. L. Moehring, K. C. Younge, and C. Monroe. *Measurement of the lifetime of the* $6p\ ^2P^o_{1/2}$ *level of* Yb^{+}. Phys. Rev. A [2009]. **80**:022502. doi:10.1103/PhysRevA.80.022502. URL https://link.aps.org/doi/10.1103/PhysRevA.80.022502.

[65] N. Yu and L. Maleki. *Lifetime measurements of the 4f5d metastable states in single ytterbium ions*. Physical Review A [2000]. **61(2)**:022507. ISSN 1050-2947. doi:10.1103/PhysRevA.61.022507. URL http://link.aps.org/doi/10.1103/PhysRevA.61.022507.

[66] Hendrik M. Meyer, Matthias Steiner, Lothar Ratschbacher, Christoph Zipkes, and Michael Köhl. *Laser spectroscopy and cooling of yb^+ ions on a deep-uv transition*. Phys. Rev. A [2012]. **85**:012502. doi:10.1103/PhysRevA.85.012502. URL https://link.aps.org/doi/10.1103/PhysRevA.85.012502.

[67] D. J. Berkeland and M. G. Boshier. *Destabilization of dark states and optical spectroscopy in Zeeman-degenerate atomic systems*. Physical Review A [2002]. **65(3)**:033413. ISSN 1050-2947. doi:10.1103/PhysRevA.65.033413. URL http://link.aps.org/doi/10.1103/PhysRevA.65.033413.

[68] Daniel Adam Steck. *Quantum and Atom Optics*. Book [2007]. URL http://atomoptics-nas.uoregon.edu/~dsteck/teaching/quantum-optics/quantum-optics-notes.pdf.

[69] M. Jardino and M. Desaintfuscien. *Measurement of relaxation time constants of optically pumped stored mercury ions*. IEEE Transactions on Instrumentation and Measurement [1980]. **29(3)**:163–167. ISSN 0018-9456. doi:10.1109/TIM.1980.4314900.

[70] Peter D D Schwindt, Thai M Hoang, Yuan-Yu Jau, and Richard Overstreet. *Operating a 171 Yb + Microwave Ion Clock in a Continuous Mode*. In *2018 IFCS Proceedings*. IEEE [2018] pages 493–496.

[71] M. Jardino, M. Desaintfuscien, R. Barillet, J. Viennet, P. Petit, and C. Audoin. *Frequency stability of a mercury ion frequency standard*. Applied physics [1981]. **24(2)**:107–112. ISSN 1432-0630. doi:10.1007/BF00902264. URL https://doi.org/10.1007/BF00902264.

[72] P. T. H. Fisk, M. J. Sellars, M. A. Lawn, and G. Coles. *Accurate measurement of the 12.6 GHz "clock" transition in trapped ^{171}Yb ions*. IEEE Transactions on Ultrasonics, Ferroelectrics, and Frequency Control [1997]. **44(2)**:344–354. ISSN 0885-3010. doi:10.1109/58.585119.

[73] Y. Y. Jau, H. Partner, P. D.D. Schwindt, J. D. Prestage, J. R. Kellogg, and N. Yu. *Low-power, miniature ^{171}Yb ion clock using an ultra-small vacuum package*. Applied Physics Letters [2012]. **101(25)**:253518. ISSN 00036951. doi:10.1063/1.4767454.

[74] S. J. Park, P. J. Manson, M. J. Wouters, R. B. Warrington, M. A. Lawn, and P. T. H. Fisk. *$^{171}Yb^+$ Microwave Frequency Standard*. In *2007 IEEE IFCS-EFTF Proceedings*. ISSN 2327-1914 [2007] pages 613–616. doi:10.1109/FREQ.2007.4319145.

[75] James C. Camparo, C. M. Klimcak, and S. J. Herbulock. *Frequency equilibration in the vapor-cell atomic clock*. IEEE Transactions on Instrumentation and Measurement [2005]. **54(5)**:1873–1880. ISSN 00189456. doi:10.1109/TIM.2005.853217.

[76] C W Chou, D B Hume, T Rosenband, and D J Wineland. *Optical clocks and relativity.* Science (New York, N.Y.) [2010]. **329(5999)**:1630–1633.

[77] S. Schiller, G. M. Tino, P. Gill, C. Salomon, U. Sterr, E. Peik, A. Nevsky, A. Görlitz, D. Svehla, G. Ferrari, N. Poli, L. Lusanna, H. Klein, H. Margolis, P. Lemonde, P. Laurent, G. Santarelli, A. Clairon, W. Ertmer, E. Rasel, J. Müller, L. Iorio, C. Lämmerzahl, H. Dittus, E. Gill, M. Rothacher, F. Flechner, U. Schreiber, V. Flambaum, Wei Tou Ni, Liang Liu, Xuzong Chen, Jingbiao Chen, Kelin Gao, L. Cacciapuoti, R. Holzwarth, M. P. Heß, and W. Schäfer. *Einstein gravity explorer-a medium-class fundamental physics mission.* Experimental Astronomy [2009]. **23(2)**:573–610.

[78] R. H. Dicke. *The Effect of Collisions upon the Doppler Width of Spectral Lines.* Physical Review [1953]. **89(2)**:472,473.

[79] C. Meis, M. Desaintfuscien, and M. Jardino. *Analytical calculation of the space charge potential and the temperature of stored ions in an rf quadrupole trap.* Applied Physics B Photophysics and Laser Chemistry [1988]. **45(2)**:59–64. ISSN 07217269. doi:10.1007/BF00694316.

[80] PTH Fisk, MJ Sellars, MA Lawn, and C Coles. *Performance of a prototype microwave frequency standard based on laser-detected, trapped 171 Yb+ ions.* Applied Physics B: Lasers and Optics [1995]. **60(6)**:519–527. URL http://www.springerlink.com/index/KQ273N236L386R27.pdf.

[81] Y.-Y. Jau, H. Partner, P. D. D. Schwindt, J. D. Prestage, J. R. Kellogg, and N. Yu. *Low-power, miniature 171Yb ion clock using an ultra-small vacuum package.* Applied Physics Letters [2012]. **101(25)**:253518. ISSN 00036951. doi:10.1063/1.4767454. URL http://scitation.aip.org/content/aip/journal/apl/101/25/10.1063/1.4767454.

[82] G. K. Woodgate. *Elementary Atomic Structure.* OUP, second edition edition [1983].

[83] C. Tamm, D. Schnier, and A. Bauch. *Radio-frequency laser double-resonance spectroscopy of trapped171Yb ions and determination of line shifts of the ground-state hyperfine resonance.* Applied Physics B Laser and Optics [1995]. **60(1)**:19–29. ISSN 09462171. doi:10.1007/BF01082068.

[84] E. J. Angstmann, V. A. Dzuba, and V. V. Flambaum. *Frequency shift of hyperfine transitions due to blackbody radiation.* Physical Review A - Atomic, Molecular, and Optical Physics [2006]. **74(2)**:1–8. ISSN 10502947. doi:10.1103/PhysRevA.74.023405. 0605163.

[85] U. I. Safronova, M. S. Safronova, U. I. Safronova, and M. S. Safronova. *Third-order relativistic many-body calculations of energies, transition rates, hyperfine constants, and blackbody radiation shift in* $^{171}Yb^{+}$. Phys. Rev. A [2009]. **79**:022512. doi:10.1103/PhysRevA.79.022512. URL https://link.aps.org/doi/10.1103/PhysRevA.79.022512.

[86] Charles Baynham. *Temperature controller*. Github repository [2018]. URL https://github.com/charlesbaynham/DigitalTemperatureController.

[87] Toptica. *Toptica DL100-PRO EDCL Datasheet* [2015].

[88] K Toyoda, A. Miura, S. Urabe, K. Hayasaka, and M. Watanabe. *Laser cooling of calcium ions by use of ultraviolet laser diodes: significant induction of electron-shelving transitions*. Optics Letters [2001]. **26(23)**:1897. ISSN 0146-9592. doi: 10.1364/OL.26.001897. URL http://ol.osa.org/abstract.cfm?URI=ol-26-23-1897.

[89] S. Rauch and J. Sacher. *Compact bragg grating stabilized ridge waveguide laser module with a power of 380 mw at 780 nm*. IEEE Photonics Technology Letters [2015]. **27(16)**:1737–1740. ISSN 1041-1135. doi:10.1109/LPT.2015.2438545.

[90] G P Barwood, P Gill, G Huang, and H A Klein. *Automatic laser control for a $^{88}Sr^{+}$ optical frequency standard*. Measurement Science and Technology [2012]. **23(5)**:055201. ISSN 0957-0233. doi:10.1088/0957-0233/23/5/055201. URL http://stacks.iop.org/0957-0233/23/i=5/a=055201?key=crossref.a387329b3eb219eb4642f5dd31695515.

[91] Michael W Lee, Marie Claire Jarratt, Christian Marciniak, and Michael J Biercuk. *Frequency Stabilization of a 369 nm Diode Laser by Nonlinear Spectroscopy of Ytterbium Ions in a Discharge*. ArXiv [2014]. **759(2006)**:757–759. ISSN 1094-4087. doi:10.1364/OE.22.007210. URL http://arxiv.org/abs/1402.1248. 1402.1248.

[92] W. R.C. Rowley. *The performance of a longitudinal Zeeman-stabilised He-Ne laser (633 nm) with thermal modulation and control*. Measurement Science and Technology [1990]. **1(4)**:348–351. ISSN 09570233. doi:10.1088/0957-0233/1/4/006.

[93] L.S. Rothman, I.E. Gordon, Y. Babikov, A. Barbe, D. Chris Benner, P.F. Bernath, M. Birk, L. Bizzocchi, V. Boudon, L.R. Brown, A. Campargue, K. Chance, E.A. Cohen, L.H. Coudert, V.M. Devi, B.J. Drouin, A. Fayt, J.-M. Flaud, R.R. Gamache, J.J. Harrison, J.-M. Hartmann, C. Hill, J.T. Hodges, D. Jacquemart, A. Jolly, J. Lamouroux, R.J. Le Roy, G. Li, D.A. Long, O.M. Lyulin, C.J. Mackie, S.T. Massie, S. Mikhailenko, H.S.P. Müller, O.V. Naumenko, A.V. Nikitin, J. Orphal, V. Perevalov, A. Perrin, E.R. Polovtseva, C. Richard, M.A.H. Smith, E. Starikova, K. Sung, S. Tashkun, J. Tennyson, G.C. Toon, Vl.G. Tyuterev, and G. Wagner. *The HITRAN2012 molecular spectroscopic database*. Journal of Quantitative Spectroscopy and Radiative Transfer [2013]. **130**:4–50. ISSN 0022-4073. doi:10.1016/J.JQSRT.2013.07.002. URL https://www.sciencedirect.com/science/article/pii/S0022407313002859?via{%}3Dihub.

[94] R. Ifflander and G. Werth. *Optical detection of ions confined in a rf quadrupole trap*. Metrologia [1977]. **170(13)**:167–170. ISSN 00261394. doi:10.1088/0026-1394/13/3/017. URL http://iopscience.iop.org/0026-1394/13/3/017.

[95] H. Leuthner and G. Werth. *Buffer-gas-cooled ion clouds in a classical Paul trap: superimposed stability diagrams and trapping capacity investigations.* Applied Physics B [2014]. **114(1-2)**:89–98. ISSN 0946-2171. doi:10.1007/s00340-013-5657-1. URL http://link.springer.com/10.1007/s00340-013-5657-1.

[96] M. Drewsen, C. Brodersen, L. Hornekær, J. S. Hangst, and J. P. Schifffer. *Large Ion Crystals in a Linear Paul Trap.* Physical Review Letters [1998]. **81(14)**:2878–2881. ISSN 0031-9007. doi:10.1103/PhysRevLett.81.2878. URL http://link.aps.org/doi/10.1103/PhysRevLett.81.2878.

[97] Y-Y Jau, F M Benito, H Partner, and P D D Schwindt. *Low power high-performance radio frequency oscillator for driving ion traps.* Review of Scientific Instruments [2011]. **82(2)**:023118. ISSN 1089-7623. doi:10.1063/1.3558569. URL http://www.ncbi.nlm.nih.gov/pubmed/21361584.

[98] Christopher J. Erickson, Marshall Van Zijll, Greg Doermann, and Dallin S. Durfee. *An ultrahigh stability, low-noise laser current driver with digital control.* Review of Scientific Instruments [2008]. **79(7)**:073107. doi:10.1063/1.2953597. URL https://doi.org/10.1063/1.2953597. https://doi.org/10.1063/1.2953597.

[99] K. Mølhave and M. Drewsen. *Formation of translationally cold* MgH^+ *and* MgD^+ *molecules in an ion trap.* Phys. Rev. A [2000]. **62**:011401. doi:10.1103/PhysRevA.62.011401. URL https://link.aps.org/doi/10.1103/PhysRevA.62.011401.

[100] Peter Schwindt. *Ion loss.* private communication [2018].

[101] M. M. Schauer, J. R. Danielson, A. T. Nguyen, L. B. Wang, X. Zhao, and J. R. Torgerson. *Collisional population transfer in trapped Yb+ ions.* Physical Review A - Atomic, Molecular, and Optical Physics [2009]. **79(6)**:2–6. ISSN 10502947. doi:10.1103/PhysRevA.79.062705.

[102] Kazuhiko Sugiyama and Jun Yoda. *Disappearance of Yb+ in excited states from rf trap by background gases.* Japanese Journal of Applied Physics [1995]. **34(5A)**:L 584–L 586. ISSN 13474065. doi:10.1143/JJAP.34.L584.

[103] F.G. Major, V.N. Gherorghe, and G. Werth. *Charged Particle Traps* [2005]. ISBN 978-3-540-22043-5. doi:10.1007/978-3-540-92261-2.

[104] Kazuhiko Sugiyama and Jun Yoda. *Production of* YbH^+ *by chemical reaction of* Yb^+ *in excited states with* H_2 *gas.* Phys. Rev. A [1997]. **55**:R10–R13. doi:10.1103/PhysRevA.55.R10. URL https://link.aps.org/doi/10.1103/PhysRevA.55.R10.

[105] Brice Dubost. *Light-matter interaction with atomic ensembles.* Ph.D. thesis, Universitï¿œ Paris-Diderot - Paris VII; Universitat Politï¿œcnica de Catalunya [2012].

[106] L. Hornekær, N. Kjærgaard, A. M. Thommesen, and M. Drewsen. *Structural properties of two-component Coulomb crystals in linear Paul traps*. Physical Review Letters [2001]. **86(10)**:1994–1997. ISSN 00319007. doi:10.1103/PhysRevLett.86.1994.

[107] M. Drewsen, A. Mortensen, R. Martinussen, P. Staanum, and J. L. Sørensen. *Nondestructive identification of cold and extremely localized single molecular ions*. Physical Review Letters [2004]. **93(24)**:1–4. ISSN 00319007. doi:10.1103/PhysRevLett.93.243201. 0406088.

[108] Kevin Sheridan and Matthias Keller. *Weighing of trapped ion crystals and its applications*. New Journal of Physics [2011]. **13**. ISSN 13672630. doi:10.1088/1367-2630/13/12/123002. 1106.2771.

[109] G John Dick. *Local oscillator induced instabilities in trapped ion frequency standards*. In *Proceedings of the 19th Annual Precise Time and Time Interval Systems and Applications Meeting, Redondo Beach* [1987] pages 133–147.

[110] G. Santarelli, C. Audoin, A. Makdissi, P. Laurent, G. J. Dick, and A. Clairon. *Frequency stability degradation of an oscillator slaved to a periodically interrogated atomic resonator*. IEEE Transactions on Ultrasonics, Ferroelectrics, and Frequency Control [1998]. **45(4)**:887–894. ISSN 0885-3010. doi:10.1109/58.710548.

[111] Charles A. Greenhall. *A derivation of the long-term degradation of a pulsed atomic frequency standard from a control-loop model*. IEEE Transactions on Ultrasonics, Ferroelectrics, and Frequency Control [1998]. **45(4)**:895–898. ISSN 08853010. doi:10.1109/58.710550.

[112] A. Clairon, P. Laurent, G. Santarelli, S. Ghezali, S. N. Lea, and M. Bahoura. *A Cesium Fountain Frequency Standard: Preliminary Results*. IEEE Transactions on Instrumentation and Measurement [1995]. **44(2)**:128–131. ISSN 15579662. doi:10.1109/19.377790.

[113] J. P. Schiffer. *Melting of Crystalline Confined Plasmas*. Physical Review Letters [2002]. **88(20)**:205003. ISSN 0031-9007. doi:10.1103/PhysRevLett.88.205003. URL http://apps.webofknowledge.com/full{_}record.do?product=UA{&}search{_}mode=GeneralSearch{&}qid=1{&}SID=V1stXFgzyvcF7iRUv8U{&}page=1{&}doc=5.

[114] Brian R. Eichelberger, Theodore P. Snow, and Veronica M. Bierbaum. *Collision rate constants for polarizable ions*. Journal of the American Society for Mass Spectrometry [2003]. **14(5)**:501–505. ISSN 1879-1123. doi:10.1016/S1044-0305(03)00134-X. URL https://doi.org/10.1016/S1044-0305(03)00134-X.

[115] Steven A King. *Sub-hertz optical frequency metrology using a single ion of 171 Yb +*. Ph.D. thesis, University of Oxford [2012].

[116] South Western Railway. *Kingston Loop and Shepperton to London Waterloo Train times 20 May to 8 December 2018* [2018]. URL https://www.southwesternrailway.com/plan-my-journey/timetables.

Appendix A

Engineering Drawings

This appendix contains engineering drawings for the vacuum chamber, magnetic shields and Mark 3 ion trap that were used in this project.

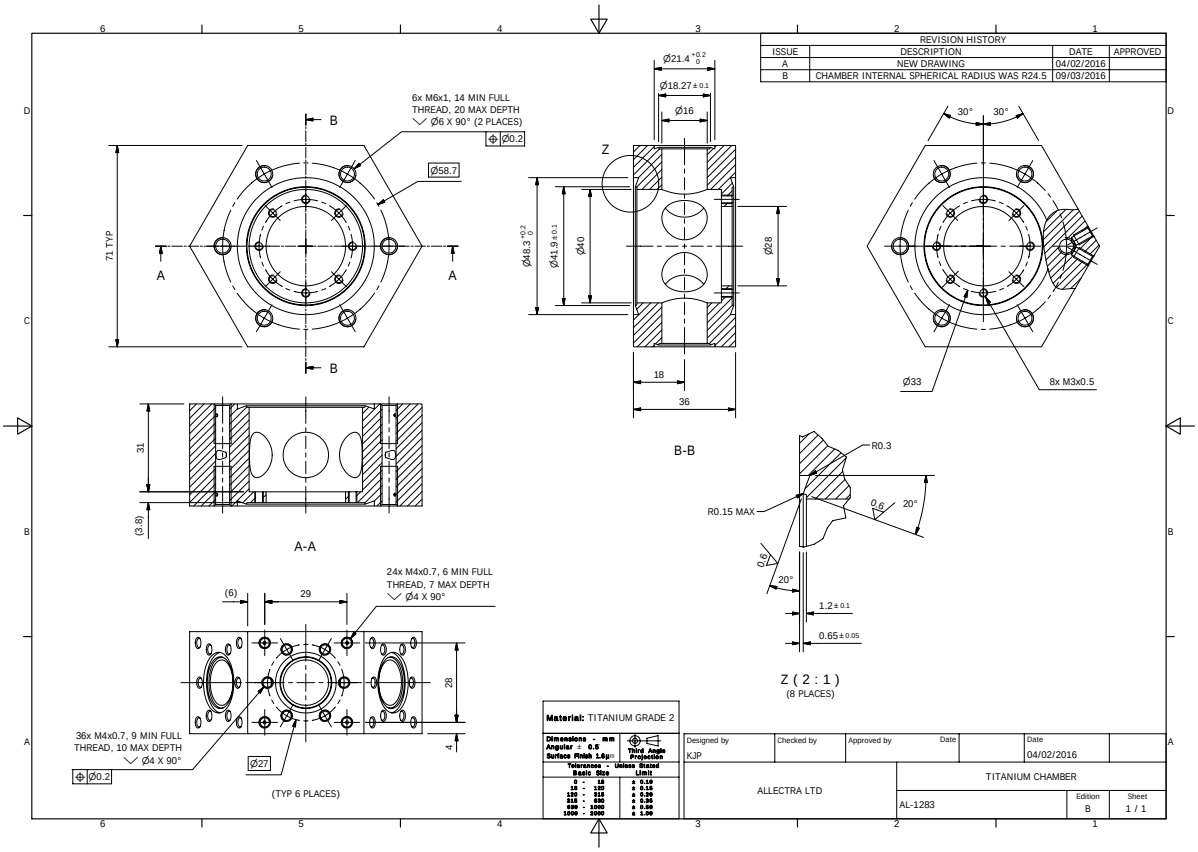


Figure A.1: 'Hex chamber' drawings

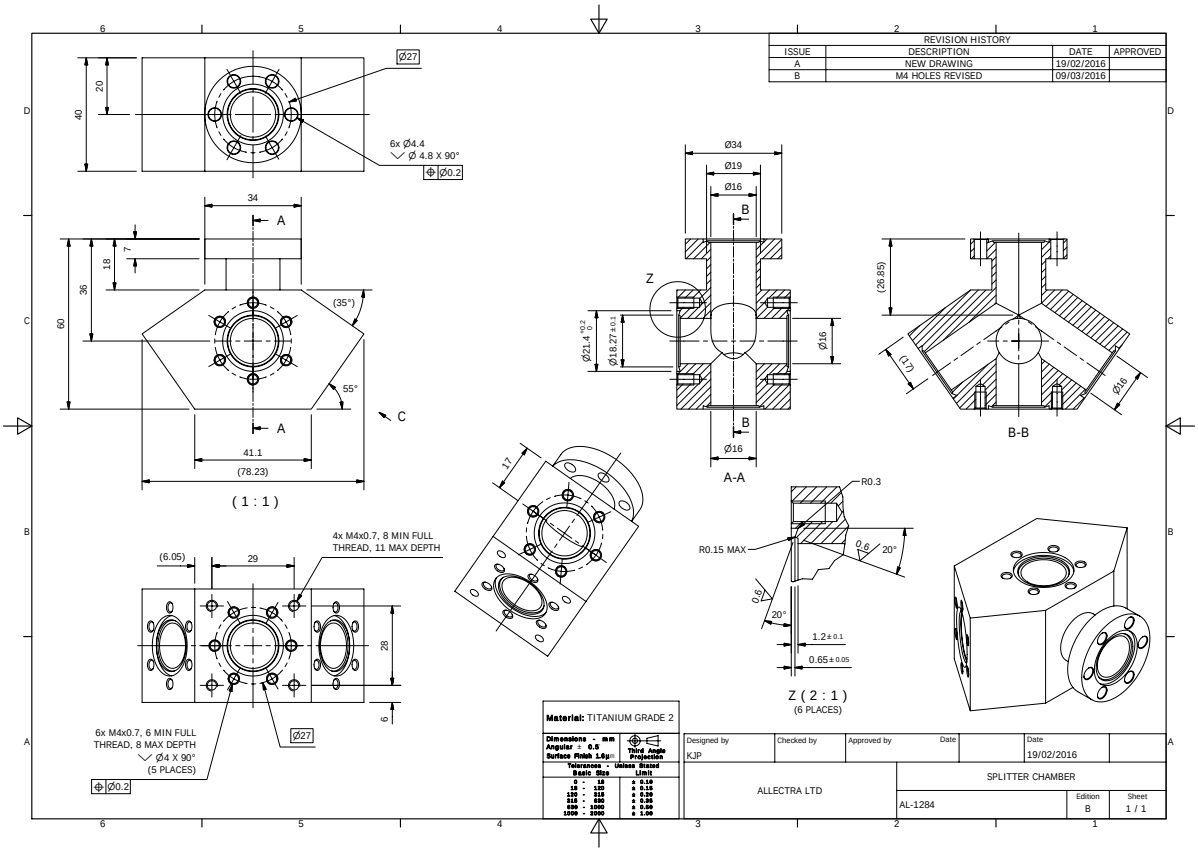


Figure A.2: 'Splitter chamber' drawings

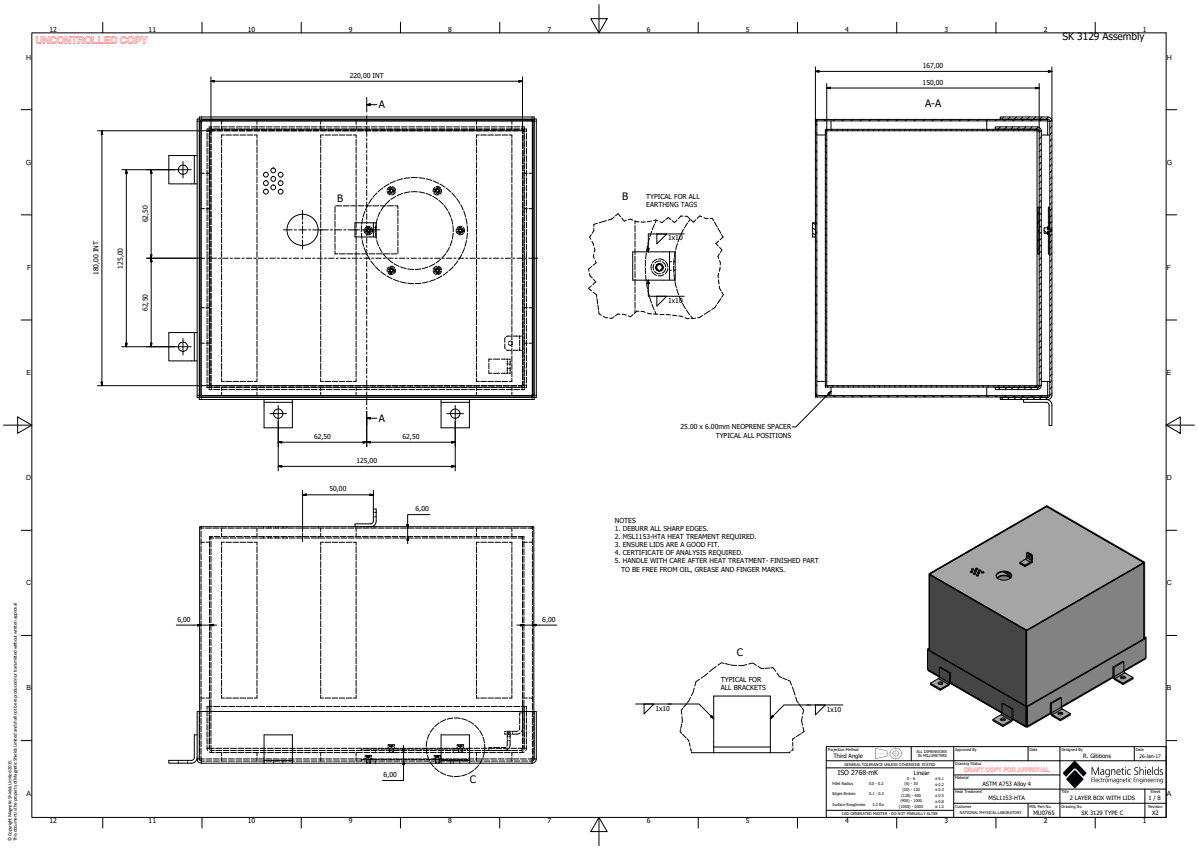
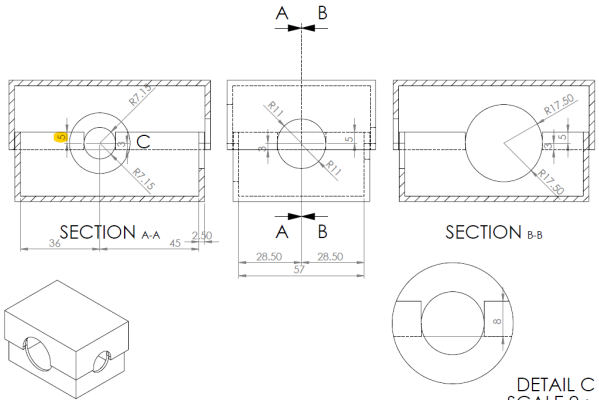
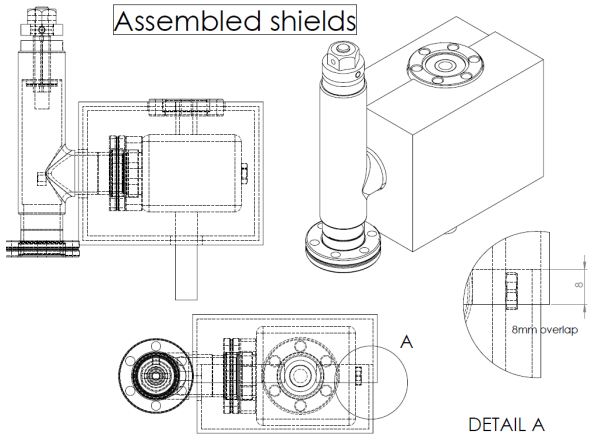


Figure A.3: Mu-metal shields



(a)



(b)

Figure A.4: Soft-iron ion pump shields. Designed by Hugh Klein

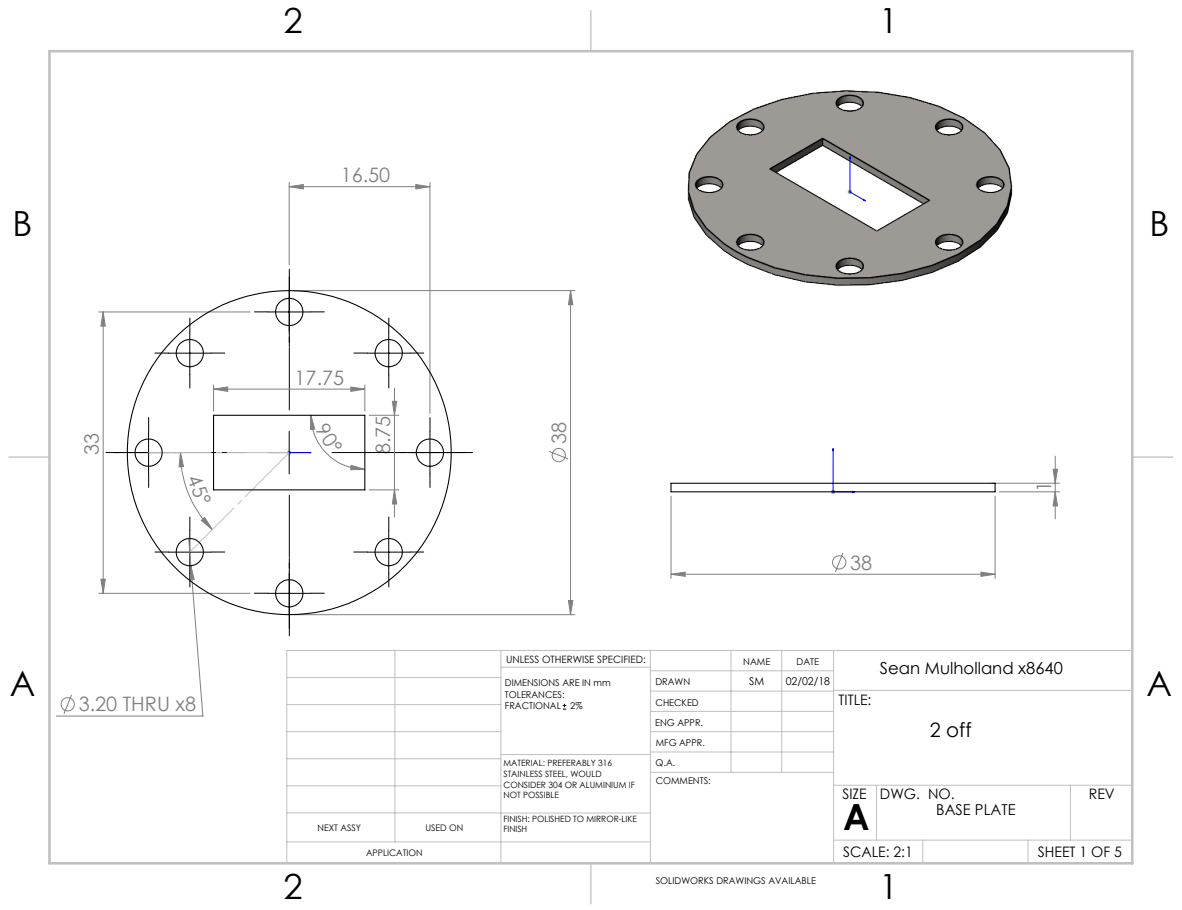


Figure A.5: Vertical compensation plate electrode

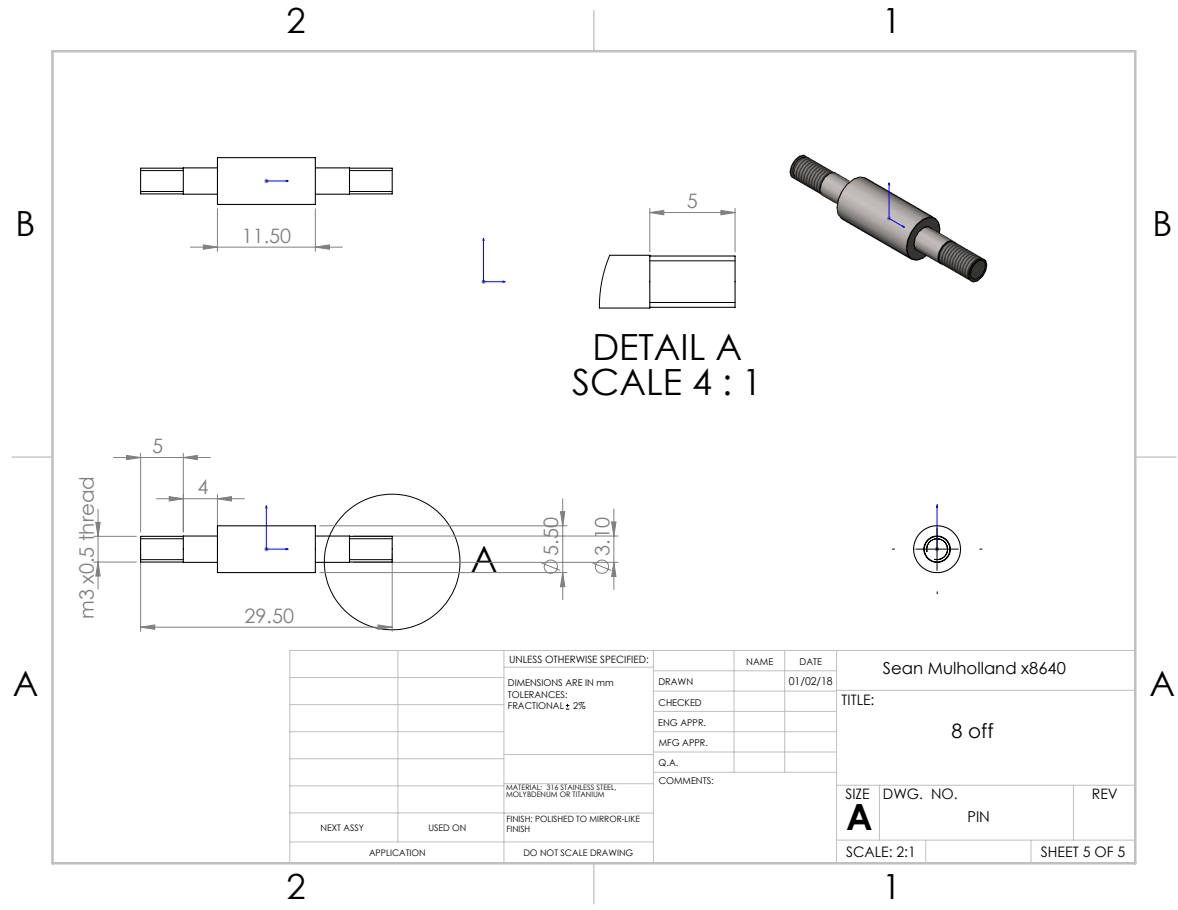


Figure A.6: Rod electrodes

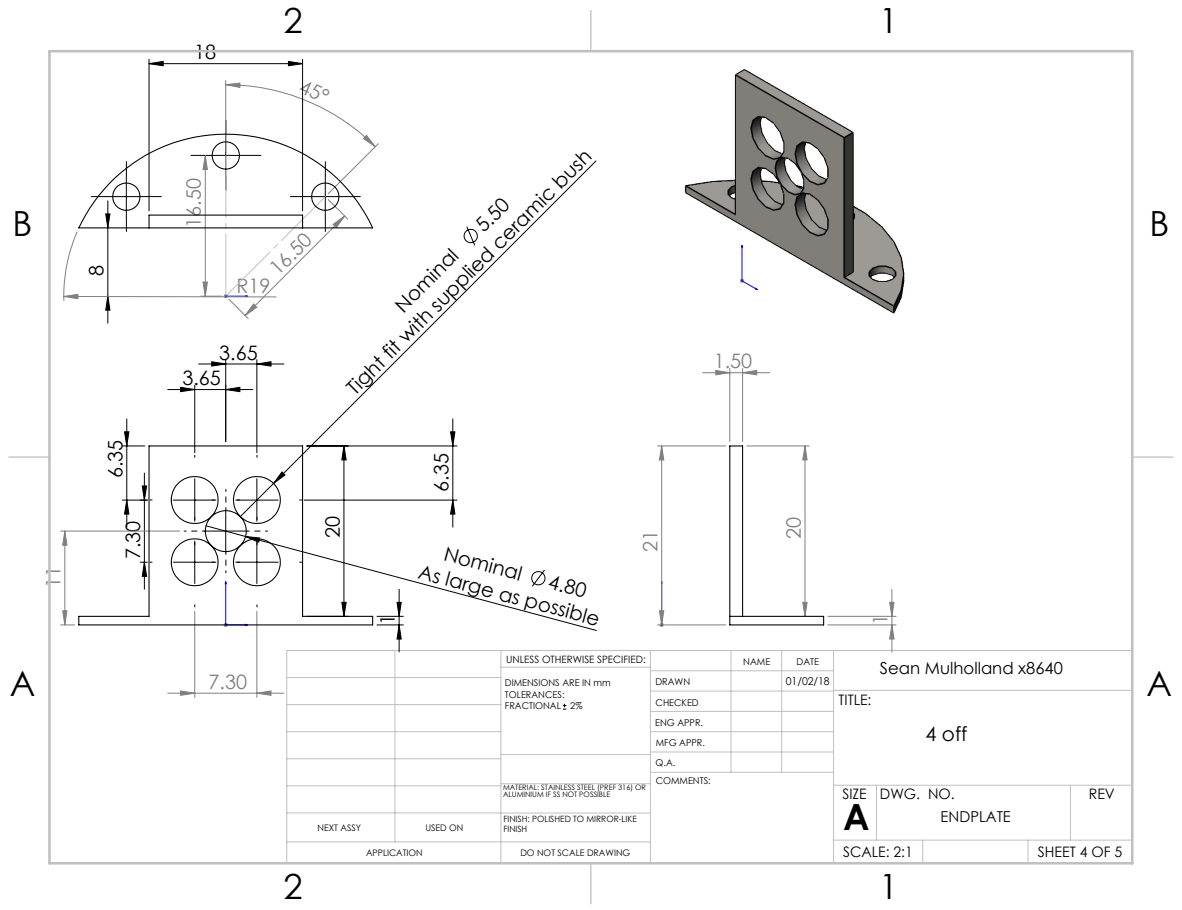


Figure A.7: Endplate electrodes

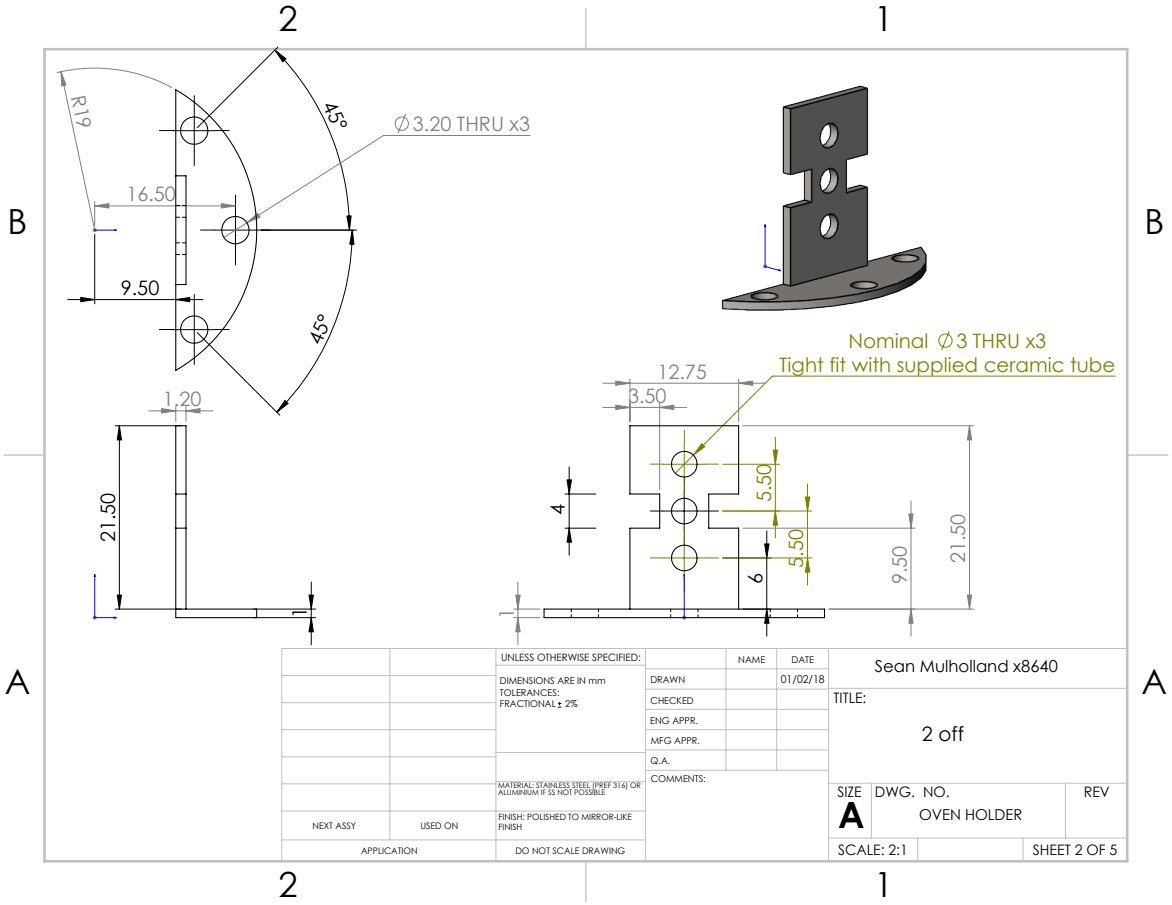


Figure A.8: Horizontal compensation plate electrode and oven holder

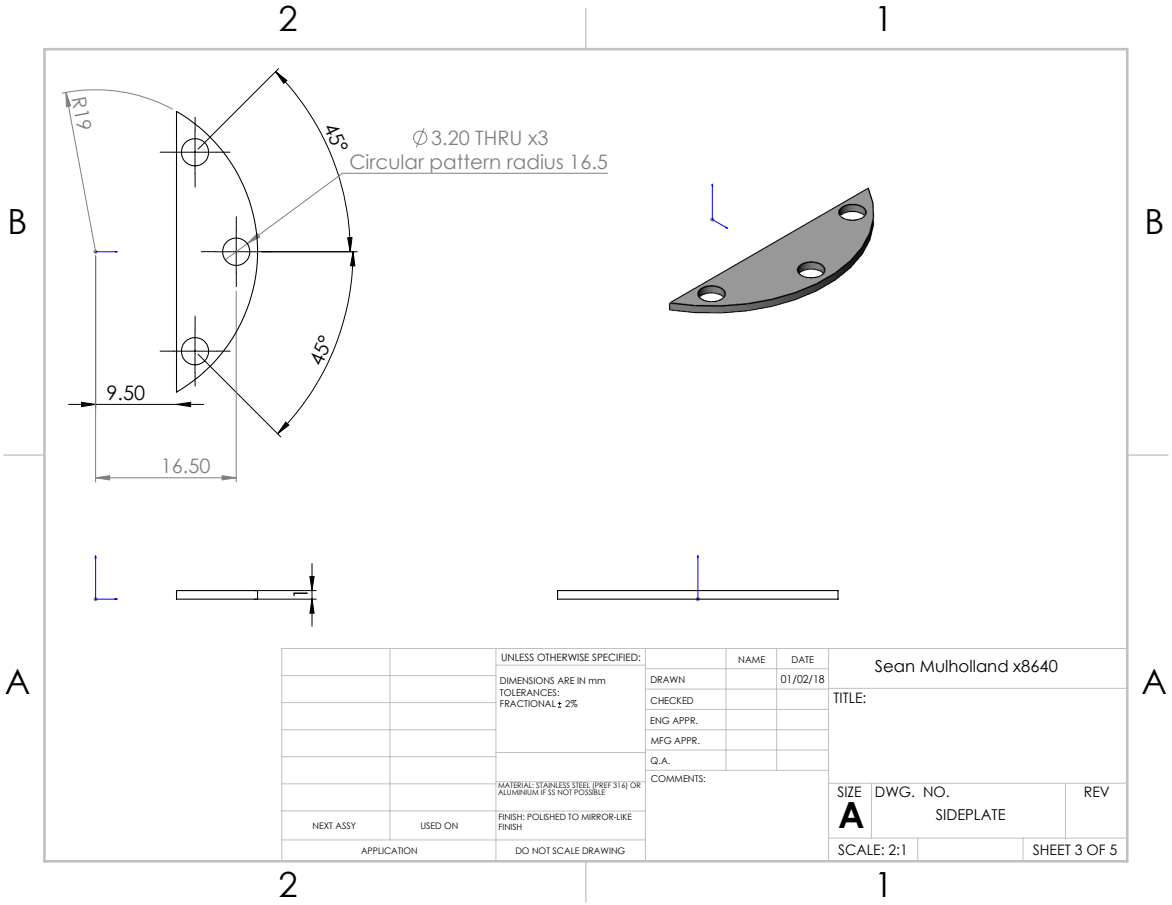


Figure A.9: Ground plate electrode

Appendix B

Electronic Schematics

This appendix contains electronic schematics for some of the boards that were used in this project.

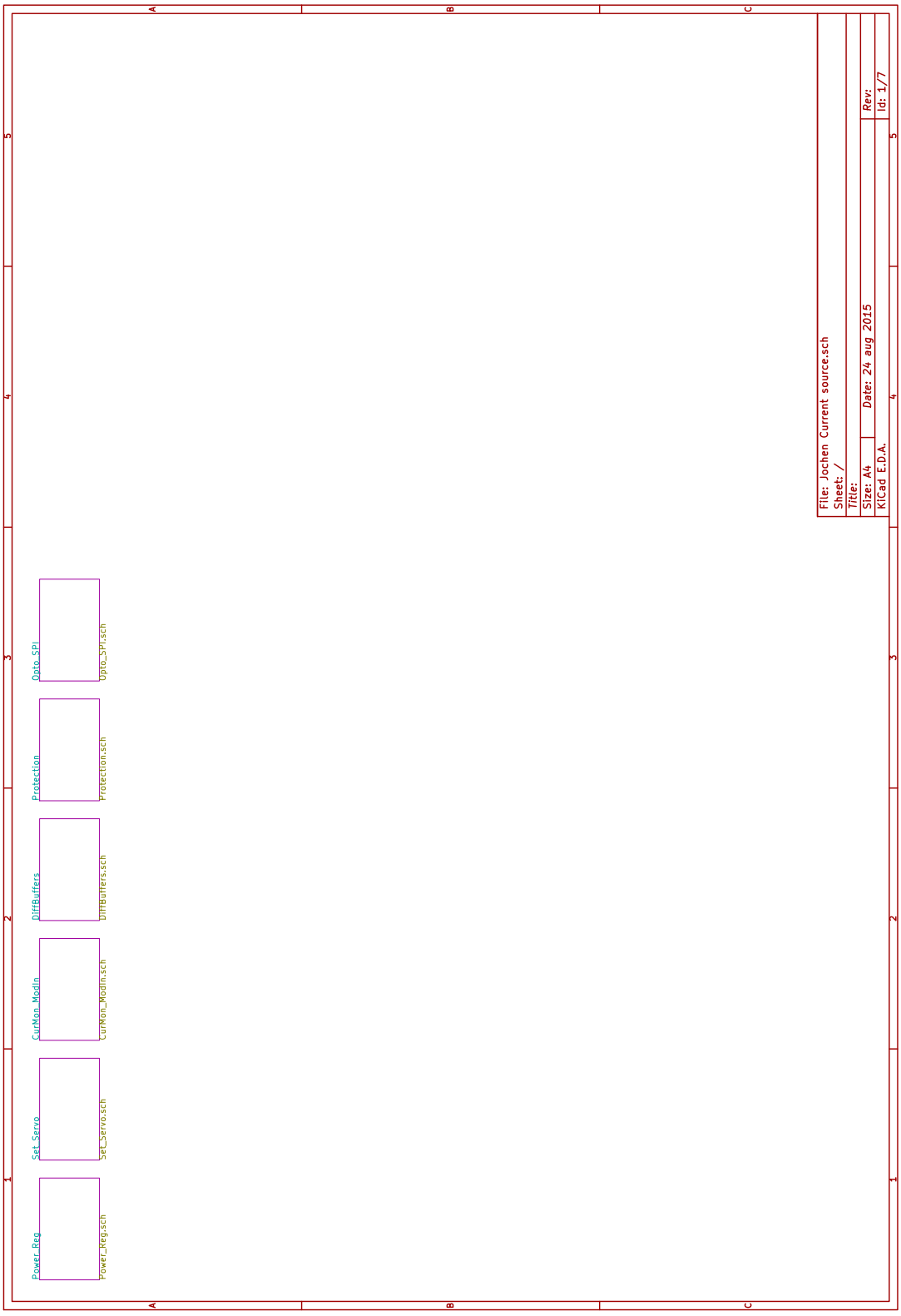


Figure B.1: Stable current source 1/7

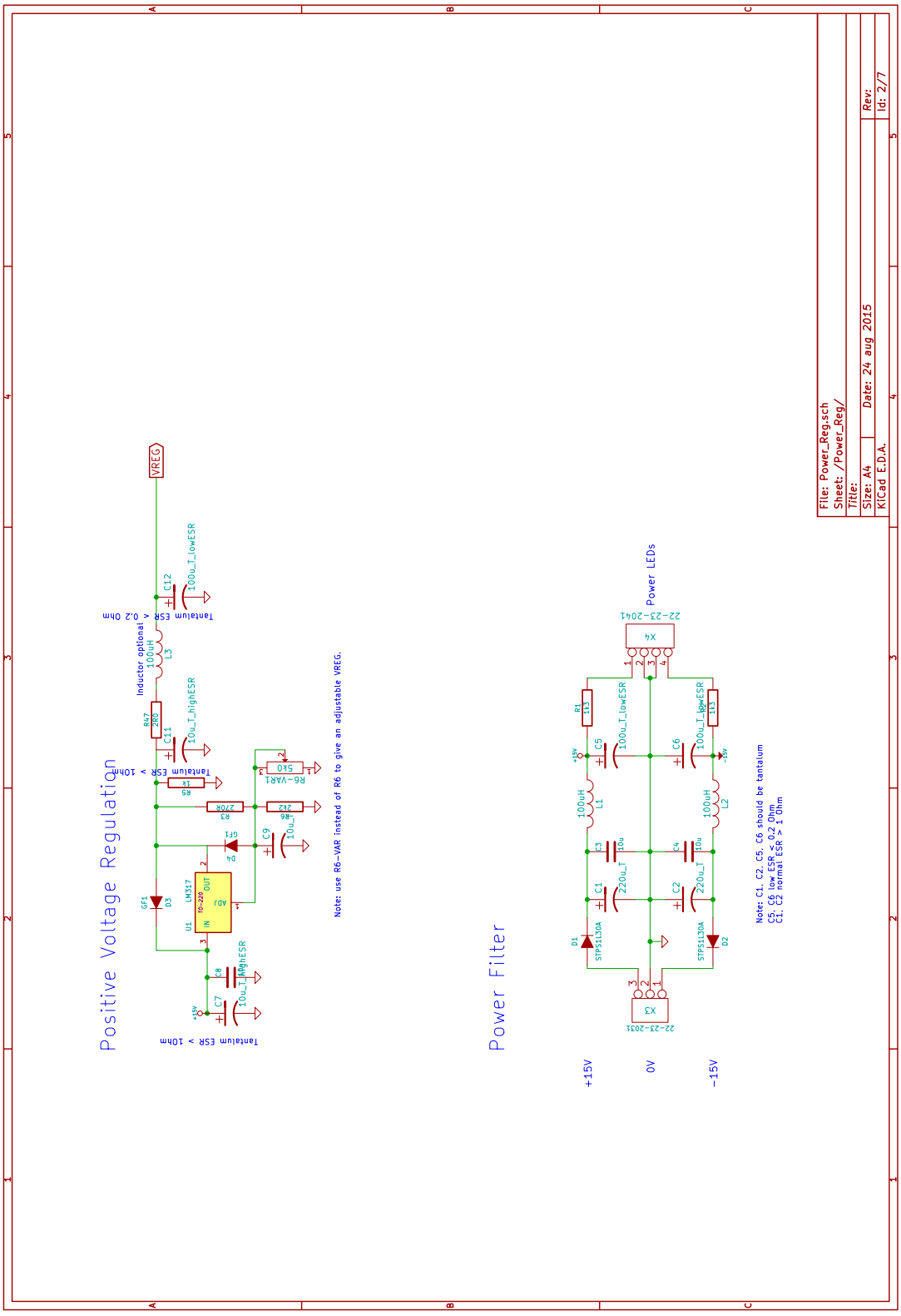


Figure B.2: Stable current source 2/7

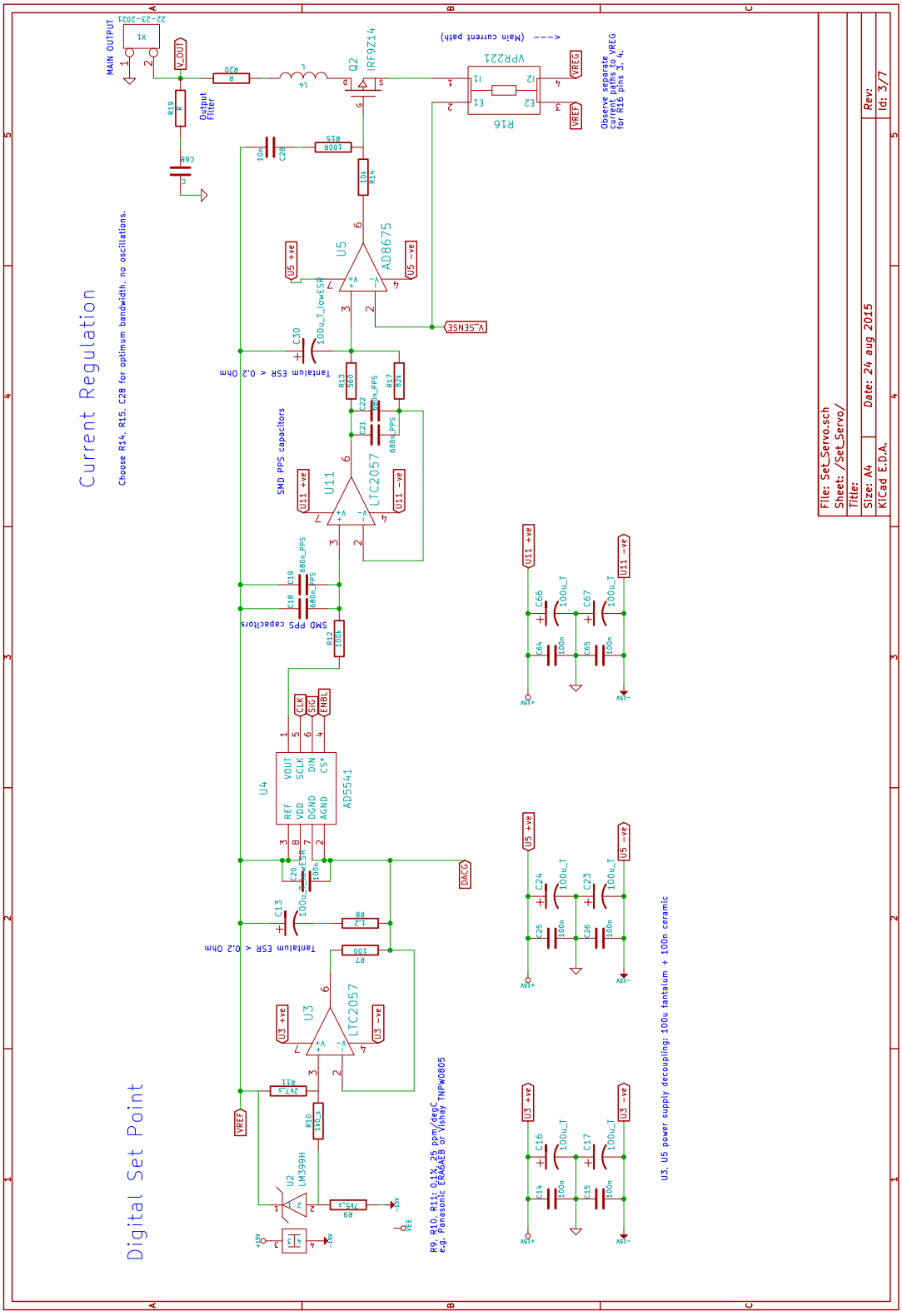


Figure B.3: Stable current source 3/7

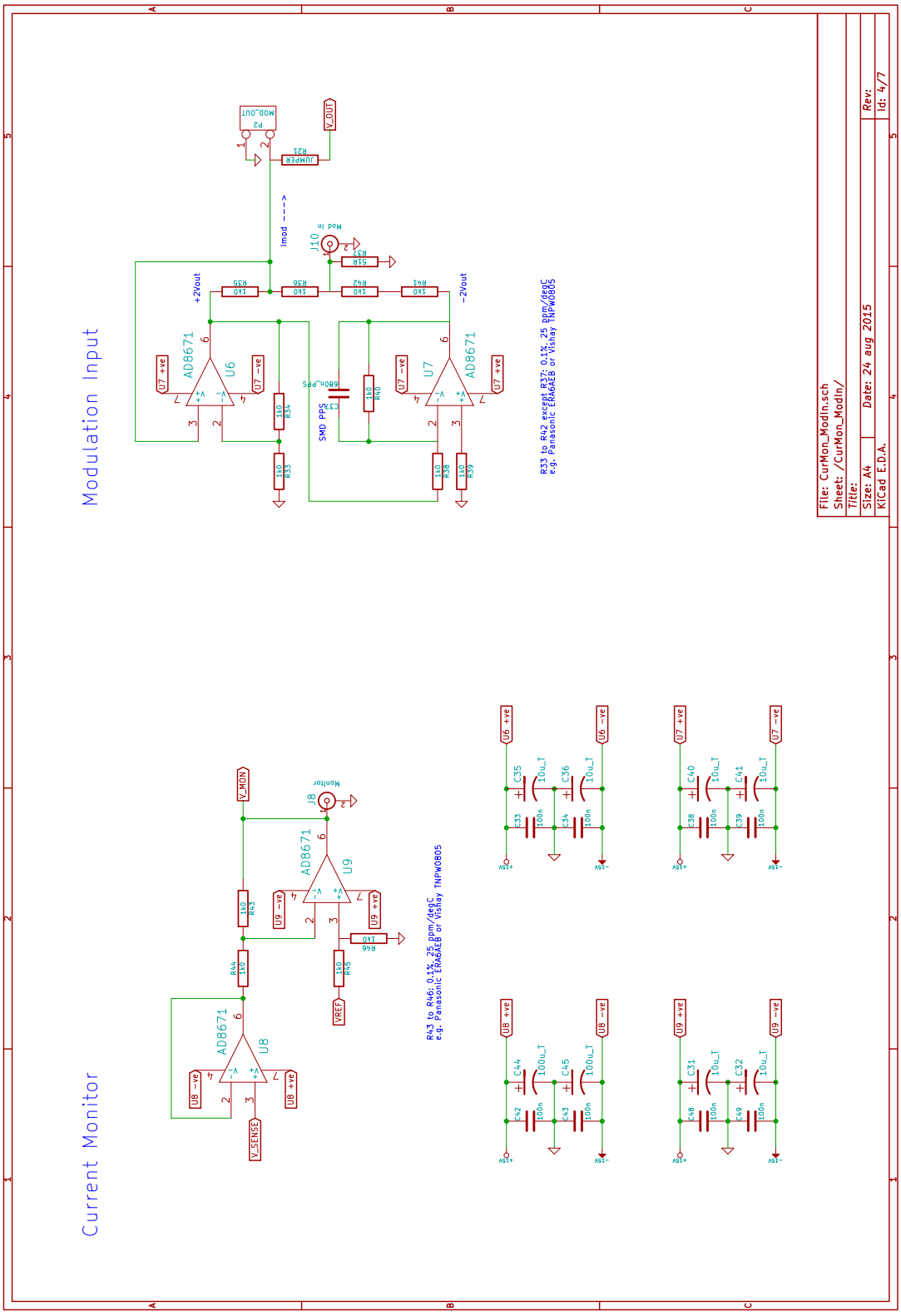


Figure B.4: Stable current source 4/7

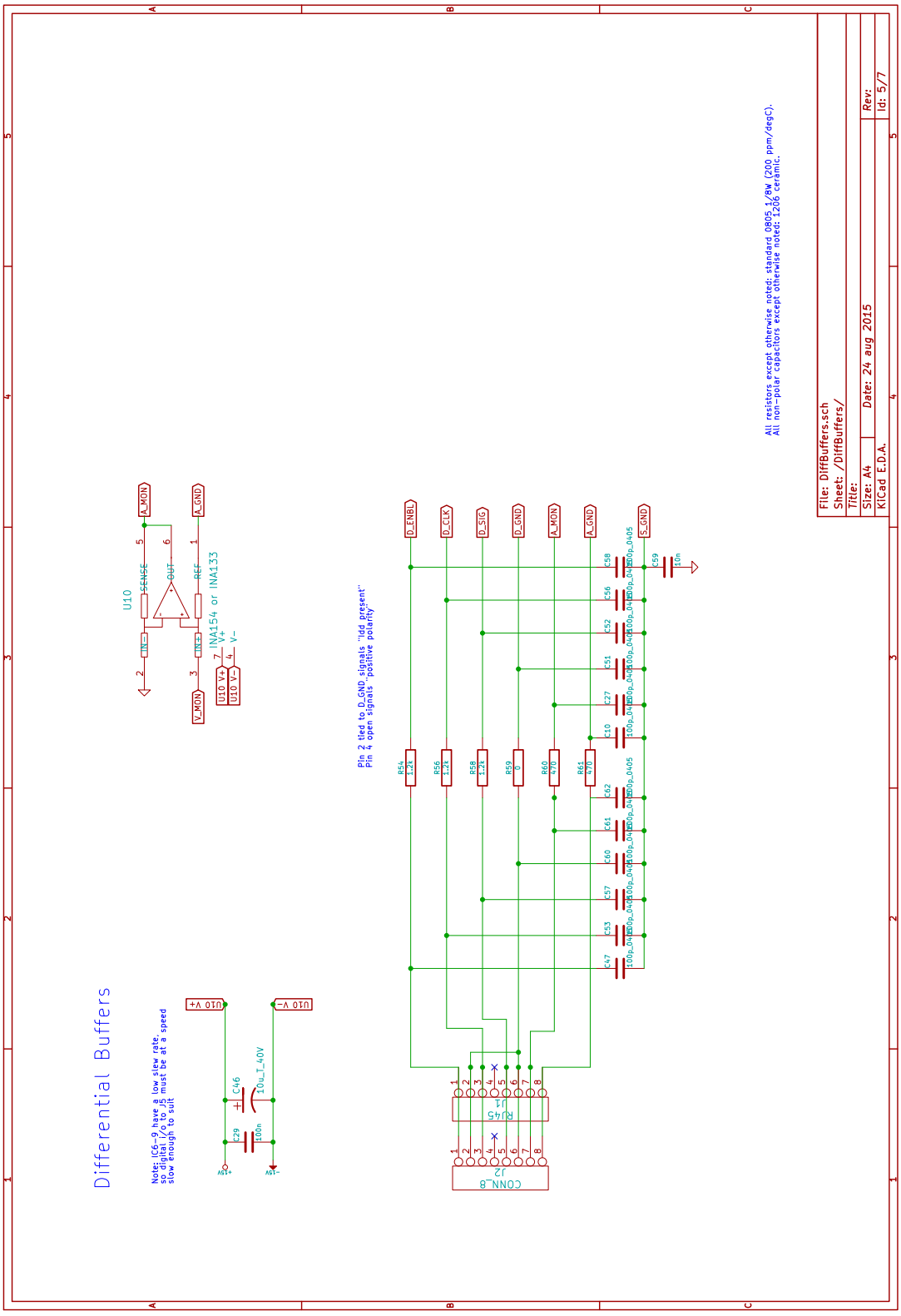


Figure B.5: Stable current source 5/7

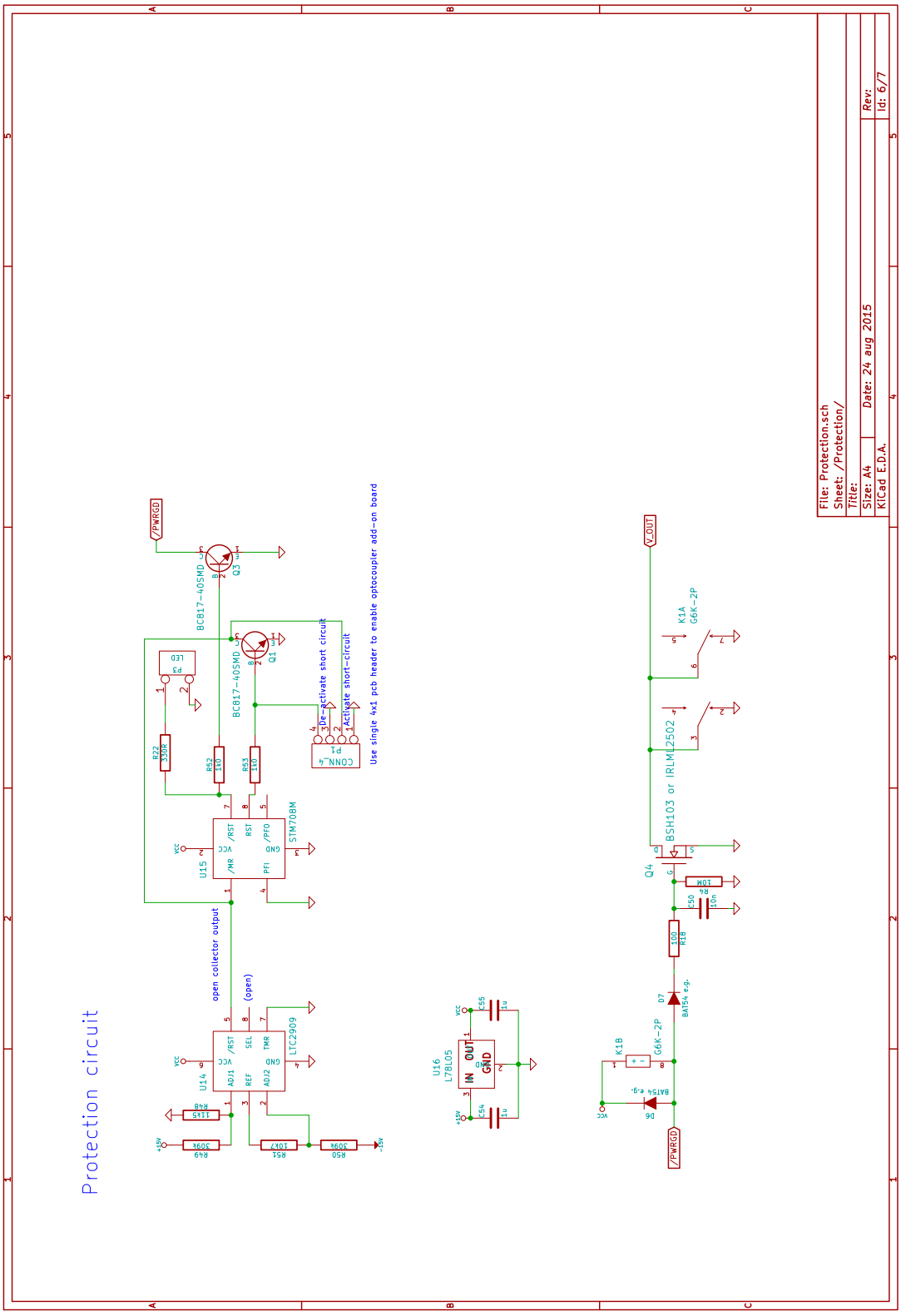


Figure B.6: Stable current source 6/7

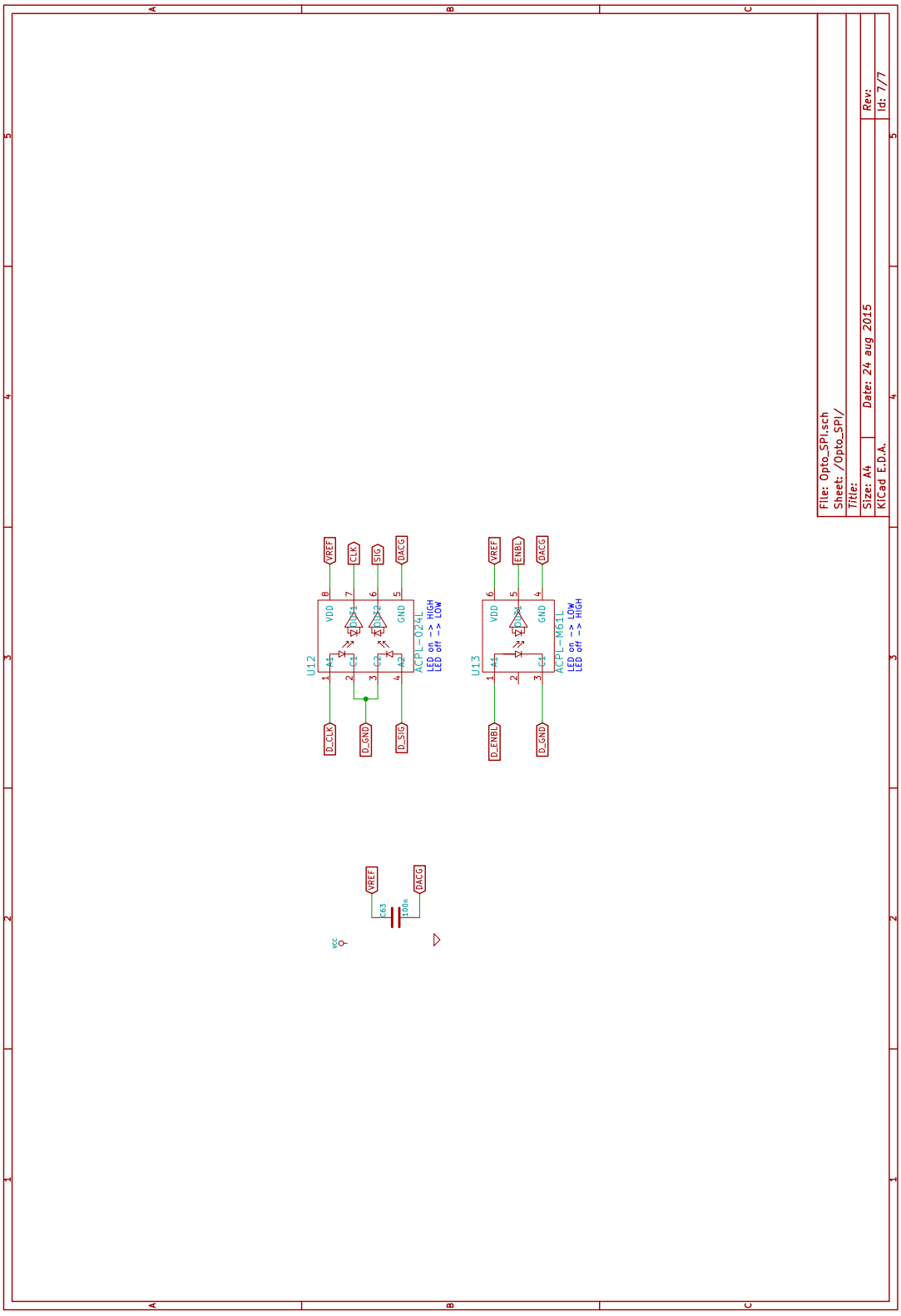


Figure B.7: Stable current source 7/7

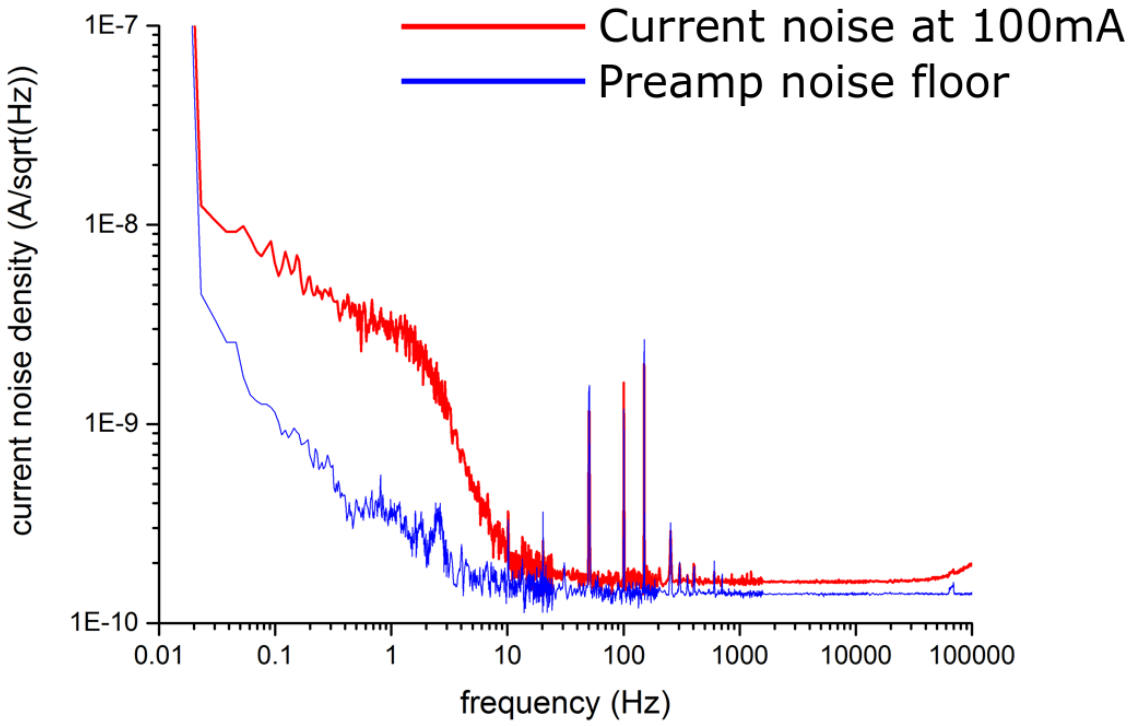


Figure B.8: Current noise density of stable current source. Courtesy of Jochen Kronjaeger.

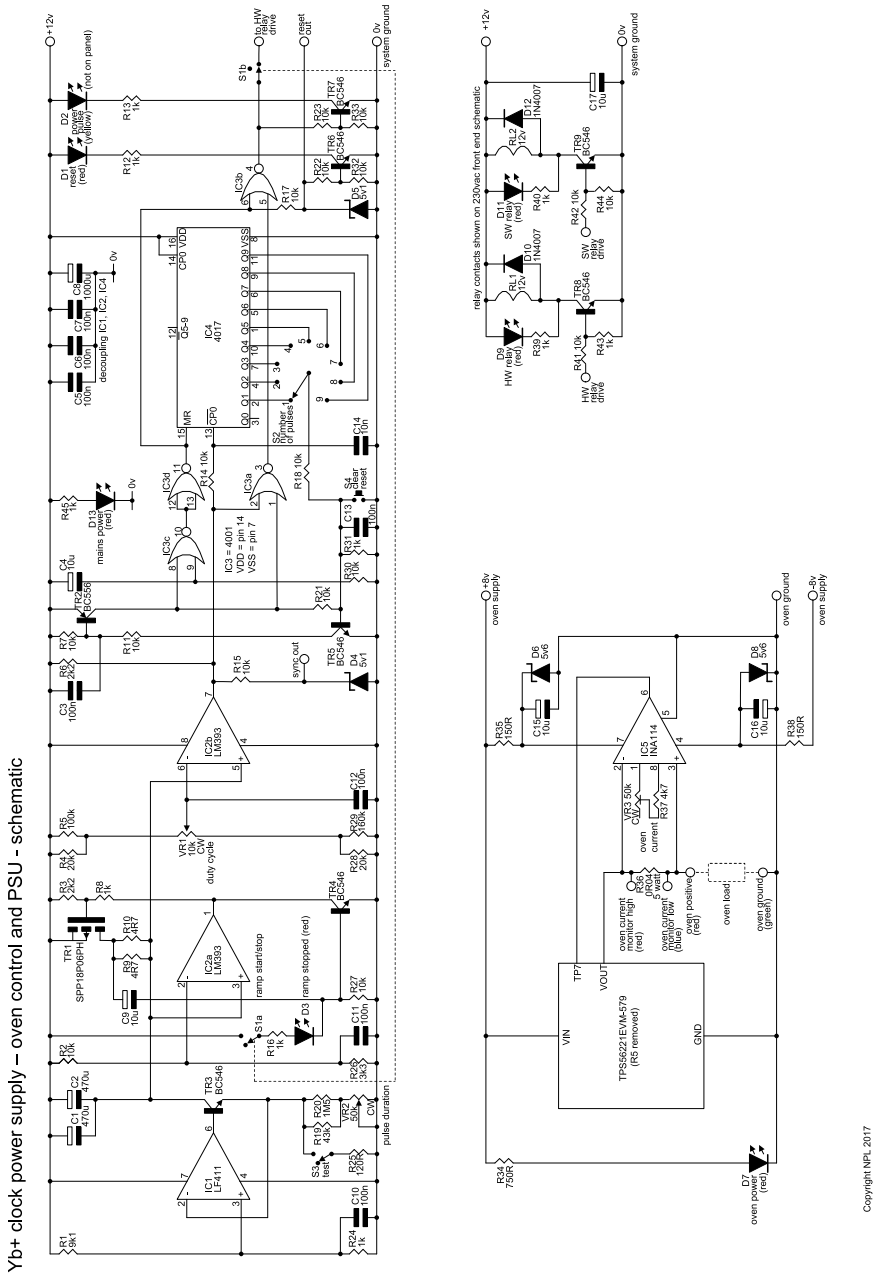


Figure B.9: Oven control and PSU. IC1, IC2a, TR1, TR3, TR4 and associated components generate a linear negative-going ramp with threshold-initiated flyback (sawtooth oscillator). The ramp appears at TR3 collector. The oscillator period, and therefore oven pulse duration, is controlled by VR2. IC2b is a ramp slicing comparator, with VR1 controlling the slicing level, from which pulse duty cycle is derived. IC3 and IC4 provide logic and counting for up to nine pulses, with TR2 and TR5 forming a latch to stop the pulse train after the required number. The relay drive signal is derived from IC3b output. On the power side, R36 is a current sensing resistor, the voltage across which is monitored by IC5. The output of IC5 is the feedback signal for the TPS56221 module — a 1 Volt, 25 Amp supply. The gain of IC5 is controlled by VR3 (panel mounted preset), allowing the oven current to be adjusted. TR8 and TR9 are the hardware and software relay drivers.

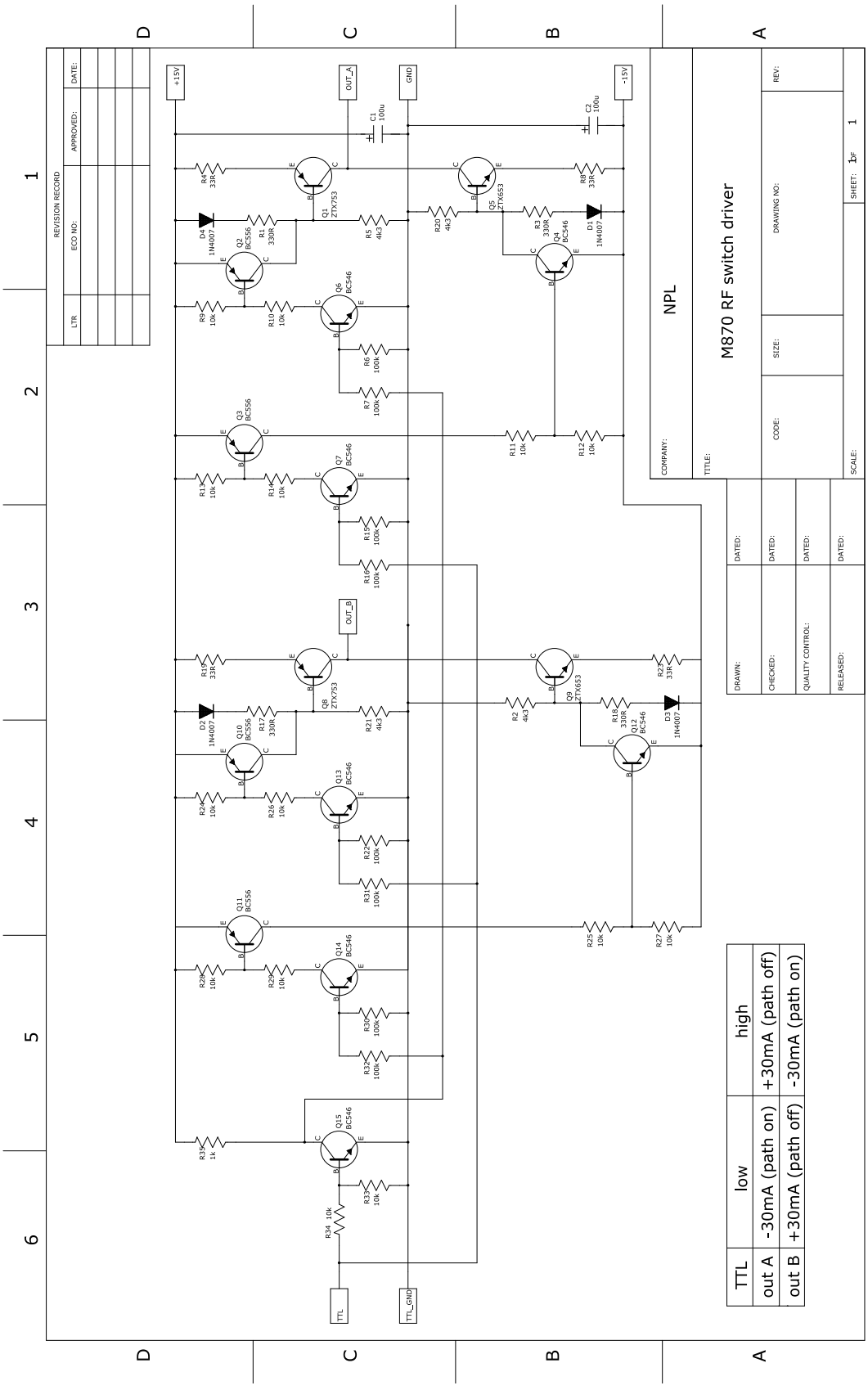


Figure B.10: Microwave switch driver

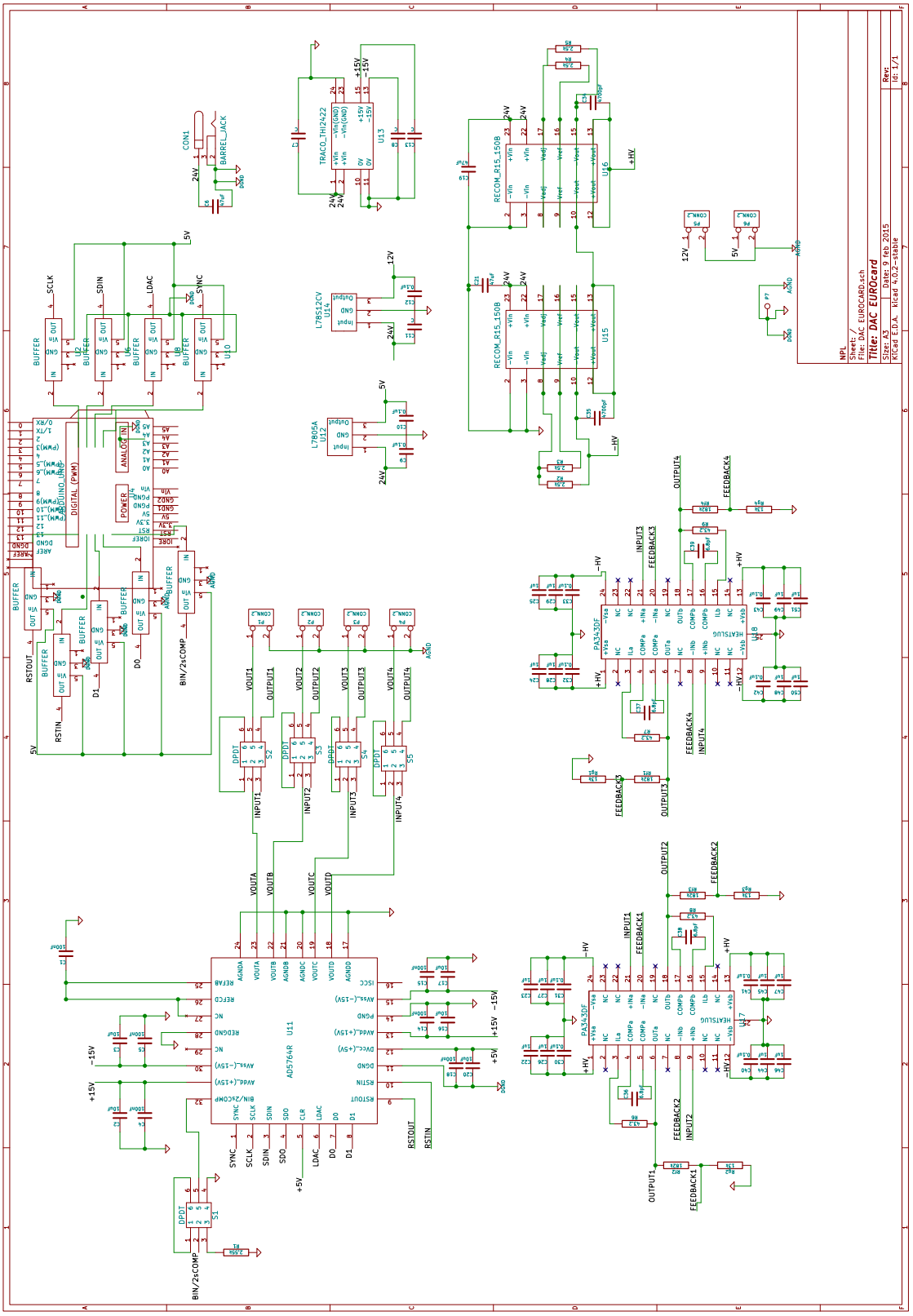


Figure B.11: Stable voltage sources

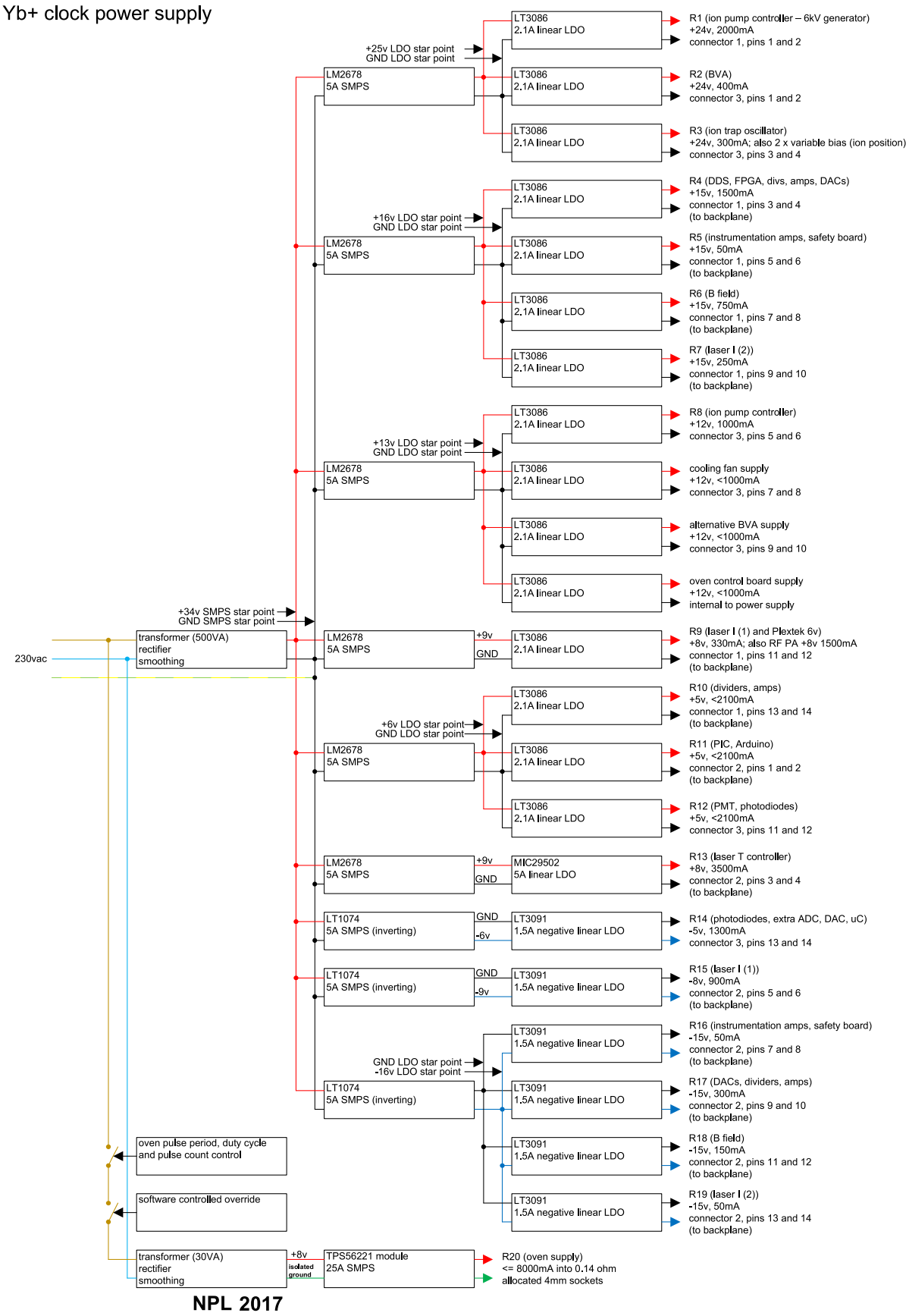
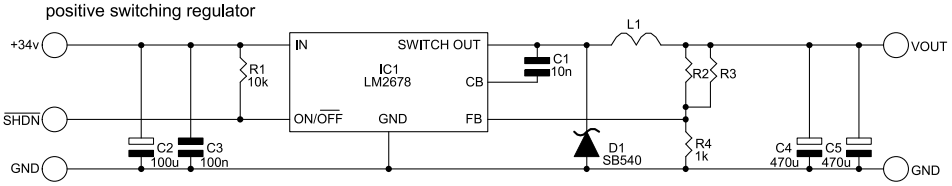


Figure B.12: Power supply block diagram

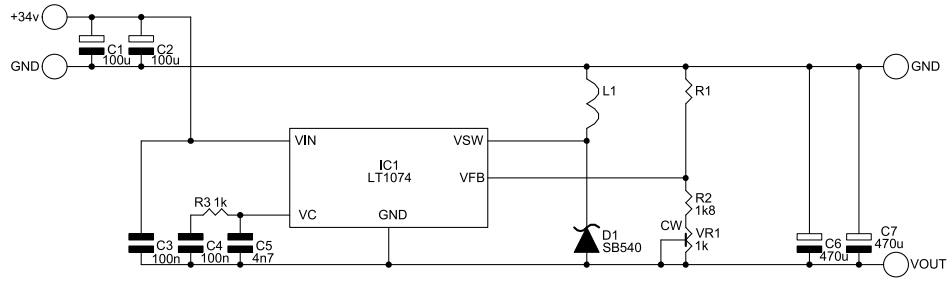
Yb+ clock power supply – switching and linear regulators - schematics

positive switching regulator



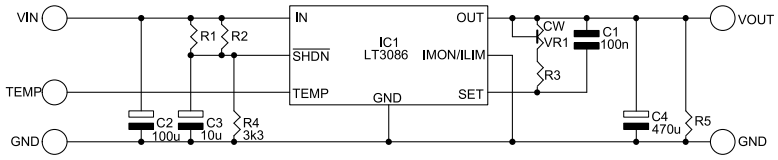
VOUT	L1(uH)	R2(kohm)	R3(kohm)
+25v	100	20	1200
+16v	68	13	200
+13v	100	10	390
+9v	100	6.8	120
+6v	33	4.3	51

inverting (negative) switching regulator



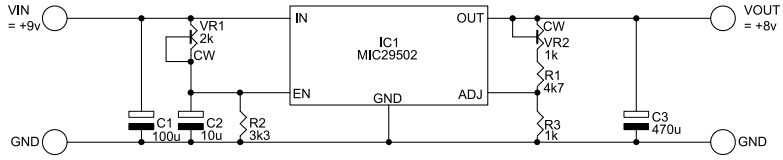
VOUT	L1(uH)	R1(kohm)
-6v	22	3.9
-9v	47	6.8
-16v	47	15

positive linear regulator (1)

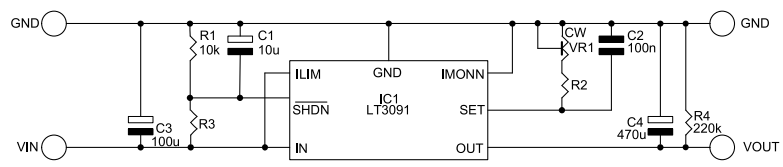


VOUT	VIN	R1(kohm)	R2(kohm)	R3(kohm)	R5(kohm)	VR1(kohm)
+24v	+25v	62	DNI	430	10	100
+15v	+16v	39	910	270	10	50
+12v	+13v	30	DNI	200	10	50
+8v	+9v	20	DNI	120	4.7	50
+5v	+6v	12	DNI	82	4.7	20

positive linear regulator (2) (5 amp)



negative linear regulator



VOUT	VIN	R2(kohm)	R3(kohm)	VR1(kohm)
-5v	-6v	91	36	20
-8v	-9v	150	56	20
-15v	-16v	270	100	50

Figure B.13: Switching and linear regulators

Yb+ clock power supply – 230V ac front end – schematic

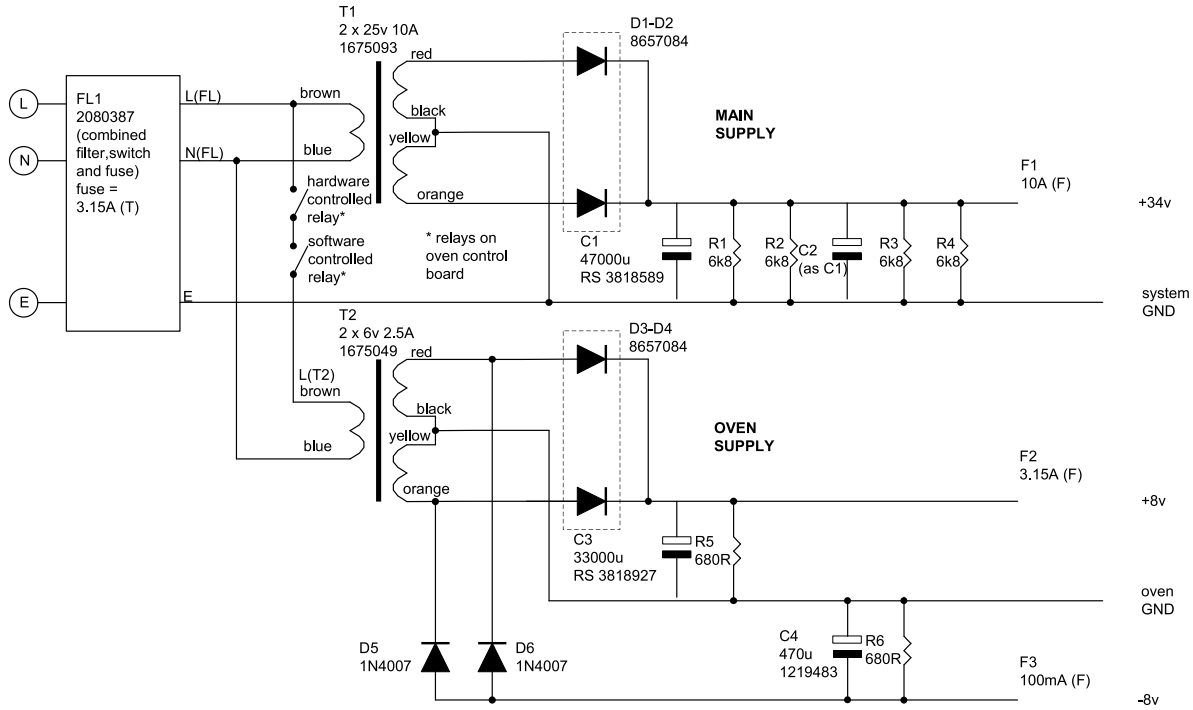


Figure B.14: Power supply schematic